Phase-Sensitive Light: Coherence Theory and Applications to Optical Imaging

by

Baris I. Erkmen

M. Eng., Electrical Engineering
Massachusetts Institute of Technology, 2003

S. B., Electrical Engineering
Massachusetts Institute of Technology, 2002

Submitted to the Department of Electrical Engineering and Computer Science
in partial fulfillment of the requirements for the degree of

Doctor of Philosophy in Electrical Engineering

at the

MASSACHUSETTS INSTITUTE OF TECHNOLOGY

June 2008

Author .....
Department of Electrical Engineering and Computer Science
March 26, 2008

Certified by .....
Jeffrey H. Shapiro
Julius A. Stratton Professor
Thesis Supervisor

Accepted by .....
Terry P. Orlando
Chair, Department Committee on Graduate Students

Phase-Sensitive Light: Coherence Theory and Applications to Optical Imaging

by

Baris I. Erkmen

Submitted to the Department of Electrical Engineering and Computer Science
on March 26, 2008, in partial fulfillment of the
requirements for the degree of
Doctor of Philosophy in Electrical Engineering

Abstract

Spontaneous parametric downconversion (SPDC) can produce pairs of entangled photons, i.e., a stream of biphotons. SPDC has been utilized in a number of optical imaging applications, such as optical coherence tomography, ghost imaging, holography and lithography, to obtain performance that cannot be realized with standard optical sources. However, a debate continues as to whether the improved imaging characteristics of such systems should be attributed to the entanglement property of the photon pairs. This thesis sets out to unify—and generalize—classical and quantum imaging within the framework of Gaussian-state light fields, which encompasses thermal light—the source used in conventional imagers—and biphoton-state light as special instances. Within this framework, we are able to provide a complete understanding of the boundary between classical and quantum behavior in optical coherence tomography (OCT), ghost imaging and two-photon imaging. Furthermore, we show that almost all characteristics of biphoton-state imagers are due to phase-sensitive cross correlations, and hence are obtainable with classical phase-sensitive sources.

Thesis Supervisor: Jeffrey H. Shapiro
Title: Julius A. Stratton Professor

Acknowledgments

Prof. Jeffrey H. Shapiro has been a true mentor, starting from my joining his group as a young and naive undergraduate researcher in 1999, and throughout my graduate school years to this date. His technical rigor in research, his attention to detail, and his insistence on determining the right question before embarking on a solution, is an inspiration to me today, and will continue to be so tomorrow.

I thank my committee members (in alphabetical order) Prof. Vincent W. S. Chan, Prof. Seth Lloyd and, Dr. Franco N. C. Wong, whom all have taken the time to seek the answers to my technical questions, provide advice in research and career matters alike, and have always been supportive of my doctoral research.

The ability to convey thoughts coherently to colleagues and younger generations is indispensable for a successful research career. I thank Prof. Alan V. Oppenheim and Prof. George C. Verghese for providing the opportunity to teach tutorials as a Teaching Assistant in Introduction to Communication, Control and Signal Processing, and their supportive feedback to help improve my teaching skills. It is their enthusiasm for teaching and their neverending dedication to improving the course that has kindled a strong desire in my heart to pursue teaching opportunities in the future.

Graduate students learn the most from each other, and I am grateful to my colleagues, Saikat Guha, Taehyun Kim, Onur Kuzucu, Dr. Mohsen Razavi and Prof. Brent Yen, for the many hours they have spent over the years answering my—not always intelligent!—technical questions.

I owe a great debt of gratitude to my parents, Aydan M. Erkmen and Ismet Erkmen, for not only their love and support throughout the many years of my undergraduate and graduate life, but also for their courage, their vision, and above all, their belief in my ability to succeed in pursuing a dream of excellence, no matter how far from home. This thesis is a tribute to their lifelong dedication to providing the best for their children. Likewise, I am infinitely grateful to my sister, Burcu N. Erkmen, for always providing unconditional love, support and care.

The most memorable years of my life have truly been the last six I have shared with my—almost!—fianceé, Alexandra H. Chau. From the bursts of laughter that ensue out of the most trivial of happenstance, to the long and serious technical discussions about our

research, she has brought indescribable fulfillment to my life.

In closing, I would like to express my professional gratitude to MIT as an institution, for its strong commitment to an open and collaborative research environment.

This work was supported by the U. S. Army Research Office MURI Grant W911NF-05-1-0197.

Contents

1 Introduction **15**

2 Preliminaries **19**

2.1 Semiclassical versus quantum photodetection 19

2.2 Phase-sensitive coherence in single-mode Gaussian states 21

2.3 Continuous-wave parametric downconversion 25

3 Coherence Theory for Phase-Sensitive Light **29**

3.1 Phase-sensitive coherence 30

3.2 Wolf equations for phase-sensitive correlations 33

3.3 Quasimonochromatic, paraxial correlation propagation 34

3.4 Normal-mode decomposition 41

3.5 From classical fields to quantum operators 48

3.6 Discussion 50

4 Optical Coherence Tomography with Phase-Sensitive Light **53**

4.1 Classical and nonclassical Gaussian-state light 54

4.2 OCT configurations and their interference signatures 56

4.3 Signal-to-noise ratio 61

4.4 Discussion 63

5 Unified Theory of Ghost Imaging with Gaussian-State Light **67**

5.1 Analysis 69

5.1.1 Jointly Gaussian states 71

5.1.2 Coherence propagation 76

5.1.3 Near-field versus far-field propagation 79

5.2 Near- and far-field ghost imaging with Gaussian-states 81
5.2.1 Ghost imaging with phase-insensitive light 81
5.2.2 Ghost imaging with phase-sensitive light 82
5.3 Image contrast 85
5.4 Relay optics 88
5.5 Discussion 89

6 Gaussian-State Theory of Two-Photon Imaging 95
6.1 Second-order coherence propagation 96
6.2 An exercise in far-field coherence propagation 101
6.2.1 Image contrast 106
6.3 Broadband imaging with a lens 108
6.4 Discussion 118

7 Gaussian-State Theory of Pulsed Parametric Downconversion 123
7.1 Preliminaries 125
7.2 Exact solution with flat-top pump pulse 130
7.3 From classical fields to quantum field operators 134
7.4 Full-interaction dominated output regime 135
7.5 Frequency-scaling and spectral phase conjugation 141
7.6 Coincident-frequency biphoton generation 143
7.7 Discussion 149

8 Axial Imaging with Spectrally White Phase-Sensitive Light 153
8.1 Self-referenced interferometry with phase-sensitive light 154
8.1.1 Mean signature 157
8.1.2 Signal-to-noise ratio 159
8.2 Discussion 162

9 Conclusions 167

A Proof for the Normal-Mode Decomposition 173

B Classical Gaussian States with Arbitrary Cross-Correlations 177

C Exact Solution to Coupled-Mode Equations **181**

D Commutator Invariance of Truncated Coupled-Mode Equations **189**

E Classical versus Quantum Sum-Coordinate Correlations **193**

List of Figures

2-1 The Wigner distribution and the time-evolution of the real quadrature is plotted for a quantum harmonic oscillator in a nonzero-mean, phase-insensitive Gaussian state. (a) Top view of the isotropic Wigner distribution. (b) The mean sinusoid (red) of the real quadrature is embedded in stationary noise, whose one standard-deviation noise-band is shown as the shaded region. . . 21

2-2 The Wigner distribution and the time-evolution of the real quadrature is plotted for a quantum harmonic oscillator in a nonzero-mean, phase-squeezed ($\phi = \pi/2$), quantum ((a)–(b)) and classical ((c)–(d)) phase-sensitive Gaussian state. 22

2-3 The Wigner distribution and the time-evolution of the real quadrature is plotted for a quantum harmonic oscillator in a nonzero-mean, amplitude-squeezed ($\phi = 3\pi/2$), quantum ((a)–(b)) and classical ((c)–(d)) phase-sensitive Gaussian state. 23

3-1 Ratio of normalized phase-sensitive to phase-insensitive on-axis correlations, $s_L^{(p)}/s_L^{(n)}$, plotted versus the inverse Fresnel number, D_o^{-1}, that distinguishes near-field from far-field propagation. 37

3-2 Comparison between the intensity radii of the phase-sensitive and phase-insensitive correlation spectra, $a_p(L)$ and $a_n(L)$, for a collimated Gaussian-Schell beam undergoing paraxial propagation. $a_p(L)$ and $a_n(L)$ are plotted versus the inverse Fresnel number, D_o^{-1}, showing the transition from near-field to far-field behavior. For illustrative purposes $\rho_0/a_T = 0.1$ is assumed, so that $D_d = 0.1D_o$ and $D_s = 10D_o$. 38

3-3 Comparison between coherence lengths of the phase-sensitive and phase-insensitive correlation spectra, $b_p(L)$ and $\rho(L)$, for a collimated Gaussian-Schell beam undergoing paraxial propagation. $b_p(L)$ and $\rho(L)$ are plotted versus the inverse Fresnel number, D_o^{-1}, showing the transition from near-field to far-field behavior. For illustrative purposes $\rho_0/a_T = 0.1$ is assumed, so that $D_d = 0.1D_o$ and $D_s = 10D_o$. 39

3-4 Level curves corresponding to the e^{-2} attenuation level for the phase-sensitive and phase-insensitive correlation spectra, both in the near field and the far field regimes (after L-m of propagation). The beam diameter at the source is a_T, ρ_0 is its coherence length and k_0 denotes the center wavenumber. . . 40

4-1 Phase-conjugate OCT configuration. 57

4-2 Conventional OCT configuration. 58

4-3 Quantum OCT configuration. 59

5-1 A simple ghost imaging setup. 70

5-2 Photodetection model. 71

5-3 Ghost imaging setup with relay optics. 89

6-1 Imaging the far-field diffraction pattern of a transmission mask. 102

6-2 Near-field imaging of a transmission mask. 109

6-3 Comparison of the imaging point-spread functions for phase-insensitive (PIS) and phase-sensitive (PS) correlations when $W/\omega_0 = 0.25$, and when the imaging source is quasimonochromatic (QM). The normalizing coefficient is $\kappa \equiv I_0\omega_0^2R^4/4c^2d_1^2d_2^2$. 113

6-4 Comparison of the imaging point-spread functions for phase-insensitive (PIS) and phase-sensitive (PS) correlations in the asymptotic broadband limit ($W/\omega_0 = 1$), and the quasimonochromatic (QM) limit. The normalizing coefficient is $\kappa \equiv I_0\omega_0^2R^4/4c^2d_1^2d_2^2$. 114

6-5 Image-plane spot diameters for different frequency components of a broadband point source. 115

6-6 Detecting the image-plane phase-sensitive cross-correlation via optical phase-conjugation. 117

7-1 The interaction region inside the crystal, which is determined by the overlap of the pump pulse and the crystal, is shown in the laboratory frame of reference (z, t) and the pump frame of reference (z', t'). 131

7-2 Time intervals of the signal (red) and idler (blue) inputs that undergo different interactions inside the crystal are shown at $z' = 0$. Similarly, time intervals of the output fields that result from different interaction regimes inside the crystal are marked at $z' = L$. Dashed line segments refer to input and output segments that do not overlap with the pump inside the crystal. The solid lines show the input field intervals that begin interacting with the pump inside the crystal and their one-to-one mapping onto the interaction region boundary. The dotted lines refer to the output fields that complete the interaction inside the crystal and separate from the pump, yielding a one-to-one mapping from the interaction rectangle. The dash-dotted segments indicate incomplete interactions due to the partial overlap between the pump and the crystal. 132

7-3 The frequency-domain envelope and phase modulation of $V(\Omega)$ is plotted for three different values of the interaction-strength parameter, $|\beta_P|T_P < \pi/2$. In the latter plot, $\phi_P = 0$ is assumed. 140

7-4 The second-order correlation spectra of $\hat{\mathcal{A}}_{S,W}(t)$ and $\hat{\mathcal{A}}_{I,W}(t)$ are plotted against baseband frequency, Ω. (a) The common fluorescence spectrum of the two field operators. The dash-dotted envelope shows that the spectrum decays as $|\beta_P|^2/\Omega^2$. (b) The real-valued phase-sensitive cross-correlation spectrum ($\phi_P = 0$). For comparison, the fluorescence spectrum is included as dash-dotted line. $S^{(p)}(\Omega)$ decays as $|\beta_P|/|\Omega|$, which is appreciably slower than the decay rate of the fluorescence spectrum. 145

7-5 Contour plots of the DB-state biphoton wavefunction magnitude from (7.74). The common parameters used in generating the figures are $|\beta_P|T_P = 7.182\pi \times 10^{-7}$, $|\Delta v_{PS}| = \Delta v_{PI} = 7.114 \times 10^3\,\mu$m/ps and $T_P = 75\,$fs. 148

8-1 Block diagram of imager using phase-sensitive, spectrally-white signal and reference fields in orthogonal polarizations. The receiver consists of a signal-arm spectral conjugator and a reference-arm variable time delay, followed by a second-order (Michelson) interferometer. PBS: polarizing beam splitter, HWP: half-wave plate, q: electron charge. 155

8-2 Block diagram of imager using phase-sensitive, spectrally-white, co-polarized signal and reference fields. The receiver consists of a signal-arm spectral conjugator and a reference-arm variable time delay, followed by a second-order (Michelson) interferometer. q is electron charge. 163

Chapter 1

Introduction

The past decade has witnessed significant attention devoted to utilizing biphotons—i.e. a pair of photons in an entangled quantum state—in optical imaging. Biphoton sources, in combination with coincidence counting, have been used to implement quantum versions of optical coherence tomography [1, 2, 3], ghost imaging [4, 5], holography [6] and lithography [7, 8]. In all of these applications, the ability to acquire an image has been attributed to the entanglement between the two photons, which implies that classical physics cannot account for their generation and detection. This understanding has been under much scrutiny, particularly since there have been successful experimental demonstrations of ghost imaging with thermal light sources, which can be described by classical physics [9, 10, 11, 12].

Unfortunately, the theoretical framework most often utilized in biphoton analysis focuses on the particle-like nature of the two photons, hence describing their state in terms of a wavefunction that is a superposition of their transverse positions, or in terms of an equivalent variable such as their momenta. This approach significantly differs from the theoretical framework used in traditional optical imaging analysis, which focuses on the wave-like nature of light and describes its coherence properties rather than the behavior of individual quanta [13, 14]. The incongruent nature of the two approaches and the lack of a theory that unifies the vast literature on biphoton and thermal-light imaging has made it difficult to provide analysis that satisfies both schools of thought. There have been a number of attempts to overcome the barrier between the two theories by developing analogies between the coherence properties of thermal light and the entanglement properties of biphotons [15, 16, 17]. Yet, because the analogies are still drawn between the particle nature of a

photon and the wave nature of a thermal field, these efforts fall short of a completely unifying theory.

In this thesis we will work within a framework that permits the unification of the two cases described above. In particular, we will assume that the sources generate Gaussian-state fields [18]. Gaussian states are defined as the class of optical fields for which the (Wigner) characteristic function is of Gaussian form, which also implies that the states of such fields are fully described by their first and second moments. Both the biphoton state and thermal states are instances of Gaussian-state light. In particular, the biphoton is the low-flux limit of a two-mode Gaussian-state field, in which the two modes share the maximum permitted phase-sensitive cross-correlation [18, 19]. On the other hand, thermal light is simply a Gaussian state with a circularly-symmetric (isotropic) Wigner characteristic function [14]. Thus, the class of Gaussian-state fields provide an excellent framework for unifying the theory of classical and quantum optical imaging.

Currently, a popular method for generating entangled biphotons is parametric down-conversion. The output fields of a parametric downconverter are in a nonclassical jointly Gaussian state, characterized completely by their phase-insensitive auto-correlations and a phase-sensitive cross-correlation that is higher than the maximum limit allowed in classical physics [19]. The biphoton state corresponds to the low-flux limit of such a state. This Gaussian-state description of the parametric downconverter's output reveals two fundamental differences between biphoton imagers and traditional thermal-light imagers. The first is the fact that the coherence between the two modes in a parametric downconverter is a phase-sensitive correlation, whereas thermal sources have phase-insensitive correlation. The second feature is that the phase-sensitive cross-correlation in a biphoton is stronger than the limit set by classical physics (for Gaussian states this is equivalent to stating that the two modes of the light are entangled). Distinguishing between these two features is relevant, because classical light may also have phase-sensitive correlation, and therefore, those features observed in biphoton imagers that do not require a stronger-than-classical correlation can, in principle, be replicated with classical light. The unified Gaussian-state treatment of classical and quantum sources will permit us to identify these features, and establish a quantum/classical boundary for the performance of optical imagers. Furthermore, this classification will allow us to explore new imaging configurations that capture the features of biphoton imagers which fall in the former category, without the need for

nonclassical light sources.

Because images obtained from biphoton imagers exploit the phase-sensitive coherence of the source, a fundamental understanding of phase-sensitive coherence theory is a prerequisite to identifying the characteristics of the images obtained using such sources. However, the vast literature on optical coherence theory—both classical and quantum—is almost entirely devoted to the study of the phase-insensitive correlations in a field, perhaps because most commonly employed classical sources, such as the sun, laser light, LED's etc., generate fields with only phase-insensitive correlations. Thus at a fundamental level, there is a need to develop a corresponding theory for the coherence properties of phase-sensitive optical fields, which is another goal of this thesis.

This thesis is organized as follows. In Chapter 2 we establish the foundation for the remaining chapters by reviewing several key concepts. In Section 2.1 we quantify the classical and quantum states of light. Section 2.2 is devoted to reviewing classical and quantum phase-sensitive coherence for Gaussian states. Finally, the chapter concludes in Section 2.3, with an analysis of continuous-wave spontaneous parametric downconversion.

The novel contributions of this thesis begin with Chapter 3, which studies the coherence properties of scalar, classical and quantum phase-sensitive light in free-space[1]. Sections 3.2–3.4 are devoted to coherence theory for classical phase-sensitive light, whereas Section 3.5 converts and extends these classical results to those for quantum field operators whose state has phase-sensitive coherence.

We then turn our attention to several imaging applications in which this coherence is exploited. Chapter 4 proposes a new configuration for optical coherence tomography that relies on classical-state phase-sensitive light[2], yet achieves the same improvements observed in optical coherence tomography performed with a biphoton source [1, 2, 3]. The theory of ghost imaging is developed in Chapter 5, utilizing a Gaussian-state framework that unifies prior ghost imaging work—on thermal-state and biphoton-state configurations—and provides a complete understanding of the boundary between classical and quantum behavior in such systems.[3] Finally, Chapter 6 applies Gaussian-state analysis to imaging of a transmission mask at the image-plane and at the Fourier-plane of a lens, which yields a generalized and complete understanding of its classical and quantum properties.

[1]This chapter is based on results reported in [20].
[2]This configuration has been proposed and analyzed in [21, 22].
[3]This chapter is based on [23, 24].

Whereas Chapters 2–6 consider complex-stationary source statistics, starting with Chapter 7 our attention shifts to a nonstationary phase-sensitive Gaussian-state source, which consists of a superposition of independently-squeezed frequency components. Sections 7.1–7.4 provide a complete derivation of the input/output relation for the pulsed parametric downconverter that generates this state. Several applications of this downconversion process are then considered in Section 7.5, and the output Gaussian state with the desired nonstationary phase-sensitive correlation is derived for vacuum inputs in Section 7.6.

In Chapter 8, we propose a phase-sensitive white-light imager which uses the Gaussian-state source studied in the previous chapter to infer the complex-valued frequency response of a linear system. Both classical and quantum Gaussian states are considered in the analysis and the signal-to-noise ratio properties are discussed in detail.

Finally, we conclude this thesis in Chapter 9, with a summary of its novel contributions, and a discussion of possible future extensions to the material presented herein.

Chapter 2

Preliminaries

The subsequent chapters depend on several fundamental concepts from classical and quantum optics, which are worth reviewing in this chapter, prior to moving forward. A principal goal of this thesis is to identify the classical/quantum boundary in low-coherence optical imaging applications via the study of sources in classical and quantum states with phase-sensitive coherence. Therefore, in Section 2.1, we first establish a formal definition of 'classical' states, based on the semiclassical and quantum theories of photodetection. We then motivate phase-sensitive coherence in Section 2.2, using single-mode Gaussian states as an example. The emphasis in this section is on the common and distinct features of the phase-sensitive correlation found in classical and quantum Gaussian states. Finally, in Section 2.3, we briefly review continuous-wave parametric downconversion and determine the jointly-Gaussian state of the two output fields.

2.1 Semiclassical versus quantum photodetection

Consider an ideal photodetector, i.e, one with unity quantum efficiency, zero dark current and infinite electrical bandwidth, for which individual photon detection events are registered instantaneously as current impulses carrying charge q. In semiclassical theory, the scalar optical field impinging on the photosensitive surface of the photodetector at transverse coordinate $\boldsymbol{\rho}$ and time t is a positive-frequency classical electromagnetic wave, denoted by $E(\boldsymbol{\rho}, t)e^{-i\omega_0 t}$. We assume that this field is paraxial, normalized to have units $\sqrt{\text{photons/m}^2\text{s}}$, and has center frequency ω_0. Conditioned on knowledge of the field impinging on the photodetector, we have that $i(t)/q$, the charge normalized photocurrent, is

an inhomogeneous Poisson impulse train with rate function [25, 26]

$$\mu(t) = \int_{\mathcal{A}} \mathrm{d}\boldsymbol{\rho}\, |E(\boldsymbol{\rho}, t)|^2 \,, \tag{2.1}$$

where $\mathcal{A}$ is the detector's photosensitive region. Thus, regardless of whether the illuminating field is deterministic or random, the photocurrent is subject to the noise that is inherent in this Poisson process, which yields the well known shot-noise floor of semiclassical photodetection theory [18]. Randomness in the illumination is then accounted for by taking $E(\boldsymbol{\rho}, t)$ to be a stochastic process, as is done in classical statistical optics [13].

In the quantum theory of photodetection, the classical photocurrent produced by the same ideal photodetector is a stochastic process whose statistics coincide with those of the photon-flux operator measurement scaled by the electron charge [27],

$$\hat{\imath}(t) = q \int_{\mathcal{A}} \mathrm{d}\boldsymbol{\rho}\, \hat{E}^\dagger(\boldsymbol{\rho}, t)\hat{E}(\boldsymbol{\rho}, t) \,. \tag{2.2}$$

The photocurrent statistics are then governed by the state of the field operator $\hat{E}(\boldsymbol{\rho}, t)$, so the shot-noise limit of semiclassical theory can be surpassed by some states, such as amplitude-squeezed states, or the eigenkets of continuous-time photodetection [18, 27, 28].

In our quantum treatment of imaging, the states of the optical field operator $\hat{E}(\boldsymbol{\rho}, t)$ that we shall deem *classical* are those for which the measurement statistics predicted by quantum photodetection theory match those predicted by the semiclassical theory. It has long been known [18, 27] that when $\hat{E}(\boldsymbol{\rho}, t)$ is in the coherent state $|E(\boldsymbol{\rho}, t)\rangle$, indexed by its eigenfunction $E(\boldsymbol{\rho}, t)$ and satisfying

$$\hat{E}(\boldsymbol{\rho}, t)|E(\boldsymbol{\rho}, t)\rangle = E(\boldsymbol{\rho}, t)|E(\boldsymbol{\rho}, t)\rangle \,, \tag{2.3}$$

the statistics of the $\hat{\imath}(t)$ measurement are identical to those from the semiclassical theory with the impinging classical field taken to be $E(\boldsymbol{\rho}, t)$. More generally, the two photodetection theories yield identical statistics for any quantum state that is a classical statistical mixture of coherent states—viz., for all states that have proper P-representations [14]—when the classical field used in the semiclassical theory is comprised of the same statistical mixture of the coherent-state eigenfunctions [18, 19, 29]. Moreover, mixtures of coherent states are the only quantum states for which all quantum photodetection statistics coincide with the

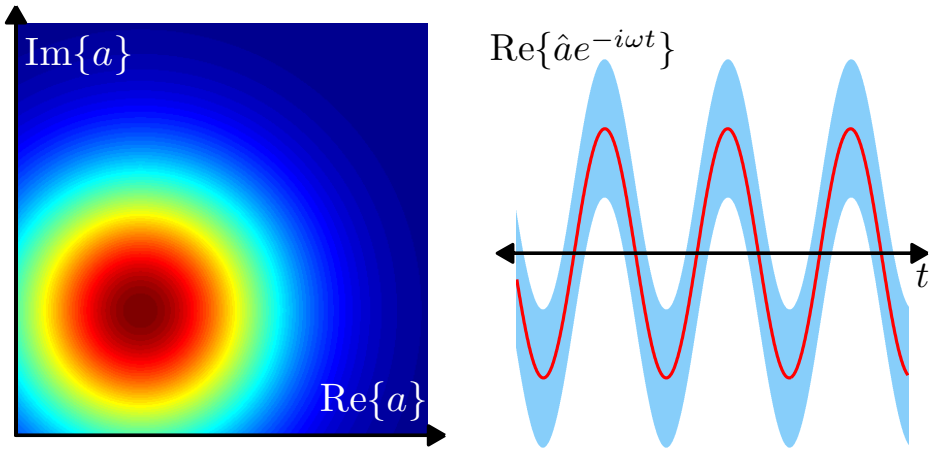

(a) Wigner distribution **(b)** Real quadrature

Figure 2-1: The Wigner distribution and the time-evolution of the real quadrature is plotted for a quantum harmonic oscillator in a nonzero-mean, phase-insensitive Gaussian state. (a) Top view of the isotropic Wigner distribution. (b) The mean sinusoid (red) of the real quadrature is embedded in stationary noise, whose one standard-deviation noise-band is shown as the shaded region.

corresponding results found from the semiclassical theory.

The quantum and semiclassical theories of photodetection accord very different physical interpretations to their fundamental noise sources—quantum noise of the illuminating field versus shot noise arising from the discreteness of the electron charge—but for quantum states with proper P-representations their predictions are quantitatively indistinguishable. So, because all imaging configurations in this thesis derive their image signatures from photodetection measurements, their performance with classical states of light may be derived from the semiclassical theory with no loss of generality. Throughout the subsequent chapters, we often utilize this quantitative equivalence to determine the classical performance of various imagers.

2.2 Phase-sensitive coherence in single-mode Gaussian states

Consider a single spatiotemporal mode of an optical field, described via an annihilation operator $\hat{a}$, which satisfies the commutator relation $[\hat{a}, \hat{a}^\dagger] = 1$. The density operator of this mode, $\hat{\rho}$, represents a Gaussian state if its Wigner characteristic function is a Gaussian,

$$\chi_W^{(\hat{\rho})}(\zeta, \zeta^*) \equiv \mathrm{Tr}(\hat{\rho} e^{-\zeta^* \hat{a} + \zeta \hat{a}^\dagger}) = e^{-\zeta^* \langle \hat{a} \rangle + \zeta \langle \hat{a} \rangle^* - (\langle \Delta \hat{a}^\dagger \Delta \hat{a} \rangle + 1/2)|\zeta|^2 + \Re\{\zeta^2 \langle \Delta \hat{a}^2 \rangle^*\}}, \tag{2.4}$$

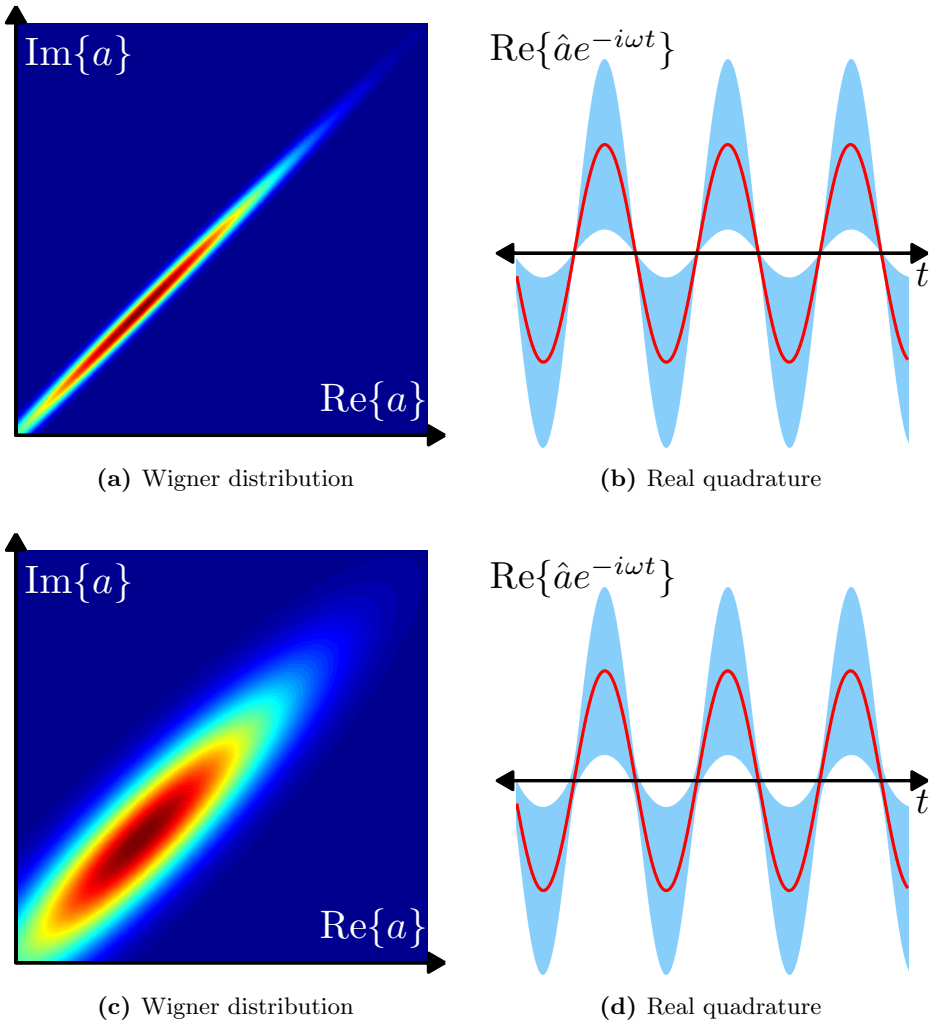

(a) Wigner distribution

(b) Real quadrature

(c) Wigner distribution

(d) Real quadrature

Figure 2-2: The Wigner distribution and the time-evolution of the real quadrature is plotted for a quantum harmonic oscillator in a nonzero-mean, phase-squeezed ($\phi = \pi/2$), quantum ((a)–(b)) and classical ((c)–(d)) phase-sensitive Gaussian state.

where $\langle \hat{a} \rangle$ denotes the mean, $\langle \Delta\hat{a}^\dagger \Delta\hat{a} \rangle$ is the (normally-ordered) variance, and $\langle \Delta\hat{a}^2 \rangle$ is the phase-sensitive covariance, in terms of the zero-mean field operator $\Delta\hat{a} \equiv \hat{a} - \langle \hat{a} \rangle$.

Let us compare three subclasses of Gaussian states that are of primary interest in the upcoming chapters. A phase-insensitive Gaussian state with $\langle \hat{a} \rangle = \alpha_0$, $\langle \Delta\hat{a}^\dagger \Delta\hat{a} \rangle = N$ and $\langle \Delta\hat{a}^2 \rangle = 0$, is an isotropic mixture of coherent states (mean-displaced thermal state) with a proper P-representation,

$$\hat{\rho} = \int_{\mathbb{R}^2} \mathrm{d}^2\alpha \left[e^{-|\alpha - \alpha_0|^2/N} / (\pi N) \right] |\alpha\rangle\langle\alpha|, \tag{2.5}$$

where $|\alpha\rangle$ represents a coherent state with eigenvalue $\alpha \in \mathbb{C}$. The Wigner distribution

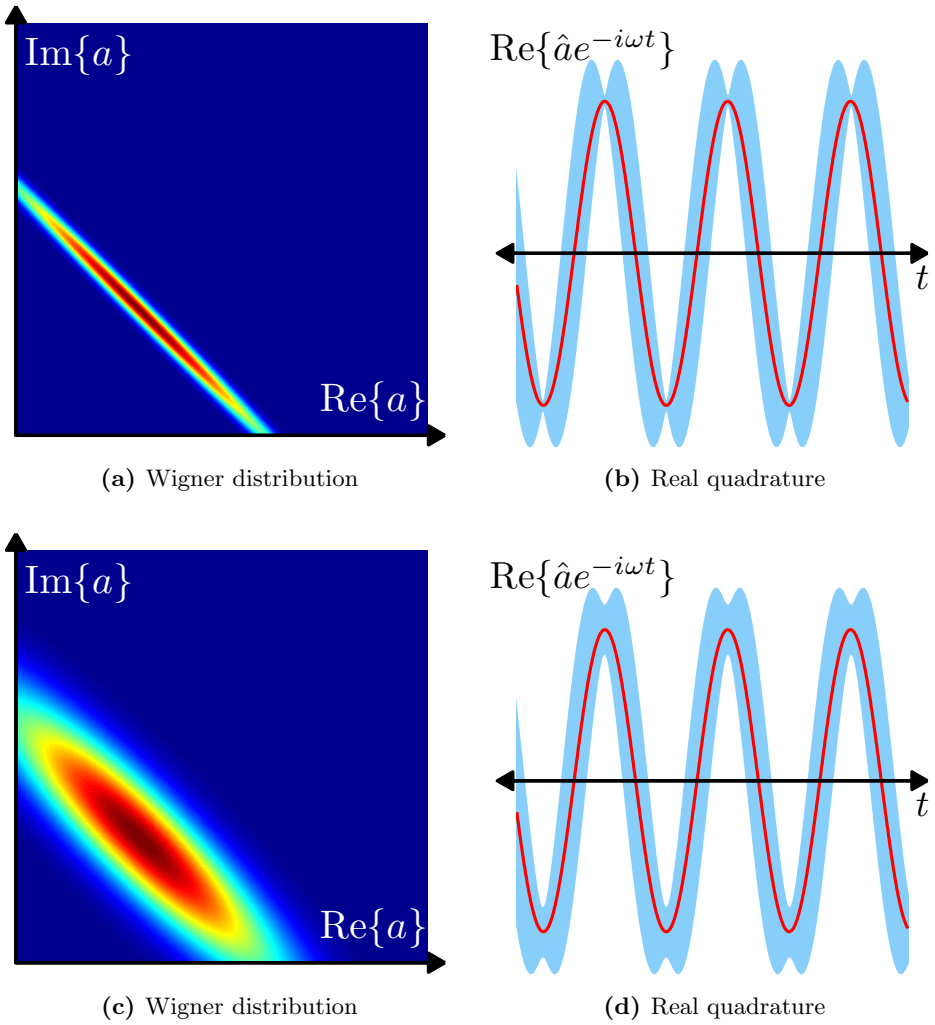

(a) Wigner distribution

(b) Real quadrature

(c) Wigner distribution

(d) Real quadrature

Figure 2-3: The Wigner distribution and the time-evolution of the real quadrature is plotted for a quantum harmonic oscillator in a nonzero-mean, amplitude-squeezed ($\phi = 3\pi/2$), quantum ((a)–(b)) and classical ((c)–(d)) phase-sensitive Gaussian state.

(inverse Fourier transform of the Wigner characteristic function) for this state is shown in Figure 2-1(a). Due to the zero phase-sensitive covariance, the Wigner distribution is isotropic around the mean-value. Consequently, the mean sinusoid of the real quadrature $\Re\{\hat{a}e^{-i\omega t}\}$, shown Figure 2-1(b), is embedded in stationary noise, denoted in the figure by the uniform shaded region corresponding to one standard deviation around the mean. The lack of phase-dependence in this noise motivates the terminology 'phase-insensitive noise.'

Next, we consider a Gaussian state with the same mean and variance as before, but $\langle \Delta\hat{a}^2 \rangle = \sqrt{N(1+N)}e^{i\phi}$, which is a *nonclassical* Gaussian state with maximum phase-sensitive covariance magnitude, given the variance N [18]. This is a squeezed state which

may be obtained by first squeezing a vacuum-state mode via the Bogoliubov transformation

$$\hat{a} = \sqrt{1+N}e^{i\phi}\hat{a}_{vac} + \sqrt{N}\hat{a}^{\dagger}_{vac}\,, \tag{2.6}$$

and then displacing it by α_0. Figure 2-2(a) and Figure 2-3(a) show the resulting Wigner distributions for $\phi = \pi/2$ and $\phi = 3\pi/2$ respectively. Because squeezed states are minimum-uncertainty-product states, the circularly symmetric isocontours of the Wigner distribution is transformed into ellipses of the same area, and with their major axes $\phi/2$-rotated with respect to the real axis. Consequently, the real quadrature of $\hat{a}$ consists of a mean sinusoid embedded in *nonstationary* noise whose strength varies as a function of the phase of the sinusoid. In particular, Figure 2-2(b) shows phase-squeezed noise, because the noise is minimum at the zeros of the mean, whereas Figure 2-3(b) is amplitude-squeezed noise, because the noise is minimum at the peaks and troughs of the mean.

It is worth emphasizing at this juncture that phase-sensitive noise behavior is *not* restricted to nonclassical states. To see this, we consider a Gaussian state with the same mean and variance as the previous case, but now with phase-sensitive covariance reduced to $\langle \Delta\hat{a}^2 \rangle = Ne^{i\phi}$. Via the Cauchy-Schwarz inequality for classical complex random variables, it is straightforward to verify that this is the maximum attainable phase-sensitive covariance magnitude with a *classical* Gaussian state of variance N [19]. In particular, the density operator of this state is given as

$$\hat{\rho}_{cl} = \int_{-\infty}^{\infty} \mathrm{d}x \left[e^{-x^2/2N}/\sqrt{2\pi N} \right] |xe^{i\phi/2} + \alpha_0\rangle\langle xe^{i\phi/2} + \alpha_0| \,. \tag{2.7}$$

The resulting Wigner distributions for $\phi = \pi/2, 3\pi/2$ are shown in Figure 2-2(c) and Figure 2-3(c) respectively. The mixed-state nature of these classical phase-sensitive states is reflected in the larger area of the isocontour ellipses in comparison to those of the corresponding squeezed states. However, the quadrature noise behavior shown in Figure 2-2(d) and Figure 2-3(d) for the $\phi = \pi/2, 3\pi/2$ cases respectively, display similar phase-sensitive noise behavior to their squeezed-state counterparts. The only apparent difference between the two cases is the minimum attainable noise: the classical phase-sensitive state cannot surpass the minimum noise variance of 1/4 (sometimes referred to as the shot-noise limit) because it is a mixture of coherent states, whereas the noise minimum for a squeezed state is strictly less than 1/4, because it is a minimum-uncertainty-product pure state [14, 30].

The conclusions from this simple single-mode discussion generalize to multiple spatiotemporal modes and multiple-field Gaussian states as well. In particular, phase-sensitive quadrature noise is *not* exclusive to quantum (nonclassical) Gaussian states. However, attaining minimum noise variance below the shot-noise limit is possible only with nonclassical (phase-sensitive) Gaussian states.[1]

2.3 Continuous-wave parametric downconversion

Pairs of entangled photons (biphotons) that are generated via spontaneous parametric downconversion (SPDC) are the predominant source used in quantum imaging experiments. Therefore proper characterization of the source fields' joint state is relevant to ascertaining the classical/quantum boundary in optical imaging. In this section, we derive the output state of this process assuming the region of interest is tightly confined around the optical axis, so that the fields may be approximated as plane waves.

Consider a second-order ($\chi^{(2)}$) nonlinear, length-L crystal that is type-II phase-matched at degeneracy, and has its input facet aligned at $z = 0$. When this crystal is pumped with a nondepleting, z-propagating, frequency-$2\omega_0$ (monochromatic), plane-wave pump, the interaction of pump photons with phase-matched vacuum fluctuations inside the crystal generates two broadband fields at its output, with equal center-frequencies ω_0, and in orthogonal polarizations. The photon-units ($\sqrt{\text{photons/s}}$), positive-frequency and scalar signal field operator is given by

$$\hat{E}_S(L,t)e^{-i\omega_0 t} = \int \frac{\mathrm{d}\Omega}{2\pi}\, \hat{A}_S(L,\Omega)\, e^{ik_S(\omega_0+\Omega)\, L - i(\omega_0+\Omega)t}\,, \tag{2.8}$$

and the corresponding reference field operator is[2]

$$\hat{E}_R(L,t)e^{-i\omega_0 t} = \int \frac{\mathrm{d}\Omega}{2\pi}\, \hat{A}_R(L,\Omega)\, e^{ik_R(\omega_0+\Omega)\, L - i(\omega_0+\Omega)t}\,, \tag{2.9}$$

where $k_m(\omega)$, for $m = S, R$, denotes the dispersion relations for the respective polarizations of the signal and reference. Here the frequency-domain, baseband field operators, $\hat{A}_S(L,\Omega)$

[1] Here we are restricting our discussion to Gaussian states. Of course, non-Gaussian states with zero phase-sensitive covariance can easily surpass the shot-noise limit, e.g., number (Fock) states.

[2] While it is conventional practice to refer to the output fields from SPDC as signal and idler, we will denote them signal and reference in keeping with the use of the latter as a reference field in quantum imaging configurations that we will study.

and $\hat{A}_R(L,\Omega)$, satisfy the free-space commutator brackets,

$$[\hat{A}_m(z,\Omega_1), \hat{A}_k^\dagger(z,\Omega_2)] = \delta_{m,k}\, 2\pi\delta(\Omega_2 - \Omega_1)\,, \tag{2.10}$$

$$[\hat{A}_m(z,\Omega_1), \hat{A}_k(z,\Omega_2)] = 0\,, \tag{2.11}$$

for $m,k = S,R$, and are solutions to the (commutator-preserving) coupled-mode equations,

$$\frac{\partial}{\partial z}\hat{A}_S(z,\Omega) = i\kappa\hat{A}_R^\dagger(z,-\Omega)e^{i\Omega\Delta k' z}\,, \tag{2.12}$$

$$\frac{\partial}{\partial z}\hat{A}_R(z,-\Omega) = i\kappa\hat{A}_S^\dagger(z,\Omega)e^{i\Omega\Delta k' z}\,, \tag{2.13}$$

where $\Delta k' \equiv 1/v_S - 1/v_R$ is the mismatch between the signal group velocity v_S and that of the reference v_R, and κ is the coupling coefficient in units of m^{-1}.

Consequently, the baseband field-operators at $z = L$ are two-field Bogoliubov transformations of the vacuum-state input fields at $z = 0$,

$$\hat{A}_S(L,\Omega) = \hat{A}_S(0,\Omega)\, M(\Omega) + \hat{A}_R^\dagger(0,-\Omega)\, V(\Omega)\,, \tag{2.14}$$

$$\hat{A}_R(L,-\Omega) = \hat{A}_R(0,-\Omega)\, M(\Omega) + \hat{A}_S^\dagger(0,\Omega)\, V(\Omega)\,, \tag{2.15}$$

where

$$M(\Omega) = e^{i\Omega\Delta k' L/2}\big[\cosh(pL) - i(\Omega\Delta k'/2p)\sinh(pL)\big]\,, \tag{2.16}$$

$$V(\Omega) = e^{i\Omega\Delta k' L/2} i(\kappa/p)\sinh(pL)\,, \tag{2.17}$$

in terms of the interaction-strength parameter, $p \equiv \sqrt{|\kappa|^2 - (\Omega\Delta k'/2)^2}$.

Because the vacuum-state inputs correspond to a pure, minimum-uncertainty-product, zero-mean jointly-Gaussian state, and the Bogoliubov transformations are linear, the output fields are also in a pure, minimum-uncertainty-product, zero-mean jointly Gaussian state, determined completely by the second-order correlation functions of the output. It is easy to verify from (2.14) and (2.15) that the only nonzero second moments of the outputs are the phase-insensitive (normally-ordered) auto-correlation functions,

$$\langle \hat{A}_m^\dagger(L,\Omega_1)\hat{A}_m(L,\Omega_2)\rangle = S^{(n)}(\Omega_1)\, 2\pi\delta(\Omega_2 - \Omega_1)\,, \tag{2.18}$$

for $m = S, R$, and the phase-sensitive cross-correlation function between the two fields,

$$\langle \hat{A}_S(L, \Omega_1) \hat{A}_R(L, \Omega_2) \rangle = S^{(p)}(\Omega_1)\, 2\pi\delta(\Omega_2 + \Omega_1)\,, \tag{2.19}$$

where $S^{(n)}(\Omega) = |V(\Omega)|^2$ is the identical fluorescence spectrum of the two fields, and $S^{(p)}(\Omega) = M(\Omega)V(\Omega)$ is the phase-sensitive cross-correlation strength between frequencies whose average is the center frequency, ω_0.

Similar to single-mode squeezing, the phase-sensitive cross-correlation spectrum's magnitude satisfies $|S^{(p)}(\Omega)| = \sqrt{S^{(n)}(\Omega)(1 + S^{(n)}(\Omega))}$, which is the maximum for any two fields in a nonclassical joint state and with fluorescence spectra $S^{(n)}(\Omega)$ [18]. Thus, the (joint) output state of a parametric downconverter is a zero-mean, nonclassical Gaussian state with identical fluorescence spectra for the signal and reference, and maximum phase-sensitive cross-correlation, but with no phase-sensitive auto-correlations and no phase-insensitive cross-correlation.

Chapter 3

Coherence Theory for Phase-Sensitive Light

Arbitrary second moments of the complex envelope of a stochastic, scalar optical field are completely characterized by that field's phase-insensitive and phase-sensitive correlation functions. Optical coherence theory—for both classical and quantum fields—has been developed almost exclusively for phase-insensitive light fields, because most commonly encountered sources, such as sunlight, LED's, and lasers, have only phase-insensitive correlations [13, 14]. However, advances in nonlinear and quantum optics have opened the door to generating fields with nonzero phase-sensitive correlations. The best known light fields possessing phase-sensitive correlations are the squeezed states of light [31]. Less well known is the fact that the biphoton state [32], which has received a great deal of recent attention owing to its entanglement properties, is the low-flux limit of phase-sensitive Gaussian-state light generated by parametric downconversion [19]. Although these examples are both nonclassical states, classical optical field states with phase-sensitive coherence can also be generated, for example, via complex (amplitude and phase) modulations of coherent-state light, or by exploiting the classical regime (high-flux limit) of nonlinear processes involving phase conjugation. Thus, at a fundamental level, there is a need to investigate the coherence properties of phase-sensitive optical fields, and to develop a unified framework within which nonclassical phase-sensitive coherence and classical phase-sensitive coherence may be compared.

As a first step toward fulfilling the preceding need, this chapter will establish some new

results in phase-sensitive coherence theory. The majority of the chapter will be devoted to studying classical scalar fields with phase-sensitive fluctuations, and the connection to quantum field operators will be established thereafter. We begin, in Section 3.1, by identifying a class of fields that is sufficiently broad to allow a systematic study of phase-sensitive coherence, yet restrictive enough to allow us to draw some physical conclusions. Then, in Section 3.2, we show how the Wolf equations—for propagating a phase-insensitive coherence through free space—apply to free-space propagation of phase-sensitive correlation functions. Next, in Section 3.3, we specialize our attention to paraxial free-space propagation for Gaussian-Schell model sources with phase-sensitive fluctuations. We return to the Wolf equations in Section 3.4, where we use a symplectic basis to find the normal-mode decomposition for free-space propagation of phase-sensitive light. In Section 3.5, we explain how to convert our coherence theory for classical phase-sensitive fields to one for quantum field operators in states with phase-sensitive noise, and in Section 3.6, we relate the latter to previous work on the coherence properties of the biphoton state [15, 16, 17, 33].

3.1 Phase-sensitive coherence

Consider a stochastic, scalar electric field with center frequency ω_0 and baseband complex envelope $E(\mathbf{r},t) \equiv E_R(\mathbf{r},t) + iE_I(\mathbf{r},t)$, where $E_R(\mathbf{r},t)$ and $E_I(\mathbf{r},t)$ denote the real and imaginary parts respectively. Without loss of generality, we shall assume that this field has zero mean, $\langle E(\mathbf{r},t)\rangle = 0$, so that the second-order characterization of the complex envelope is fully specified by three real-valued functions: the auto-correlation functions of the real and imaginary parts, $K_{R,R}(\mathbf{r_1},t_1,\mathbf{r_2},t_2) \equiv \langle E_R(\mathbf{r_1},t_1)E_R(\mathbf{r_2},t_2)\rangle$ and $K_{I,I}(\mathbf{r_1},t_1,\mathbf{r_2},t_2)) \equiv \langle E_I(\mathbf{r_1},t_1)E_I(\mathbf{r_2},t_2)\rangle$ respectively, and the cross-correlation between the real and imaginary part, $K_{R,I}(\mathbf{r_1},t_1,\mathbf{r_2},t_2) \equiv \langle E_R(\mathbf{r_1},t_1)E_I(\mathbf{r_2},t_2)\rangle$, where we have used angle brackets to denote the expectation over a classical ensemble of functions. These three real functions can be expressed more compactly as two complex-valued functions, namely as the phase-insensitive correlation function

$$\begin{aligned} &K^{(n)}(\mathbf{r}_1,t_1,\mathbf{r}_2,t_2) \equiv \langle E^*(\mathbf{r}_1,t_1)E(\mathbf{r}_2,t_2)\rangle \\ &= K_{R,R}(\mathbf{r}_1,t_1,\mathbf{r}_2,t_2)+K_{I,I}(\mathbf{r}_1,t_1,\mathbf{r}_2,t_2)+i\big[K_{R,I}(\mathbf{r}_1,t_1,\mathbf{r}_2,t_2)-K_{R,I}(\mathbf{r}_2,t_2,\mathbf{r}_1,t_1)\big], \quad (3.1) \end{aligned}$$

and the phase-sensitive correlation function

$$K^{(p)}(\mathbf{r}_1,t_1,\mathbf{r}_2,t_2) \equiv \langle E(\mathbf{r}_1,t_1)E(\mathbf{r}_2,t_2)\rangle$$
$$= K_{R,R}(\mathbf{r}_1,t_1,\mathbf{r}_2,t_2) - K_{I,I}(\mathbf{r}_1,t_1,\mathbf{r}_2,t_2) + i\big[K_{R,I}(\mathbf{r}_1,t_1,\mathbf{r}_2,t_2) + K_{R,I}(\mathbf{r}_2,t_2,\mathbf{r}_1,t_1)\big]. \quad (3.2)$$

The superscript (n) in (3.1) labels normally-ordered (phase-insensitive) correlation functions, in which all conjugated field terms inside the expectation appear to the left of the nonconjugated terms. Whereas this is a matter of convenience for classical fields (because scalar fields commute with their conjugates), when we quantize the classical fields to obtain field operators the ordering will become significant (because field operators do not commute with their adjoint operators). The (p) superscript in (3.2) labels the phase-sensitive correlation functions.

The nomenclature for (3.1) and (3.2) can be motivated as follows. A complex-valued, zero-mean random variable E has $\langle |E|^2\rangle$ independent of the phase of E, unlike $\langle E^2\rangle$. When carried over to random processes, it is not strictly true that the phase-insensitive correlation function is completely insensitive to the phase of the random process. However, the phase-insensitive correlation function depends only on the relative phase between the field at $(\mathbf{r}_1,t_1)$ and $(\mathbf{r}_2,t_2)$, whereas the phase-sensitive correlation function depends on the absolute phases. For example, $K^{(n)}(\mathbf{r}_1,t_1,\mathbf{r}_1,t_1)$ is indeed insensitive to the phase of the complex baseband field, whereas this is not true for the phase-sensitive auto-correlation function. To avoid introducing new terminology, we continue to designate (3.1) as the phase-insensitive correlation function and (3.2) as the phase-sensitive correlation function.

Not all zero-mean random fields can possess a nonzero phase-sensitive correlation. In particular, if

$$\mathcal{E}(\mathbf{r},t) \equiv \mathrm{Re}[E(\mathbf{r},t)e^{-i\omega_0 t}], \quad (3.3)$$

the real part of the positive-frequency field associated with $E(\mathbf{r},t)$, is a wide-sense stationary random process, then $E(\mathbf{r},t)$ cannot have a nonzero phase-sensitive correlation. However, a broad class of optical fields fall outside of this category. This should not be surprising. The prototypical example of phase-sensitive light is the squeezed state, whose passband noise properties are nonstationary even when its complex-envelope noise behavior is stationary.

To develop insight into phase-sensitive coherence, we will predominantly focus on con-

tinuous-wave fields whose phase-insensitive and phase-sensitive correlation functions each depend only on the time difference between the two spatiotemporal samples. We call such fields *complex-stationary*, and use

$$K^{(n)}(\mathbf{r}_1, \mathbf{r}_2, \tau) \equiv \langle E^*(\mathbf{r}_1, t) E(\mathbf{r}_2, t+\tau) \rangle \text{ and} \tag{3.4}$$

$$K^{(p)}(\mathbf{r}_1, \mathbf{r}_2, \tau) \equiv \langle E(\mathbf{r}_1, t) E(\mathbf{r}_2, t+\tau) \rangle \,, \tag{3.5}$$

to denote their correlation functions. As we will see shortly, the Fourier transforms

$$S^{(x)}(\mathbf{r}_1, \mathbf{r}_2, \Omega) \equiv \int_{-\infty}^{\infty} \mathrm{d}\tau \, K^{(x)}(\mathbf{r}_1, \mathbf{r}_2, \tau) e^{i\Omega\tau} \text{ for } x = n, p, \tag{3.6}$$

also have physical significance, and are hereafter referred to as the phase-insensitive and phase-sensitive spectra, respectively. Ignoring the niceties of generalized-function theory, let us define the frequency-domain field by

$$\widetilde{E}(\mathbf{r}, \Omega) \equiv \int_{-\infty}^{\infty} \mathrm{d}t \, E(\mathbf{r}, t) e^{i\Omega t} \,, \tag{3.7}$$

whence

$$\langle \widetilde{E}^*(\mathbf{r}_1, \Omega_1) \widetilde{E}(\mathbf{r}_2, \Omega_2) \rangle = 2\pi \; S^{(n)}(\mathbf{r}_1, \mathbf{r}_2, \Omega_1) \; \delta(\Omega_1 - \Omega_2) \,, \tag{3.8}$$

$$\langle \widetilde{E}(\mathbf{r}_1, \Omega_1) \widetilde{E}(\mathbf{r}_2, \Omega_2) \rangle = 2\pi \; S^{(p)}(\mathbf{r}_1, \mathbf{r}_2, \Omega_2) \; \delta(\Omega_1 + \Omega_2) \,. \tag{3.9}$$

Equation (3.8) shows that distinct frequency components of $E(\mathbf{r}, t)$ have no phase-insensitive correlation. Therefore $S^{(n)}(\mathbf{r}_1, \mathbf{r}_2, \Omega)$ gives the spectral strength of correlation at frequency Ω between spatial samples of the field at $\mathbf{r}_1$ and $\mathbf{r}_2$.[1] On the other hand, (3.9) indicates that only the $\pm\Omega$ frequency components of $E(\mathbf{r}, t)$ have a phase-sensitive cross-correlation, and that $S^{(p)}(\mathbf{r}_1, \mathbf{r}_2, \Omega)$ determines the spatial distribution of this phase-sensitive correlation.

The preceding link between $S^{(n)}(\mathbf{r}_1, \mathbf{r}_2; \Omega)$ and the phase-insensitive auto-correlation function of a monochromatic field is well known from coherence theory developed for phase-insensitive light [13, 14]. It allows any phase-insensitive field to be treated as a superposition of uncorrelated monochromatic fields. Equation (3.9), extends this argument to electric

[1] Because $E(\mathbf{r}, t)$ is a complex-valued baseband field, Ω represents a frequency detuning (from ω_0) for the real-valued passband field $\mathcal{E}(\mathbf{r}, t)$.

fields with both types of coherence. For such fields, frequency components $\pm\Omega$ around the center frequency have phase-sensitive correlation. Therefore, such a field must be treated as a collection of uncorrelated bichromatic fields, where each bichromatic component is comprised of a frequency $\omega_0 + \Omega$ field and a frequency $\omega_0 - \Omega$ field. These fields possess phase-insensitive auto-correlations $S^{(n)}(\mathbf{r}_1, \mathbf{r}_2, \Omega)$ and $S^{(n)}(\mathbf{r}_1, \mathbf{r}_2, -\Omega)$, and a phase-sensitive cross-correlation $S^{(p)}(\mathbf{r}_1, \mathbf{r}_2, \Omega)$, with all other second-order moments being zero.

3.2 Wolf equations for phase-sensitive correlations

The Cartesian components of the electric field in a source-free region of free space satisfy the scalar wave equation

$$\left(\nabla^2 - \frac{1}{c^2}\frac{\partial^2}{\partial t^2}\right)\mathcal{E}(\mathbf{r}, t) = 0\,, \tag{3.10}$$

where c is the speed of light, from which it follows that the positive-frequency electric field,

$$E^{(+)}(\mathbf{r}, t) \equiv E(\mathbf{r}, t)e^{-i\omega_0 t} \tag{3.11}$$

obeys the same wave equation. Defining

$$\mathcal{K}^{(p)}(\mathbf{r}_1, t_1, \mathbf{r}_2, t_2) \equiv \langle E^{(+)}(\mathbf{r}_1, t_1)E^{(+)}(\mathbf{r}_2, t_2)\rangle = K^{(p)}(\mathbf{r}_1, t_1, \mathbf{r}_2, t_2)e^{-i\omega_0(t_1+t_2)}, \tag{3.12}$$

we can use the wave equation to obtain the phase-sensitive variant of Wolf equations [14]

$$\left(\nabla_m^2 - \frac{1}{c^2}\frac{\partial^2}{\partial t_m^2}\right)\mathcal{K}^{(p)}(\mathbf{r}_1, t_1, \mathbf{r}_2, t_2) = 0 \quad \text{for } m = 1, 2, \tag{3.13}$$

which are identical to those for the phase-insensitive correlation

$$\mathcal{K}^{(n)}(\mathbf{r}_1, t_1, \mathbf{r}_2, t_2) \equiv \langle E^{(+)^*}(\mathbf{r}_1, t_1)E^{(+)}(\mathbf{r}_2, t_2)\rangle = K^{(n)}(\mathbf{r}_1, t_1, \mathbf{r}_2, t_2)e^{i\omega_0(t_1-t_2)}. \tag{3.14}$$

Let us now specialize these results to complex-stationary fields. For such fields, (3.13) yields

$$\left(\nabla_m^2 - \frac{1}{c^2}\left[\frac{\partial^2}{\partial \tau^2} + 2(-i\omega_0)(-1)^m\frac{\partial}{\partial \tau} + (-i\omega_0)^2\right]\right)K^{(p)}(\mathbf{r}_1, \mathbf{r}_2, \tau) = 0, \quad \text{for } m = 1, 2, \tag{3.15}$$

which, after Fourier transformation, gives

$$\left(\nabla_m^2 + \frac{1}{c^2}\left(\omega_0 + (-1)^m\Omega\right)^2\right) S^{(p)}(\mathbf{r}_1, \mathbf{r}_2, \Omega) = 0, \quad \text{for } m = 1, 2, \tag{3.16}$$

for the evolution of the phase-sensitive spectrum. For the phase-insensitive spectrum the usual Wolf equations lead to

$$\left(\nabla_m^2 + \frac{1}{c^2}\left(\omega_0 + \Omega\right)^2\right) S^{(n)}(\mathbf{r}_1, \mathbf{r}_2, \Omega) = 0, \quad \text{for } m = 1, 2. \tag{3.17}$$

The differential equations in (3.16) and (3.17) characterize the spatial propagation of the phase-sensitive and phase-insensitive spectra, and they manifest the frequency behavior noted in the previous section. Thus, phase-insensitive spectra propagate in a monochromatic fashion, i.e., (3.17) applies independently to each value of $\omega_0 + \Omega$, but phase-sensitive spectra are bichromatic, with the $\mathbf{r}_m$-coordinate propagating in accord with the Helmholtz equation for frequency $\omega_0 + (-1)^m\Omega$. The two-frequency dependence of (3.16) has another important consequence. Assume that $E(\mathbf{r}, t)$ is homogeneous in addition to its being complex-stationary, and let $S^{(n)}(\mathbf{r}_1 - \mathbf{r}_2, \Omega)$ and $S^{(p)}(\mathbf{r}_1 - \mathbf{r}_2, \Omega)$ be its two spectra. Substituting this homogeneous form of the phase-sensitive spectrum into the Wolf equations we obtain

$$\left(\nabla^2 + \frac{1}{c^2}\big(\omega_0 + (-1)^m\Omega\big)^2\right) S^{(p)}(\mathbf{r}, \Omega) = 0 \quad \text{, for } m = 1, 2. \tag{3.18}$$

Taking the difference between the $m = 1$ and $m = 2$ equations then yields $\Omega S^{(p)}(\mathbf{r}, \Omega) = 0$, which implies that $S^{(p)}(\mathbf{r}, \Omega) = 0$ for all $\Omega \neq 0$. Thus, for a spatially homogeneous, complex-stationary field to possess phase-sensitive fluctuations, it must be monochromatic.

3.3 Quasimonochromatic, paraxial correlation propagation

We now restrict our attention to paraxial beams—propagating from a source plane, $z = 0$, to an observation plane, $z = L$—that are quasimonochromatic. Using $E_0(\boldsymbol{\rho}, t)$, $E_L(\boldsymbol{\rho}', t)$ for the baseband fields at transverse coordinates $\boldsymbol{\rho} = (x, y)$ and $\boldsymbol{\rho}' = (x', y')$ in the source and observation planes, the Huygens-Fresnel principle implies that

$$E_L(\boldsymbol{\rho}', t) = \int \mathrm{d}\boldsymbol{\rho}\, E_0(\boldsymbol{\rho}, t - L/c) h_L(\boldsymbol{\rho}' - \boldsymbol{\rho}), \tag{3.19}$$

where

$$h_L(\boldsymbol{\rho}) = \frac{\exp(ik_0L + ik_0|\boldsymbol{\rho}|^2/2L)}{i\lambda_0 L}, \tag{3.20}$$

is the paraxial-propagation Green's function at the wave number $k_0 \equiv \omega_0/c$, and wavelength $\lambda_0 \equiv 2\pi c/\omega_0$, associated with the source's center frequency. A complex-stationary $E_0(\boldsymbol{\rho}, t)$ then yields a complex-stationary $E_L(\boldsymbol{\rho}', t)$, whose phase-sensitive spectrum is given by

$$S_L^{(p)}(\boldsymbol{\rho}_1', \boldsymbol{\rho}_2', \Omega) = \int\int \mathrm{d}\boldsymbol{\rho}_1\, \mathrm{d}\boldsymbol{\rho}_2\, S_0^{(p)}(\boldsymbol{\rho}_1, \boldsymbol{\rho}_2, \Omega) h_L(\boldsymbol{\rho}_1' - \boldsymbol{\rho}_1) h_L(\boldsymbol{\rho}_2' - \boldsymbol{\rho}_2), \tag{3.21}$$

in terms of the phase-sensitive spectrum of $E_0(\boldsymbol{\rho}, t)$. Because (3.21) is a convolution in both the $\boldsymbol{\rho}_1$ and $\boldsymbol{\rho}_2$ coordinates, the phase-sensitive spectrum is expressed much simpler in the spatial-frequency domain, viz.,

$$\widetilde{S}_L^{(p)}(\boldsymbol{k}_1, \boldsymbol{k}_2, \Omega) = \widetilde{S}_0^{(p)}(\boldsymbol{k}_1, \boldsymbol{k}_2, \Omega)\, \widetilde{h}_L(\boldsymbol{k}_1)\, \widetilde{h}_L(\boldsymbol{k}_2)\,, \tag{3.22}$$

where

$$\widetilde{S}^{(p)}(\boldsymbol{k}_1, \boldsymbol{k}_2, \Omega) \equiv \iint \mathrm{d}\boldsymbol{\rho}_1\, \mathrm{d}\boldsymbol{\rho}_2\, \widetilde{S}^{(p)}(\boldsymbol{\rho}_1, \boldsymbol{\rho}_2, \Omega) e^{i(\boldsymbol{k}_1\cdot\boldsymbol{\rho}_1 + \boldsymbol{k}_2\cdot\boldsymbol{\rho}_2)}, \tag{3.23}$$

and $\widetilde{h}_L(\boldsymbol{k}) = \exp(ik_0L - iL|\boldsymbol{k}|^2/2k_0)$ is the spatial Fourier transform of $h_L(\boldsymbol{\rho})$.

It is common, in optical coherence theory, to assume that the phase-insensitive spectrum in the source plane separates into the product of three terms. The first is a temporal spectrum that is solely a function of Ω. The second is a frequency-independent, spatially homogenous term, which is a function of the difference coordinate $\boldsymbol{\rho}_d \equiv \boldsymbol{\rho}_2 - \boldsymbol{\rho}_1$, that represents the spatial coherence of the source. The third is a frequency-independent term, which depends only on the sum coordinate $\boldsymbol{\rho}_s \equiv (\boldsymbol{\rho}_1 + \boldsymbol{\rho}_2)/2$, that represents the beam's intensity profile [13, 14]. We shall extend this assumption to the phase-sensitive spectrum, and write $S_0^{(p)}(\boldsymbol{\rho}_1, \boldsymbol{\rho}_2, \Omega) = S^{(p)}(\Omega) F_0(\boldsymbol{\rho}_s) G_0(\boldsymbol{\rho}_d)$. We can then express $\widetilde{S}_L^{(p)}(\boldsymbol{k}_1, \boldsymbol{k}_2, \Omega)$ in terms of the spatial-frequency sum, $\boldsymbol{k}_s = \boldsymbol{k}_1 + \boldsymbol{k}_2$, and difference, $\boldsymbol{k}_d = (\boldsymbol{k}_2 - \boldsymbol{k}_1)/2$, variables as follows:

$$\widetilde{S}_L^{(p)}(\boldsymbol{k}_1, \boldsymbol{k}_2, \Omega) = e^{i3k_0L/4} S^{(p)}(\Omega) \left[e^{ik_0L/4 - iL|\boldsymbol{k}_s|^2/4k_0} \widetilde{F}_0(\boldsymbol{k}_s)\right] \left[e^{ik_0L - iL|\boldsymbol{k}_d|^2/k_0} \widetilde{G}_0(\boldsymbol{k}_d)\right]. \tag{3.24}$$

Equation (3.24) tells us that the phase-sensitive spectrum remains separable on all transverse planes, and at $z = L$ its $\boldsymbol{\rho}_s$ component is an $L/4$-propagated version of $F_0(\boldsymbol{\rho}_s)$, while

its $\boldsymbol{\rho}_d$ term is an L-propagated version of $G_0(\boldsymbol{\rho}_d)$.

In order to assess the physical implications of (3.24), we will assume a collimated, coherence-separable, Gaussian-Schell source at $z = 0$, which is a source model often used in coherence theory for the study of phase-insensitive correlation propagation [14]. The phase-insensitive Gaussian-Schell source consists of a beam with a Gaussian intensity profile and a Gaussian phase-insensitive coherence profile, expressed in sum and difference coordinates as

$$S_0^{(n)}(\boldsymbol{\rho}_1, \boldsymbol{\rho}_2, \Omega) = \frac{2S^{(n)}(\Omega)}{\pi a_T^2} \exp\left[-\frac{2}{a_T^2}|\boldsymbol{\rho}_s|^2 - \frac{1}{2}\left(\frac{1}{a_T^2} + \frac{1}{\rho_0^2}\right)|\boldsymbol{\rho}_d|^2\right], \tag{3.25}$$

for the phase-insensitive spectrum. Here, a_T is the e^{-2} attenuation radius of the intensity profile, and ρ_0 is the transverse coherence length of the beam at $z = 0$, which we shall assume is much smaller than a_T. To facilitate a comparison of the propagation characteristics of phase-insensitive and phase-sensitive spectra, we assume they both have the same spatial dependence at the source plane. Therefore, the phase-sensitive spectrum of this beam at $z = 0$ will also be given by (3.25), but with $S^{(n)}(\Omega)$ replaced by its phase-sensitive counterpart, $S^{(p)}(\Omega)$.[2]

Evaluating (3.24) and taking its inverse Fourier transform results in a phase-sensitive spectrum at $z = L$ with magnitude

$$|S_L^{(p)}(\boldsymbol{\rho}_1, \boldsymbol{\rho}_2, \Omega)| = \frac{2|S^{(p)}(\Omega)|}{\pi a_n^2(L)} \frac{1 + D_s^{-1}D_d^{-1}}{\sqrt{(1 + D_s^{-2})(1 + D_d^{-2})}} \exp\left\{-2a_p^{-2}(L)|\boldsymbol{\rho}_s|^2 - 2^{-1}b_p^{-2}(L)|\boldsymbol{\rho}_d|^2\right\}, \tag{3.26}$$

and a phase-insensitive spectrum with magnitude

$$|S_L^{(n)}(\boldsymbol{\rho}_1, \boldsymbol{\rho}_2, \Omega)| = \frac{2S^{(n)}(\Omega)}{\pi a_n^2(L)} \exp\left\{-2a_n^{-2}(L)|\boldsymbol{\rho}_s|^2 - 2^{-1}\rho^{-2}(L)|\boldsymbol{\rho}_d|^2\right\}. \tag{3.27}$$

Here: $D_s = k_0 a_T^2/2L$ and $D_d = k_0\rho_0^2/2L$ are the Fresnel numbers for the sum- and difference-coordinate Gaussian functions in (3.25); $a_p^2(L) = a_T^2(1 + D_s^{-2})$ and $b_p^2(L) = \rho_0^2(1 + D_d^{-2})$ are the sum- and difference-coordinate e^{-2}-attenuation radii of the phase-sensitive spectrum at $z = L$; and $a_n^2(L) = a_T^2(1 + D_s^{-1}D_d^{-1})$ and $\rho^2(L) = \rho_0^2(1 + D_s^{-1}D_d^{-1})$ are the e^{-2}-attenuation radii of the intensity and the phase-insensitive coherence at $z = L$. We see from these

[2]Because auto-correlations place constraints on the permissible cross-correlations we must have that our assumed $S^{(p)}(\Omega)$ does not violate those constraints.

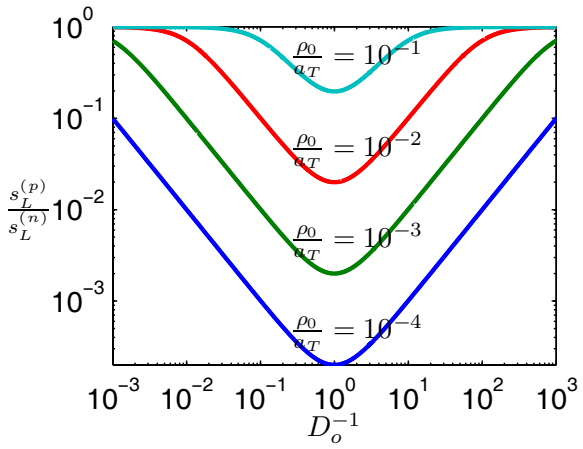

Figure 3-1: Ratio of normalized phase-sensitive to phase-insensitive on-axis correlations, $s_L^{(p)}/s_L^{(n)}$, plotted versus the inverse Fresnel number, D_o^{-1}, that distinguishes near-field from far-field propagation.

expressions that propagation of the phase-sensitive spectrum is governed by two Fresnel numbers D_s and D_d, where $D_s \gg D_d$ because we have assumed that $a_T \gg \rho_0$. Propagation of the phase-insensitive spectrum, on the other hand, is governed by a single Fresnel number $D_o \equiv \sqrt{D_s D_d}$.

Consider the normalized (frequency independent) on-axis phase-sensitive correlation, $s_L^{(p)} \equiv |S_L^{(p)}(\mathbf{0},\mathbf{0},\Omega)/S^{(p)}(\Omega)|$ and phase-insensitive correlation $s_L^{(n)} \equiv S_L^{(n)}(\mathbf{0},\mathbf{0},\Omega)/S^{(n)}(\Omega)$. From Eqs. (3.26) and (3.27) we have that

$$\frac{s_L^{(p)}}{s_L^{(n)}} = \frac{1 + D_s^{-1} D_d^{-1}}{\sqrt{(1 + D_s^{-2})(1 + D_d^{-2})}}, \tag{3.28}$$

which we have plotted, in Fig. 3-1, versus D_o^{-1} for several values of ρ_0/a_T. The Fig. 3-1 abscissa is the Fresnel number that controls the beam size at $z = L$, with the near field (no beam-diameter expansion) and far field (beam diameter proportional to L) corresponding to D_o being much greater than unity and much less than unity, respectively. Thus this figure shows that the strength of the on-axis phase-sensitive correlation, relative to that of the on-axis phase-insensitive correlation, is preserved deep in the near and far fields. However, in the intermediate region the phase-sensitive correlation suffers an attenuation relative to the phase-insensitive correlation, with $\min\{s_L^{(p)}/s_L^{(n)}\} \approx 2\rho_0/a_T \ll 1$ occurring at $D_o = 1$.

The spatial properties of the spectra are each governed by two parameters: $a_p(L)$ and $b_p(L)$ for the phase-sensitive spectrum, and $a_n(L)$ and $\rho(L)$ for the phase-insensitive

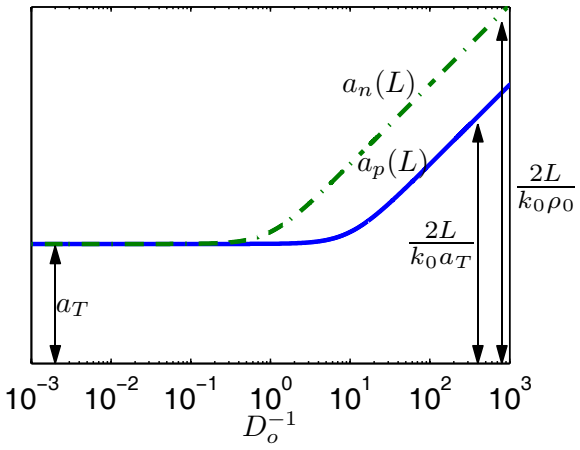

Figure 3-2: Comparison between the intensity radii of the phase-sensitive and phase-insensitive correlation spectra, $a_p(L)$ and $a_n(L)$, for a collimated Gaussian-Schell beam undergoing paraxial propagation. $a_p(L)$ and $a_n(L)$ are plotted versus the inverse Fresnel number, D_o^{-1}, showing the transition from near-field to far-field behavior. For illustrative purposes $\rho_0/a_T = 0.1$ is assumed, so that $D_d = 0.1D_o$ and $D_s = 10D_o$.

spectrum. In the near field ($D_o \gg 1$), we have $a_p(L) \approx a_n(L) \approx a_T$ and, if $D_d \gg 1$, $b_p(L) \approx \rho(L) \approx \rho_0$. In this region, the beam has intensity radius a_T, and appreciable phase-insensitive correlation between field samples within that beam radius whose separation is less than the coherence length ρ_0. A similar interpretation holds for the phase-sensitive spectrum: appreciable phase-sensitive correlation exists between field samples within the beam radius whose separation is less than the coherence length ρ_0.

In the far field ($D_s \ll 1$), however, the behavior changes significantly. Here the correlation spectra simplify to[3]

$$|S_L^{(p)}(\boldsymbol{\rho}_1, \boldsymbol{\rho}_2, \Omega)| = \frac{k_0^2 |S^{(p)}(\Omega)| \rho_0^2}{2\pi L^2} \exp\left(-\frac{k_0^2 a_T^2}{2L^2}|\boldsymbol{\rho}_s|^2 - \frac{k_0^2 \rho_0^2}{8L^2}|\boldsymbol{\rho}_d|^2\right), \tag{3.29}$$

$$|S_L^{(n)}(\boldsymbol{\rho}_1, \boldsymbol{\rho}_2, \Omega)| = \frac{k_0^2 S^{(n)}(\Omega) \rho_0^2}{2\pi L^2} \exp\left(-\frac{k_0^2 \rho_0^2}{2L^2}|\boldsymbol{\rho}_s|^2 - \frac{k_0^2 a_T^2}{8L^2}|\boldsymbol{\rho}_d|^2\right). \tag{3.30}$$

From (3.30) we see that the beam's intensity radius has grown to $2L/k_0\rho_0$, and that field samples within that expanded beam radius have appreciable phase-insensitive correlation when they are separated by less than $2L/k_0 a_T$. On the other hand, the phase-sensitive spectrum given in (3.29) exhibits the opposite behavior. Now, a field sample at $\boldsymbol{\rho}$, located inside the beam radius $2L/k_0\rho_0$, has a significant phase-sensitive correlation with field

[3] $D_s \ll 1$ denotes the regime in which both (3.29) and (3.30) are valid, but $S_L^{(n)}$ is valid within the broader $D_o \ll 1$ regime.

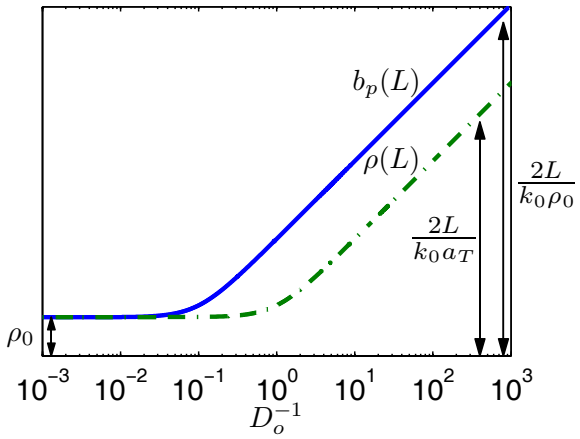

Figure 3-3: Comparison between coherence lengths of the phase-sensitive and phase-insensitive correlation spectra, $b_p(L)$ and $\rho(L)$, for a collimated Gaussian-Schell beam undergoing paraxial propagation. $b_p(L)$ and $\rho(L)$ are plotted versus the inverse Fresnel number, D_o^{-1}, showing the transition from near-field to far-field behavior. For illustrative purposes $\rho_0/a_T = 0.1$ is assumed, so that $D_d = 0.1D_o$ and $D_s = 10D_o$.

samples in the vicinity of $-\boldsymbol{\rho}$. In particular, a pair of field samples from within the beam radius have appreciable phase-sensitive correlation only if their vector sum, rather than their difference, has magnitude less than $2L/k_0a_T$. Figure 3-2 shows the behavior of the parameters $a_p(L)$, $a_n(L)$ as the Fresnel number D_o is varied from the near field to the far field. Figure 3-3 is a similar plot for $b_p(L)$ and $\rho(L)$. In both of these plots $\rho_0/a_T = 0.1$ is assumed for concreteness, such that $D_d = 0.1D_o$ and $D_s = 10D_o$. These figures show that $a_p(L) \approx a_n(L)$, and $b_p(L) \approx \rho(L)$ prevail in the near field ($D_d \gg 1$), but $b_p(L) \approx a_n(L)$, and $a_p(L) \approx \rho(L)$ occur in the far field ($D_s \ll 1$). Furthermore, as discussed previously, D_d governs the diffraction of $b_p(L)$ and D_s governs that of $a_p(L)$, whereas the diffraction of the phase-insensitive parameters, $a_n(L)$ and $\rho(L)$, are both determined by D_o.

In the far field, the Gaussian-Schell model source produces phase-sensitive correlations between field samples at $\pm\boldsymbol{\rho}$. It turns out that this is true in far-field diffraction for all sources that have separable phase-sensitive correlation spectra in the $z = 0$ plane, as we now show. Fraunhofer diffraction, which applies in the far field, gives us

$$E_L(\boldsymbol{\rho}', t) = \int \mathrm{d}\boldsymbol{\rho}\, E_0(\boldsymbol{\rho}, t - L/c) \frac{\exp(ik_0L + ik_0|\boldsymbol{\rho}'|^2/2L - ik_0\boldsymbol{\rho}'\cdot\boldsymbol{\rho}/L)}{i\lambda_0 L}. \tag{3.31}$$

It follows that a phase-sensitive source spectrum that is separable into sum and difference

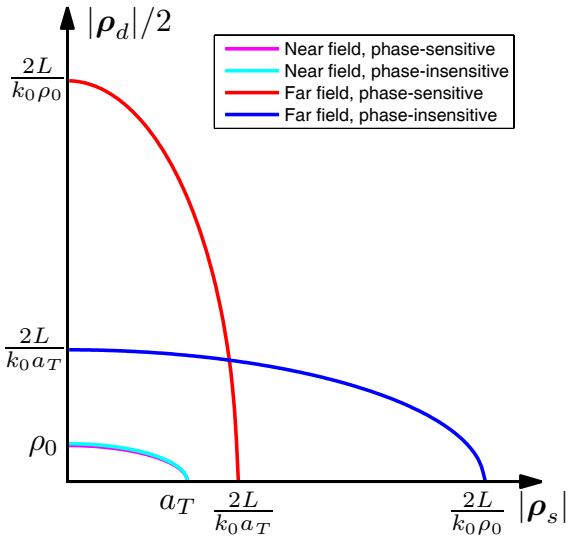

Figure 3-4: Level curves corresponding to the e^{-2} attenuation level for the phase-sensitive and phase-insensitive correlation spectra, both in the near field and the far field regimes (after L-m of propagation). The beam diameter at the source is a_T, ρ_0 is its coherence length and k_0 denotes the center wavenumber.

coordinates, $S_0^{(p)}(\boldsymbol{\rho}_1, \boldsymbol{\rho}_2, \Omega) = S^{(p)}(\Omega) F_0(\boldsymbol{\rho}_s) G_0(\boldsymbol{\rho}_d)$, will propagate into the $z = L$ plane as

$$S_L^{(p)}(\boldsymbol{\rho}_1', \boldsymbol{\rho}_2', \Omega) = \frac{S^{(p)}(\Omega)}{(i\lambda_0 L)^2} e^{i(2k_0 L + k_0|\boldsymbol{\rho}_s'|^2/L + k_0|\boldsymbol{\rho}_d'|^2/4L)} \times \iint \mathrm{d}\boldsymbol{\rho}_s \, \mathrm{d}\boldsymbol{\rho}_d \, e^{-i2k_0 \boldsymbol{\rho}_s' \cdot \boldsymbol{\rho}_s / L - ik_0 \boldsymbol{\rho}_d' \cdot \boldsymbol{\rho}_d / 2L} F_0(\boldsymbol{\rho}_s) G_0(\boldsymbol{\rho}_d) \,, \quad (3.32)$$

where $\boldsymbol{\rho}_s' \equiv (\boldsymbol{\rho}_2' + \boldsymbol{\rho}_1')/2$ and $\boldsymbol{\rho}_d' \equiv \boldsymbol{\rho}_2' - \boldsymbol{\rho}_1'$. On the other hand, a separable phase-insensitive source spectrum, given by $S_0^{(n)}(\boldsymbol{\rho}_1, \boldsymbol{\rho}_2, \Omega) = S^{(n)}(\Omega) F_0(\boldsymbol{\rho}_s) G_0(\boldsymbol{\rho}_d)$, will yield

$$S_L^{(n)}(\boldsymbol{\rho}_1', \boldsymbol{\rho}_2', \Omega) = \frac{S^{(n)}(\Omega)}{(\lambda_0 L)^2} e^{ik_0 \boldsymbol{\rho}_s' \cdot \boldsymbol{\rho}_d' / L} \iint \mathrm{d}\boldsymbol{\rho}_s \, \mathrm{d}\boldsymbol{\rho}_d \, e^{-ik_0(\boldsymbol{\rho}_d' \cdot \boldsymbol{\rho}_s + \boldsymbol{\rho}_s' \cdot \boldsymbol{\rho}_d)/L} F_0(\boldsymbol{\rho}_s) G_0(\boldsymbol{\rho}_d), \quad (3.33)$$

at $z = L$. The double integrals in (3.32) and (3.33) are 2-D Fourier transforms, whence

$$|S_L^{(p)}(\boldsymbol{\rho}_1', \boldsymbol{\rho}_2', \Omega)| = \frac{|S^{(p)}(\Omega)|}{(\lambda_0 L)^2} \left| \widetilde{F}_0 \left(-\frac{2k_0}{L} \boldsymbol{\rho}_s' \right) \widetilde{G}_0 \left(-\frac{k_0}{2L} \boldsymbol{\rho}_d' \right) \right| , \quad (3.34)$$

$$|S_L^{(n)}(\boldsymbol{\rho}_1', \boldsymbol{\rho}_2', \Omega)| = \frac{S^{(n)}(\Omega)}{(\lambda_0 L)^2} \left| \widetilde{F}_0 \left(-\frac{k_0}{L} \boldsymbol{\rho}_d' \right) \widetilde{G}_0 \left(-\frac{k_0}{L} \boldsymbol{\rho}_s' \right) \right| . \quad (3.35)$$

Equations (3.34) and (3.35) are the van Cittert-Zernike Theorems for phase-sensitive and phase-insensitive correlation spectra, respectively. When the source consists of a narrow

function $G_0(\boldsymbol{\rho}_d)$ times a much broader function $F_0(\boldsymbol{\rho}_s)$, as we have assumed for the Gaussian-Schell model, the phase-sensitive spectrum at $z = L$ will consist of a narrow function of $\boldsymbol{\rho}'_s$ times a much broader function of $\boldsymbol{\rho}'_d$, because of the Fourier transform uncertainty principle. On the other hand, the phase-insensitive spectrum at $z = L$ will consist of a narrow function of $\boldsymbol{\rho}'_d$ times a much broader function of $\boldsymbol{\rho}'_s$, by virtue of this same uncertainty principle. Over the region in which $\widetilde{G}_0$ is nearly constant, the phase-sensitive spectrum will be dominated by a rapidly-decaying function of $\boldsymbol{\rho}'_s$, whereas the phase-insensitive spectrum will be dominated, over the same region, by a rapidly-decaying function of $\boldsymbol{\rho}'_d$. Hence points symmetric about the origin will have appreciable phase-sensitive correlation, whereas the phase-insensitive correlation is highest in the immediate neighborhood of a single point. Figure 3-4 illustrates this behavior for the Gaussian-Schell source considered in this section. The figure plots the e^{-2} attenuation contours for the magnitudes of the phase-sensitive and phase-insensitive correlation spectra in terms of the sum and difference transverse coordinates. Thus, all points on a transverse plane that constitute the interior region of a contour are considered both coherent and intense. It turns out, the level curves of both phase-sensitive and phase insensitive Gaussian-Schell sources describe ellipses. In the near field, because of the low-coherence assumption of the source, these ellipses have the minor axes along the difference coordinate. When the beam propagates to the far field, the level curve for the phase-insensitive correlation spectrum diffracts in both coordinates in equal proportion, such that the minor axis remains aligned with the $|\boldsymbol{\rho}_d|$-axis.[4] On the other hand, the level curve corresponding to the far field phase-sensitive spectrum shows opposite behavior, with the minor axis aligned with the sum coordinate and the major axis along the difference coordinate. Thus, the far field phase-insensitive correlation spectrum is indeed dominated by a narrow function of the difference coordinate $\boldsymbol{\rho}_d$, whereas the far field phase-sensitive correlation spectrum is a narrow function of the sum coordinate $\boldsymbol{\rho}_s$.

3.4 Normal-mode decomposition

In studying optical fields it is common to make reference to their mode decompositions, which describe the field as a superposition of decoupled radiators and their associated spatiotemporal profiles. If one has a complete physical description of the process generating

[4] To establish consistent notation with that used in Figure 3-4, in this discussion we use non-primed transverse spatial coordinates in the far-field plane.

an optical field, such as all the parameters of a laser cavity, it is possible to derive these modes starting from first principles. However, in many scenarios, the details of the optical sources are not known, and it is necessary to infer the modes from a (generally incomplete) statistical description of the optical field, either estimated from measurements or derived from broad assumptions about the source [13, 14].

One of the central results in optical coherence theory that addresses this problem is the normal-mode decomposition, in which an arbitrary zero-mean field[5] with zero phase-sensitive correlation—but arbitrary phase-insensitive correlation—can be expressed as

$$E(\mathbf{r},t) = \sum_{m=1}^{\infty} a_m \phi_m(\mathbf{r},t), \tag{3.36}$$

where the $\{a_m\}$ are zero-mean, uncorrelated, isotropic random variables, i.e. $\langle a_m \rangle = 0$, $\langle a_m a_k \rangle = 0$, and $\langle a_m^* a_k \rangle = \lambda_m \delta_{mk}$ with $\lambda_m \geq 0$. The $\{\phi_m(\mathbf{r},t)\}$, which form a complete and orthonormal set of functions, are the eigenfunctions of the Hermitian kernel $K^{(n)}(\mathbf{r}_1,t_1,\mathbf{r}_2,t_2)$, with the $\{\lambda_m\}$ being their associated eigenvalues. Also, the $\{\phi_m(\mathbf{r},t)\}$ satisfy the scalar wave equation for propagation through a source-free region of free space.

It is natural to ask if such a decomposition extends to zero-mean fields with arbitrary phase-sensitive and phase-insensitive correlations. One may expect that the decomposition still assumes the form (3.36), but with the uncorrelated a_m coefficients now having both phase-sensitive and phase-insensitive correlations. However, the following proposition demonstrates that this is not a valid decomposition for an arbitrary zero-mean random field.

Proposition 1. *Let $E(\mathbf{x})$, where $\mathbf{x} = (\mathbf{r},t)$, be a zero-mean random field over a finite space-time region, $\mathbf{x} \in \mathcal{S} \subset \mathbb{R}^4$, with second-order phase-insensitive and phase-sensitive correlation functions,*

$$K^{(n)}(\mathbf{x}_1,\mathbf{x}_2) \equiv \langle E^*(\mathbf{x}_1) E(\mathbf{x}_2) \rangle, \quad \textit{and} \tag{3.37}$$

$$K^{(p)}(\mathbf{x}_1,\mathbf{x}_2) \equiv \langle E(\mathbf{x}_1) E(\mathbf{x}_2) \rangle, \tag{3.38}$$

that are well-defined kernels on the Hilbert space of square-integrable functions. $E(\mathbf{x})$ admits

[5] We limit our discussion to the zero mean case for simplicity, but no loss of generality ensues from this assumption. For nonzero-mean fields, we replace the correlation functions with covariance functions, and afterwards add the appropriate mean value to each random coefficient in the decomposition.

an expansion of form

$$E(\mathbf{x}) = \sum_{m=1}^{\infty} a_m \phi_m(\mathbf{x}), \tag{3.39}$$

where $\langle a_m \rangle = 0$, $\langle a_m^* a_k \rangle = \lambda_m \delta_{m,k} \geq 0$, $\langle a_m a_k \rangle = \gamma_m \delta_{m,k} \geq 0$, *and* $\{\phi_m(\mathbf{x})\}$ *is a complete and orthonormal set of square-integrable functions, if and only if* $K^{(n)}(\mathbf{x}_1, \mathbf{x}_2)$ *and* $K^{(p)}(\mathbf{x}_1, \mathbf{x}_2)$ *share a common set of input eigenfunctions, i.e.,* $K^{(n)}(\mathbf{x}_1, \mathbf{x}_2)$, *and*

$$K_2^{(p)}(\mathbf{x}_1, \mathbf{x}_2) \equiv \int_{\mathcal{S}} \mathrm{d}\mathbf{x}\, K^{(p)*}(\mathbf{x}_1, \mathbf{x}) K^{(p)}(\mathbf{x}, \mathbf{x}_2) \tag{3.40}$$

are commuting Hermitian kernels.

Proof. To prove the forward direction, we assume that $E(\mathbf{x})$ admits the expansion in (3.39). Then, the second-order correlation functions become

$$K^{(n)}(\mathbf{x}_1, \mathbf{x}_2) = \sum_{m=1}^{\infty} \lambda_m \phi_m^*(\mathbf{x}_1) \phi_m(\mathbf{x}_2), \tag{3.41}$$

$$K^{(p)}(\mathbf{x}_1, \mathbf{x}_2) = \sum_{m=1}^{\infty} \gamma_m \phi_m(\mathbf{x}_1) \phi_m(\mathbf{x}_2), \tag{3.42}$$

which have $\{\phi_m^*(\mathbf{x})\}$ as their common set of input eigenfunctions. That $K^{(n)}(\mathbf{x}_1, \mathbf{x}_2)$ and

$$K_2^{(p)}(\mathbf{x}_1, \mathbf{x}_2) = \sum_{m=1}^{\infty} |\gamma_m|^2 \phi_m^*(\mathbf{x}_1) \phi_m(\mathbf{x}_2) \tag{3.43}$$

commute, follows from the two kernels having a common set of eigenfunctions.

To prove the reverse direction, we assume $K^{(n)}$ and $K_2^{(p)}$ commute, and we use $\{\phi_m^*(\mathbf{x})\}$ to denote their common eigenfunctions. The $\lambda_m \geq 0$ are given uniquely by the eigenvalue spectrum of the phase-insensitive correlation function, and the $\gamma_m \geq 0$ are found (uniquely) from the eigenvalues of $K_2^{(p)}(\mathbf{x}_1, \mathbf{x}_2)$. Note that diagonalizing $K^{(n)}$ or $K_2^{(p)}$ determines $\{\phi_m(\mathbf{x})\}$ only up to a constant phase factor. For modes with $\gamma_m > 0$ these phases are determined uniquely from the singular-value decomposition of $K^{(p)}(\mathbf{x}_1, \mathbf{x}_2)$, which has $\{\phi_m^*(\mathbf{x})\}$ as its input eigenfunctions, and $\{\phi_m(\mathbf{x})\}$ as its output eigenfunctions. □

Because, the phase-insensitive and phase-sensitive correlation functions of $E(\mathbf{x})$ need not commute, Proposition 1 implies that we cannot decompose an arbitrary random field into the form given in (3.39). We now provide a general method for decomposing fields into their modes when they carry arbitrary phase-insensitive and phase-sensitive correlations.

Theorem 2. *Let $E(\mathbf{x})$, where $\mathbf{x} = (\mathbf{r}, t)$, be a zero-mean random field over a finite space-time region denoted by the set $\mathcal{S} \subset \mathbb{R}^4$, and assume $E(\mathbf{x})$ has a matrix-valued correlation function*

$$\mathrm{K}(\mathbf{x}_1, \mathbf{x}_2) \equiv \left\langle \begin{bmatrix} E(\mathbf{x}_1) \\ E^*(\mathbf{x}_1) \end{bmatrix} \begin{bmatrix} E^*(\mathbf{x}_2) & E(\mathbf{x}_2) \end{bmatrix} \right\rangle = \begin{bmatrix} K^{(n)*}(\mathbf{x}_1, \mathbf{x}_2) & K^{(p)}(\mathbf{x}_1, \mathbf{x}_2) \\ K^{(p)*}(\mathbf{x}_1, \mathbf{x}_2) & K^{(n)}(\mathbf{x}_1, \mathbf{x}_2) \end{bmatrix} . \quad (3.44)$$

Furthermore, assume this kernel is defined on the Hilbert space of 2×1 square-integrable functions over $\mathcal{S}$, i.e., $\ell_2 \oplus \ell_2[\mathcal{S}] \xrightarrow{\mathrm{K}} \ell_2 \oplus \ell_2[\mathcal{S}]$. Then, the positive semidefinite kernel $\mathrm{K}(\mathbf{x}_1, \mathbf{x}_2)$ admits an expansion

$$\mathrm{K}(\mathbf{x}_1, \mathbf{x}_2) = \sum_{m=1}^{\infty} \lambda_m \mathrm{V}_m(\mathbf{x}_1) \mathrm{V}_m^H(\mathbf{x}_2) , \quad (3.45)$$

where ^{H} denotes Hermitian transpose, $\lambda_m \geq 0$, for $m = 1, 2, \ldots$, and the 2×2 matrix-valued functions

$$\mathrm{V}_m(\mathbf{x}) = \begin{bmatrix} v_{m1}(\mathbf{x}) & v_{m2}(\mathbf{x}) \\ v_{m2}^*(\mathbf{x}) & v_{m1}^*(\mathbf{x}) \end{bmatrix} \quad (3.46)$$

satisfy the completeness relation

$$\sum_{m=1}^{\infty} \mathrm{V}_m(\mathbf{x}_1) \mathrm{Q} \mathrm{V}_m^H(\mathbf{x}_2) = \delta(\mathbf{x}_1 - \mathbf{x}_2) \, \mathrm{Q} , \quad (3.47)$$

and the orthogonality relation

$$\int_{\mathcal{S}} \mathrm{V}_m^H(\mathbf{x}) \mathrm{Q} \mathrm{V}_k(\mathbf{x}) \mathrm{d}\mathbf{x} = \delta_{mk} \, \mathrm{Q} , \quad (3.48)$$

with

$$\mathrm{Q} = \begin{bmatrix} 1 & 0 \\ 0 & -1 \end{bmatrix} . \quad (3.49)$$

The functions $\mathrm{V}_m(\mathbf{x})$ are unique up to a diagonal phase matrix, i.e., if the $\{\lambda_m\}$ are distinct, for any admissible $\mathrm{V}_m(\mathbf{x})$ we have that

$$\mathrm{V}_m(\mathbf{x}) \begin{bmatrix} e^{i\theta_m} & 0 \\ 0 & e^{-i\theta_m} \end{bmatrix} , \quad (3.50)$$

is also an admissible solution. Additional admissible solutions exist if the $\{\lambda_m\}$ *are not distinct.*

Proof. See Appendix A. □

The preceding decomposition is called symplectic, because it derives from concepts developed for symplectic vector spaces [34]. It should be noted that other decompositions have been derived previously, in which the 2×2 matrix-valued eigenfunctions are rank-two and unitary, and the random variables in the associated field expansion are uncorrelated, yet have phase-insensitive and phase-sensitive auto-correlations [35, 36]. The distinguishing feature of the Theorem 1 decomposition is that each random variable is now isotropic. Furthermore, as will be discussed in Section 3.5, this decomposition leads naturally to a similar result for quantum field operators.

Making use of the completeness and orthogonality properties of the $\{\mathrm{V}_m(\mathbf{x})\}$, we can obtain the following expansion for the electric field:

$$\begin{bmatrix} E(\mathbf{x}) \\ E^*(\mathbf{x}) \end{bmatrix} = \sum_{m=1}^{\infty} \mathrm{V}_m(\mathbf{x}) \begin{bmatrix} a_m \\ a_m^* \end{bmatrix}, \tag{3.51}$$

where the random variables $\{\, a_m : m = 1, 2, \dots \}$, given by

$$\begin{bmatrix} a_m \\ a_m^* \end{bmatrix} = \mathrm{Q} \int_{\mathcal{S}} \mathrm{V}_m^H(\mathbf{x}) \mathrm{Q} \begin{bmatrix} E(\mathbf{x}) \\ E^*(\mathbf{x}) \end{bmatrix} \mathrm{d}\mathbf{x}\,, \tag{3.52}$$

satisfy $\langle a_m \rangle = 0$, $\langle a_m a_k \rangle = 0$, and $\langle a_m^* a_k \rangle = \lambda_m \delta_{mk}$.

We have shown in Section 3.2 that both the phase-insensitive and phase-sensitive correlation functions of a positive-frequency electromagnetic field satisfies the same Wolf equations. Therefore, taking the (3.45) expansion to be that of the passband-field correlation function matrix and substituting it into the Wolf equations, we obtain

$$\left(\nabla_\ell^2 - \frac{1}{c^2} \frac{\partial^2}{\partial t_\ell^2} \right) \mathrm{K}(\mathbf{x}_1, \mathbf{x}_2) = 0\,, \tag{3.53}$$

where $\mathbf{x}_\ell = (\mathbf{r}_\ell, t_\ell)$ for $\ell = 1, 2$, and the right-hand side is the 2×2 zero matrix. Then setting $\ell = 1$, multiplying both sides of the equality from the right by $\mathrm{Q}\mathrm{V}_m(\mathbf{r}_2, t_2)\mathrm{Q}$, and

integrating over $(\mathbf{r}_2, t_2) \in \mathcal{S}$ yields the result

$$\left(\nabla^2 - \frac{1}{c^2}\frac{\partial^2}{\partial t^2}\right) \mathrm{V}_m(\mathbf{x}) = 0\,, \tag{3.54}$$

i.e., for all modes $m = 1, 2, \ldots$, both $v_{m1}(\mathbf{x})$ and $v_{m2}(\mathbf{x})$ satisfy the scalar wave equation. Furthermore, if (3.45) represents the modal decomposition for the *baseband* electric field envelope, it is straightforward to parallel the above procedure to show that $v_{m1}(\mathbf{r}, t)e^{-i\omega_0 t}$ and $v_{m2}(\mathbf{r}, t)e^{-i\omega_0 t}$ in each mode satisfy the scalar wave equation.

We close this section by returning to the example we described in the beginning, namely the case in which $E(\mathbf{x})$ admits an orthogonal decomposition of the form given in Proposition 1. Motivated by the symplectic decomposition, we express each a_m in (3.39) as a Bogoliubov transformation of another zero-mean, isotropic complex random variable b_m, i.e., we define $a_m \equiv \mu_m b_m + \nu_m b_m^*$, with $|\mu_m|^2 - |\nu_m|^2 = 1$, $\langle b_m \rangle = \langle b_m b_k \rangle = 0$, and $\langle b_m^* b_k \rangle = N_m \delta_{m,k} \geq 0$. Solving for $\{N_m, \mu_m, \nu_m\}$ from $\{\lambda_m, \gamma_m\}$, we obtain the symplectic decomposition of $E(\mathbf{x})$ as given in (3.51), in terms of the zero-mean, complex isotropic random variables $\{b_m\}$, and the matrix-valued symplectic eigenfunctions

$$\mathrm{V}_m(\mathbf{x}) = \begin{bmatrix} \phi_m(\mathbf{x}) & 0 \\ 0 & \phi_m^*(\mathbf{x}) \end{bmatrix} \begin{bmatrix} \mu_m & \nu_m \\ \nu_m^* & \mu_m^* \end{bmatrix}, \tag{3.55}$$

where the $\{\phi_m(\mathbf{x})\}$ are the orthonormal eigenfunctions from (3.39).

Determining whether the symplectic decomposition reduces to an orthonormal representation, without explicitly deriving the symplectic form, requires verifying

$$\int_{\mathcal{S}} \mathrm{d}\mathbf{x}\, K_2^{(p)}(\mathbf{x}_1, \mathbf{x}) K^{(n)}(\mathbf{x}, \mathbf{x}_2) - \int_{\mathcal{S}} \mathrm{d}\mathbf{x}\, K^{(n)}(\mathbf{x}_1, \mathbf{x}) K_2^{(p)}(\mathbf{x}, \mathbf{x}_2) = 0, \tag{3.56}$$

where the left-hand side is the commutator for $K_2^{(p)}$ and $K^{(n)}$. The following Proposition determines an alternative necessary and sufficient condition that is often easier to evaluate.

Proposition 3. *Suppose the zero-mean random $E(\mathbf{x})$, where $\mathbf{x} \in \mathcal{S}$, has the matrix-valued correlation function in* (3.44)*. $E(\mathbf{x})$ admits the orthonormal expansion in* (3.39) *if and only if*

$$\int_{\mathcal{S}} \mathrm{d}\mathbf{x}\, \mathrm{K}(\mathbf{x}_1, \mathbf{x}) \mathrm{Q} \mathrm{K}(\mathbf{x}, \mathbf{x}_2) = \begin{bmatrix} f(\mathbf{x}_2, \mathbf{x}_1) & 0 \\ 0 & -f(\mathbf{x}_1, \mathbf{x}_2) \end{bmatrix}, \tag{3.57}$$

for some positive semidefinite scalar kernel $f(\mathbf{x}_1, \mathbf{x}_2)$.

Proof. For an arbitrary matrix-valued correlation function given in (3.44), we have

$$\int_{\mathcal{S}} \mathrm{d}\mathbf{x}\, \mathrm{K}(\mathbf{x}_1, \mathbf{x}) \mathrm{Q} \mathrm{K}(\mathbf{x}, \mathbf{x}_2) = \begin{bmatrix} f^*(\mathbf{x}_1, \mathbf{x}_2) & g(\mathbf{x}_1, \mathbf{x}_2) \\ g^*(\mathbf{x}_1, \mathbf{x}_2) & -f(\mathbf{x}_1, \mathbf{x}_2) \end{bmatrix}, \tag{3.58}$$

where,

$$f(\mathbf{x}_1, \mathbf{x}_2) = \int_{\mathcal{S}} \mathrm{d}\mathbf{x} \left[K^{(n)}(\mathbf{x}_1, \mathbf{x}) K^{(n)}(\mathbf{x}, \mathbf{x}_2) - K^{(p)*}(\mathbf{x}_1, \mathbf{x}) K^{(p)}(\mathbf{x}, \mathbf{x}_2) \right], \tag{3.59}$$

$$g(\mathbf{x}_1, \mathbf{x}_2) = \int_{\mathcal{S}} \mathrm{d}\mathbf{x} \left[K^{(n)*}(\mathbf{x}_1, \mathbf{x}) K^{(p)}(\mathbf{x}, \mathbf{x}_2) - K^{(p)}(\mathbf{x}_1, \mathbf{x}) K^{(n)}(\mathbf{x}, \mathbf{x}_2) \right]. \tag{3.60}$$

Showing that $g(\mathbf{x}_1, \mathbf{x}_2) = 0$ when $K^{(n)}(\mathbf{x}_1, \mathbf{x}_2)$ and $K_2^{(p)}(\mathbf{x}_1, \mathbf{x}_2)$ commute is a straightforward exercise that follows from their diagonal forms given in (3.41) and (3.42). Thus, we only consider the forward direction here, i.e., we will show that if $g(\mathbf{x}_1, \mathbf{x}_2) = 0$, then $K^{(n)}(\mathbf{x}_1, \mathbf{x}_2)$ and $K_2^{(p)}(\mathbf{x}_1, \mathbf{x}_2)$ commute.

If (3.60) is zero, then

$$\int_{\mathcal{S}} \mathrm{d}\mathbf{x}_3\, K^{(p)*}(\mathbf{x}_1, \mathbf{x}_3) g(\mathbf{x}_3, \mathbf{x}_2) = 0. \tag{3.61}$$

First, expanding $g(\mathbf{x}_3, \mathbf{x}_2)$ via the right-hand side of (3.60), and then adding and subtracting the kernel term $K^{(n)}(\mathbf{x}_1, \mathbf{x}) K^{(p)*}(\mathbf{x}, \mathbf{x}_3) K^{(p)}(\mathbf{x}_3, \mathbf{x}_2)$ in the integrand, yields

$$\left[K_2^{(p)}(\mathbf{x}_1, \mathbf{x}_2), K^{(n)}(\mathbf{x}_1, \mathbf{x}_2) \right] + \int_{\mathcal{S}} \mathrm{d}\mathbf{x}_3\, g^*(\mathbf{x}_1, \mathbf{x}_3) K^{(p)}(\mathbf{x}_3, \mathbf{x}_2) = 0\,, \tag{3.62}$$

where the first term is short-hand notation for the commutator given on left-hand side of (3.56), and the second term is zero because $g(\mathbf{x}_1, \mathbf{x}_3) = 0$. Thus, a vanishing $g(\mathbf{x}_1, \mathbf{x}_2)$ implies that $K_2^{(p)}$ and $K^{(n)}$ commute.

As a final step, we utilize the diagonal representations in (3.41) and (3.42) to find

$$f(\mathbf{x}_1, \mathbf{x}_2) = \sum_{m=1}^{\infty} \left(\lambda_m^2 - |\gamma_m|^2 \right) \phi_m^*(\mathbf{x}_1) \phi_m(\mathbf{x}_2)\,, \tag{3.63}$$

which is a positive semidefinite kernel because the eigenvalues satisfy $\left(\lambda_m^2 - |\gamma_m|^2 \right) \geq 0$, via the Cauchy-Schwarz inequality. □

In concluding this section, it is relevant to note that the random coefficients in the (symplectic or orthonormal) normal-mode decompositions are uncorrelated, but generally they are not independent. Therefore, the utility of these representations are limited to the first- and second-order moments of $E(\mathbf{x})$. An important exception, however, is when $E(\mathbf{x})$ is a Gaussian random process, such that it is completely characterized by its first and second moments. In this case, the random coefficients become *statistically independent*, which renders the decomposition a powerful analytical tool for characterizing $E(\mathbf{x})$.

3.5 From classical fields to quantum operators

Thus far, we have limited our development to *classical* electric fields. It is important, therefore, to point out that the results presented in this chapter have natural extensions to quantum field operators. In particular, our classical coherence theory for the quasi-monochromatic, paraxial case applies, without change, when we normalize $E_0(\boldsymbol{\rho}, t)$ and $E_L(\boldsymbol{\rho}', t)$ so that their dimensions are $\sqrt{\text{photons/m}^2\text{s}}$ instead of V/m. When quantized, these new fields become field operators, $\hat{E}_0(\boldsymbol{\rho}, t)$ and $\hat{E}_L(\boldsymbol{\rho}', t)$, with the nonzero canonical commutators $[\hat{E}_0(\boldsymbol{\rho}_1, t_1), \hat{E}_0^\dagger(\boldsymbol{\rho}_2, t_2)] = \delta(\boldsymbol{\rho}_2 - \boldsymbol{\rho}_1)\delta(t_2 - t_1)$ and $[\hat{E}_L(\boldsymbol{\rho}_1', t_1), \hat{E}_L^\dagger(\boldsymbol{\rho}_2', t_2)] = \delta(\boldsymbol{\rho}_2' - \boldsymbol{\rho}_1')\delta(t_2 - t_1)$, that obey the propagation integral [37]

$$\hat{E}_L(\boldsymbol{\rho}', t) = \int_{\mathbb{R}^2} \mathrm{d}\boldsymbol{\rho}\, \hat{E}_0(\boldsymbol{\rho}, t - L/c)\, h_L(\boldsymbol{\rho}' - \boldsymbol{\rho}), \tag{3.64}$$

with the same free-space Green's function as in the classical case (cf. (3.19) and (3.20)). It follows that the phase-insensitive (normally-ordered) and phase-sensitive correlation functions,

$$K_0^{(n)}(\boldsymbol{\rho}_1, t_1, \boldsymbol{\rho}_2, t_2) \equiv \langle \hat{E}_0^\dagger(\boldsymbol{\rho}_1, t_1) \hat{E}_0(\boldsymbol{\rho}_2, t_2) \rangle \text{ and} \tag{3.65}$$

$$K_0^{(p)}(\boldsymbol{\rho}_1, t_1, \boldsymbol{\rho}_2, t_2) \equiv \langle \hat{E}_0(\boldsymbol{\rho}_1, t_1) \hat{E}_0(\boldsymbol{\rho}_2, t_2) \rangle, \tag{3.66}$$

undergo the same propagation processes as their classical counterparts.[6] Thus, for quantum states that make these correlation functions complex-stationary, the results of Section 3.3 are directly applicable.

More generally, when we relax the quasimonochromatic and paraxial assumptions, the

[6]The angle brackets now denote quantum averages of operators.

resulting positive-frequency electric field operator $\hat{E}(\mathbf{r},t)$ still satisfies the scalar wave equation in free-space [14]. Hence, the quantum correlation functions $\mathcal{K}^{(n)}(\mathbf{r}_1,t_1,\mathbf{r}_2,t_2) \equiv \langle \hat{E}^\dagger(\mathbf{r}_1,t_1)\hat{E}(\mathbf{r}_2,t_2)\rangle$ and $\mathcal{K}^{(p)}(\mathbf{r}_1,t_1,\mathbf{r}_2,t_2) \equiv \langle \hat{E}(\mathbf{r}_1,t_1)\hat{E}(\mathbf{r}_2,t_2)\rangle$, obey the same Wolf equations, (3.13), as their classical-field counterparts, (3.14) and (3.12) respectively.

Furthermore, the modal decomposition of quantum fields can be carried out using Theorem 2, by replacing the classical correlation function matrix with the symmetrized quantum correlation function matrix,

$$\begin{aligned}\mathrm{K}(\mathbf{x}_1,\mathbf{x}_2) &\equiv \left\langle \begin{bmatrix} \hat{E}(\mathbf{x}_1) \\ \hat{E}^\dagger(\mathbf{x}_1) \end{bmatrix} \begin{bmatrix} \hat{E}^\dagger(\mathbf{x}_2) & \hat{E}(\mathbf{x}_2) \end{bmatrix} \right\rangle - (1/2)\delta(\mathbf{x}_2-\mathbf{x}_1)\mathrm{Q} \\ &= \begin{bmatrix} K^{(n)*}(\mathbf{x}_1,\mathbf{x}_2) & K^{(p)}(\mathbf{x}_1,\mathbf{x}_2) \\ K^{(p)*}(\mathbf{x}_1,\mathbf{x}_2) & K^{(n)}(\mathbf{x}_1,\mathbf{x}_2) \end{bmatrix}. \end{aligned} \tag{3.67}$$

where $K^{(n)}(\mathbf{x}_1,\mathbf{x}_2) \equiv (\langle \hat{E}^\dagger(\mathbf{x}_1)\hat{E}(\mathbf{x}_2)\rangle + \langle \hat{E}(\mathbf{x}_2)\hat{E}^\dagger(\mathbf{x}_1)\rangle)/2$. Note, however, $\mathrm{K}(\mathbf{x}_1,\mathbf{x}_2)$ is *positive-definite* and $\lambda_m \geq 1/2$ (due to the uncertainty principle), so the quantum (symmetrized) correlation matrices are a subset of those admissible for classical random fields. This decomposition yields an expansion for the field operator $\hat{E}(\mathbf{x})$ as

$$\begin{bmatrix} \hat{E}(\mathbf{x}) \\ \hat{E}^\dagger(\mathbf{x}) \end{bmatrix} = \sum_{m=1}^{\infty} \mathrm{V}_m(\mathbf{x}) \begin{bmatrix} \hat{a}_m \\ \hat{a}_m^\dagger \end{bmatrix}, \tag{3.68}$$

where the operators $\{\, \hat{a}_m : m = 1,2,\dots \}$, given by

$$\begin{bmatrix} \hat{a}_m \\ \hat{a}_m^\dagger \end{bmatrix} = \mathrm{Q} \int_{\mathcal{S}} \mathrm{V}_m^H(\mathbf{x})\mathrm{Q} \begin{bmatrix} \hat{E}(\mathbf{x}) \\ \hat{E}^\dagger(\mathbf{x}) \end{bmatrix} \mathrm{d}\mathbf{x}\,, \tag{3.69}$$

and satisfying the canonical commutation relations $[\hat{a}_m, \hat{a}_k^\dagger] = \delta_{m,k}$ and $[\hat{a}_m, \hat{a}_k] = 0$, are in isotropic and uncorrelated states with $\langle \hat{a}_m \rangle = 0$, $\langle \hat{a}_m^\dagger \hat{a}_k \rangle = (\lambda_m - 1/2)\delta_{mk}$, and $\langle \hat{a}_m \hat{a}_k \rangle = 0$. The advantage of the symplectic diagonalization is now evident. Whereas the symplectic diagonalization yields uncorrelated mode operators with the correct commutator relations, other (unitary) diagonalization methods do not, in general, yield mode operators with proper commutators [35, 36].

The uncorrelated modes in these decompositions are not necessarily in a product state, so their advantages are, in general, limited to dealing with the first- and second-order

moments of $\hat{E}(\mathbf{x})$. An important exception to this is when $\hat{E}(\mathbf{x})$ is in a Gaussian state, which implies that the $\{\hat{a}_m\}$ modes are in product Gaussian states. This renders the mode decomposition a powerful analytical tool for Gaussian-state $\hat{E}(\mathbf{x})$. For example, we can prove the following proposition for pure Gaussian states using Proposition 3 (which is true for an arbitrary state of $\hat{E}(\mathbf{x})$).

Proposition 4. *If $\hat{E}(\mathbf{x})$ is in a zero-mean pure Gaussian state, it admits an orthonormal expansion of form* (3.39) *(with the classical fields and random variables replaced by their quantum counterparts).*

Proof. Because $\hat{E}(\mathbf{x})$ is in a zero-mean pure Gaussian state, the $\{\hat{a}_m\}$ mode operators are in a product-state of pure[7] zero-mean Gaussian states with $\langle \hat{a}_m^2 \rangle = 0$ and $\langle \hat{a}_m^\dagger \hat{a}_m \rangle = \lambda_m - 1/2$, i.e., the modes must all be in *vacuum* ($\lambda_m = 1/2$), because the only pure thermal state is the vacuum state.

Evaluating (3.57) with the correlation function matrix expansion in (3.45), we arrive at

$$\int_{\mathcal{S}} \mathrm{d}\mathbf{x}\, \mathrm{K}(\mathbf{x}_1, \mathbf{x}) \mathrm{Q} \mathrm{K}(\mathbf{x}, \mathbf{x}_2) = \sum_{m=1}^{\infty} (1/4) \mathrm{V}_m(\mathbf{x}_1) \mathrm{Q} \mathrm{V}_m^H(\mathbf{x}_2) = (1/4) \delta(\mathbf{x}_2 - \mathbf{x}_1) \mathrm{Q}\,, \tag{3.70}$$

which satisfies the condition in Proposition 3, so a pure Gaussian state always admits an orthonormal expansion. □

3.6 Discussion

In this chapter we have begun exploring the coherence properties of light that has phase-sensitive fluctuations. The majority of our derivations focused on classical, scalar random optical fields. We first established general equations that govern the spatiotemporal evolution of phase-sensitive correlations, owing to the fact that they represent correlations of physical fields. We then turned our attention to the spatial effects of propagation when the field is complex-stationary, quasimonochromatic, and paraxial. We used the Gaussian-Schell model to highlight the significant differences between the propagation of phase-insensitive and phase-sensitive correlations. Finally, we turned to the normal-mode representation of fields with arbitrary phase-sensitive and phase-insensitive correlations. We found that such

[7] To verify that each mode is in a pure state, note that $\hat{\rho}_E \equiv \bigotimes_{m=1}^{\infty} \hat{\rho}_m$, where $\hat{\rho}_E$ is the state of the field operator $\hat{E}(\mathbf{x})$, and $\hat{\rho}_m$ denotes the state of each mode $\hat{a}_m$.

fields can be represented as the superposition of deterministic spatiotemporal fields that satisfy the wave equation, weighted by uncorrelated, complex, isotropic random coefficients and their conjugates. In addition, we determined a condition that is necessary and sufficient to simplify this representation to a superposition of deterministic orthonormal fields (which satisfy the wave equation), weighted by complex random coefficients that are still uncorrelated, but now have both phase-insensitive and phase-sensitive auto-correlations.

In Section 3.5 we shifted our focus to quantized fields, and showed that all of the classical results derived in this chapter are applicable to the phase-insensitive and phase-sensitive correlation functions of quantum field operators. Nonetheless, there is one significant advantage quantum mechanics offers over classical physics in regards to phase-sensitive correlations: quantum theory permits phase-sensitive correlations to exceed the Cauchy-Schwarz limits of classical phase-sensitive correlations [19]. As a result, nonclassical fields—fields that require a quantum description—may have phase-sensitive coherence benefits that are not seen in classical fields. A well known example is the coincidence-counting dip observed in a Hong-Ou-Mandel (HOM) interferometer when it is illuminated by the biphoton state obtained from spontaneous parametric downconversion. Classical fields with phase-sensitive correlations can produce an HOM dip, but it is too shallow to be observable [19].

Finally, we note that there have been several recent publications addressing the duality between optical coherence theory for phase-insensitive correlations, and the coherence properties of an entangled biphoton [15, 16, 17]. The results presented in these papers, apart from notational differences, are almost identical to what we have found for phase-sensitive coherence. This is not surprising. Spontaneous parametric downconversion—the principal source of entangled biphotons—produces signal and idler beams that are in a joint Gaussian state with a nonclassical, phase-sensitive cross-correlation function [18]. The entangled biphoton state is the low-flux limit of that Gaussian state. Hence, the coherence properties of the biphoton are precisely those of a phase-sensitive cross-correlation. This leads us to wonder whether classical phase-sensitive correlations are sufficient to accomplish objectives previously thought to be the sole province of the entangled biphoton state. Indeed, the remaining chapters of this thesis aim to quantify and clarify the classical/quantum boundary in imaging applications, by comparing the performance of phase-sensitive classical and quantum sources. The results obtained in this chapter, therefore, will play a central role in accomplishing that goal.

Chapter 4

Optical Coherence Tomography with Phase-Sensitive Light

Optical coherence tomography (OCT) produces 3-D imagery through a combination of focused-beam scanning (for transverse resolution) and interference measurements (for axial resolution). Conventional OCT (C-OCT) uses classical-state signal and reference light beams, with a phase-insensitive cross-correlation, and measures their second-order interference via Michelson interferometry [38, 39]. In quantum OCT (Q-OCT), on the other hand, the signal and reference beams are in an entangled biphoton state generated by spontaneous parametric down-conversion, and their fourth-order interference is measured by Hong-Ou-Mandel interferometry. In comparison to C-OCT, Q-OCT offers a two-fold improvement in axial resolution and even-order dispersion cancellation [1, 3], advantages that have been ascribed to the nonclassical nature of the entangled biphoton state. We shall describe a new configuration for optical coherence tomography that relies on classical-state light yet achieves the same factor-of-two axial resolution improvement and even-order dispersion cancellation that are the key features of Q-OCT. This new form of optical coherence tomography uses a phase-conjugate amplifier in conjunction with a Michelson interferometer to detect interference between two classical light fields with a nonzero phase-sensitive cross-correlation. Under appropriate conditions, this imaging arrangement—which we call phase-conjugate optical coherence tomography (PC-OCT)—can achieve a signal-to-noise ratio that is comparable to that of C-OCT. Before beginning our presentation of PC-OCT and its performance characteristics, we will digress to discuss the properties of classical

and nonclassical Gaussian-state light beams with phase-sensitive cross-correlations. This material is essential to understanding both PC-OCT and Q-OCT, because the biphoton state produced by SPDC is a limiting case of nonclassical Gaussian-state light.

4.1 Classical and nonclassical Gaussian-state light

Consider a classical light source that produces signal (S) and reference (R) beams with a common center frequency ω_0 and baseband complex envelopes $E_K(t)$ for $K = S, R$, where, for both signal and reference, we are concerned with a single polarization of particular spatial modes. For convenience in linking to the case of a nonclassical light source, we shall normalize these fields so that their powers are $\hbar\omega_0|E_K(t)|^2$. Suppose that $E_S(t)$ and $E_R(t)$ are stationary, zero-mean, jointly-Gaussian, complex-valued random processes. They are then completely characterized by the following auto- and cross-correlation functions:[1]

$$K_{JK}^{(n)}(\tau) \equiv \langle E_J^*(t+\tau)E_K(t)\rangle = \int_{-\infty}^{\infty} \frac{\mathrm{d}\Omega}{2\pi}\, S_{JK}^{(n)}(\Omega)e^{-i\Omega\tau} \tag{4.1}$$

$$K_{JK}^{(p)}(\tau) \equiv \langle E_J(t+\tau)E_K(t)\rangle = \int_{-\infty}^{\infty} \frac{\mathrm{d}\Omega}{2\pi}\, S_{JK}^{(p)}(\Omega)e^{-i\Omega\tau}, \tag{4.2}$$

for $J, K = S, R$, where $S_{JK}^{(n)}(\Omega)$ and $S_{JK}^{(p)}(\Omega)$ are the associated spectral densities at detuning Ω from ω_0, and, in keeping with the quantum case to come, the superscripts (n) and (p) label normally-ordered (phase-insensitive) and phase-sensitive correlations, respectively.

A thermal-state light source, as is ordinarily used in C-OCT, satisfies the preceding statistical assumptions with

$$K_{SS}^{(n)}(\tau) = K_{RR}^{(n)}(\tau) = K_{SR}^{(n)}(\tau) \tag{4.3}$$

being the only nonzero correlation functions. In the spectral domain, we then get

$$S_{SS}^{(n)}(\Omega) = S_{RR}^{(n)}(\Omega) = S_{SR}^{(n)}(\Omega), \tag{4.4}$$

[1] In this chapter, with no loss of generality, we have flipped the sign of τ in the correlation functions, with respect to (3.4) and (3.5), for analytic convenience.

which saturates the Cauchy-Schwarz bound

$$|S_{SR}^{(n)}(\Omega)| \leq \sqrt{S_{SS}^{(n)}(\Omega) S_{RR}^{(n)}(\Omega)}. \tag{4.5}$$

For PC-OCT we will employ signal and reference beams that are stationary, zero-mean, jointly-Gaussian, complex-valued random processes whose nonzero correlation functions satisfy

$$K_{SS}^{(n)}(\tau) = K_{RR}^{(n)}(\tau) = K_{SR}^{(p)}(\tau), \tag{4.6}$$

with their common spectral density, $S(\Omega)$, being an even nonnegative function of detuning. From the Cauchy-Schwarz bound

$$|S_{SR}^{(p)}(\Omega)| \leq \sqrt{S_{SS}^{(n)}(-\Omega) S_{RR}^{(n)}(\Omega)} \tag{4.7}$$

it follows that these light beams have the strongest phase-sensitive correlation permitted by classical physics [19].

Now let us turn to the case of nonclassical light. Here the complex envelopes of the signal and reference beams are replaced by photon-units field operators, $\hat{E}_S(t)$ and $\hat{E}_R(t)$, with the nonzero commutators

$$[\hat{E}_J(t), \hat{E}_K^\dagger(u)] = \delta_{JK}\delta(t-u), \text{ for } J, K = S, R. \tag{4.8}$$

As we have reviewed in Section 2.3, by means of continuous-wave SPDC we can produce signal and reference beams that are in a stationary, zero-mean, jointly-Gaussian state with the following nonzero correlations

$$K_{SS}^{(n)}(\tau) = K_{RR}^{(n)}(\tau) = \int_{-\infty}^{\infty} \frac{\mathrm{d}\Omega}{2\pi} S(\Omega) e^{-i\Omega\tau}, \tag{4.9}$$

$$K_{SR}^{(p)}(\tau) = \int_{-\infty}^{\infty} \frac{\mathrm{d}\Omega}{2\pi} \sqrt{S(\Omega)(S(\Omega)+1)} e^{-i\Omega\tau}, \tag{4.10}$$

for $S(\Omega) = S(-\Omega) \geq 0$. This state has the strongest phase-sensitive correlation permitted by quantum physics [19]. Moreover, $S(\Omega) \ll 1$ prevails in the typical low-brightness operating regime for continuous-wave SPDC, from which we see that $|S_{SR}^{(p)}(\Omega)| \approx \sqrt{S(\Omega)}$ greatly exceeds the classical limit $\sqrt{S_{SS}^{(n)}(-\Omega) S_{RR}^{(n)}(\Omega)} = S(\Omega)$ in this case. Furthermore, in the low-

flux limit of low-brightness SPDC the outputs comprise a stream of individually detectable biphotons, as used in Q-OCT.

4.2 OCT configurations and their interference signatures

The basic block diagram for continuous-wave PC-OCT is shown in Figure 4-1. We have suppressed all spatial coordinates, to focus our attention on the axial behavior, and we have drawn a transmission geometry, whereas the actual system would employ a bistatic geometry in reflection. The signal and reference beams at the PC-OCT input are classical fields, with complex envelopes $E_S(t)$ and $E_R(t)$, whose statistics are as given in the previous section. The signal beam is focused on a transverse spot on the sample yielding a superposition of reflections from various depths such that the complex envelope of the overall return from the sample is $E_H(t) = E_S(t) \star h(t)$, where $\star$ denotes convolution and

$$H(\Omega) \equiv \int_{-\infty}^{\infty} \mathrm{d}t\, h(t) e^{i\Omega t} = \int_{0}^{\infty} \mathrm{d}z\, r(z,\Omega) e^{i2\phi(z,\Omega)} \tag{4.11}$$

is the sample's baseband impulse response. In (4.11), $r(z,\Omega)$ is the complex reflection coefficient at depth z and detuning Ω, and $\phi(z,\Omega)$ is the phase acquired through propagation to depth z in the sample. Conjugate amplification of $E_H(t)$ yields the complex envelope $E_C(t) = [E_H^*(t) + w(t)] \star \nu(t)$, where $w(t)$, a zero-mean, circulo-complex, white Gaussian noise with correlation function $\langle w^*(t+\tau)w(t)\rangle = \delta(\tau)$, is the quantum noise injected by the conjugation process, and

$$\nu(t) = \int_{-\infty}^{\infty} \frac{\mathrm{d}\Omega}{2\pi}\, V(\Omega) e^{-i\Omega t} \tag{4.12}$$

gives the conjugator's baseband impulse response in terms of its frequency response. The output of the conjugator is refocused onto the sample resulting in the positive-frequency field $E_1(t) = [E_C(t) \star h(t)] e^{-i\omega_0 t}$, which is interfered with the delayed reference beam $E_2(t) = E_R(t-T)e^{-i\omega_0(t-T)}$ in a Michelson interferometer. The detectors in Figure 4-1 are assumed to have quantum efficiency η, no dark current, and thermal noise with a white current spectral density $S_{i_{\mathrm{th}}}$. The average amplified difference current, which constitutes the PC-OCT interference signature, is then

$$\langle i_d(t)\rangle = 2q\eta G_A \,\mathrm{Re}\left(\int_{-\infty}^{\infty} \frac{\mathrm{d}\Omega}{2\pi}\, H^*(-\Omega) H(\Omega) V^*(-\Omega) S(\Omega) e^{-i(\Omega-\omega_0)T} \right), \tag{4.13}$$

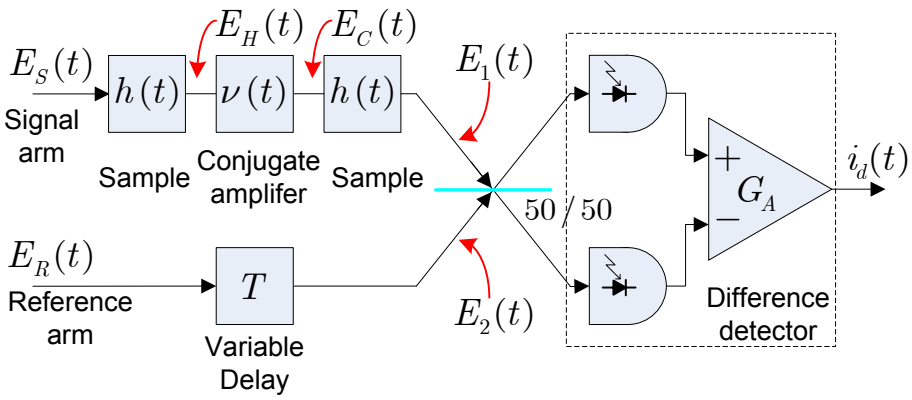

Figure 4-1: Phase-conjugate OCT configuration.

where q is the electron charge.

For comparison with C-OCT and Q-OCT, consider the behavior of the preceding signature when

$$V^*(-\Omega)S(\Omega) \approx V^*S(\Omega) = \left(|V|e^{-i\theta_V} P_S \sqrt{2\pi/\Omega_S^2}\right) e^{-\Omega^2/2\Omega_S^2} \tag{4.14}$$

and

$$H(\Omega) = re^{i(\omega_0+\Omega)T_0}\,, \tag{4.15}$$

with $r \equiv |r|e^{i\theta_r}$, and $|r| \ll 1$. Physically, this corresponds to a signal-reference source with a Gaussian-shaped power spectrum, a conjugate amplifier whose bandwidth is much broader than that of this source, and a sample that is a weakly-reflecting mirror at delay T_0. Equation (4.13) then gives

$$\langle i_d(t)\rangle = 2q\eta G_A|V|P_S\,|r|^2\, e^{-2\Omega_S^2(T_0-T/2)^2}\cos(\omega_0 T - \theta_V), \tag{4.16}$$

i.e., a sinusoidal fringe pattern with a Gaussian-shaped visibility function $e^{-2\Omega_S^2(T_0-T/2)^2}$. Thus, defining the axial resolution of PC-OCT to be the full-width between the e^{-2} attenuation points in this visibility envelope, viewed as a function of T_0, shows that a source bandwidth Ω_S yields an axial resolution equal to $2/\Omega_S$.

The basic setup for C-OCT is shown in Figure 4-2. Its signal and reference beams are classical fields, with complex envelopes $E_S(t)$ and $E_R(t)$, whose statistics are as given in the previous section for thermal-state light. C-OCT illuminates the sample with the signal

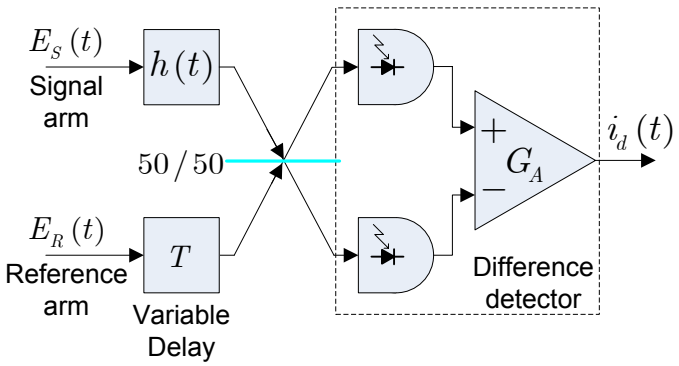

Figure 4-2: Conventional OCT configuration.

beam and interferes the reflected signal, given by convolution of $E_S(t)$ with $h(t)$, with the delayed reference beam in a Michelson interferometer. The average amplified difference current is found to be

$$\langle i_d(t)\rangle = 2q\eta G_A \,\mathrm{Re}\left(\int_{-\infty}^{\infty} \frac{\mathrm{d}\Omega}{2\pi}\, H^*(-\Omega)S(\Omega)e^{-i(\Omega-\omega_0)T}\right), \tag{4.17}$$

which reduces to

$$\langle i_d(t)\rangle = 2q\eta G_A P_S\,|r|\, e^{-\Omega_S^2(T_0-T)^2/2}\cos(\omega_0(T-T_0)-\theta_r) \tag{4.18}$$

for the weakly-reflecting mirror example. Once again we get a sinusoidal fringe pattern with a Gaussian-shaped visibility function, only this time the axial resolution is $4/\Omega_S$, viz., a factor of two worse than that of PC-OCT for the same source bandwidth.

The configuration for Q-OCT appears in Figure 4-3. To analyze its performance, we use photon-units field operators, $\hat{E}_S(t)$ and $\hat{E}_R(t)$, to describe the signal and reference beams, and we assume that these quantum fields are in the nonclassical Gaussian state described in the previous section. The familiar biphoton HOM dip can then be obtained theoretically in a manner that is the natural quantum generalization of the classical Gaussian-state analysis we have used so far in this paper [19]. In the usual biphoton limit wherein HOM interferometry is performed, $S(\Omega) \ll 1$ prevails, and the average photon-coincidence counting signature can be shown to be

$$\langle C(T)\rangle = \frac{q^2\eta^2}{2}\left[\int_{-\infty}^{\infty}\frac{\mathrm{d}\Omega}{2\pi}\,|H(\Omega)|^2 S(\Omega) - \mathrm{Re}\left(\int_{-\infty}^{\infty}\frac{\mathrm{d}\Omega}{2\pi}H^*(-\Omega)H(\Omega)S(\Omega)e^{-i2\Omega T}\right)\right]. \tag{4.19}$$

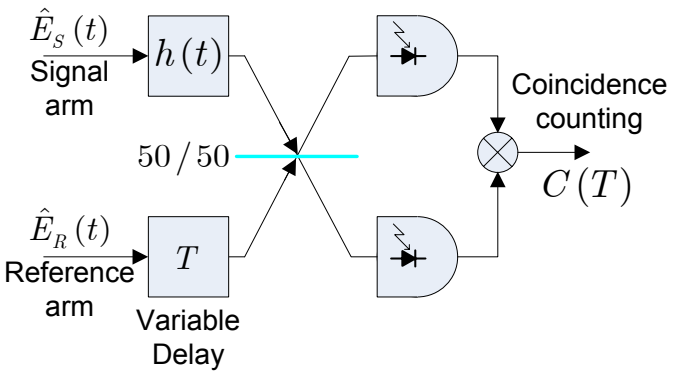

Figure 4-3: Quantum OCT configuration.

It is the second term in this coincidence signature that carries useful information about the sample. Note that it has the same basic structure as the PC-OCT signature, i.e., it is an inverse Fourier transform integral whose integrand is proportional to $H^*(-\Omega)H(\Omega)S(\Omega)$. For our weakly-reflecting mirror, the Q-OCT signature takes the following simple form:

$$\langle C(T)\rangle = \frac{q^2\eta^2|r|^2P_S}{2}(1 - e^{-2\Omega_S^2(T_0-T)^2}), \tag{4.20}$$

which dips to zero at $T_0 = T$. Taking its axial resolution to be the full-width between the e^{-2} attenuation points in the Gaussian-dip term, viewed as a function of T_0, we see that Q-OCT achieves the same axial resolution as PC-OCT.

To probe the effect of dispersion on PC-OCT, C-OCT, and Q-OCT, we modify the sample's frequency response to

$$H(\Omega) = re^{i[(\omega_0+\Omega)T_0+b\Omega^2/2]}, \tag{4.21}$$

where b is a nonzero real constant representing second-order (group-delay) dispersion. Because the sample's frequency response enters the PC-OCT and Q-OCT signatures as $H^*(-\Omega)H(\Omega)$, this dispersion term cancels out in both, leaving their signatures unaffected. For C-OCT, however, we find that the Gaussian envelope of the average amplified difference current is now proportional to $e^{-\Omega_S^2(T_0-T)^2/2(1+\Omega_S^4b^2)}$. Therefore, the axial resolution becomes badly degraded when $\Omega_S^4b^2 \gg 1$. More generally, for

$$H(\Omega) = re^{i[(\omega_0+\Omega)T_0+\beta(\Omega)]}, \tag{4.22}$$

PC-OCT and Q-OCT are immune to dispersion created by the even-order terms in the Taylor series expansion of $\beta(\Omega)$, whereas C-OCT's resolution is affected by them.

The axial resolution and dispersion cancellation benefits that accrue to PC-OCT and Q-OCT arise from their interference signatures containing the product $H^*(-\Omega)H(\Omega)$, whereas C-OCT's interference signature involves only $H^*(-\Omega)$. It is worth noting, therefore, that the former leads to more complicated to interpret results when the sample is comprised of reflections from multiple depths. To see that this is so, suppose that

$$H(\Omega) = r_0 e^{i(\omega_0+\Omega)T_0} + r_1 e^{i(\omega_0+\Omega)T_1}, \tag{4.23}$$

corresponding to a sample consisting of two weakly-reflecting mirrors, with $r_m = |r_m|e^{i\theta_{rm}}$ for $m = 0, 1$. The interference signature of C-OCT is linear in $H(\Omega)$, thus we get the superposition of the signatures from each mirror, viz.,

$$\begin{aligned}\langle i_d(t)\rangle = 2q\eta G_A P_S \Big[&|r_0|e^{-\Omega_S^2(T_0-T)^2/2}\cos\big(\omega_0(T-T_0)-\theta_{r_0}\big) \\ &+ |r_1|e^{-\Omega_S^2(T_1-T)^2/2}\cos\big(\omega_0(T-T_1)-\theta_{r_1}\big)\Big].\end{aligned} \tag{4.24}$$

The interference signature of PC-OCT is not linear in $H(\Omega)$, so that the two-mirror sample yields

$$\begin{aligned}\langle i_d(t)\rangle = 2q\eta G_A|V|P_S \Bigg\{ &\Big[|r_0|^2 e^{-2\Omega_S^2(T_0-T/2)^2} + |r_1|^2 e^{-2\Omega_S^2(T_1-T/2)^2}\Big]\cos(\omega_0 T - \theta_V) \\ &+ |r_0||r_1|e^{-\Omega_S^2(T_0+T_1-T)^2/2}\Big[\cos\big(\omega_0(T+\Delta T)-\theta_V+\Delta\theta\big) \\ &+ \cos\big(\omega_0(T-\Delta T)-\theta_V-\Delta\theta\big)\Big]\Bigg\}.\end{aligned} \tag{4.25}$$

where $\Delta T \equiv T_1 - T_0$ and $\Delta\theta \equiv \theta_{r_1} - \theta_{r_0}$. The terms on the first line are due to reflections from the same mirror in both passes through the sample, and the term on the second line corresponds to reflections from different mirrors in each pass through the sample. Similar behavior occurs for the two-mirror sample in Q-OCT, i.e., in addition to the superposition of self-reflection terms that give single-mirror HOM dips, there is a cross-reflection term akin to what we have just exhibited for PC-OCT.

Equation (4.25) shows that the cross-layer interference term is sensitive to the relative

phase between the reflective layers in the sample. In particular, the peak amplitude of this cross-layer interference term is a function of $\Delta\theta$, the relative phase between the complex reflectivities of the two mirrors. With appropriate post-processing, this phase difference may be inferred from the interference envelope, something that is not possible in C-OCT when the separation between the mirrors greatly exceeds the system's axial resolution. Now suppose that the mirrors are dispersive, so that the frequency response of the sample becomes

$$H(\Omega) = r_0 e^{i[(\omega_0+\Omega)T_0 + b_0\Omega^2/2]} + r_1 e^{i[(\omega_0+\Omega)T_1 + b_1\Omega^2/2]}. \tag{4.26}$$

The self-reflection terms in (4.25) are, of course, unaffected by the group-delay dispersion. However, the envelope of the cross-layer interference is sensitive to $\Delta b \equiv b_1 - b_0$, which represents group-delay dispersion from the intervening medium between the two mirrors. Therefore the cross-layer interference envelope provides information about the sample's dispersion properties.

The simple two-layer example above demonstrates that the nonlinear $H(\Omega)$ dependence of the interference signatures from PC-OCT and Q-OCT affords these imagers more information about the sample than is available from C-OCT. However, tapping into this additional information will require more elaborate post-processing than is needed by C-OCT. Because Q-OCT has only recently been demonstrated, limited attention has been paid to optimal processing of its signature, particularly when that signature is obtained from multilayer micron-scale media [1, 2, 3]. However, because the baseband envelope of the PC-OCT signature and the Q-OCT signature share the same fundamental features, parameter estimation algorithms developed for processing the Q-OCT signature will likely be applicable to PC-OCT as well.

4.3 Signal-to-noise ratio

Having shown that PC-OCT retains the key advantages of Q-OCT, let us turn to its signal-to-noise ratio (SNR) behavior. Because Q-OCT relies on SPDC to generate the entangled biphoton state, and Geiger-mode avalanche photodiodes to perform photon-coincidence counting, its image acquisition is much slower than that of C-OCT, which can use bright sources and linear-mode detectors. To assess the SNR of PC-OCT we shall continue to use the Gaussian spectrum for $S(\Omega)$ and the nondispersing single mirror for $H(\Omega)$, but,

in order to limit its quantum noise, we take the conjugator's frequency response to be $V(\Omega) = Ve^{-\Omega^2/4\Omega_V^2}$. We assume that $i_d(t)$ is time averaged for T_I sec (denoted $\langle i_d(t)\rangle_{T_I}$) at the reference-arm delay that maximizes the interference signature, and we define

$$\mathrm{SNR}_{\text{PC-OCT}} = \langle i_d(t)\rangle^2 / \mathrm{var}[\langle i_d(t)\rangle_{T_I}]\,, \tag{4.27}$$

where var[·] denotes the variance of its argument. When the $w(t)$ (quantum noise) contribution to the conjugator's output dominates the $E_H(t)$ (sample reflection) contribution we find that

$$\mathrm{SNR}_{\mathrm{PC-OCT}} = \frac{8\,T_I\,\eta\,|r|^4\,|V|^2\,P_S^2\,\Omega_V^2/(\Omega_S^2+2\Omega_V^2)}{\left[\Omega_{\mathrm{th}} + P_S + |rV|^2\sqrt{\Omega_V^2/2\pi} + \dfrac{2\eta\,|rV|^2 P_S\,\Omega_V}{\sqrt{\Omega_S^2+\Omega_V^2}}\right]}\,, \tag{4.28}$$

where $\Omega_{\mathrm{th}} \equiv S_{i_{\mathrm{th}}}/q^2\eta$. From left to right the terms in the noise denominator are the thermal noise, the reference-arm shot noise, the conjugate-amplifier quantum noise, and the intrinsic noise of the signal×reference interference pattern itself. Best performance is achieved when the conjugator gain $|V|^2$ is large enough to neglect the first two noise terms, and the input power P_S is large enough such that the intrinsic noise greatly exceeds the conjugator's quantum noise. In this case we get

$$\mathrm{SNR}_{\text{PC-OCT}} = \frac{4T_I|r|^2 P_S \Omega_V \sqrt{\Omega_S^2+\Omega_V^2}}{\Omega_S^2+2\Omega_V^2}\,. \tag{4.29}$$

To compare the preceding SNR to that for C-OCT, we define

$$\mathrm{SNR}_{\text{C-OCT}} = \langle i_d(t)\rangle^2 / \mathrm{var}[\langle i_d(t)\rangle_{T_I}] \tag{4.30}$$

for the Figure 4-2 configuration at the peak of the C-OCT interference signature. When the reflected signal field is much weaker than the reference field, we find that

$$\mathrm{SNR}_{\text{C-OCT}} = 4\eta T_I |r|^2 P_S\,, \tag{4.31}$$

which can be *smaller* than the ultimate $\mathrm{SNR}_{\text{PC-OCT}}$ result. However, if PC-OCT's conjugator gain is too low to reach its ultimate performance, but its reference-arm shot noise

dominates the other noise terms, we get

$$\mathrm{SNR}_{\text{PC-OCT}} = \frac{8\eta T_I |r|^4 |V|^2 P_S \Omega_V^2}{\Omega_S^2 + 2\Omega_V^2}\,, \tag{4.32}$$

which is substantially *lower* than $\mathrm{SNR}_{\text{C-OCT}}$, because $|rV|^2 \ll 1$ is implicit in our assumption that the reference shot noise is dominant as high detector quantum efficiency can be expected. Thus we can conclude that PC-OCT will have SNR similar to that of C-OCT, but only if high-gain phase conjugation is available.[2]

4.4 Discussion

At this juncture it is worth emphasizing the fundamental physical point revealed by the preceding analysis. The use of entangled biphotons and fourth-order interference measurement in an HOM interferometer enable Q-OCT's two performance advantages over C-OCT: a factor-of-two improvement in axial resolution and cancellation of even-order dispersion [1, 3]. Classical phase-sensitive light also produces an HOM dip with even-order dispersion cancellation, but this dip is essentially unobservable because it rides on a much stronger background term [19]. Thus the nonclassical character of the entangled biphoton is essential to observing Q-OCT's benefits, from which it might be concluded that nonclassical light is the source of these performance advantages over C-OCT. Such is not the case, however, because our PC-OCT configuration reaps the same advantages as Q-OCT, using *classical* phase-sensitive light and a second-order Michelson interferometer. However, because phase-sensitive cross-correlations cannot be seen in the second-order interference measurements used in C-OCT, PC-OCT phase conjugates one of the phase-sensitive cross-correlated beams, converting their phase-sensitive cross-correlation into a phase-insensitive cross-correlation that can be seen in second-order interference. Hence, it is really phase-sensitive cross-correlations between the signal and reference beams that are at the root of axial resolution enhancement and even-order dispersion cancellation. Our treatment of PC-OCT assumed classical-state light, and, because we need $S(0) \gg 1$ for high-SNR PC-OCT operation, little further can be expected in the way of performance improvement by using nonclassical light in PC-OCT. This can be seen by comparing the cross-spectra $S(\Omega)$ and

[2]Some care should be exercised in making this SNR comparison, because $\hbar\omega_0 P_S$ is the total power that illuminates the sample in C-OCT, but it is only the initial sample illumination power in PC-OCT, i.e., there is also the power that illuminates the sample after the phase-conjugation operation.

$\sqrt{S(\Omega)(S(\Omega)+1)}$ when $S(\Omega) = (P_S\sqrt{2\pi/\Omega_S^2})e^{-\Omega^2/2\Omega_S^2}$ with $P_S\sqrt{2\pi/\Omega_S^2} \gg 1$.

The intimate physical relation between PC-OCT and Q-OCT can be further elucidated by considering the way in which the sample's frequency response enters their measurement averages. We again assume $V^*(-\Omega)S(\Omega) \approx V^*S(\Omega)$, so that both imagers yield signatures $\propto \int \mathrm{d}\Omega\, H^*(-\Omega)H(\Omega)S(\Omega)$. Abouraddy *et al.* [1] use Klyshko's advanced-wave interpretation [40] to account for the $H^*(-\Omega)H(\Omega)$ factor in the Q-OCT signature as the product of an actual sample illumination and a virtual sample illumination. In our PC-OCT imager, this same $H^*(-\Omega)H(\Omega)$ factor comes from the two sample illuminations, one before phase conjugation and one after. In both cases, it is the phase-sensitive cross-correlation that is responsible for this factor. Q-OCT uses nonclassical light and fourth-order interference while PC-OCT can use classical light and second-order interference to obtain the same sample information.

The advantages PC-OCT accrues over C-OCT via two sample illuminations lead naturally to considering whether C-OCT would also benefit from two sample illuminations. Consider the Figure 4-1 system with $E_S(t)$ and $E_R(t)$ arising from a C-OCT light source, and the phase-conjugate amplifier replaced with a conventional phase-insensitive amplifier of field gain $G(\Omega) = Ge^{-\Omega^2/4\Omega_G^2}$ with $|G| \gg 1$. This two-pass C-OCT arrangement then yields an interference signature with the Gaussian-shaped visibility function $e^{-2\Omega_S^2(T_0-T/2)^2}$ for the weakly-reflecting mirror when the amplifier is sufficiently broadband. In addition, the SNR is given by Eq. (4.28) with V replaced by G and Ω_V replaced by Ω_G.[3] Thus two-pass C-OCT has the same axial resolution advantage and SNR behavior as PC-OCT. However, instead of providing even-order dispersion cancellation, two-pass C-OCT doubles all the even-order dispersion coefficients.

Let us conclude by briefly addressing the implementation issues that arise with PC-OCT. Our imager requires: signal and reference light beams with a strong and broadband phase-sensitive cross-correlation; an illumination setup in which the signal beam is focused on and reflected from a sample, undergoes conjugate amplification, is refocused onto the same sample, and then interfered with the time-delayed reference beam; and a broadband, high-gain phase conjugator. Strong signal and reference beams that have a phase-sensitive cross-correlation can be produced by splitting a single laser beam in two, and then imposing

[3] Because there is no amplification noise when $|G(\Omega)| < 1$, the SNR expression by making these replacements in (4.28) is a lower bound on the SNR of double-pass C-OCT. However, for $|G| \gg 1$ this lower bound is very close to the actual SNR value.

appropriate amplitude and phase noises on these beams through electro-optic modulators. Existing optical telecommunication modulators, however, do not have sufficient bandwidth for high-resolution OCT. A better approach to the PC-OCT source problem is to exploit nonlinear optics. SPDC can have THz phase-matching bandwidths, and might be suitable for the PC-OCT application. Unlike Q-OCT, which relies on SPDC for its entangled biphotons, a down-conversion source for PC-OCT can—and should—be driven at maximum pump strength, i.e., there is no need to limit its photon-pair generation rate so that these biphoton states are time-resolved by the ∼MHz bandwidth single-photon detectors that are used in Q-OCT's coincidence counter. Hence pulsed pumping will surely be needed. SPDC is also a possibility for the phase conjugation operation. In a frequency-degenerate type-II phase matched down-converter, the reflected signal $E_H(t)$ is applied in one input polarization (call it the signal polarization) and a vacuum state field in the other (idler) polarization. The idler output then has the characteristics needed for PC-OCT, viz., it consists of a phase-conjugated version of the signal input plus the minimum quantum noise needed to preserve free-field commutator brackets [18]. Similar phase-conjugate operation can also be obtained from frequency-degenerate four-wave mixing [41, 42, 43]. In both cases, pulsed operation will be needed to achieve the gain-bandwidth product for high-performance PC-OCT.

The final point we shall make about PC-OCT concerns phase stability. Interference fringe visibility decreases significantly when there are randomly-varying phase shifts in the signal and reference branches of the PC-OCT interferometer. As seen directly from (4.13), the fringe visibility of PC-OCT is susceptible to random phase fluctuations in the conjugator impulse response. Let us assume the conjugator impulse response is subject to a random phase $\phi(\Omega)$, such that it is given by $e^{i\phi(\Omega)}V(\Omega)$, where $\phi(\Omega)$ is a zero-mean, stationary, real-valued Gaussian random process with correlation function $K(\Omega') = \langle\phi(\Omega+\Omega')\phi(\Omega)\rangle$, and is independent of all other random processes. The fringe pattern in (4.13) is then scaled by $e^{-K(0)/2}$, which decreases the fringe visibility exponentially with increasing phase variance $K(0)$. An additional source of random phase fluctuations in time-domain OCT systems is the variable time delay, typically implemented with a moving mirror that changes the path length of the reference arm. In C-OCT, current technology allows full axial scans at KHz rates, and at such rates aberrations due to mirror motion are the limiting factor in stability [44]. If PC-OCT achieves similar imaging speeds—which would be feasible if the

SNR is close to its maximum value derived in the previous section—mirror stability will also become relevant for fringe visibility in PC-OCT.

In summary, in this chapter we have analyzed a phase-conjugate OCT imager that combines many of the best features of conventional OCT and quantum OCT. Like C-OCT, PC-OCT relies on second-order interference in a Michelson interferometer. Thus it can use linear-mode avalanche photodiodes (APDs), rather than the lower bandwidth and less efficient Geiger-mode APDs employed in Q-OCT. Like Q-OCT, PC-OCT enjoys a factor-of-two axial resolution advantage over C-OCT, and automatic cancellation of even-order dispersion terms. The source of these advantages, for both Q-OCT and PC-OCT, is the phase-sensitive cross-correlation between the signal and reference beams. In PC-OCT, however, this cross-correlation need not be beyond the limits of classical physics, as is required for Q-OCT. Finally, PC-OCT may achieve an SNR comparable to that of C-OCT, thus realizing much faster image acquisition than is currently possible in Q-OCT. All of these PC-OCT benefits are contingent on developing an appropriate source for producing signal and reference light beams with a strong and broadband phase-sensitive cross-correlation, and a phase conjugation system with suitably high gain-bandwidth product.

Chapter 5

Unified Theory of Ghost Imaging with Gaussian-State Light

Ghost imaging is the acquisition of an object's transverse transmittance pattern by means of photocurrent correlation measurements. In a generic ghost imaging experiment (see the example in Figure 5-1), a classical or quantum source that generates two paraxial optical fields is utilized. These fields propagate in two different directions, through a linear system of optical elements that may include lenses and mirrors, and arrive at their respective detection planes. At one detection plane, the incident field illuminates a thin transmission mask, whose spatial transmissivity is the pattern to be measured, and is subsequently detected by a bucket detector that provides no transverse spatial resolution. At the other detection plane, the incident field, which has never interacted with the transmission mask, is detected by a pinhole detector centered at some transverse coordinate $\boldsymbol{\rho}_1$. The two photocurrents are then correlated and the output value is registered. This process is repeated as the pinhole detector is scanned along the transverse plane. The resulting correlation measurements, when viewed as a function of $\boldsymbol{\rho}_1$, reveal the power transmissivity of the mask. The image obtained by this procedure has been called a "ghost image," because the bucket detector that captures the optical field which illuminated the transmission mask has no spatial resolution, and the the pinhole detector measures a field that never interacted with the transmission mask.[1]

[1]Other ghost imaging configurations replace the scanning pinhole detector with a CCD array for parallel data acquisition, or separate the object plane and the detection plane to allow greater flexibility in implementation, or image in reflectance rather than transmission. These variations do not affect the fundamental physics that governs ghost imaging, and, with the exception of separating the object and detection planes,

The first demonstration of ghost imaging utilized biphoton-state light obtained from spontaneous parametric downconversion together with photon-counting bucket and pinhole detectors. This arrangement yielded a background-free image that was interpreted as a quantum phenomenon, owing to the entanglement of the source photons [5]. However, subsequent experimental [12, 45] and theoretical [10, 11] considerations demonstrated that ghost imaging can be performed with thermalized laser light, utilizing either photon-counting detectors or CCD detector arrays to obtain ghost images, albeit with a background.

The theory of biphoton ghost imaging requires quantum descriptions for both the optical source and its photodetection statistics, whereas thermal-light ghost imaging admits to a semiclassical description employing classical fields and shot-noise limited detectors. This disparity has sparked interest [46, 47, 48, 49] in establishing a unifying theory that characterizes the fundamental physics of ghost imaging and delineates the boundary between classical and quantum behavior. In this chapter we develop that unifying theory within the framework of Gaussian-state (classical and nonclassical) sources.

The foundation of our work is laid in Section 5.1. Here we begin by expressing the photocurrent cross-correlation—the ghost image—as a filtered fourth-moment of the field operators illuminating the detectors. Next, we briefly review the Schell-model correlations found in classical and quantum zero-mean Gaussian states. Then, using the moment-factoring theorem for zero-mean Gaussian states, we obtain our fundamental expression for the Gaussian-state ghost image in terms of the phase-insensitive and phase-sensitive cross-correlations between the two detected fields, plus a background. The final part of Section 5.1 sets the stage for detailed understanding of ghost imaging by summarizing the relevant results from Chapter 3 on coherence propagation of phase-sensitive field states.

In Section 5.2 we analyze ghost imaging performed with three classes of Gaussian-state sources. We first consider a source possessing the maximum phase-insensitive cross-correlation—as constrained by its auto-correlation functions—but no phase-sensitive cross-correlation. Such a source always produces a classical state. Thermal light is of this class. We also consider a source with the maximum *classical* phase-sensitive cross-correlation, given the same auto-correlations as in the previous case, but no phase-insensitive cross-correlation. Finally, we treat the latter source when its phase-sensitive cross-correlation is the maximum permitted by quantum mechanics. The low-brightness, low-flux limit of

will not be discussed herein.

this quantum source is the biphoton state. Thus these source classes span the experiments reported in [5, 12, 45] within a unified analytical framework while admitting classical phase-sensitive light as a new possibility. In Section 5.3 we discuss the image-contrast behavior that is obtained with these sources, and in Section 5.4 we generalize the Figure 5-1 configuration to allow for a nonzero separation between the transmission mask and the bucket detector. We conclude, in Section 5.5, with a discussion of the ghost-imaging physics that has been revealed by our analysis.

5.1 Analysis

Consider the ghost imaging configuration shown, using quantum field and quantum photodetection notation, in Figure 5-1. An optical source generates two fields, a signal $\hat{E}_S(\boldsymbol{\rho}, t)e^{-i\omega_0 t}$ and a reference $\hat{E}_R(\boldsymbol{\rho}, t)e^{-i\omega_0 t}$, that are scalar, positive frequency, paraxial field operators normalized to have units $\sqrt{\text{photons/m}^2\text{s}}$. Here, ω_0 is their common center frequency and $\boldsymbol{\rho}$ is the transverse coordinate with respect to each one's optical axis. The commutation relations, within this paraxial approximation, for the baseband field operators are [37]

$$[\hat{E}_m(\boldsymbol{\rho}_1, t_1), \hat{E}_\ell(\boldsymbol{\rho}_2, t_2)] = 0 \tag{5.1}$$

$$[\hat{E}_m(\boldsymbol{\rho}_1, t_1), \hat{E}^\dagger_\ell(\boldsymbol{\rho}_2, t_2)] = \delta_{m,\ell}\, \delta(\boldsymbol{\rho}_1 - \boldsymbol{\rho}_2)\delta(t_1 - t_2)\,, \tag{5.2}$$

where $\delta_{m,\ell}$ is the Kronecker delta function, $m, \ell = S, R$, and $\delta(\cdot)$ is the unit impulse. Both beams undergo quasimonochromatic paraxial diffraction along their respective optical axes, over an L-m-long free-space path, yielding detection-plane field operators [37]

$$\hat{E}_\ell(\boldsymbol{\rho}, t) = \int \mathrm{d}\boldsymbol{\rho}'\, \hat{E}_m\big(\boldsymbol{\rho}', t - L/c\big) h_L(\boldsymbol{\rho} - \boldsymbol{\rho}'), \tag{5.3}$$

where $(\ell, m) = (1, S)$ or $(2, R)$, c is the speed of light, and $h_L(\boldsymbol{\rho})$ is the Huygens-Fresnel Green's function,

$$h_L(\boldsymbol{\rho}) \equiv \frac{k_0 e^{ik_0(L + |\boldsymbol{\rho}|^2/2L)}}{i2\pi L}\,, \tag{5.4}$$

in terms of $k_0 = \omega_0/c$, the wave number associated with the center frequency. At the detection planes, $\hat{E}_1(\boldsymbol{\rho}, t)$ illuminates a quantum-limited pinhole photodetector of area A_1 whose photosensitive region $\boldsymbol{\rho} \in \mathcal{A}_1$ is centered at the transverse coordinate $\boldsymbol{\rho}_1$, while

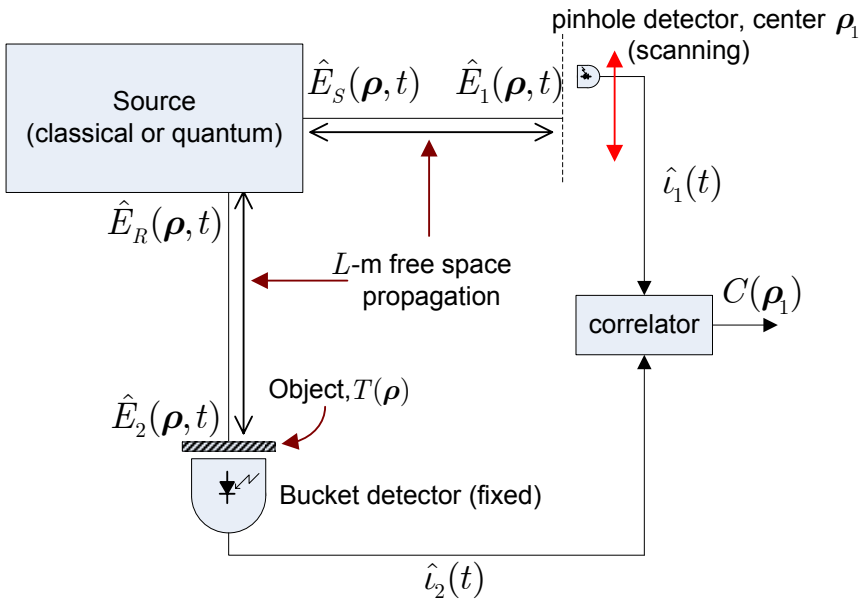

Figure 5-1: A simple ghost imaging setup.

$\hat{E}_2(\boldsymbol{\rho},t)$, illuminates an amplitude-transmission mask $T(\boldsymbol{\rho})$ located immediately in front of a quantum-limited bucket photodetector with photosensitive region $\boldsymbol{\rho} \in \mathcal{A}_2$.

The photodetectors are assumed to have identical sub-unity quantum efficiencies and finite electrical bandwidths, but no dark current or thermal noise (from subsequent electronics) contributes to the output currents. Figure 5-2 shows the model utilized for the photodetectors, in which a beam splitter with field-transmissivity $\sqrt{\eta}$ precedes an ideal photodetector to model the real detector's sub-unity quantum efficiency, and a low-pass filter with a real impulse response $h_B(t)$ follows the ideal photodetector to model the real detector's finite electrical bandwidth. It follows that the classical output currents from the two detectors correspond to the following quantum measurements [18, 27, 30]:

$$\hat{\imath}_m(t) = q \int \mathrm{d}u \int_{\mathcal{A}_m} \mathrm{d}\boldsymbol{\rho}\, \hat{E}^{\dagger}_{\eta,m}(\boldsymbol{\rho},u)\hat{E}_{\eta,m}(\boldsymbol{\rho},u)h_B(t-u), \tag{5.5}$$

for $m = 1, 2$, where q is the electron charge,

$$\hat{E}_{\eta,1}(\boldsymbol{\rho},t) = \sqrt{\eta}\,\hat{E}_1(\boldsymbol{\rho},t) + \sqrt{1-\eta}\,\hat{E}_{vac,1}(\boldsymbol{\rho},t)\,, \tag{5.6}$$

$$\hat{E}_{\eta,2}(\boldsymbol{\rho},t) = \sqrt{\eta}T(\boldsymbol{\rho})\hat{E}_m(\boldsymbol{\rho},t) + \sqrt{1-\eta|T(\boldsymbol{\rho})|^2}\,\hat{E}_{vac,2}(\boldsymbol{\rho},t)\,, \tag{5.7}$$

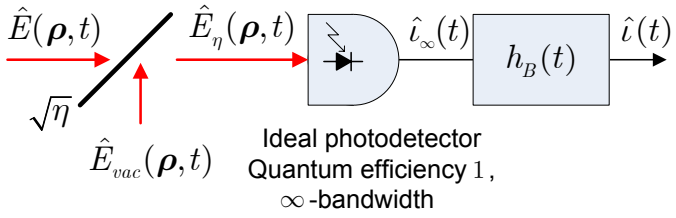

Figure 5-2: Photodetection model.

and $\hat{E}_{vac,m}(\boldsymbol{\rho},t)$ are vacuum-state field operators.

The ghost image at transverse location $\boldsymbol{\rho}_1$ is formed by time-averaging the product of the detector photocurrents to obtain an estimate of the ensemble-average equal-time photocurrent cross-correlation function, which is given by

$$C(\boldsymbol{\rho}_1) = \langle \hat{\imath}_1(t)\hat{\imath}_2(t)\rangle = q^2\eta^2 A_1 \int_{\mathcal{A}_2} \mathrm{d}\boldsymbol{\rho} \int \mathrm{d}u_1 \int \mathrm{d}u_2\, h_B(t-u_1)h_B(t-u_2)|T(\boldsymbol{\rho})|^2$$
$$\times \langle \hat{E}_1^{\dagger}(\boldsymbol{\rho}_1,u_1)\hat{E}_2^{\dagger}(\boldsymbol{\rho},u_2)\hat{E}_1(\boldsymbol{\rho}_1,u_1)\hat{E}_2(\boldsymbol{\rho},u_2)\rangle\,, \quad (5.8)$$

where we have approximated the integral over the pinhole detector's photosensitive region as the value of the integrand at $\boldsymbol{\rho}_1$ times the photosensitive area, A_1.

So far we have opted for the quantum description of our ghost imaging configuration, because it applies equally well to both classical-state and nonclassical-state sources. For the former case, however, we could have arrived at an equivalent answer by use of semiclassical theory, due to the quantitative equivalence described in Section 2.1. In particular, for a source state with a proper-P representation, we could replace the field operators with scalar classical electromagnetic fields, then employ scalar diffraction theory plus the shot-noise theory for photodetection to arrive at the photocurrent correlation expression in (5.8), but with the field-operator fourth moment replaced by a classical-field fourth moment. Therefore, any truly quantum features of ghost imaging must be exclusive to optical field states that do *not* possess proper P-representations.

5.1.1 Jointly Gaussian states

Gaussian states offer both a practically relevant and a theoretically convenient framework for studying ghost imaging. Their practical relevance stems from thermal states and the

biphoton state being special instances of Gaussian states. Their theoretical convenience arises from their being completely determined by the first and second moments of the field operators, and from their closure under linear transformations on these field operators. Moreover, as noted earlier, Gaussian-state sources span the experiments reported in [5, 12, 45] and admit to the additional case of classical phase-sensitive light. Hence they provide an excellent unifying framework within which to probe the distinction between quantum and classical behavior in ghost imaging.

Because the experiments in [5, 12, 45] employed zero-mean states, we shall assume that $\hat{E}_S(\boldsymbol{\rho}, t)$ and $\hat{E}_R(\boldsymbol{\rho}, t)$ are in a zero-mean, jointly Gaussian state, i.e., the characteristic functional of their joint state has a Gaussian form [18] specified by the (normally-ordered) phase-insensitive auto- and cross-correlations $\langle \hat{E}_m^\dagger(\boldsymbol{\rho}_1, t_1)\hat{E}_\ell(\boldsymbol{\rho}_2, t_2)\rangle$, and the phase-sensitive auto- and cross-correlations $\langle \hat{E}_m(\boldsymbol{\rho}_1, t_1)\hat{E}_\ell(\boldsymbol{\rho}_2, t_2)\rangle$, where $m, \ell = S, R$. Because the experiments in [5, 12, 45] employed states whose phase-sensitive auto-correlations were zero, we shall assume that $\langle \hat{E}_m(\boldsymbol{\rho}_1, t_1)\hat{E}_m(\boldsymbol{\rho}_2, t_2)\rangle = 0$ for $m = S, R$. Finally, to simplify our analytical treatment, while preserving the essential physics of ghost imaging, we shall assume that the signal and reference fields are cross-spectrally pure, complex-stationary and have identical auto-correlations, i.e.,

$$\langle \hat{E}_m^\dagger(\boldsymbol{\rho}_1, t_1)\hat{E}_m(\boldsymbol{\rho}_2, t_2)\rangle = K^{(n)}(\boldsymbol{\rho}_1, \boldsymbol{\rho}_2)R^{(n)}(t_2 - t_1)\,, \tag{5.9}$$

$$\langle \hat{E}_S^\dagger(\boldsymbol{\rho}_1, t_1)\hat{E}_R(\boldsymbol{\rho}_2, t_2)\rangle = K_{S,R}^{(n)}(\boldsymbol{\rho}_1, \boldsymbol{\rho}_2)R_{S,R}^{(n)}(t_2 - t_1)\,, \tag{5.10}$$

$$\langle \hat{E}_S(\boldsymbol{\rho}_1, t_1)\hat{E}_R(\boldsymbol{\rho}_2, t_2)\rangle = K_{S,R}^{(p)}(\boldsymbol{\rho}_1, \boldsymbol{\rho}_2)R_{S,R}^{(p)}(t_2 - t_1)\,, \tag{5.11}$$

for $m = S, R$, where the superscripts (n) and (p) label normally-ordered (phase-insensitive) and phase-sensitive terms, respectively. For convenience, and with no loss of generality, we shall assume that

$$R^{(n)}(0) = R_{S,R}^{(n)}(0) = R_{S,R}^{(p)}(0) = 1\,. \tag{5.12}$$

With the exception of the behavior of a background term, the physics of ghost imaging will be shown to arise entirely from the spatial terms in the preceding correlation functions. These will be taken to have Schell-model forms [14],

$$K^{(n)}(\boldsymbol{\rho}_1, \boldsymbol{\rho}_2) = A^*(\boldsymbol{\rho}_1)A(\boldsymbol{\rho}_2)G^{(n)}(\boldsymbol{\rho}_2 - \boldsymbol{\rho}_1)\,, \tag{5.13}$$

$$K_{S,R}^{(n)}(\boldsymbol{\rho}_1, \boldsymbol{\rho}_2) = A^*(\boldsymbol{\rho}_1)A(\boldsymbol{\rho}_2)G_{S,R}^{(n)}(\boldsymbol{\rho}_2 - \boldsymbol{\rho}_1)\,, \tag{5.14}$$

$$K_{S,R}^{(p)}(\boldsymbol{\rho}_1, \boldsymbol{\rho}_2) = A(\boldsymbol{\rho}_1)A(\boldsymbol{\rho}_2)G_{S,R}^{(p)}(\boldsymbol{\rho}_2 - \boldsymbol{\rho}_1)\,, \tag{5.15}$$

with $|A(\boldsymbol{\rho})| \leq 1$, so that this function may be regarded as a (possibly complex-valued) pupil function that truncates two statistically homogeneous random fields with phase-insensitive auto-correlations $G^{(n)}(\boldsymbol{\rho}_2 - \boldsymbol{\rho}_1)$, phase-insensitive cross-correlation $G_{S,R}^{(n)}(\boldsymbol{\rho}_2 - \boldsymbol{\rho}_1)$, and phase-sensitive cross-correlation $G_{S,R}^{(p)}(\boldsymbol{\rho}_2 - \boldsymbol{\rho}_1)$. We shall also assume that $G^{(n)}(\boldsymbol{\rho})$ is a real-valued even function of its argument.[2] Our task, in the rest of this subsection, is to establish the correlation-function bounds that distinguish between classical and quantum behavior for the preceding jointly Gaussian states.

Let us begin with Gaussian-state signal and reference fields that have only phase-insensitive correlations, i.e., assume that $\langle \hat{E}_S(\boldsymbol{\rho}_1, t_1)\hat{E}_R(\boldsymbol{\rho}_2, t_2)\rangle = 0$. Then, the phase-insensitive correlation spectra, given by the three-dimensional Fourier transforms

$$\tilde{g}^{(n)}(\boldsymbol{k}, \Omega) \equiv \mathcal{F}\left\{G^{(n)}(\boldsymbol{\rho})R^{(n)}(\tau)\right\}, \tag{5.16}$$

$$\tilde{g}_{S,R}^{(n)}(\boldsymbol{k}, \Omega) \equiv \mathcal{F}\left\{G_{S,R}^{(n)}(\boldsymbol{\rho})R_{S,R}^{(n)}(\tau)\right\}, \tag{5.17}$$

must satisfy [18, 19] the Cauchy-Schwarz inequality,

$$|\tilde{g}_{S,R}^{(n)}(\boldsymbol{k}, \Omega)| \leq \tilde{g}^{(n)}(\boldsymbol{k}, \Omega)\,, \tag{5.18}$$

from stochastic process theory [50]. Because the correlation spectra in (5.18) fully determine the zero-mean, phase-insensitive, Gaussian state we are considering, this inequality is both necessary and sufficient to conclude (via the equivalence developed in Section 2.1) that all phase-insensitive Gaussian states have proper P-representations, and are therefore classical.[3] The 50/50 beam splitting of a continuous-wave laser beam that has first been

[2] The signal and reference fields obtained from spontaneous parametric downconversion (SPDC) will not have space-time correlation functions that take these specific forms, because of the space-time coupling that is inherent in SPDC phase-matching relations. However, these assumptions, which are commonly-employed in coherence theory, simplify the analytical treatment without compromising the fundamental physics that yield a ghost image [13, 14].

[3] Because zero-mean Gaussian states are completely determined by their correlation functions, (5.18) implies, via the moment-factoring theorem for Gaussian states, that all higher-order moments of the signal and reference fields will be admissible moments for a pair of classical stochastic processes. Therefore, the characteristic functional for this Gaussian state—which is a generating function for all of its moments—must be an admissible characteristic functional for a pair of classical stochastic processes. Then, via Section 2.1, the zero-mean jointly Gaussian state is representable as a classical statistical mixture of $\hat{E}_S$ and $\hat{E}_R$'s coherent

transmitted through a rotating ground-glass diffuser—as was done in the experiments of [12, 45]—yields signal and reference fields that are in a zero-mean, phase-insensitive, jointly Gaussian state in which (5.18) is satisfied with equality.

Now let us examine the more interesting case in which the zero-mean Gaussian-state signal and reference fields have a nonzero phase-sensitive cross-correlation, but no phase-insensitive cross-correlation. Here we will find that their joint state need *not* have a proper P-representation, viz., the state may be nonclassical. We have that the phase-sensitive cross-correlation spectrum of the signal and reference fields,

$$\tilde{g}^{(p)}_{S,R}(\boldsymbol{k},\Omega) \equiv \mathcal{F}\left\{G^{(p)}_{S,R}(\boldsymbol{\rho})R^{(p)}_{S,R}(\tau)\right\}\,, \tag{5.19}$$

satisfies [18, 19]

$$|\tilde{g}^{(p)}_{S,R}(\boldsymbol{k},\Omega)| \leq \sqrt{\left[1+\tilde{g}^{(n)}(\boldsymbol{k},\Omega)\right]\tilde{g}^{(n)}(\boldsymbol{k},\Omega)}\,, \tag{5.20}$$

whereas the Cauchy-Schwarz inequality for the phase-sensitive cross-correlation spectrum of a pair of classical stochastic processes imposes the more restrictive condition [18, 19]

$$|\tilde{g}^{(p)}_{S,R}(\boldsymbol{k},\Omega)| \leq \tilde{g}^{(n)}(\boldsymbol{k},\Omega)\,. \tag{5.21}$$

Zero-mean Gaussian states whose phase-sensitive cross-correlation spectra satisfy (5.21) have characteristic functionals consistent with that of a pair of classical stochastic processes. Hence these states have proper P-representations and are therefore classical. On the other hand, zero-mean Gaussian states whose phase-sensitive cross-correlation spectra violate (5.21) have characteristic functionals that are inadmissible in stochastic process theory and are therefore nonclassical. In short, equality in (5.21) constitutes a well-defined boundary between classical and nonclassical zero-mean Gaussian states.

The difference between inequalities (5.20) and (5.21) has a simple physical origin. Both derive from the fact that linear combinations of signal and reference fields have nonnegative measurement variances. In the quantum case, however, the variance calculation leading to (5.20) must invoke the field-operator commutators, whereas the derivation of (5.21) has no such need. (Note that commutator issues do *not* arise in deriving (5.18), which is why this

states (whose sample functions constitute the eigenfunctions of the coherent states, and the probability density of their occurrence constitutes the mixture-weights of these coherent states), viz., the joint state has a proper P-representation.

inequality is the same for the quantum and classical cases.) The upper bounds in (5.20) and (5.21) are similar for $\tilde{g}^{(n)}(\boldsymbol{k},\Omega) \gg 1$. Thus it might seem that there is little distinction between classical and quantum Gaussian states in this limit. While this will be seen below to be so for ghost imaging (when background is neglected), 50/50 linear combinations of the signal and reference fields will be highly squeezed—thus highly nonclassical—when $\tilde{g}^{(n)}(\boldsymbol{k},\Omega) \gg 1$. At the other extreme, for $\tilde{g}^{(n)}(\boldsymbol{k},\Omega) \ll 1$, the quantum upper bound is approximately $\sqrt{\tilde{g}^{(n)}(\boldsymbol{k},\Omega)}$, which is significantly greater than the classical upper bound $\tilde{g}^{(n)}(\boldsymbol{k},\Omega)$. The phase-insensitive correlation spectrum $\tilde{g}^{(n)}(\boldsymbol{k},\Omega)$ specifies the brightness of the signal and idler fields in units of photons. Thus $\tilde{g}^{(n)}(\boldsymbol{k},\Omega) \ll 1$ is a low-brightness condition. In this regime we will see that there are appreciable differences between the ghost image formed with classical phase-sensitive light and quantum phase-sensitive light.

Spontaneous parametric downconversion, which was used in the original ghost imaging experiment [5], produces signal and reference fields that are in a zero-mean jointly Gaussian state with no phase-insensitive cross-correlation and no phase-sensitive auto-correlation, but with a phase-sensitive cross-correlation that saturates the upper bound in (5.20). Furthermore, for continuous-wave SPDC operating at frequency degeneracy, this state is a two-field minimum-uncertainty-product pure state, generated by the Bogoliubov transformation [51, 52]

$$\hat{E}_S(\boldsymbol{k},\Omega) = M(\boldsymbol{k},\Omega)\hat{E}_{S_v}(\boldsymbol{k},\Omega) + V(\boldsymbol{k},\Omega)\hat{E}^{\dagger}_{R_v}(-\boldsymbol{k},-\Omega)\,, \tag{5.22}$$

$$\hat{E}_R(-\boldsymbol{k},-\Omega) = M(\boldsymbol{k},\Omega)\hat{E}_{R_v}(-\boldsymbol{k},-\Omega) + V(\boldsymbol{k},\Omega)\hat{E}^{\dagger}_{S_v}(\boldsymbol{k},\Omega)\,, \tag{5.23}$$

of the vacuum-state input fields, $\hat{E}_{S_v}(\boldsymbol{k},\Omega)$ and $\hat{E}_{R_v}(\boldsymbol{k},\Omega)$, where the transfer functions satisfy $|M(\boldsymbol{k},\Omega)|^2 - |V(\boldsymbol{k},\Omega)|^2 = 1$ to preserve the free-field commutator relations given in (5.1) and (5.2).

In the low-brightness, low-flux regime, wherein $\tilde{g}^{(n)}(\boldsymbol{k},\Omega) \ll 1$, $|\tilde{g}^{(p)}_{S,R}(\boldsymbol{k},\Omega)| \approx \sqrt{\tilde{g}^{(n)}(\boldsymbol{k},\Omega)}$ and at most one signal-reference photon pair is present in the electrical time constant of the ghost imager's photodetectors, the first and second-order moments of this Gaussian state match those obtained from the unnormalizable pure state comprised of a superposition of a dominant multimode vacuum and a weak biphoton component [52], i.e.,

$$|\psi\rangle = |\boldsymbol{0}\rangle_S|\boldsymbol{0}\rangle_R + \int \mathrm{d}\boldsymbol{k} \int \mathrm{d}\Omega \sqrt{\tilde{g}^{(n)}(\boldsymbol{k},\Omega)}\, e^{i\phi(\boldsymbol{k},\Omega)}|\boldsymbol{k},\Omega\rangle_S\,|-\boldsymbol{k},-\Omega\rangle_R\,, \tag{5.24}$$

where $\phi(\boldsymbol{k},\Omega) \equiv \angle\tilde{g}^{(p)}_{S,R}(\boldsymbol{k},\Omega)$ and $|\mathbf{0}\rangle_S|\mathbf{0}\rangle_R$ is the multimode vacuum state of the signal and reference. In the biphoton term, $|\boldsymbol{k},\Omega\rangle_S$ denotes the single-photon signal-field state with transverse wave vector $\boldsymbol{k}$ and frequency detuning Ω from degeneracy; a similar interpretation applies to the reference-field state $|{-}\boldsymbol{k},-\Omega\rangle_R$. So, because the pure state given in (5.24) is the low-brightness, low-flux equivalent of the zero-mean jointly Gaussian state with maximum phase-sensitive cross-correlation and no phase-insensitive cross-correlation, it is clear that Gaussian-state analysis encompasses the previous biphoton treatments of ghost imaging using SPDC.

As a final point about jointly Gaussian states, let us note how one may obtain classical phase-sensitive cross-correlations between the signal and reference fields. Such fields can be generated by imposing complex-conjugate zero-mean Gaussian-noise modulations, in space and time, on the fields obtained by 50/50 beam splitting of a continuous-wave laser beam. This saturates the upper bound in (5.21), because the resulting joint state is a Gaussian statistical mixture of the coherent states $|E(\boldsymbol{\rho},t)\rangle_S|E^*(\boldsymbol{\rho},t)\rangle_R$. Existing modulator technology will limit the bandwidth achievable with such an arrangement to tens of GHz. Substantially broader bandwidths might be realized by exploiting the classical (high-photon-flux) limit of nonlinear processes that generate phase-conjugate beams [53].

5.1.2 Coherence propagation

The previous subsection laid out the statistical source models that we shall employ in our ghost imaging analysis; it was grounded in the second moments of the source-plane field operators $\hat{E}_S$ and $\hat{E}_R$ that completely characterize their zero-mean, jointly Gaussian state. However, our expression for the photocurrent correlation $C(\boldsymbol{\rho}_1)$ in the Figure 5-1 ghost-imaging configuration is given by (5.8), which requires a fourth moment of the detection-plane field operators $\hat{E}_1$ and $\hat{E}_2$. These detection-plane operators result from L m free-space propagation of the source-plane operators, as given by (5.3). Jointly Gaussian states remain jointly Gaussian under linear transformations, such as (5.3), and zero-mean states remain zero-mean as well. Thus, free-space diffraction over the L-m-long propagation paths transform the zero-mean, jointly Gaussian state of the source, with correlation functions given in (5.9)–(5.11), into a zero-mean, jointly Gaussian state at the detection planes whose

correlation functions are cross-spectrally pure and given by

$$\langle \hat{E}_m^\dagger(\boldsymbol{\rho}_1, t_1)\hat{E}_\ell(\boldsymbol{\rho}_2, t_2)\rangle = K_{m,\ell}^{(n)}(\boldsymbol{\rho}_1, \boldsymbol{\rho}_2)R_{m,\ell}^{(n)}(t_2 - t_1)\,, \tag{5.25}$$

$$\langle \hat{E}_1(\boldsymbol{\rho}_1, t_1)\hat{E}_2(\boldsymbol{\rho}_2, t_2)\rangle = K_{1,2}^{(p)}(\boldsymbol{\rho}_1, \boldsymbol{\rho}_2)R_{1,2}^{(p)}(t_2 - t_1)\,, \tag{5.26}$$

for $m, \ell = 1, 2$. In these expressions,

$$K_{m,\ell}^{(n)}(\boldsymbol{\rho}_1, \boldsymbol{\rho}_2) = \int \mathrm{d}\boldsymbol{\rho}_1' \int \mathrm{d}\boldsymbol{\rho}_2'\, K_{m',\ell'}^{(n)}(\boldsymbol{\rho}_1', \boldsymbol{\rho}_2')h_L^*(\boldsymbol{\rho}_1 - \boldsymbol{\rho}_1')h_L(\boldsymbol{\rho}_2 - \boldsymbol{\rho}_2')\,, \tag{5.27}$$

$$K_{1,2}^{(p)}(\boldsymbol{\rho}_1, \boldsymbol{\rho}_2) = \int \mathrm{d}\boldsymbol{\rho}_1' \int \mathrm{d}\boldsymbol{\rho}_2'\, K_{S,R}^{(p)}(\boldsymbol{\rho}_1', \boldsymbol{\rho}_2')h_L(\boldsymbol{\rho}_1 - \boldsymbol{\rho}_1')h_L(\boldsymbol{\rho}_2 - \boldsymbol{\rho}_2')\,, \tag{5.28}$$

$$R_{m,\ell}^{(n)}(\tau) = R_{m',\ell'}^{(n)}(\tau)\,, \tag{5.29}$$

$$R_{1,2}^{(p)}(\tau) = R_{S,R}^{(p)}(\tau)\,, \tag{5.30}$$

for $(m, m') = (1, S)$ or $(2, R)$, and likewise for (ℓ, ℓ'). Note that the temporal correlation behavior is unaffected by propagation, because the quasimonochromatic quantum Huygens-Fresnel principle, (5.3), only involves delay in time. It follows that the fundamental difference between the propagation of phase-insensitive and phase-sensitive correlation functions is the lack of conjugation in the propagation kernel of the latter, something which is responsible for the propagation characteristics presented in Chapter 3, and summarized in Section 5.1.3 [20].

Previous work on biphoton imaging has shown that the biphoton state propagates through free space in the same manner shown above for the phase-sensitive cross-correlation function [15]. This is *not* coincidental. We know from (5.24) that the biphoton wavefunction is the phase-sensitive cross-correlation between signal and reference fields with maximum phase-sensitive cross-correlation in the low-brightness, low-flux limit. For more general Gaussian states—which can have arbitrary brightness and photon flux, and can be classical or nonclassical—it is necessary to consider the propagation of the phase-sensitive cross-correlation function.

Having related second moments of the detection-plane fields to their source-plane counterparts, we still need to find a fourth moment of those detection-plane fields in order to evaluate (5.8). For zero-mean jointly Gaussian states this step is easy. From the Gaussian

moment-factoring theorem [14] we find that the fourth-order moment in (5.8) is given by

$$\langle \hat{E}_1^\dagger(\boldsymbol{\rho}_1,u_1)\hat{E}_2^\dagger(\boldsymbol{\rho},u_2)\hat{E}_1(\boldsymbol{\rho}_1,u_1)\hat{E}_2(\boldsymbol{\rho},u_2)\rangle = \\ \langle \hat{E}_1^\dagger(\boldsymbol{\rho}_1,u_1)\hat{E}_1(\boldsymbol{\rho}_1,u_1)\rangle\langle \hat{E}_2^\dagger(\boldsymbol{\rho},u_2)\hat{E}_2(\boldsymbol{\rho},u_2)\rangle + \\ |\langle \hat{E}_1^\dagger(\boldsymbol{\rho}_1,u_1)\hat{E}_2(\boldsymbol{\rho},u_2)\rangle|^2 + |\langle \hat{E}_1(\boldsymbol{\rho}_1,u_1)\hat{E}_2(\boldsymbol{\rho},u_2)\rangle|^2. \quad (5.31)$$

Substituting (5.31) into (5.8), along with Eqs. (5.25) and (5.26), simplifies the photocurrent cross-correlation expression to

$$C(\boldsymbol{\rho}_1) = C_0(\boldsymbol{\rho}_1) + C_n \int_{\mathcal{A}_2} \mathrm{d}\boldsymbol{\rho}\, |K_{1,2}^{(n)}(\boldsymbol{\rho}_1,\boldsymbol{\rho})|^2 |T(\boldsymbol{\rho})|^2 + C_p \int_{\mathcal{A}_2} \mathrm{d}\boldsymbol{\rho}\, |K_{1,2}^{(p)}(\boldsymbol{\rho}_1,\boldsymbol{\rho})|^2 |T(\boldsymbol{\rho})|^2\,, \quad (5.32)$$

where

$$C_0(\boldsymbol{\rho}_1) = q^2\eta^2 A_1 R_{1,1}^{(n)}(0) R_{2,2}^{(n)}(0) \left[\int h_B(t)\mathrm{d}t\right]^2 K_{1,1}^{(n)}(\boldsymbol{\rho}_1,\boldsymbol{\rho}_1) \int_{\mathcal{A}_2} \mathrm{d}\boldsymbol{\rho}\, K_{2,2}^{(n)}(\boldsymbol{\rho},\boldsymbol{\rho}) |T(\boldsymbol{\rho})|^2, \quad (5.33)$$

is a nonnegative non-image-bearing background, and

$$C_n = q^2\eta^2 A_1 \left[|R_{1,2}^{(n)}(t)|^2 \star h_B(t) \star h_B(-t) \right]_{t=0}\,, \quad (5.34)$$

$$C_p = q^2\eta^2 A_1 \left[|R_{1,2}^{(p)}(t)|^2 \star h_B(t) \star h_B(-t) \right]_{t=0}\,, \quad (5.35)$$

are constants that depend on the temporal cross-correlations between $\hat{E}_1$ and $\hat{E}_2$. Here $\star$ denotes convolution.

The image-bearing term in $C(\boldsymbol{\rho}_1)$ is seen, from (5.32), to be the object's intensity transmission profile, $|T(\boldsymbol{\rho})|^2$, filtered through a linear, space-varying filter whose point-spread function is given by a weighted sum of the squared magnitudes of the phase-insensitive and phase-sensitive cross-correlation functions at the detection planes. In thermal-state ghost imaging, the phase-sensitive term vanishes, so that the point-spread function depends only on the phase-insensitive cross-correlation. In biphoton-state ghost imaging, the phase-insensitive cross-correlation is zero, thus yielding an image filter that depends only on the phase-sensitive cross-correlation. For general Gaussian-state signal and reference fields, however, both cross-correlations contribute to the image filter.

Because the image-bearing part of (5.32) only depends on the cross-correlations be-

tween the detected fields, whereas the non-image-bearing background depends only on the phase-insensitive auto-correlations, it is germane to note (see Appendix B) that *any* pair of phase-insensitive and phase-sensitive cross-correlation functions can be associated with a *classical* zero-mean jointly Gaussian state, by appropriate choices of its phase-insensitive auto-correlation functions. Thus, if no constraint is placed on the background level in which the image is embedded, i.e., if the auto-correlation functions are not constrained, any image-bearing term attainable from (5.32) with a nonclassical Gaussian state source can be replicated *identically* by a classical Gaussian-state source. Hence, ghost-image formation is intrinsically classical.

5.1.3 Near-field versus far-field propagation

Here we give a brief summary of the relevant results from Chapter 3, on paraxial, quasi-monochromatic, phase-insensitive and phase-sensitive coherence propagation through free space [20], which will be combined, in the next section, with (5.32) to identify the imaging properties of the Figure 5-1 configuration. Because (5.27) and (5.28) show that propagation only affects the correlation functions' spatial components, we shall focus exclusively on them. As in Section 3.3, we consider (real and even) Gaussian-Schell model spatial phase-insensitive and phase-sensitive cross-correlation functions, i.e., we assume [4]

$$K_{S,R}^{(x)}(\boldsymbol{\rho}_1, \boldsymbol{\rho}_2) = \frac{2P}{\pi a_0^2} e^{-(|\boldsymbol{\rho}_1|^2 + |\boldsymbol{\rho}_2|^2)/a_0^2 - |\boldsymbol{\rho}_2 - \boldsymbol{\rho}_1|^2/2\rho_0^2}, \tag{5.36}$$

for $x = n, p$, where P is the photon flux of the signal (and reference), a_0 is the e^{-2} attenuation radius of the transverse intensity profile, and ρ_0 is the transverse coherence radius, which is assumed to satisfy the low-coherence condition $\rho_0 \ll a_0$.

Let us review phase-insensitive and phase-sensitive correlation propagation in two limiting regimes: the near field, which corresponds to the region in which diffraction effects are negligible, and the far field, in which diffraction spread is dominant. For phase-insensitive coherence propagation, it is well known that a single Fresnel number, $D_0 = k_0 \rho_0 a_0 / 2L$, distinguishes between these regimes, with $D_0 \gg 1$ corresponding to the near field and $D_0 \ll 1$ being the far field [13, 14]. Note that this Fresnel number differs from that for the

[4] The distinction between auto- and cross-correlation propagation is irrelevant here, because both the signal and reference beams undergo identical transformations. Thus, even though we state our results only for the cross-correlation functions, these results also apply to auto-correlation propagation.

diffraction of a coherent laser beam with intensity radius a_0, which is $D_C = k_0 a_0^2/2L$. This difference reflects the coupling between coherence radius and intensity radius that occurs in free-space diffraction of partially-coherent light. In particular, far-field propagation of the phase-insensitive correlation function from (5.36) results in an intensity radius satisfying $a_L = a_0/D_0 = 2L/k_0\rho_0$ and a coherence radius given by $\rho_L = \rho_0/D_0 = 2L/k_0 a_0$, i.e., the far-field intensity radius is inversely proportional to its source-plane coherence length and the far-field coherence length is inversely proportional to the source-plane intensity radius (cf. (3.35)).

The phase-sensitive correlation function from (5.36) propagates in a distinctly different manner from its phase-insensitive counterpart. In this case we find that coherence-radius diffraction and intensity-radius diffraction are decoupled [20]. Two Fresnel numbers are then required to distinguish the near field from the far field: the Fresnel number for diffraction of the coherence length, $D_N = k_0\rho_0^2/2L$; and the Fresnel number for diffraction of the intensity radius, $D_F = k_0 a_0^2/2L$. The near-field regime for phase-sensitive correlation propagation occurs when *both* Fresnel numbers are much greater than one, and the far-field regime is when both are much less than one. Because we have imposed the low-coherence condition, $\rho_0 \ll a_0$, we can say that the near-field regime for phase-sensitive coherence propagation is $D_N \gg 1$ and its far-field regime is $D_F \ll 1$. Each of these conditions is more stringent than the corresponding condition for phase-insensitive light. Nevertheless, the far-field propagation of the Gaussian-Schell model phase-sensitive correlation function from (5.36) still yields a_0/D_0 for the far-field intensity radius and ρ_0/D_0 for the far-field coherence radius (cf. (3.34)). However, whereas the far-field phase-insensitive correlation is highest for two points with equal transverse-plane coordinates, the far-field phase-sensitive correlation is highest for two points that are symmetrically disposed about the origin on the transverse plane [15, 20]. Figure 3-4, from Section 3.3, highlights the difference between propagation of the phase-insensitive and phase-sensitive correlation functions by plotting their e^{-2}-attenuation isocontours in the near- and far-field regimes. Whereas in the near field both correlations have isocontours that are narrow in the difference coordinate $|\boldsymbol{\rho}_d| \equiv |\boldsymbol{\rho}_2 - \boldsymbol{\rho}_1|$, the far-field isocontours differ for the two correlation functions: the phase-insensitive correlation function remains a narrow function of the difference coordinate $|\boldsymbol{\rho}_d|$, whereas the far-field phase-sensitive correlation function becomes a narrow function in the sum coordinate $|\boldsymbol{\rho}_s| = |\boldsymbol{\rho}_2 + \boldsymbol{\rho}_1|/2$.

5.2 Near- and far-field ghost imaging with Gaussian-states

We are now fully equipped to compare the ghost-imaging performance achieved in the Figure 5-1 configuration with various Gaussian-state sources. We shall assume that the signal and reference fields $\hat{E}_S$ and $\hat{E}_R$ are in a zero-mean, jointly Gaussian state with identical phase-insensitive auto-correlations given by the following Gaussian-Schell model:

$$K^{(n)}(\boldsymbol{\rho}_1, \boldsymbol{\rho}_2) R^{(n)}(t_2 - t_1) = \frac{2P}{\pi a_0^2} e^{-(|\boldsymbol{\rho}_1|^2 + |\boldsymbol{\rho}_2|^2)/a_0^2 - |\boldsymbol{\rho}_2 - \boldsymbol{\rho}_1|^2/2\rho_0^2} e^{-(t_2 - t_1)^2/2T_0^2}, \tag{5.37}$$

where $\rho_0 \ll a_0$, T_0 is the coherence time, and P is the photon flux. We will begin our treatment with the thermal-state source, for which the signal and reference have a nonzero phase-insensitive cross-correlation, but no phase-sensitive cross-correlation. As noted in Section 5.1.1, such states are always classical.

5.2.1 Ghost imaging with phase-insensitive light

Consider jointly Gaussian signal and reference fields with auto-correlations given by (5.37), and with no phase-sensitive auto- or cross-correlations. Inequality (5.18) implies that $|\langle \hat{E}_S^\dagger(\boldsymbol{\rho}_1, t_1) \hat{E}_R(\boldsymbol{\rho}_2, t_2) \rangle|$ is maximum when it equals the auto-correlation function (5.37). We will take this to be so—to maximize the strength of the ghost image—and assume that this phase-insensitive cross-correlation is real-valued and nonnegative. Because near-field ($D_0 \gg 1$) detection-plane correlations coincide with source-plane correlations, we can now obtain the near-field ghost image by substituting the right-hand side of (5.37) into (5.32). Doing so gives us the following result,

$$C(\boldsymbol{\rho}_1) = C_0(\boldsymbol{\rho}_1) + C_n (2P/\pi a_0^2)^2 \, e^{-2|\boldsymbol{\rho}_1|^2/a_0^2} \int_{\mathcal{A}_2} \mathrm{d}\boldsymbol{\rho} \, e^{-|\boldsymbol{\rho}_1 - \boldsymbol{\rho}|^2/\rho_0^2} e^{-2|\boldsymbol{\rho}|^2/a_0^2} |T(\boldsymbol{\rho})|^2 . \tag{5.38}$$

Equation (5.38) reveals three significant features of the near-field, thermal-state ghost image. First, the ghost image is space-limited by the reference beam's average intensity profile, so that the object must be placed in the field of view a_0.[5] Second, the useful transverse scanning range of the pinhole detector is restricted to the field of view a_0. Finally, and most importantly, the finite cross-correlation coherence length ρ_0 limits the resolution of the image. When field-of-view limitations can be neglected, the ghost image in (5.38)

[5] Field of view usually refers to a solid-angle region, but we will use the intensity radius at a transverse plane as our field-of-view measure.

is proportional to the convolution of the object's intensity transmission, $|T(\boldsymbol{\rho})|^2$, with the Gaussian point-spread function $e^{-|\boldsymbol{\rho}|^2/\rho_0^2}$. Thus the spatial resolution, defined here as the radius to the e^{-2}-level in the point-spread function, is $\sqrt{2}\rho_0$.

Now let us suppose that the ghost image is formed in the far field, when $D_0 \ll 1$, with the source correlations as assumed for the near-field regime. In this case we must first propagate source correlations—given by the right-hand side of (5.37)—to the detection planes via (5.27). It turns out that the detection-plane signal and reference fields still have maximum phase-insensitive cross-correlation,

$$|K^{(n)}_{m,\ell}(\boldsymbol{\rho}_1,\boldsymbol{\rho}_2)|R^{(n)}_{m,\ell}(t_2-t_1) = \frac{2P}{\pi a_L^2} e^{-(|\boldsymbol{\rho}_1|^2+|\boldsymbol{\rho}_2|^2)/a_L^2 - |\boldsymbol{\rho}_2-\boldsymbol{\rho}_1|^2/2\rho_L^2} e^{-(t_2-t_1)^2/2T_0^2}\,, \tag{5.39}$$

where $m,\ell \in \{1,2\}$, $a_L = 2L/k_0\rho_0$ and $\rho_L = 2L/k_0 a_0$, and the ghost image signature becomes,

$$C(\boldsymbol{\rho}_1) = C_0(\boldsymbol{\rho}_1) + C_n(2P/\pi a_L^2)^2\, e^{-2|\boldsymbol{\rho}_1|^2/a_L^2} \int_{\mathcal{A}_2} \mathrm{d}\boldsymbol{\rho}\, e^{-|\boldsymbol{\rho}_1-\boldsymbol{\rho}|^2/\rho_L^2} e^{-2|\boldsymbol{\rho}|^2/a_L^2} |T(\boldsymbol{\rho})|^2\,. \tag{5.40}$$

Therefore, the far-field field of view increases to $2L/k_0\rho_0$ while the image resolution degrades to $2\sqrt{2}L/k_0 a_0$, but the three conclusions drawn from the near-field image signature (5.38) remain valid in the far-field regime. Because the resolution of the image degrades with propagation, so long as field of view is not the limiting factor, it is more desirable to place the object in the source's near field.

5.2.2 Ghost imaging with phase-sensitive light

Now we shall shift our focus to Gaussian-state signal and reference fields that have a nonzero phase-sensitive cross-correlation, but zero phase-insensitive cross-correlation. Applying the Cauchy-Schwarz bound (5.21) to the Gaussian-Schell model auto-correlations in (5.37) we find that the maximum $|\langle \hat{E}_S(\boldsymbol{\rho}_1,t_1)\hat{E}_R(\boldsymbol{\rho}_2,t_2)\rangle|$ for a *classical* Gaussian state is also given by (5.37). Similar to what we did for the phase-insensitive case, we shall take the phase-sensitive cross-correlation to achieve its classical magnitude limit and assume that it is real-valued and nonnegative. Then, because the detection-plane cross-correlation equals the source-plane cross-correlation in the near field ($D_N \gg 1$), we can immediately get the

near-field ghost image by substituting the right-hand side of (5.37) into (5.32), obtaining

$$C(\boldsymbol{\rho}_1) = C_0(\boldsymbol{\rho}_1) + C_p(2P/\pi a_0^2)^2\, e^{-2|\boldsymbol{\rho}_1|^2/a_0^2} \int_{\mathcal{A}_2} \mathrm{d}\boldsymbol{\rho}\, e^{-|\boldsymbol{\rho}_1-\boldsymbol{\rho}|^2/\rho_0^2} e^{-2|\boldsymbol{\rho}|^2/a_0^2} |T(\boldsymbol{\rho})|^2 \,. \tag{5.41}$$

Equations (5.34) and (5.35) give $C_n = C_p$ for our Gaussian-Schell model source, making the near-field ghost image formed with classical phase-sensitive light *identical* to the near-field ghost image formed with phase-insensitive light, with the exception that the near-field condition for phase-sensitive coherence propagation is far more stringent than that for its phase-insensitive counterpart, because $D_N \ll D_0$.

When the source-to-object separation is in the far-field regime for phase-sensitive coherence propagation ($D_F \ll 1$), then the source-plane phase-sensitive cross-correlation that gave the preceding near-field ghost image gives rise to the following detection-plane phase-sensitive cross-correlation [20],

$$|K_{1,2}^{(p)}(\boldsymbol{\rho}_1, \boldsymbol{\rho}_2)| R_{1,2}^{(p)}(t_2 - t_1) = \frac{2P}{\pi a_L^2} e^{-(|\boldsymbol{\rho}_1|^2 + |\boldsymbol{\rho}_2|^2)/a_L^2 - |\boldsymbol{\rho}_2 + \boldsymbol{\rho}_1|^2/2\rho_L^2} e^{-(t_2-t_1)^2/2T_0^2} \,, \tag{5.42}$$

which leads to

$$C(\boldsymbol{\rho}_1) = C_0(\boldsymbol{\rho}_1) + C_p(2P/\pi a_L^2)^2\, e^{-2|\boldsymbol{\rho}_1|^2/a_L^2} \int_{\mathcal{A}_2} \mathrm{d}\boldsymbol{\rho}\, e^{-|\boldsymbol{\rho}_1+\boldsymbol{\rho}|^2/\rho_L^2} e^{-2|\boldsymbol{\rho}|^2/a_L^2} |T(\boldsymbol{\rho})|^2 \,, \tag{5.43}$$

for the far-field ghost image formed with classical phase-sensitive light. Again invoking $C_p = C_n$ for our Gaussian-Schell model source, we see that the far-field ghost image formed with classical phase-sensitive light is an inverted version of the corresponding far-field ghost image formed with phase-insensitive light, i.e., it has field of view a_L and spatial resolution $\sqrt{2}\,\rho_L$, as did the phase-insensitive ghost image, but the phase-sensitive ghost image is proportional to $|T(-\boldsymbol{\rho})|^2 \star e^{-|\boldsymbol{\rho}|^2/\rho_L^2}$ whereas the phase-insensitive ghost image was proportional to $|T(\boldsymbol{\rho})|^2 \star e^{-|\boldsymbol{\rho}|^2/\rho_L^2}$. As seen for the near-field, the far-field condition for phase-sensitive coherence propagation is much more stringent than that for the phase-insensitive case, because $D_F \gg D_0$.

Finally, we turn to the ghost image produced using a nonclassical Gaussian state, i.e., one whose phase-sensitive cross-correlation violates (5.21). In what follows we will restrict our attention to two limiting cases in which the phase-sensitive cross-correlation is coherence separable, so that we may continue to utilize the machinery developed earlier in this chapter.

In both cases we will take $\langle \hat{E}_S(\boldsymbol{\rho}_1, t_1)\hat{E}_R(\boldsymbol{\rho}_2, t_2)\rangle$ to be real-valued and nonnegative with the maximum magnitude permitted by quantum theory. The limits of interest for this source will be those of high brightness, $\tilde{g}^{(n)}(\boldsymbol{k}, \Omega) \gg 1$, and low brightness, $\tilde{g}^{(n)}(\boldsymbol{k}, \Omega) \ll 1$ when the source's auto-correlations are given by (5.37).

At high brightness, the distinction between the cross-correlation functions of the quantum and classical phase-sensitive sources becomes insignificant, so that results given above for the ghost image formed with classical phase-sensitive light are excellent approximations for the quantum case. At low brightness, however, our assumptions yield a phase-sensitive cross-correlation spectrum satisfying

$$|\tilde{g}^{(p)}_{S,R}(\boldsymbol{k}, \Omega)| \approx \sqrt{\tilde{g}^{(n)}(\boldsymbol{k}, \Omega)} \tag{5.44}$$

$$= 2(2\pi)^{1/4} \sqrt{\frac{PT_0\rho_0^2}{a_0^2}}\, e^{-\rho_0^2|\boldsymbol{k}|^2/4}\, e^{-\Omega^2 T_0^2/4}\,, \tag{5.45}$$

from which we see that the low-brightness regime corresponds to $PT_0\rho_0^2/a_0^2 \ll 1$. The source-plane phase-sensitive cross-correlation in this regime is then found to be

$$\langle \hat{E}_S(\boldsymbol{\rho}_1, t_1)\hat{E}_R(\boldsymbol{\rho}_2, t_2)\rangle = (2/\pi)^{1/4} \sqrt{\frac{a_0^2}{PT_0\rho_0^2}} \times \frac{2P}{\pi a_0^2} e^{-(|\boldsymbol{\rho}_1|^2+|\boldsymbol{\rho}_2|^2)/a_0^2 - |\boldsymbol{\rho}_2-\boldsymbol{\rho}_1|^2/\rho_0^2} e^{-(t_2-t_1)^2/T_0^2}\,. \tag{5.46}$$

Note that (5.46) is still a Gaussian-Schell, cross-spectrally pure correlation function, so that in the source's near field we get

$$C(\boldsymbol{\rho}_1) = C_0(\boldsymbol{\rho}_1) + \sqrt{\frac{2}{\pi}}\, \frac{a_0^2}{PT_0\rho_0^2}\, C_p \left(\frac{2P}{\pi a_0^2}\right)^2 e^{-2|\boldsymbol{\rho}_1|^2/a_0^2} \times \int_{\mathcal{A}_2} \mathrm{d}\boldsymbol{\rho}\, e^{-2|\boldsymbol{\rho}_1-\boldsymbol{\rho}|^2/\rho_0^2} e^{-2|\boldsymbol{\rho}|^2/a_0^2} |T(\boldsymbol{\rho})|^2\,. \tag{5.47}$$

This near-field ghost image has the same field of view, a_0, as the near-field ghost images formed with classical (phase-insensitive or phase-sensitive) light, but its spatial resolution, ρ_0, is a factor-of-$\sqrt{2}$ better than the spatial resolutions of those classical near-field imagers. In addition, the quantum case's image-to-background ratio is much higher than those of the classical imagers, because $a_0^2/PT_0\rho_0^2 \gg 1$ in the low-brightness regime. Finally, C_P (which we evaluate explicitly in the next section) has a different value here than that found in

(5.41), because the cross-correlation coherence time is a factor-of-$\sqrt{2}$ shorter than it is for the classical phase-sensitive cross-correlation considered previously.

The far-field ghost image for the nonclassical source is obtained by propagating its phase-sensitive cross-correlation from (5.46) to the detector planes and substituting that result into (5.32). The result we obtain is

$$C(\boldsymbol{\rho}_1) = C_0(\boldsymbol{\rho}_1) + \sqrt{\frac{2}{\pi}}\,\frac{a_0^2}{PT_0\rho_0^2}\,C_p\!\left(\frac{P}{\pi a_L^2}\right)^2 e^{-|\boldsymbol{\rho}_1|^2/a_L^2} \times \int_{\mathcal{A}_2} \mathrm{d}\boldsymbol{\rho}\, e^{-|\boldsymbol{\rho}_1+\boldsymbol{\rho}|^2/\rho_L^2} e^{-|\boldsymbol{\rho}|^2/a_L^2} |T(\boldsymbol{\rho})|^2. \quad (5.48)$$

Thus, the far-field resolution achieved with the quantum source equals those realized using the classical sources considered earlier, but the field of view has been increased by a factor of $\sqrt{2}$. It is worth pointing out that the quantum-enhancement factors—of spatial resolution in the near field and field of view in the far field—derive from the broadening of the weak spectrum, $\tilde{g}^{(n)}(\boldsymbol{k}, \Omega)$, when its square root is taken. That these enhancement factors both equal $\sqrt{2}$ depends, therefore, on our choosing to use a Gaussian-Schell correlation model. Other correlation functions would lead to different enhancement factors. Also, because the temporal part of the cross-correlation is unchanged from the near field, C_P will again be different from its classical counterpart. Finally, as found above for the near-field case, the quantum source yields dramatically higher image-to-background ratio in far-field ghost imaging than both its phase-insensitive and phase-sensitive classical counterparts.

5.3 Image contrast

Thus far we have concentrated on the image-bearing terms in the photocurrent correlation from (5.32). These image-bearing terms are embedded in a background $C_0(\boldsymbol{\rho}_1)$, which, as we have seen in the preceding section, is much stronger for classical-source ghost imaging than it is for low-brightness quantum-source ghost imaging. It therefore behooves us to pay some attention to the effect of background on ghost-imaging systems. For the sake of brevity, we will limit our discussion to the near-field imagers; the far-field cases can be shown to have similar image-contrast issues. Also, we shall assume that the transmittance pattern being imaged lies well within the field of view of all these ghost imagers, and restrict ourselves to considering the behavior of $C(\boldsymbol{\rho}_1)$ in an observation region $\mathcal{R}$ that encompasses

the image-bearing terms while satisfying $|\boldsymbol{\rho}_1| \ll a_0$. In this case

$$\mathcal{C} \equiv \frac{\max_{\mathcal{R}}[C(\boldsymbol{\rho}_1)] - \min_{\mathcal{R}}[C(\boldsymbol{\rho}_1)]}{C_0(\mathbf{0})} \tag{5.49}$$

is a meaningful contrast definition. Its numerator quantifies the dynamic range of the image-bearing terms in the photocurrent correlation $C(\boldsymbol{\rho}_1)$, while its denominator is the featureless background that is present within the observation region.

For analytical convenience, let us take the baseband impulse response $h_B(t)$ to be a Gaussian with e^{-2}-attenuation time duration T_d,

$$h_B(t) = e^{-8t^2/T_d^2}\sqrt{8/\pi T_d^2}\,. \tag{5.50}$$

The contrast for the classical (phase-sensitive or phase-insensitive) ghost imagers then satisfies

$$\mathcal{C}^{(c)} = \mathcal{C}_s^{(c)}\mathcal{C}_t^{(c)}, \tag{5.51}$$

where the spatial (s) factor is given by

$$\mathcal{C}_s^{(c)} = \frac{\max_{\boldsymbol{\rho}_1}[\mathcal{I}_c(\boldsymbol{\rho}_1)] - \min_{\boldsymbol{\rho}_1}[\mathcal{I}_c(\boldsymbol{\rho}_1)]}{\int_{\mathcal{A}_2}\mathrm{d}\boldsymbol{\rho}\,|T(\boldsymbol{\rho})|^2}, \tag{5.52}$$

with

$$\mathcal{I}_c(\boldsymbol{\rho}_1) \equiv \int_{\mathcal{A}_2}\mathrm{d}\boldsymbol{\rho}\, e^{-|\boldsymbol{\rho}_1-\boldsymbol{\rho}|^2/\rho_0^2}|T(\boldsymbol{\rho})|^2, \tag{5.53}$$

being the point-spread degraded image of $|T(\boldsymbol{\rho})|^2$, and the temporal (t) factor obeys

$$\mathcal{C}_t^{(c)} = 1/\sqrt{1+(T_d/2T_0)^2}. \tag{5.54}$$

Likewise, for the low-brightness regime quantum imager we find that its contrast, $\mathcal{C}^{(q)}$, factors into the product of a spatial term

$$\mathcal{C}_s^{(q)} = \sqrt{\frac{2}{\pi}}\frac{a_0^2}{PT_0\rho_0^2}\frac{\max_{\boldsymbol{\rho}_1}[\mathcal{I}_q(\boldsymbol{\rho}_1)] - \min_{\boldsymbol{\rho}_1}[\mathcal{I}_q(\boldsymbol{\rho}_1)]}{\int_{\mathcal{A}_2}\mathrm{d}\boldsymbol{\rho}\,|T(\boldsymbol{\rho})|^2}, \tag{5.55}$$

with

$$\mathcal{I}_q(\boldsymbol{\rho}_1) \equiv \int_{\mathcal{A}_2}\mathrm{d}\boldsymbol{\rho}\, e^{-2|\boldsymbol{\rho}_1-\boldsymbol{\rho}|^2/\rho_0^2}|T(\boldsymbol{\rho})|^2, \tag{5.56}$$

being its point-spread degraded image of $|T(\boldsymbol{\rho})|^2$, times a temporal term

$$\mathcal{C}_t^{(q)} = 1/\sqrt{1 + T_d^2/2T_0^2}\,. \tag{5.57}$$

The preceding classical and quantum contrast expressions possess interesting and physically significant behavior. We shall first explore the classical case. To get at its contrast behavior, we will assume that $T(\boldsymbol{\rho})$ is a binary amplitude mask, as has often been the case in ghost imaging experiments. It follows that

$$\mathcal{C}_s^{(c)} \approx \rho_0^2/A_T \ll 1, \tag{5.58}$$

where

$$A_T \equiv \int \mathrm{d}\boldsymbol{\rho}\, |T(\boldsymbol{\rho})|^2, \tag{5.59}$$

and the inequality in (5.58) holds because A_T/ρ_0^2 is approximately the number of resolution cells in the ghost image. Combined with the fact that $\mathcal{C}_t^{(c)} \leq 1$, (5.58) shows that classical-source ghost imaging *always* has low contrast according to our contrast definition. This is why classical-source ghost imaging has been performed with thermalized laser light and has used AC-coupling of the photocurrents to the correlator [49]. Thermalized laser light is a narrowband source, for which $T_d \ll T_0$ so that $\mathcal{C}_t^{(c)} \approx 1$. The use of AC-coupling implies that the correlator is estimating the *cross-covariance* between the photocurrents produced by detectors 1 and 2, rather than their cross-correlation. This ensemble-average cross-covariance is given by $C(\boldsymbol{\rho}_1) - C_0(\boldsymbol{\rho}_1)$, so it might seem that covariance estimation alleviates all concerns with the background term. Such is not the case. Even though the background term does not appear in the photocurrents' cross-covariance, its shot noise and excess noise dictate that a much longer averaging time will be required to obtain an accurate estimate of this cross-covariance function, i.e., to get a high signal-to-noise ratio ghost image. Now suppose that classical-source ghost imaging is attempted using broadband light for which $T_d/T_0 \sim 10^3$, corresponding to a THz-bandwidth source and GHz electrical-bandwidth photodetectors. In comparison with a narrowband classical-source ghost imager of the same photon flux P, the broadband imager must use a 10^6-times longer time-averaging interval to achieve the same signal-to-shot-noise ratio.

Turning now to the contrast behavior of the low-brightness quantum-source ghost im-

ager, our assumption of a binary amplitude mask leads to

$$\mathcal{C}_s^{(q)} \approx \frac{a_0^2}{PT_0A_T} \gg 1/PT_0 \tag{5.60}$$

because of our field-of-view assumption. Thus in broadband, low-brightness, low-flux quantum ghost imaging we find that

$$\mathcal{C}^{(q)} \gg 1/PT_d \gg 1, \tag{5.61}$$

where the last inequality invokes the low-flux condition. This is why biphoton sources yield background-free ghost images [5, 10, 11], despite SPDC being a broadband process.

5.4 Relay optics

Our analysis has assumed that the detector plane coincides with the object plane, but a realistic ghost-imaging scenario will likely require a separation between these two planes, as shown in Figure 5-3. In this figure, the bucket detector is placed L_R m away from the object and we assume no control over this path, but we allow ourselves to freely modify the signal-arm path. Thus we place a focal-length-f lens d_1 m behind the object plane and d_2 m in front of the detector plane, such that $1/d_1 + 1/d_2 = 1/f$. In addition, because the optical path lengths may be different, we introduce a $(L_R - d_1 - d_2)/c$ post-detection electronic time delay to maximize the temporal cross-correlation of the two detected fields. The resulting photocurrent cross-correlation is then

$$C'(\boldsymbol{\rho}_1) = C_0(\boldsymbol{\rho}_1) + C_n \int_{\mathcal{A}_2} d\boldsymbol{\rho}_2 \, |K^{(n)}_{1',2'}(\boldsymbol{\rho}_1, \boldsymbol{\rho}_2)|^2 + C_p \int_{\mathcal{A}_2} d\boldsymbol{\rho}_2 \, |K^{(p)}_{1',2'}(\boldsymbol{\rho}_1, \boldsymbol{\rho}_2)|^2 , \tag{5.62}$$

in terms of the phase-insensitive and phase-sensitive cross-correlations, $K^{(x)}_{1',2'}(\boldsymbol{\rho}_1, \boldsymbol{\rho}_2)$ for $x = n, p$, of the detected fields $\hat{E}_{1'}$ and $\hat{E}_{2'}$.

The magnitudes of these detection-plane cross-correlations are easily found from thin-lens imaging theory, with the following results:

$$|K^{(x)}_{1',2'}(\boldsymbol{\rho}_1, \boldsymbol{\rho}_2)| = \left| \frac{k_0 M}{2\pi L_R} \int \mathrm{d}\boldsymbol{\rho}' e^{-ik_0(2\boldsymbol{\rho}_2 \cdot \boldsymbol{\rho}' - |\boldsymbol{\rho}'|^2)/2L_R} \; K^{(x)}_{1,2}(M\boldsymbol{\rho}_1, \boldsymbol{\rho}') T(\boldsymbol{\rho}') \right|, \tag{5.63}$$

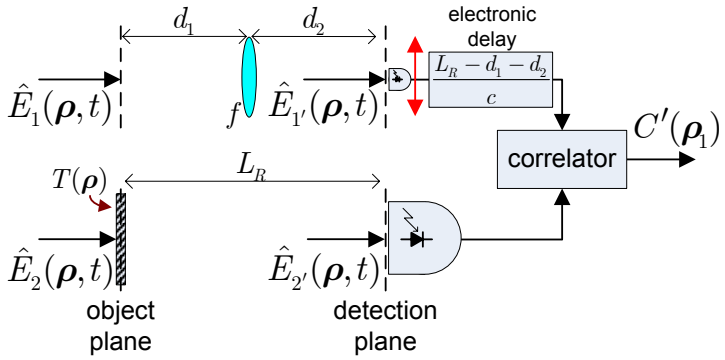

Figure 5-3: Ghost imaging setup with relay optics.

where $M \equiv -d_2/d_1$ is the signal-arm magnification factor. For a sufficiently large bucket detector we can approximate the integrals in (5.62) as covering the entire plane, viz.,

$$C_x \int_{\mathcal{A}_2} d\boldsymbol{\rho}_2 \, |K^{(x)}_{1',2'}(\boldsymbol{\rho}_1, \boldsymbol{\rho}_2)|^2 \approx C_x \int \mathrm{d}\boldsymbol{\rho}_2 \, |K^{(x)}_{1',2'}(\boldsymbol{\rho}_1, \boldsymbol{\rho}_2)|^2 \tag{5.64}$$

$$= M^2 C_x \int \mathrm{d}\boldsymbol{\rho} \, |K^{(x)}_{1,2}(M\boldsymbol{\rho}_1, \boldsymbol{\rho})|^2 |T(\boldsymbol{\rho})|^2 \,, \tag{5.65}$$

for $x = n, p$, where the last equality follows from Parseval's theorem. In this limit, $C'(\boldsymbol{\rho}_1) = M^2 C(M\boldsymbol{\rho}_1)$, where $C(\boldsymbol{\rho}_1)$ is given by (5.32). Hence choosing $d_1 = d_2 = 2f$ will yield an inverted version of the object-plane ghost image. Image resolution and field of view are then determined by the phase-sensitive and phase-insensitive coherence properties of the object-plane fields, and the placement of the detectors relative to this plane only determines the signal-arm optics that are needed to obtain this object-plane ghost image.

5.5 Discussion

The fundamental source property that enables acquisition of a ghost image—whether the source is classical or quantum—is the nonzero cross-covariance between the photon-flux densities of the two detected fields, i.e., the cross-correlation of the photon-flux densities minus the product of their mean values. In particular, the product of mean values generates the background term, while the cross-covariance produces the image-bearing terms. For zero-mean, Gaussian-state sources, the cross-correlation of the photon-flux densities, which is a fourth-order field moment, reduces to a sum of terms involving second-order field moments. Consequently, both phase-sensitive and phase-insensitive field-operator cross-

correlations can contribute to the ghost image. In Appendix B we show that any pair of phase-sensitive and phase-insensitive cross-correlation functions can be obtained with two classical Gaussian-state fields, so long as there are no restrictions on these fields' auto-correlation functions. In this respect, the ghost image does *not* contain any quantum signature *per se*. However, if we compare sources that have identical auto-correlation functions, we find that nonclassical fields with low brightness and maximum phase-sensitive cross-correlation offer a spatial resolution advantage in the source's near field and a field-of-view expansion in its far field. The field of view in the near field and the resolution in the far field are determined by the beam sizes at the source, and hence are identical for classical and nonclassical fields.

The primary advantage of biphoton-state ghost imaging over classical-state ghost imaging is the improved contrast in the former. Therefore, in photon-flux-limited ghost imaging scenarios (limited in either the photon flux of the source or in the maximum permitted photon flux on the target) it is worthwhile to consider utilizing the entangled photon pairs generated by SPDC in the low-brightness, low-flux limit of its output fields' state. Nonetheless, we must be aware of the limitations of this contrast advantage. Consider an outdoor imaging scenario in which the reference arm of the ghost imaging configuration is subject to background light from the environment. We denote this as a thermalizing classical-noise channel, in which the reference-arm field operator just before the transmission mask is given by $\hat{E}_2(\boldsymbol{\rho},t)+n(\boldsymbol{\rho},t)\hat{I}$, with $\hat{I}$ denoting the identity operator and $n(\boldsymbol{\rho},t)$ representing classical zero-mean phase-insensitive Gaussian noise that is statistically independent of the field-state associated with $\hat{E}_2(\boldsymbol{\rho},t)$. Because of this independence, the noise has no bearing on the image terms of (5.32).[6] However, the featureless background is now given by $C_0(\boldsymbol{\rho}_1)+C_{0,B}(\boldsymbol{\rho}_1)$, where the first term is the background contribution of the reference-arm source field given by (5.33), and the second term is the background-light contribution of the thermal noise, given by

$$C_{0,B}(\boldsymbol{\rho}_1)\equiv q^2\eta^2 A_1 R_{1,1}^{(n)}(0)\left[\int h_B(t)\mathrm{d}t\right]^2 K_{1,1}^{(n)}(\boldsymbol{\rho}_1,\boldsymbol{\rho}_1)\int_{\mathcal{A}_2}\mathrm{d}\boldsymbol{\rho}\,K_B^{(n)}(\boldsymbol{\rho},\boldsymbol{\rho},0)|T(\boldsymbol{\rho})|^2, \quad (5.66)$$

in terms of $K_B^{(n)}(\boldsymbol{\rho}_1,\boldsymbol{\rho}_2,t_2-t_1)$, the phase-insensitive second-order complex-stationary correlation function of $n(\boldsymbol{\rho},t)$. Applying the same approximations stated in Section 5.3, and

[6] A thermalized zero-mean Gaussian state is still a zero-mean Gaussian state. Hence the moment factoring theorem applies to this case as well.

assuming that the average photon flux density of the background is uniform, we arrive at

$$\mathcal{C}_B^{(q)} = \mathcal{C}^{(q)} \left[1 + \frac{N_B 4\pi a_0^2}{P\rho_0^2 \max\{T_0, T_d\}} \right]^{-1} \tag{5.67}$$

for the contrast achieved in the presence of the thermalizing classical noise, where $\mathcal{C}^{(q)}$ is the contrast value in the absence of that noise. In this expression, N_B is the background noise photon density per detected spatiotemporal mode, and $P\rho_0^2 \max\{T_0, T_d\}/4\pi a_0^2$ is the corresponding photon density for the reference field state.[7] Therefore, when the background photons per mode significantly exceed that of the reference field, the contrast advantage of biphoton-state ghost imaging is substantially reduced. Recall that high contrast is achieved when $PT_d \ll 1$ and $T_0 \ll T_d$ so that there is only a small fraction of a source photon per spatiotemporal mode. For example, with $P = 10^6$ photons/s, $T_d = 1\,\text{ns}$, $a_0 = 1\,\text{cm}$ and $\rho_0 = 10\,\mu\text{m}$, the number of photons per mode is 7.96×10^{-11}. The number of thermal background photons in each mode due to atmospheric scattering[8] is given by [54]

$$N_B = \frac{\lambda_0^3 \times 10^6}{\hbar\omega_0^2} N_\lambda \,, \tag{5.68}$$

where N_λ is the spectral radiance in $\text{Watts/m}^2\,\text{SR}\,\mu\text{m}$ and $\lambda_0 = 2\pi/\omega_0 c$ is the center wavelength. A typical value for daytime spectral radiance is $N_\lambda = 100$, so that $\lambda_0 = 1\,\mu\text{m}$ gives $N_B = 2.87 \times 10^{-7}$ photons per mode, which will eliminate any contrast advantage expected from the biphoton state. On the other hand in nighttime imaging, with a typical spectral radiance of $N_\lambda = 10^{-4}$ yielding $N_B = 2.87 \times 10^{-13}$ photons per mode [54], the contrast advantage offered by the biphoton state may be observable. Therefore, it is relevant to carefully consider the limiting noise factors in any practical biphoton-state ghost imaging scenario to develop an accurate estimate of the contrast. Notice, the featureless background from atmospheric scattering is not a limiting factor in classical-state ghost imaging, because there are many reference-field source photons per spatiotemporal mode.

A number of recent publications have implied that ghost imaging with thermal-state light cannot be explained by classical electromagnetic theory in combination with semiclas-

[7] To obtain this expression we have assumed that a pre-detection filter limits the optical bandwidth of the detector to $4\pi/\max\{T_0, T_d\}$, and the receiver geometry limits the number of detected spatial modes to $2A_T/\pi\rho_0^2$, such that no extraneous background modes couple to the photodetector.

[8] For outdoor applications thermal background noise from atmospheric scattering will dominate over blackbody thermal noise radiation.

sical photodetection theory, but that a strictly quantum-mechanical interpretation involving nonlocality must be used to understand such experiments [49, 55]. A key conclusion from our work, however, is that the classical theory of ghost imaging is *quantitatively indistinguishable* from the quantum theory of ghost imaging for any optical source that is in a classical state, regardless of the propagation geometry. Here, a classical state is one whose density operator has a proper P-representation, so that its photodetection statistics can be correctly quantified with classical, stochastic-field electromagnetism and detector shot noise. Thermal light—whether it is broadband, such as natural illumination, or narrowband, such as thermalized laser light—falls precisely within this category of Gaussian states. Therefore experiments utilizing thermal light sources alone cannot validate the quantum description. Furthermore, and perhaps more critically, there is no nonlocal interaction in thermal-light ghost imaging. In particular, because the joint state of the signal and reference beams is classical—in the sense noted above—it *cannot* lead to a violation of the Clauser-Horne-Shimony-Holt (CHSH) inequality [56]. We reiterate that it is the nonzero cross-covariance between the photon-flux densities of the signal and reference fields that is responsible for the image-bearing terms obtained from the Figure 5-1 setup. For Gaussian-state sources, this detection-plane cross-covariance is found, by moment factoring, from the phase-insensitive and phase-sensitive field cross-correlation functions. These detection-plane field correlations follow, in turn, from propagation of the corresponding source-plane field correlations through $L\,\mathrm{m}$ of free space. Thus, two classical fields that are generated in a correlated fashion at a source, yet propagating paraxially in two different directions, will still exhibit spatiotemporal correlations on transverse planes that are equidistant from the source, even though these planes may be physically separated from each other. This concept is both well known in and central to classical statistical optics [13, 14]. It is not at all related to nonlocality in quantum mechanics, e.g., to violation of the CHSH inequality.

It is worth connecting some of the analysis presented in this paper with recent theory for the coherence properties of biphoton wavefunctions, which has led to an elegant duality between the partial entanglement of biphotons and the classical partial coherence of phase-insensitive fields [15]. As we have shown in Section 5.1.1, the biphoton state is the low-brightness, low-flux limit of the zero-mean jointly Gaussian state with zero phase-insensitive cross-correlation but maximum phase-sensitive cross-correlation. In this limit, the biphoton wavefunction *is* the phase-sensitive cross-correlation function between the signal and refer-

ence fields, and therefore the duality between phase-insensitive coherence propagation and the biphoton wavefunction propagation is rooted in the duality between phase-insensitive and phase-sensitive coherence propagation [cf. Eqs. (5.27) and (5.28)]. Furthermore, classical fields may also have phase-sensitive coherence. Thus, to correctly understand the fundamental physics of quantum imaging, it is crucial to distinguish features that are due to the presence of this phase-sensitive correlation in the source fields from those that *require* this phase-sensitive correlation to be stronger than what is possible with classical (proper P-representation) states. The following examples clearly illustrate our point. When ghost imaging is performed with phase-sensitive light, image inversion occurs in the far field for both classical and quantum sources. This inversion is entirely due to the difference between the free-space propagation of phase-sensitive and phase-insensitive correlations, and it is not necessary for the phase-sensitive coherence to be stronger than classical. On the other hand, the background-free nature of ghost images formed with SPDC light arises from that source's phase-sensitive cross-correlation being much stronger the classical limit, as we showed in Section 5.3.

In summary, we have used Gaussian-state analysis to establish a unified treatment of classical and quantum ghost imaging. Our analysis reveals that ghost-image formation is due to phase-sensitive and phase-insensitive cross-correlations between the signal and reference fields. Because arbitrary cross-correlations can be achieved by classical and quantum sources alike, image contrast is the only distinguishing feature between a source that is classical or quantum. In particular, we emphasize that a classical source with phase-sensitive cross-correlation can produce an *identical* image to that obtained with a biphoton source—up to a different contrast and hence signal-to-noise ratio—even for ghost-imaging configurations that utilize lenses, mirrors or other linear optical elements. If we compare ghost images from classical and quantum sources having identical auto-correlations, thereby fixing the background level, the low-brightness quantum source offers resolution enhancement in near-field operation and field-of-view enhancement in far-field operation, in addition to higher contrast in both regimes. Furthermore, because far-field spatial resolution and the near-field field of view are determined by source-plane beam size, they are identical for classical and quantum sources. Finally, the conclusions in this paper are not contingent on having coincident object and detection planes. They apply so long as the signal arm can be freely modified to transfer the object-plane correlations to the detection plane via an

appropriately-positioned lens.

Chapter 6

Gaussian-State Theory of Two-Photon Imaging

Spontaneous parametric downconversion, with a continuous-wave nondepleting pump, produces two output fields—namely signal and reference—that are in a maximally-entangled zero-mean jointly-Gaussian state [18, 51]. When operated in the low-flux regime, this state reduces to the superposition of a multimode vacuum state and a pair of entangled photons (a biphoton). These biphoton states have been utilized in many imaging applications, including optical coherence tomography (OCT) [1], ghost imaging [5], holography [6] and lithography [8], yielding various advantages over conventional optical imagers, which rely on (classical) thermal- or coherent-state sources. Although the physical underpinning of these advantages have traditionally been ascribed to the entanglement between the two source photons, prior chapters in this thesis—relying on Gaussian-state analysis and phase-sensitive coherence theory—unambiguously demonstrates that the advantages in quantum OCT and ghost imaging predominantly stem from the phase-sensitive cross-correlation between the two photons, rather than their entanglement *per se*. Furthermore, because a pair of classical fields can also have nonzero phase-sensitive cross-correlation, most of the advantages seen in these biphoton-state imagers are also attainable with *classical* phase-sensitive sources as well, but conceivably at much higher photon-flux and without the need for single-photon detecting photodetectors.

Our successful application of Gaussian-state analysis, together with phase-sensitive coherence theory, to developing a unified—and generalized—understanding of the classical

and quantum regimes for OCT and ghost imaging naturally motivates the development of a unifying theory for other imaging configurations that rely on biphotons. In this chapter we study the Fourier-plane and thin-lens imaging of a transmission mask, using jointly-Gaussian source states, which encompasses the biphoton state, thermal states (used in conventional low-coherence imaging) and coherent states (used in conventional coherent imaging).

The organization of this chapter, is as follows. In Section 6.1, we review the relevant coherence theory results from Section 3.3, and expand on these results to incorporate the spatiotemporal coupling in paraxial propagation of broadband fields. In Section 6.2 we apply the phase-sensitive coherence theory results to determine the far-field diffraction properties of Gaussian-state source fields when apertured by a transmission mask at the source-plane, and identify the fundamental physics underlying the far-field image features. Section 6.3 analyzes a thin lens imaging configuration, and determines the effect of the source's bandwidth on the point-spread functions resulting from phase-insensitive and phase-sensitive Gaussian source states, respectively. Finally, in Section 6.4 we summarize the conclusions of our analysis for the two imaging configurations, and highlight the role of phase-sensitive coherence in these imaging schemes.

6.1 Second-order coherence propagation

The foci of this chapter are the imaging configurations shown in Figure 6-1 and Figure 6-2, which, respectively acquire the far-field diffraction pattern and the transverse image of a transmission mask placed at the output plane of a source. In either configuration, the source plane and the image-acquisition plane are separated by linear optical elements and a finite free-space propagation distance. Because the image is acquired via photocurrent correlation, its properties are determined by a fourth-order correlation function of the detected fields. To determine this correlation, it is necessary to propagate the same (fourth-order) source-plane correlation function, through the combination of linear elements and onto the image-acquisition plane. Fortunately, zero-mean Gaussian source states are completely determined by their phase-insensitive and phase-sensitive, second-order auto- and cross-correlation functions. Therefore, we need only consider second-order coherence transfer.

Let $\hat{E}_z(\boldsymbol{\rho}, t)e^{-i\omega_0 t}$ denote a scalar, z-propagating, positive-frequency field operator with

center-frequency ω_0, and photon units ($\sqrt{\text{photons/m}^2\text{s}}$). The commutators for the baseband envelope at a fixed transverse plane are given by [37]

$$[\hat{E}_z(\boldsymbol{\rho}_1, t_1), \hat{E}_z(\boldsymbol{\rho}_2, t_2)] = 0 \quad \text{and} \tag{6.1}$$

$$[\hat{E}_z(\boldsymbol{\rho}_1, t_1), \hat{E}_z^\dagger(\boldsymbol{\rho}_2, t_2)] = \delta(\boldsymbol{\rho}_2 - \boldsymbol{\rho}_1)\delta(t_2 - t_1)\,. \tag{6.2}$$

Free-space paraxial propagation is governed by the Huygens-Fresnel principle [37], which states that the baseband field operator at $z = L$ is a superposition integral of the field operator at $z = 0$, as

$$\hat{E}_L(\boldsymbol{\rho}, t) = \int_{-\omega_0}^{\infty} \frac{\mathrm{d}\Omega}{2\pi} \int_{\mathbb{R}^2} \mathrm{d}\boldsymbol{\rho}'\, \hat{\mathcal{E}}_0(\boldsymbol{\rho}', \Omega) h_L(\boldsymbol{\rho} - \boldsymbol{\rho}', \omega_0 + \Omega) e^{-i\Omega t}, \tag{6.3}$$

where

$$\hat{\mathcal{E}}_z(\boldsymbol{\rho}, \Omega) \equiv \int_{-\infty}^{\infty} \mathrm{d}t\, \hat{E}_z(\boldsymbol{\rho}, t) e^{i\Omega t} \tag{6.4}$$

is the Fourier transform of the baseband-envelope field operator and

$$h_L(\boldsymbol{\rho}, \omega) \equiv \frac{\omega}{i2\pi Lc} e^{i\frac{\omega}{2Lc}(2L^2 + |\boldsymbol{\rho}|^2)}\,, \tag{6.5}$$

is the Huygens-Fresnel Green's function for paraxial diffraction, in which c denotes the vacuum light speed and ω denotes a positive (optical) frequency.

The non-Hermitian baseband field operator $\hat{E}_z(\boldsymbol{\rho}, t)$ has two second-order correlation functions, namely the (normally-ordered) phase-insensitive correlation function

$$K_z^{(n)}(\boldsymbol{\rho}_1, \boldsymbol{\rho}_2, t_2 - t_1) \equiv \langle \hat{E}_z^\dagger(\boldsymbol{\rho}_1, t_1) \hat{E}_z(\boldsymbol{\rho}_2, t_2) \rangle\,, \tag{6.6}$$

and the phase-sensitive correlation function

$$K_z^{(p)}(\boldsymbol{\rho}_1, \boldsymbol{\rho}_2, t_2 - t_1) \equiv \langle \hat{E}_z(\boldsymbol{\rho}_1, t_1) \hat{E}_z(\boldsymbol{\rho}_2, t_2) \rangle\,, \tag{6.7}$$

in which we have assumed for simplicity that the baseband field operator is in a complex-stationary state, i.e. the correlation functions depend on the time difference $t_2 - t_1$, but not on the absolute times.

We will find it convenient and insightful to work with the frequency spectra associated

with (6.6) and (6.7), defined as the Fourier transforms,

$$S_z^{(x)}(\boldsymbol{\rho}_1, \boldsymbol{\rho}_2, \Omega) \equiv \int_{-\infty}^{\infty} \mathrm{d}\tau \; K_z^{(x)}(\boldsymbol{\rho}_1, \boldsymbol{\rho}_2, \tau) e^{i\Omega\tau} \,, \tag{6.8}$$

for $x = n, p$. The phase-insensitive and phase-sensitive correlation spectra at $z = L$ can be expressed in terms of the correlation spectra at $z = 0$ by evaluating (6.8) for the propagated field operators, via (6.3), which yields the following phase-insensitive spectrum,

$$S_L^{(n)}(\boldsymbol{\rho}_1, \boldsymbol{\rho}_2, \Omega) = \iint \mathrm{d}\boldsymbol{\rho}_1' \, \mathrm{d}\boldsymbol{\rho}_2' \, S_0^{(n)}(\boldsymbol{\rho}_1', \boldsymbol{\rho}_2', \Omega) \\ \times h_L^*(\boldsymbol{\rho}_1 - \boldsymbol{\rho}_1', \omega_0 + \Omega) h_L(\boldsymbol{\rho}_2 - \boldsymbol{\rho}_2', \omega_0 + \Omega) \,, \tag{6.9}$$

and the following phase-sensitive spectrum,

$$S_L^{(p)}(\boldsymbol{\rho}_1, \boldsymbol{\rho}_2, \Omega) = \iint \mathrm{d}\boldsymbol{\rho}_1' \, \mathrm{d}\boldsymbol{\rho}_2' \, S_0^{(p)}(\boldsymbol{\rho}_1', \boldsymbol{\rho}_2', \Omega) \\ \times h_L(\boldsymbol{\rho}_1 - \boldsymbol{\rho}_1', \omega_0 - \Omega) h_L(\boldsymbol{\rho}_2 - \boldsymbol{\rho}_2', \omega_0 + \Omega) \,, \tag{6.10}$$

where $*$ in the former equation denotes complex conjugation. Note that the phase-insensitive correlation spectrum is a monochromatic equation, i.e., the frequency dependence is $\omega_0 + \Omega$ on both sides of the equality, whereas the phase-sensitive spectrum is a bichromatic equation involving $\omega_0 \pm \Omega$. This result is because complex-stationary phase-insensitive correlations are uncorrelated across frequencies, whereas complex-stationary phase-sensitive correlation functions yield nonzero (phase-sensitive) correlations between the equally red- and blue-detuned frequency components, as we have seen in Section 3.1 [20].

For field states that are quasimonochromatic (narrowband), the field is excited only for $|\Omega|/\omega_0 \ll 1$. Consequently, the Huygens-Fresnel principle simplifies to

$$\hat{E}_L(\boldsymbol{\rho}, t) = \int \mathrm{d}\boldsymbol{\rho}' \, \hat{E}_0\big(\boldsymbol{\rho}', t - L/c\big) h_L(\boldsymbol{\rho} - \boldsymbol{\rho}', \omega_0), \tag{6.11}$$

and the corresponding phase-insensitive and phase-sensitive correlation spectra, i.e., (6.9) and (6.10) with $h_L(\boldsymbol{\rho}, \omega_0 \pm \Omega) \approx h_L(\boldsymbol{\rho}, \omega_0)$, coincide with the quasimonochromatic expressions given in Section 3.3.

Let us next review the far-field propagation regime. Assume that the field at the $z = 0$

plane is in a zero-mean state with spectrally pure, Schell-model (second-order) correlation spectra given by

$$S_0^{(n)}(\boldsymbol{\rho}_1, \boldsymbol{\rho}_2, \Omega) = T^*(\boldsymbol{\rho}_1) T(\boldsymbol{\rho}_2) G^{(n)}(\boldsymbol{\rho}_2 - \boldsymbol{\rho}_1) S^{(n)}(\Omega)\,, \tag{6.12}$$

$$S_0^{(p)}(\boldsymbol{\rho}_1, \boldsymbol{\rho}_2, \Omega) = T(\boldsymbol{\rho}_1) T(\boldsymbol{\rho}_2) G^{(p)}(\boldsymbol{\rho}_2 - \boldsymbol{\rho}_1) S^{(p)}(\Omega)\,. \tag{6.13}$$

With no loss of generality, we require $|T(\boldsymbol{\rho})| \leq 1$, so that it may be regarded as a (possibly complex-valued) spatial attenuation of an optical field operator[1] in a homogenous and stationary state with separable phase-insensitive spectrum $S^{(n)}(\Omega)G^{(n)}(\boldsymbol{\rho}_2 - \boldsymbol{\rho}_1)$ and phase-sensitive spectrum $S^{(p)}(\Omega)G^{(p)}(\boldsymbol{\rho}_2 - \boldsymbol{\rho}_1)$. Our primary interest is in sources with narrow $G_0^{(x)}(\boldsymbol{\rho})$, for $x = n, p$, such that the aperture $T(\boldsymbol{\rho})$ does not vary appreciably within a (phase-insensitive or phase-sensitive) coherence area. For this case, we may approximate the source correlation spectra as

$$S_0^{(n)}(\boldsymbol{\rho}_1, \boldsymbol{\rho}_2, \Omega) \approx \left|T(\boldsymbol{\rho}_s)\right|^2 G^{(n)}(\boldsymbol{\rho}_d) S^{(n)}(\Omega), \tag{6.14}$$

$$S_0^{(p)}(\boldsymbol{\rho}_1, \boldsymbol{\rho}_2, \Omega) \approx T^2(\boldsymbol{\rho}_s) G^{(p)}(\boldsymbol{\rho}_d) S^{(p)}(\Omega)\,, \tag{6.15}$$

in terms of the sum coordinate $\boldsymbol{\rho}_s \equiv (\boldsymbol{\rho}_2 + \boldsymbol{\rho}_1)/2$ and the difference coordinate $\boldsymbol{\rho}_d \equiv \boldsymbol{\rho}_2 - \boldsymbol{\rho}_1$. This approximation simplifies the subsequent analytic treatment considerably, without significant impact on the fundamental physics. The $z = L$ spectra in the quasimonochromatic regime are then given by

$$\begin{aligned} S_L^{(n)}(\boldsymbol{\rho}_1, \boldsymbol{\rho}_2, \Omega) = {} & \frac{\omega_0^2 S^{(n)}(\Omega)}{(2\pi L c)^2}\, e^{i\omega_0 \boldsymbol{\rho}_s \cdot \boldsymbol{\rho}_d / Lc} \\ & \times \int \mathrm{d}\boldsymbol{\rho}_s' \int \mathrm{d}\boldsymbol{\rho}_d'\, e^{-i\omega_0 (\boldsymbol{\rho}_s \cdot \boldsymbol{\rho}_d' + \boldsymbol{\rho}_d \cdot \boldsymbol{\rho}_s')/Lc}\, e^{i\omega_0 \boldsymbol{\rho}_s' \cdot \boldsymbol{\rho}_d'/Lc}\, |T(\boldsymbol{\rho}_s')|^2 G^{(n)}(\boldsymbol{\rho}_d'), \end{aligned} \tag{6.16}$$

and

$$\begin{aligned} S_L^{(p)}(\boldsymbol{\rho}_1, \boldsymbol{\rho}_2, \Omega) = {} & \frac{-\omega_0^2 S^{(p)}(\Omega)}{(2\pi L c)^2}\, e^{i\omega_0 \left(2L^2 + |\boldsymbol{\rho}_s|^2 + |\boldsymbol{\rho}_d|^2/4\right)/Lc} \\ & \times \int \mathrm{d}\boldsymbol{\rho}_s' \int \mathrm{d}\boldsymbol{\rho}_d'\, e^{-i\omega_0 (2\boldsymbol{\rho}_s \cdot \boldsymbol{\rho}_s' + \boldsymbol{\rho}_d \cdot \boldsymbol{\rho}_d'/2)/Lc}\, e^{i\omega_0 (|\boldsymbol{\rho}_s'|^2 + |\boldsymbol{\rho}_d'|^2/4)/Lc}\, T^2(\boldsymbol{\rho}_s') G^{(p)}(\boldsymbol{\rho}_d')\,, \end{aligned} \tag{6.17}$$

[1] This spatial attenuation $T(\boldsymbol{\rho})$ will become the transmission mask to be imaged when we turn our attention to the imaging configurations shown in Figure 6-1 and 6-2.

respectively, where, for simplicity, we have approximated the frequency-dependent leading coefficients by their values at the center frequency.[2]

Let ρ_0 denote the radius within which $G^{(x)}(\boldsymbol{\rho})$, for $x = n, p$, appreciably differ from zero (i.e, the coherence radius of the source) and let a_0 denote the transverse radius of $|T(\boldsymbol{\rho})|^2$ (i.e., the photon-flux density radius of the source field state just after the aperture), which satisfy $a_0 \gg \rho_0$ so that the approximations in (6.14) and (6.15) are valid. In far field phase-insensitive correlation propagation, when $\omega_0 a_0 \rho_0 / 2Lc \ll 1$, the phase term $e^{i\omega_0 \boldsymbol{\rho}_s' \cdot \boldsymbol{\rho}_d' / Lc}$ of the integrand can be neglected, so that (6.16) simplifies to

$$S_L^{(n)}(\boldsymbol{\rho}_1, \boldsymbol{\rho}_2, \Omega) = \frac{\omega_0^2 S^{(n)}(\Omega)}{(2\pi Lc)^2} e^{i\omega_0 \boldsymbol{\rho}_s \cdot \boldsymbol{\rho}_d / Lc} \mathcal{T}_n\Big(\frac{\omega_0 \boldsymbol{\rho}_d}{Lc}\Big) \mathcal{G}^{(n)}\Big(\frac{\omega_0 \boldsymbol{\rho}_s}{Lc}\Big) , \tag{6.18}$$

where $\mathcal{T}_n(\boldsymbol{k})$ and $\mathcal{G}^{(n)}(\boldsymbol{k})$ are the following 2-D Fourier transforms,

$$\mathcal{T}_n(\boldsymbol{k}) \equiv \int_{\mathbb{R}^2} \mathrm{d}\boldsymbol{\rho}' e^{-i\boldsymbol{k}\cdot\boldsymbol{\rho}'} |T(\boldsymbol{\rho}')|^2 , \tag{6.19}$$

$$\mathcal{G}^{(n)}(\boldsymbol{k}) \equiv \int_{\mathbb{R}^2} \mathrm{d}\boldsymbol{\rho}' e^{-i\boldsymbol{k}\cdot\boldsymbol{\rho}'} G^{(n)}(\boldsymbol{\rho}') . \tag{6.20}$$

The Fourier-transform duality between the source-plane and the far-field phase-insensitive correlation spectra is well known as the van Cittert-Zernike theorem for phase-insensitive correlation propagation, which we have studied in Section 3.3. A similar duality is present between the source-plane and the far-field phase-sensitive correlation spectra, but the far-field regime corresponds to $\omega_0 a_0^2 / 2Lc \ll 1$ (low-coherence implies $\omega_0 \rho_0^2 / 2Lc \ll 1$ as well), which is more stringent than the far-field condition for the phase-insensitive case. In this regime, the quadratic phase terms of the integrand in (6.17) become negligible, yielding

$$S_L^{(p)}(\boldsymbol{\rho}_1, \boldsymbol{\rho}_2, \Omega) = \frac{-\omega_0^2 S^{(p)}(\Omega)}{(2\pi Lc)^2} e^{i\omega_0 \left(2L^2 + |\boldsymbol{\rho}_s|^2 + |\boldsymbol{\rho}_d|^2/4\right)/Lc} \mathcal{T}_p\left(\frac{2\omega_0 \boldsymbol{\rho}_s}{Lc}\right) \mathcal{G}^{(p)}\Big(\frac{\omega_0 \boldsymbol{\rho}_d}{2Lc}\Big) , \tag{6.21}$$

for the far-field phase-sensitive correlation spectrum, with

$$\mathcal{T}_p(\boldsymbol{k}) \equiv \int_{\mathbb{R}^2} \mathrm{d}\boldsymbol{\rho}' e^{-i\boldsymbol{k}\cdot\boldsymbol{\rho}'} T^2(\boldsymbol{\rho}') \tag{6.22}$$

[2]Our primary interest in this chapter is the phase term in the Huygens-Fresnel principle (rather than the frequency dependence of the leading coefficient) over the frequency range of the source correlation spectrum, which is what motivates this approximation. More care will be paid to the leading coefficient when we treat broadband imaging within the Figure 6-2 configuration.

and

$$\mathcal{G}^{(p)}(\boldsymbol{k}) \equiv \int_{\mathbb{R}^2} \mathrm{d}\boldsymbol{\rho}' e^{-i\boldsymbol{k}\cdot\boldsymbol{\rho}'} G^{(p)}(\boldsymbol{\rho}')\,. \tag{6.23}$$

Analogous to the phase-insensitive case, we refer to the Fourier transform relation given in (6.21) as the van Cittert-Zernike theorem for phase-sensitive coherence propagation.

It is worth reviewing the relevant similarities and distinctions between (6.21) and (6.18), which were discussed in Section 3.3. The aperture in the source plane, $T(\boldsymbol{\rho})$, has been assumed to be a slowly-varying and broad function in comparison to the rapidly-decaying $G^{(x)}(\boldsymbol{\rho})$. Thus, for $x = n, p$, Fourier-transform duality implies that $\mathcal{T}_x(\boldsymbol{k})$, decays more rapidly than $\mathcal{G}^{(x)}(\boldsymbol{k})$. Therefore, in the far field, the phase-sensitive correlation function is dominated by a narrow function of $\boldsymbol{\rho}_s$ and a broad function of $\boldsymbol{\rho}_d$, whereas the phase-insensitive correlation function consists of a narrow function of $\boldsymbol{\rho}_d$ and a broad function of $\boldsymbol{\rho}_s$. Owing to this difference in the far-field regime, points on the transverse plane that are symmetric about the origin (i.e., points that satisfy $|\boldsymbol{\rho}_s| \approx 0$) have appreciable phase-sensitive correlation, whereas the phase-insensitive correlation is highest between points that are in the same vicinity on the transverse plane ($|\boldsymbol{\rho}_d| \approx 0$). In addition, if we evaluate the correlations at a single transverse point, i.e., when $\boldsymbol{\rho}_d = 0$, we find that the phase-insensitive correlation traces out the broad envelope $\mathcal{G}^{(n)}(\boldsymbol{k})$, whereas the phase-sensitive correlation traces out the narrow function $\mathcal{T}_p(\boldsymbol{k})$, a property we shall make use of in the following section. Finally, it is relevant to emphasize that (6.21) is a general property of phase-sensitive coherence propagation irrespective of whether the source is in a classical or nonclassical state [20, 23, 24].

6.2 An exercise in far-field coherence propagation

Consider the experimental setup given in Figure 6-1, whose purpose is to obtain the far-field diffraction pattern of a transmission mask placed at the source plane that has (possibly complex-valued) amplitude transmissivity $T(\boldsymbol{\rho})$. An experiment using this setup—which we will explain in detail shortly—was reported in [8] as a proof-of-principle demonstration of the spot-size improvement in biphoton-state optical lithography, in comparison to the spot size obtained with conventional (coherent-state) lithography. Our aim in this section is to use Gaussian-state analysis and (second-order) phase-sensitive coherence theory, to show that it is phase-sensitive coherence, not entanglement *per se*, that is giving the spot-size

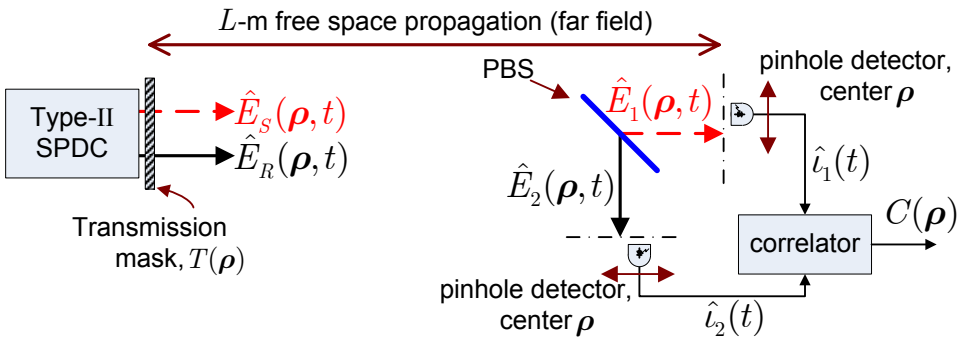

Figure 6-1: Imaging the far-field diffraction pattern of a transmission mask.

improvement. In particular, we will find that classical phase-sensitive light and biphoton-state light yield *identical* images (i.e., with half the spot-size obtained from a coherent-state beam), but the image obtained with a classical phase-sensitive source is embedded in a more prominent background than the image acquired using a biphoton state. Thus, the improvement over coherent-beam diffraction, previously ascribed to the nonclassical correlation between the photon-pairs, is in fact due to the phase-sensitive coherence present between the signal and reference photons. The entanglement between the signal and reference photons (i.e., the stronger-than-classical phase-sensitive cross-correlation between signal and reference fields) on the other hand, is responsible for improving the contrast of this image.

Consider degenerate type-II phase-matched SPDC with a continuous-wave pump, which generates two paraxial, z-propagating fields in orthogonal transverse polarizations and with equal center frequency ω_0. We will denote their positive-frequency field operators as $\hat{E}_S(\boldsymbol{\rho},t)e^{-i\omega_0 t}$ for the signal and as $\hat{E}_R(\boldsymbol{\rho},t)e^{-i\omega_0 t}$ for the reference. As shown in Section 2.3, with a nondepleting plane-wave pump and ignoring boundary effects due to the finite cross-section of the crystal, these two output fields are in a zero-mean jointly-Gaussian state that is homogeneous, stationary, and with identical fluorescence spectra and maximum phase-sensitive cross-correlation (i.e., with maximum entanglement), but with zero phase-sensitive auto-correlation and phase-insensitive cross-correlation. It follows that after passing through the transmission mask the jointly-Gaussian state is fully determined by the Schell-model auto-correlation spectra

$$S^{(n)}_{m,m}(\boldsymbol{\rho}_1,\boldsymbol{\rho}_2,\Omega) = S^{(n)}_0(\boldsymbol{\rho}_1,\boldsymbol{\rho}_2,\Omega)\,, \tag{6.24}$$

for $m = S, R$, and the phase-sensitive cross-correlation spectrum

$$S^{(p)}_{S,R}(\boldsymbol{\rho}_1, \boldsymbol{\rho}_2, \Omega) = S^{(p)}_0(\boldsymbol{\rho}_1, \boldsymbol{\rho}_2, \Omega)\,, \tag{6.25}$$

where $S^{(n)}_0$ and $S^{(p)}_0$ are given in (6.14) and (6.15), respectively.

In the experimental apparatus shown in Figure 6-1, the signal and reference fields both propagate over an L m free-space path and then are separated by a polarizing beam splitter such that they impinge on separate pinhole detectors, each centered on the transverse-plane coordinate $\boldsymbol{\rho}$ with respect to its optical axis. Because zero-mean Gaussian states modified by linear transformations—such as free-space propagation—are still zero-mean Gaussian [18], we need only determine the second-order moments at the detection planes to determine the joint state of $\hat{E}_1(\boldsymbol{\rho}, t)$ and $\hat{E}_2(\boldsymbol{\rho}, t)$, which denote the far-field propagated field operators of the signal and the reference respectively. Thus, quasimonochromatic paraxial diffraction into the far field ($\omega_0 a_0^2/2Lc \ll 1$) results in phase-insensitive auto-correlation spectra given by (6.18) and a phase-sensitive cross-correlation spectrum given by (6.21).[3]

The two pinhole photodetectors are assumed to have identical parameters: η denotes their sub-unity quantum efficiency, A is the area of their photosensitive regions, and $h_B(t)$ denotes the finite-bandwidth current pulses for each detected photon. Then, the time-average photocurrent cross-correlation at the detection planes has an ensemble average [19, 24]

$$C(\boldsymbol{\rho}) = \frac{1}{T}\int_{-T/2}^{T/2} \mathrm{d}t\, \langle \hat{\imath}_1(t)\hat{\imath}_2(t)\rangle\,, \tag{6.26}$$

in which the equal-time current cross-correlation is given by

$$\begin{aligned}\langle \hat{\imath}_1(t)\hat{\imath}_2(t)\rangle = q^2\eta^2 A^2 \int_{-\infty}^{\infty}\int_{-\infty}^{\infty} \mathrm{d}u_1 \mathrm{d}u_2 \\ \times \langle \hat{E}_1^\dagger(\boldsymbol{\rho}, u_1)\hat{E}_2^\dagger(\boldsymbol{\rho}, u_2)\hat{E}_1(\boldsymbol{\rho}, u_1)\hat{E}_2(\boldsymbol{\rho}, u_2)\rangle\, h_B(t-u_1)h_B(t-u_2)\,.\end{aligned} \tag{6.27}$$

Here, we have approximated the two spatial integrals over the pinhole detectors' photosensitive regions as the value of the integrand at $\boldsymbol{\rho}$ times A^2. With Gaussian-state $\hat{E}_1$ and $\hat{E}_2$, the fourth-order field moment in (6.27) is expressible in terms of the second-order correlation functions, a result known as the Gaussian moment-factoring theorem [14, 19]. This

[3] Because both the signal and reference beams undergo identical transformations, the auto-correlation results reported in Section 6.1 apply to cross-correlation propagation as well.

procedure simplifies the photocurrent cross-correlation expression to

$$C(\boldsymbol{\rho}) = C_0(\boldsymbol{\rho}) + C_p \left| \mathcal{G}^{(p)}(\mathbf{0})\, \mathcal{T}_p\left(\frac{2\omega_0 \boldsymbol{\rho}}{Lc}\right)\right|^2 , \tag{6.28}$$

where the non-image bearing background is

$$C_0(\boldsymbol{\rho}) = \left[\frac{\omega_0^2 q\eta A}{4\pi^2 L^2 c^2}\, \mathcal{T}_n(\mathbf{0})\, \mathcal{G}^{(n)}\Big(\frac{\omega_0 \boldsymbol{\rho}}{Lc}\Big) \int_{-\omega_0}^{\infty} \frac{\mathrm{d}\Omega}{2\pi}\, S^{(n)}(\Omega) \int_{-\infty}^{\infty} \mathrm{d}t\, h_B(t)\right]^2 . \tag{6.29}$$

The image-bearing term includes the constant

$$C_p = \left(\frac{\omega_0^2 q\eta A}{4\pi^2 L^2 c^2}\right)^2 \Big[\big|\mathcal{F}^{-1}\{S^{(p)}(\Omega)\}\big|^2 \star h_B \star \overleftarrow{h_B}\Big]_{t=0} , \tag{6.30}$$

in which $\mathcal{F}^{-1}\{\cdot\}$ denotes the inverse Fourier transform of the bracketed term (cf. (6.8) for sign convention), $\star$ denotes convolution, and $\overleftarrow{h_B}$ represents the time-reversed impulse response. Therefore, via (6.28), we observe that the image bearing term is proportional to $|\mathcal{T}_p(2\omega_0\boldsymbol{\rho}/Lc)|^2$, the diffraction pattern of the *square* of the mask transmissivity $T(\boldsymbol{\rho})$.

Let us compare the imaging characteristics of this imager to a conventional classical imager that utilizes a coherent-state beam to illuminate the mask, and a single (scanning) pinhole detector located in the far field that records the diffraction pattern. If we assume the field impinging on the transmission mask is a monochromatic plane wave at center frequency ω_0 and with photon-flux density I_0, the field just after the mask is in the coherent state

$$\hat{E}_0(\boldsymbol{\rho}, t)|\sqrt{I_0}T(\boldsymbol{\rho})\rangle = \sqrt{I_0}T(\boldsymbol{\rho})|\sqrt{I_0}T(\boldsymbol{\rho})\rangle\,. \tag{6.31}$$

Because free-space propagation is a multimode beamsplitter relation [37], the detection-plane field operator $\hat{E}_1(\boldsymbol{\rho}, t)$ is also in a coherent state, whose eigenfunction is determined by substituting $\sqrt{I_0}T(\boldsymbol{\rho})$ into the classical Huygens-Fresnel diffraction integral (i.e., (6.3), with the field operator replaced by the source-plane eigenfunction).

In the far-field regime for coherent beam diffraction, i.e., when $\omega_0 a_0^2/2Lc \ll 1$,[4] the quadratic phase term in the Huygens-Fresnel Green's function becomes negligible, and the

[4]Quasimonochromatic, paraxial diffraction of a coherent beam with center wavenumber k_0 and source-plane intensity radius a_0 has a near- and far-field regime determined by a single Fresnel number $D_C = k_0 a_0^2/2L$ [14]. The far-field regime, given by $D_C \ll 1$, coincides with that for low-coherence phase-sensitive correlation diffraction. However, the near field for a coherent beam, $D_C \gg 1$, is much less stringent than that for low-coherence phase-sensitive correlation diffraction, which corresponds to $k_0\rho_0^2/2L \ll 1$, where ρ_0 is the coherence length of the source (see Section 3.3).

mean photocurrent becomes

$$\langle \hat{\imath}(t) \rangle = \frac{\omega_0^2 q \eta A}{4\pi^2 L^2 c^2} I_0 \int_{-\infty}^{\infty} \mathrm{d}t \, h_B(t) \left| \mathcal{T}_c \left(\frac{\omega_0 \boldsymbol{\rho}}{Lc} \right) \right|^2 , \tag{6.32}$$

where the image term is given by,

$$\mathcal{T}_c(\boldsymbol{k}) \equiv \int_{\mathbb{R}^2} \mathrm{d}\boldsymbol{\rho}' \, e^{-i\boldsymbol{k}\cdot\boldsymbol{\rho}'} T(\boldsymbol{\rho}') \, . \tag{6.33}$$

Observe that if $T(\boldsymbol{\rho})$ is a binary amplitude mask, i.e., $T(\boldsymbol{\rho})$ is a function that only takes values zero or one, then $T^2(\boldsymbol{\rho}) = T(\boldsymbol{\rho})$ and the biphoton source yields a far-field diffraction pattern proportional to $|\mathcal{T}_p(2\omega_0 \boldsymbol{\rho}/Lc)|^2$, whereas the coherent diffraction pattern is proportional to $|\mathcal{T}_p(\omega_0 \boldsymbol{\rho}/Lc)|^2$. Thus, the biphoton source pattern is spatially compressed by a factor of two relative to the coherent diffraction pattern, which is the reason why such images are often referred to as beating the resolution limit. However, it is worth re-emphasizing that (6.28) is true for *both classical and quantum* Gaussian-state sources with a nonzero phase-sensitive cross-correlation between the signal and reference fields, so it is the phase-sensitive coherence of the source—and *not* the entanglement—that yields a twice-compressed far-field diffraction pattern compared to an image obtained from a coherent plane wave [8]. It is also apparent from our analysis that comparing biphoton diffraction to plane-wave diffraction is a comparison of the phase-sensitive second-order moment of the field (which depends on the absolute phase of the field state) to that of the first-order moment (ensemble average) of the field, so the factor-of-two is not an entirely surprising outcome even for classical-state fields. Finally, it is important to note that if $T(\boldsymbol{\rho})$ is not real or binary, then the diffraction pattern acquired from phase-sensitive sources will be distorted relative to that obtained with a coherent field, due to the squaring of the amplitude transmittance of the mask.

Utilizing phase-insensitive Gaussian-state light in this experimental configuration is not possible because, via (6.18), we observe that the equal-position correlation in the Fourier-plane traces $\mathcal{G}_0^{(n)}(\boldsymbol{\rho})$, which does not contain any information on the object transmittance. For this reason, we will not include the class of phase-insensitive Gaussian-state sources in our comparison. Nonetheless, it is worth pointing out that if we modify the apparatus, such that one detector scans $-\boldsymbol{\rho}$, while the other scans $\boldsymbol{\rho}$, then it becomes possible to acquire $|\mathcal{T}_n(2\omega_0 \boldsymbol{\rho}/Lc)|^2$, as defined in (6.19).

6.2.1 Image contrast

Thus far we have considered only the image term in (6.28). Now we will address the image contrast. For simplicity, we will assume that $T(\boldsymbol{\rho})$ is a real function. In accordance with the previous chapter, we restrict ourselves to an observation region $\mathcal{R}$ that encompasses the image-bearing term in (6.28), and we define the contrast as

$$\mathcal{C} \equiv \frac{\max_{\mathcal{R}}[C(\boldsymbol{\rho})] - \min_{\mathcal{R}}[C(\boldsymbol{\rho})]}{C_0(\mathbf{0})}\,, \tag{6.34}$$

so that the numerator yields the dynamic range of the image-bearing terms in the photocurrent correlation $C(\boldsymbol{\rho})$, while the denominator is the featureless background.

Here we compare the contrast from a classical and quantum source with identical auto-correlation spectra, but with maximum phase-sensitive cross-correlation allowed in classical and quantum physics, respectively. When the source is in a classical Gaussian state, with the auto-correlation spectrum given by $\mathcal{G}^{(n)}(\boldsymbol{k})S^{(n)}(\Omega)$, the maximum magnitude for the phase-sensitive cross-correlation spectrum is equal to the auto-correlation spectrum [18], i.e., the Gaussian state with maximum classical phase-sensitive cross-correlation satisfies

$$|S^{(p)}(\Omega)\mathcal{G}^{(p)}(\boldsymbol{k})| = S^{(n)}(\Omega)\mathcal{G}^{(n)}(\boldsymbol{k}). \tag{6.35}$$

Taking the phase of this phase-sensitive spectrum to be zero, and assuming $\int \mathrm{d}t\, h_B(t) = 1$, the contrast with classical phase-sensitive Gaussian-state sources can be written as

$$\mathcal{C}^{(c)} = \mathcal{C}_s^{(c)}\mathcal{C}_t^{(c)}, \tag{6.36}$$

where the spatial (s) factor is given by

$$\mathcal{C}_s^{(c)} = \frac{\max_{\boldsymbol{k}}[|\mathcal{T}_p(\boldsymbol{k})|^2] - \min_{\boldsymbol{k}}[|\mathcal{T}_p(\boldsymbol{k})|^2]}{\mathcal{T}_n^2(\mathbf{0})} \leq 1\,, \tag{6.37}$$

with equality if $T(\boldsymbol{\rho})$ is real, so that

$$\mathcal{C}^{(c)} = \mathcal{C}_t^{(c)} = \frac{\left[\left|\mathcal{F}^{-1}\{S^{(n)}(\Omega)\}\right|^2 \star h_B \star \overleftarrow{h_B}\right]_{t=0}}{\left(\int \mathrm{d}\Omega\, S^{(n)}(\Omega)/2\pi\right)^2}. \tag{6.38}$$

For analytical convenience, let us take the spectral part of the (phase-insensitive) auto-

correlation function to be Gaussian with e^{-2}-attenuation (baseband) bandwidth $2/T_0$,

$$S^{(n)}(\Omega) = \sqrt{2\pi T_0^2}\, e^{-T_0^2\Omega^2/2}\,, \tag{6.39}$$

and let us take the baseband impulse response $h_B(t)$ to be a Gaussian with e^{-2}-attenuation time duration T_d,

$$h_B(t) = e^{-8t^2/T_d^2}\sqrt{8/\pi T_d^2}. \tag{6.40}$$

With these assumptions, we find the classical contrast to be

$$\mathcal{C}^{(c)} = \frac{1}{\sqrt{1 + (T_d/2T_0)^2}}\,, \tag{6.41}$$

which is approximately unity for narrowband sources that satisfy $T_d \ll T_0$. On the other hand, in the broadband limit $T_d \gg T_0$, we have

$$\mathcal{C}^{(c)} \approx 2T_0/T_d \ll 1\,, \tag{6.42}$$

so the contrast is severely degraded.

Now consider a nonclassical Gaussian state with the maximum phase-sensitive cross-correlation. In the low-brightness regime, i.e., when $S^{(n)}(\Omega)\mathcal{G}_0^{(n)}(\boldsymbol{k}) \ll 1$, the maximum phase-sensitive cross-correlation spectrum is approximately

$$|S^{(p)}(\Omega)\mathcal{G}^{(p)}(\boldsymbol{k})| \approx \sqrt{S^{(n)}(\Omega)\mathcal{G}^{(n)}(\boldsymbol{k})}, \tag{6.43}$$

which is much higher, in this limit, than the classical maximum given by (6.35). Once again taking the phase of this correlation to be zero, the contrast is found to separate into the product of spatial and temporal terms, with $\mathcal{C}_s^{(q)} = \mathcal{C}_s^{(c)}$, and the temporal term given by

$$\mathcal{C}_t^{(q)} = \frac{\Big[\big|\mathcal{F}^{-1}\{\sqrt{S^{(n)}(\Omega)}\}\big|^2 \star h_B \star \overleftarrow{h_B}\Big]_{t=0}}{\mathcal{G}^{(n)}(\mathbf{0})\left(\int \mathrm{d}\Omega\, S^{(n)}(\Omega)/2\pi\right)^2}\,. \tag{6.44}$$

Once again using (6.39) for the fluorescence spectrum and (6.40) for the baseband current filter, we obtain

$$\mathcal{C}^{(q)} = 2/\mathcal{G}^{(n)}(\mathbf{0})S^{(n)}(0)\sqrt{1 + T_d^2/2T_0^2}\,. \tag{6.45}$$

Here, the narrowband contrast $\mathcal{C}^{(q)} = 2/\mathcal{G}^{(n)}(\mathbf{0})S^{(n)}(0)$ is very high because of the low-

brightness condition, and even for broadband fields the contrast,

$$\mathcal{C}^{(q)} = 2\sqrt{2}T_0/T_d\mathcal{G}^{(n)}(\mathbf{0})S^{(n)}(0)\,, \tag{6.46}$$

may be high. In particular, in the biphoton regime, wherein $\mathcal{G}^{(n)}(\mathbf{0})T_d \ll 1$ (low-brightness, as well as low-flux), very high contrast is predicted in this broadband limit,[5] which is in agreement with the background-free diffraction pattern reported in [8]. Therefore, low-brightness quantum Gaussian-state fields have a contrast advantage over classical phase-sensitive Gaussian-state fields (when the phase-sensitive cross-correlation is measured via a photocurrent correlation measurement), and the biphoton state yields images with negligible background even when it is a broadband state.

In summary, in this section we have studied a cornerstone proof-of-principle experiment for quantum optical lithography by applying Gaussian-state analysis and the coherence theory results from Section 6.1 (and from Chapter 3) to the propagation of (classical and quantum) phase-sensitive cross-correlation. This analysis has shown that the *only* performance difference between a biphoton-state source and a classical phase-sensitive Gaussian-state source is the contrast of the diffraction-pattern image. The resolution improvement seen with a biphoton source is entirely due to the diffraction properties of the phase-sensitive cross-correlation between the signal and reference photons, hence it is also achievable with a pair of classical Gaussian-state fields with phase-sensitive cross-correlation. However, low-brightness quantum sources achieve higher contrast than classical sources, which permits imaging with broader bandwidth quantum sources. Finally, the (broadband) biphoton state yields very high contrast images, which is the reason why biphoton-state quantum lithography experiments have yielded background-free diffraction-pattern images [8].

6.3 Broadband imaging with a lens

Let us now consider using an optical source with low spatial coherence and a thin lens to image a transmission mask placed at the source plane, as depicted in Figure 6-2. The

[5] Because pinhole detectors are utilized at the detection plane, the Fresnel number product between the source-plane pupil and the photodetector pupil is much less than unity, i.e., $D_f = (k_0 a_0^2/2L) \times (k_0 A/2\pi L) \ll 1$, so only a *single* spatial mode couples appreciably to the photodetectors at each $\boldsymbol{\rho}$ [57]. Hence, the low-flux condition stated here should be interpreted as low-flux per spatial-mode of the source. In particular, very high contrast is achieved even when multiple photon-pairs are generated at the source, as long as at most one photon-pair occupies each spatial mode.

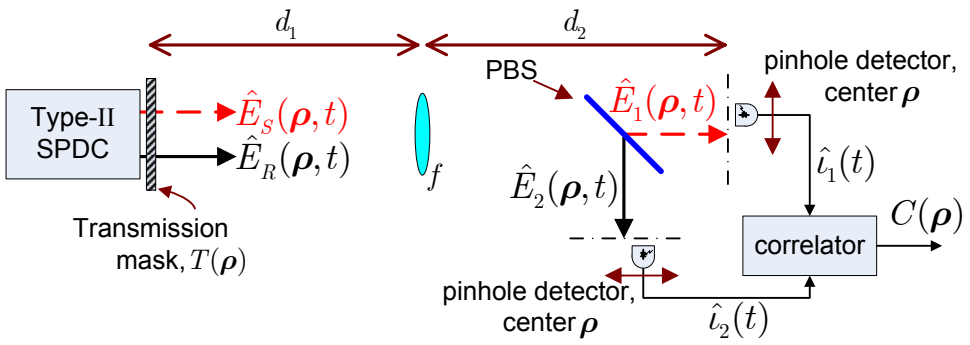

Figure 6-2: Near-field imaging of a transmission mask.

primary attention in our analysis of this experimental setup will be given to the resolution limitations imposed by the finite aperture of the lens, as previous work has claimed that a factor-or-two resolution improvement accrues when a biphoton source is employed [55].

We once again utilize the SPDC source, which generates zero-mean Gaussian-state signal and reference beams whose phase-insensitive correlation spectra at the exit plane of the transmission mask are given by (6.24) and whose phase-sensitive cross-correlation spectrum is given by (6.25). The optical fields first propagate through a d_1-m-long free-space path according to (6.3). A finite-aperture, focal-length-f lens is placed on this plane, which is assumed to have no chromatic dispersion over the frequency range of interest, i.e., each frequency component of the impinging field is multiplied by $\mathrm{circ}(|\boldsymbol{\rho}|/R)e^{-i\omega|\boldsymbol{\rho}|^2/2fc}$, where ω is a passband frequency centered around ω_0 and the circle function is

$$\mathrm{circ}(x) = \begin{cases} 1 & |x| \leq 1, \\ 0 & \text{otherwise.} \end{cases} \tag{6.47}$$

Finally the field at the exit plane of the lens propagates d_2 m in free space to reach the image plane of the lens defined by $d_1^{-1}+d_2^{-1} = f^{-1}$. The image-plane signal and reference fields are first split with a polarizing beam splitter, then each field is detected by a pinhole detector located at transverse coordinate $\boldsymbol{\rho}$ relative to its optical axis, after which the resulting photocurrents are correlated to obtain the same fourth-order field measurement given in (6.26) and (6.27) in terms of the detected fields $\hat{E}_1(\boldsymbol{\rho},t)$ and $\hat{E}_2(\boldsymbol{\rho},t)$.

The overall mapping from the source-plane optical field operators to the image-plane field operators is linear, and therefore the detected fields are in a zero-mean jointly-Gaussian

state. Combining this with the simplifying assumption that the detectors have electrical bandwidths much broader than the source spectra,[6] we can combine and reduce (6.26), (6.27) for the biphoton state to obtain

$$C(\boldsymbol{\rho}) \approx q^2\eta^2A^2\langle \hat{E}_1^\dagger(\boldsymbol{\rho},t)\hat{E}_2^\dagger(\boldsymbol{\rho},t)\hat{E}_1(\boldsymbol{\rho},t)\hat{E}_2(\boldsymbol{\rho},t)\rangle \tag{6.48}$$

$$= q^2\eta^2A^2\left[K_{1,1}^{(n)}(\boldsymbol{\rho},\boldsymbol{\rho},0)K_{2,2}^{(n)}(\boldsymbol{\rho},\boldsymbol{\rho},0) + |K_{1,2}^{(p)}(\boldsymbol{\rho},\boldsymbol{\rho},0)|^2\right], \tag{6.49}$$

where

$$K_{m,\ell}^{(n)}(\boldsymbol{\rho},\boldsymbol{\rho},\tau) \equiv \langle \hat{E}_m^\dagger(\boldsymbol{\rho},t)\hat{E}_\ell(\boldsymbol{\rho},t+\tau)\rangle, \tag{6.50}$$

$$K_{m,\ell}^{(p)}(\boldsymbol{\rho},\boldsymbol{\rho},\tau) \equiv \langle \hat{E}_m(\boldsymbol{\rho},t)\hat{E}_\ell(\boldsymbol{\rho},t+\tau)\rangle, \tag{6.51}$$

for $m,\ell = 1,2$, and (6.49) follows from the Gaussian moment-factoring theorem [14, 19]. Furthermore, as we have determined in the previous section, for maximally-entangled Gaussian states with low-brightness and low-flux, e.g., the biphoton state, the second term in (6.49) is much stronger than the first, permitting the approximation

$$C(\boldsymbol{\rho}) \approx q^2\eta^2A^2|K_{1,2}^{(p)}(\boldsymbol{\rho},\boldsymbol{\rho},0)|^2. \tag{6.52}$$

Therefore, for such states a photocurrent correlation measurement with broadband detectors is a means for measuring the magnitude-square of the phase-sensitive cross-correlation between the detected fields [19]. In this section we demonstrate that the interesting biphoton-state results predicted for this imaging configuration are a consequence of the phase-sensitive cross-correlation, and the photocurrent correlation does not play a role beyond facilitating its measurement. Hence, in the remainder of this section we shall bypass this photocurrent correlation measurement and focus directly on the phase-sensitive (and phase-insensitive) cross-correlation between the two fields at the detection planes.

The frequency-domain image-plane field operators, defined in (6.4), are given by a linear transformation of the frequency-domain source-plane field operators,

$$\hat{\mathcal{E}}_m(\boldsymbol{\rho},\Omega) = \int_{\mathbb{R}^2} \mathrm{d}\boldsymbol{\rho}'\, h(\boldsymbol{\rho},\boldsymbol{\rho}',\omega_0+\Omega)\hat{\mathcal{E}}_\ell(\boldsymbol{\rho}',\Omega) + \hat{\mathcal{L}}_m(\boldsymbol{\rho},\Omega), \tag{6.53}$$

[6] While this broadband detector assumption will certainly be valid for narrowband sources, it will almost surely fail in the very broadband sources to be considered later. Nevertheless, it is a convenient way to focus our attention on the essential physics, viz., imaging via $|K_{1,2}^{(p)}(\boldsymbol{\rho},\boldsymbol{\rho},0)|^2$ or $|K_{1,2}^{(n)}(\boldsymbol{\rho},\boldsymbol{\rho},0)|^2$.

for $(\ell, m) = (S, 1), (R, 2)$, where $\hat{\mathcal{L}}_m(\boldsymbol{\rho}, \Omega)$ is an auxiliary vacuum-state operator such that $\hat{E}_m(\boldsymbol{\rho}, t)$ satisfies the free-field commutators (6.1) and (6.2). The point-spread function $h(\boldsymbol{\rho}, \boldsymbol{\rho}', \omega)$, found from the Huygens-Fresnel principle and the lens transfer function, is given by

$$h(\boldsymbol{\rho}, \boldsymbol{\rho}', \omega) = \mathcal{H}\big(r(\boldsymbol{\rho}, \boldsymbol{\rho}'), \omega/\omega_0\big) e^{i\phi(\boldsymbol{\rho}, \boldsymbol{\rho}', \omega)}, \tag{6.54}$$

where

$$r(\boldsymbol{\rho}, \boldsymbol{\rho}') \equiv \frac{\omega_0 R}{d_1 c} |d_1 \boldsymbol{\rho}/d_2 + \boldsymbol{\rho}'| \,, \tag{6.55}$$

and

$$\mathcal{H}(r, \xi) \equiv \frac{-\omega_0^2 R^2 \xi^2}{4\pi c^2 d_1 d_2} \frac{2J_1(r\xi)}{r\xi} \,, \tag{6.56}$$

is the real amplitude of the point-spread function. Here $2J_1(x)/x$ for $x \geq 0$ is the well-known Airy function, and the phase term in (6.54) is given by

$$\phi(\boldsymbol{\rho}, \boldsymbol{\rho}', \omega) = \omega \left(d_1 + d_2 + |\boldsymbol{\rho}|^2/2d_2 + |\boldsymbol{\rho}'|^2/2d_1\right)/c, \tag{6.57}$$

which incorporates the group delay arising from the $(d_1 + d_2)$-m propagation, and the parabolic phases at the source and image planes arising from diffraction.

Because our focus in this section is on the resolution limitation imposed by the finite lens aperture rather than the source, we further simplify our analysis by assuming spatially-incoherent source statistics and appropriate focusing at the source plane to compensate for the parabolic phase in (6.57). These assumptions simplify the phase-insensitive auto-correlation functions and the phase-sensitive cross-correlation function of the I_0 photons/m^{2}s signal and reference fields—given in (6.14) and (6.15)—to

$$S_0^{(n)}(\boldsymbol{\rho}_1, \boldsymbol{\rho}_2, \Omega) = |T(\boldsymbol{\rho}_1)|^2 I_0 \big[2\pi c/(\omega_0 + \Omega)\big]^2 \delta(\boldsymbol{\rho}_2 - \boldsymbol{\rho}_1)\, S^{(n)}(\Omega) \tag{6.58}$$

and

$$S_0^{(p)}(\boldsymbol{\rho}_1, \boldsymbol{\rho}_2, \Omega) = e^{-i\frac{\omega_0}{cd_1}|\boldsymbol{\rho}_1|^2}\, T^2(\boldsymbol{\rho}_1) I_0 \big[(2\pi c)^2/(\omega_0^2 - \Omega^2)\big] \delta(\boldsymbol{\rho}_2 - \boldsymbol{\rho}_1)\, S^{(p)}(\Omega) \,, \tag{6.59}$$

respectively, where we have chosen $S^{(x)}(\Omega)/2\pi$, for $x = n, p$, to have unity area with no loss of generality.[7] Evaluating the phase-insensitive auto-correlations and the phase-sensitive

[7]The square-bracketed terms in (6.58) and (6.59) account for the fact that the coherence area in a

cross-correlation of the two detected fields at equal spatial coordinates (relative to their optical axes) and at equal time, yields

$$K^{(n)}_{m,m}(\boldsymbol{\rho},\boldsymbol{\rho},0) = \int_{\mathbb{R}^2} \mathrm{d}\boldsymbol{\rho}'\, |T(\boldsymbol{\rho}')|^2 g_n\big(r(\boldsymbol{\rho},\boldsymbol{\rho}')\big)\,, \tag{6.60}$$

for $m = 1, 2$, and

$$K^{(p)}_{1,2}(\boldsymbol{\rho},\boldsymbol{\rho},0) = e^{i\frac{\omega_0}{c}(2d_1+2d_2+|\boldsymbol{\rho}|^2/d_2)} \int_{\mathbb{R}^2} \mathrm{d}\boldsymbol{\rho}'\, T^2(\boldsymbol{\rho}') g_p\big(r(\boldsymbol{\rho},\boldsymbol{\rho}')\big)\,, \tag{6.61}$$

where $r(\boldsymbol{\rho},\boldsymbol{\rho}')$ is defined in (6.55). Here the point-spread function in the superposition integral with $|T(\boldsymbol{\rho})|^2$ is

$$g_n(r) \equiv \frac{I_0(2\pi c)^2}{\omega_0^2} \int_{-\omega_0}^{\infty} \frac{\mathrm{d}\Omega}{2\pi} S^{(n)}(\Omega)\, |\mathcal{H}(r, 1+\Omega/\omega_0)|^2/(1+\Omega/\omega_0)^2\,, \tag{6.62}$$

which yields the phase-insensitive auto-correlation functions. Likewise, the point-spread function in the superposition integral with $T^2(\boldsymbol{\rho})$ is[8]

$$g_p(r) \equiv \frac{I_0(2\pi c)^2}{\omega_0^2} \int_{-\omega_0}^{\omega_0} \frac{\mathrm{d}\Omega}{2\pi} S^{(p)}(\Omega)\, \mathcal{H}(r, 1+\Omega/\omega_0)\mathcal{H}(r, 1-\Omega/\omega_0)/(1-\Omega^2/\omega_0^2)\,, \tag{6.63}$$

which yields the phase-sensitive cross-correlation function. Therefore, the most important difference between phase-insensitive and phase-sensitive coherence propagation, apart from an unimportant parabolic phase factor, is the frequency coupling in (6.63) between $\pm\Omega/\omega_0$, which is absent in (6.62). However, in the quasimonochromatic limit this coupling becomes insignificant, because

$$1 \pm \Omega/\omega_0 \approx 1\,, \tag{6.64}$$

so that $g_n(r) = g_p(r)$ prevails whenever $S^{(n)}(\Omega) = S^{(p)}(\Omega)$. Thus the quasimonochromatic point-spread function for the phase-insensitive correlation is identical to the phase-sensitive one.

---

broadband pulse is wavelength dependent. Furthermore, the factor in the phase-insensitive spectrum depends only on the wavelength at detuning Ω, because it represents the phase-insensitive auto-correlation of each frequency, but the factor in the phase-sensitive spectrum is the geometric mean of the wavelengths at $\pm\Omega$-detuning, because it represents the phase-sensitive *cross-correlation* between these frequencies.

[8]Note that the integral in (6.63) cannot have an upper limit greater than ω_0. $S_0^{(p)}(\Omega)$ for a complex stationary field is the strength of the cross-correlation between the $\pm\Omega$ frequency components of two baseband field operators. Because the passband field *must* be positive frequency, the lower limit on the baseband frequencies is $-\omega_0$, hence for all (baseband) frequencies greater than ω_0, $S_0^{(p)}(\Omega) = 0$. This is true for all (complex-stationary) phase-sensitive auto- and cross-correlation spectra alike.

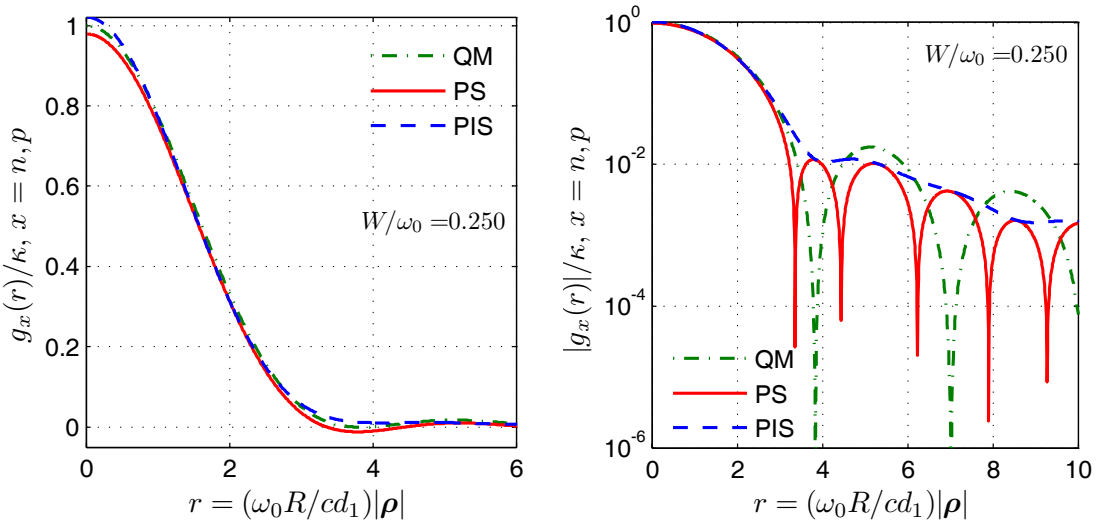

(a) Main-lobe behavior.

(b) Tail behaivor (log scale).

Figure 6-3: Comparison of the imaging point-spread functions for phase-insensitive (PIS) and phase-sensitive (PS) correlations when $W/\omega_0 = 0.25$, and when the imaging source is quasimonochromatic (QM). The normalizing coefficient is $\kappa \equiv I_0\omega_0^2 R^4/4c^2 d_1^2 d_2^2$.

However, $g_n(r)$ and $g_p(r)$ begin to differ as the bandwidth of the source increases. Suppose that the phase-insensitive and phase-sensitive source spectra are both taken to be flat over the bandwidth window $W > 0$, i.e.,

$$S^{(n)}(\Omega) = S^{(p)}(\Omega) = \begin{cases} \pi/W & |\Omega| < W \\ 0 & \text{otherwise.} \end{cases} \tag{6.65}$$

Substituting this expression into (6.62) and (6.63), the point-spread functions can be expressed as dimensionless integrals,

$$g_n(r) = \frac{I_0\omega_0^2 R^4}{2c^2 d_1^2 d_2^2 (W/\omega_0)} \int_{-W/\omega_0}^{W/\omega_0} \mathrm{d}u \, \frac{J_1^2\big(r(1+u)\big)}{r^2}\,, \tag{6.66}$$

and

$$g_p(r) = \frac{I_0\omega_0^2 R^4}{2c^2 d_1^2 d_2^2 (W/\omega_0)} \int_{-W/\omega_0}^{W/\omega_0} \mathrm{d}u \, \frac{J_1\big(r(1+u)\big)}{r} \frac{J_1\big(r(1-u)\big)}{r}\,. \tag{6.67}$$

As we have ascertained above, in the quasimonochromatic limit where $W/\omega_0 \ll 1$ holds, both point-spread functions simplify to

$$g_n(r) = g_p(r) = \frac{I_0\omega_0^2 R^4}{4c^2 d_1^2 d_2^2} \Big(\frac{2J_1(r)}{r}\Big)^2\,. \tag{6.68}$$

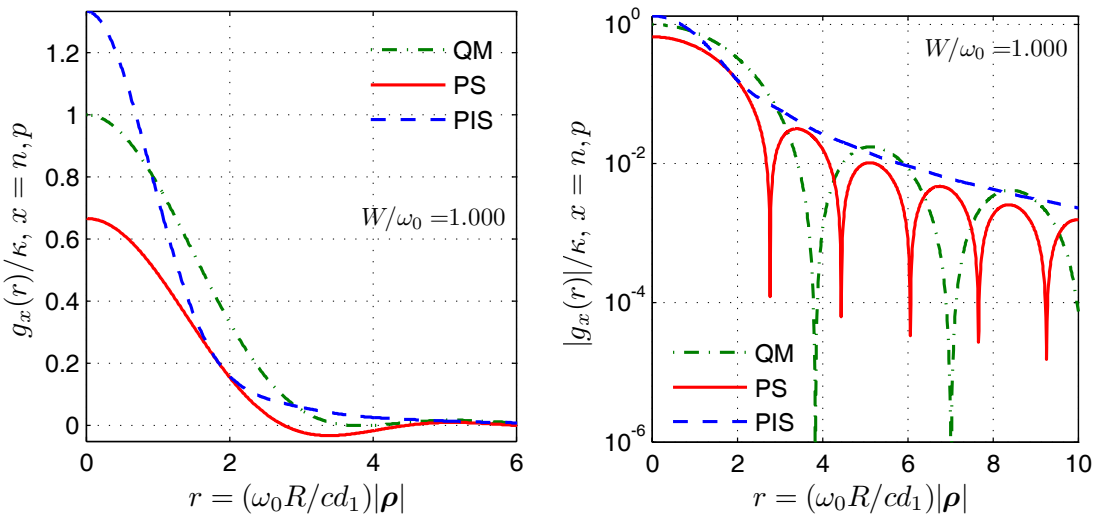

(a) Main-lobe behavior.

(b) Tail behaivor (log scale).

Figure 6-4: Comparison of the imaging point-spread functions for phase-insensitive (PIS) and phase-sensitive (PS) correlations in the asymptotic broadband limit ($W/\omega_0 = 1$), and the quasimonochromatic (QM) limit. The normalizing coefficient is $\kappa \equiv I_0\omega_0^2 R^4/4c^2 d_1^2 d_2^2$.

Hence with a quasimonochromatic source there is no difference between the image of a real-valued transmission mask acquired with phase-insensitive (thermal) illumination or phase-sensitive (classical or quantum) illumination.

The point-spread functions for broader bandwidth sources are plotted in Figure 6-3 and Figure 6-4 at two different W values. The $W = \omega_0/4$ case, shown in the former figure, represents an unusually broadband field state for parametric downconversion [58], and the unrealistic asymptotic limit $W = \omega_0$ is plotted in the latter figure as purely academic visual-aid for the subsequent discussion of broadband pulse propagation. The point-spread functions in these figures confirm that the peak amplitude of the phase-insensitive function increases to

$$g^{(n)}(0) = \frac{I_0\omega_0^2 R^4}{4c^2 d_1^2 d_2^2}\left(1 + \frac{W^2}{3\omega_0^2}\right), \tag{6.69}$$

whereas that of the phase-sensitive point-spread function attenuates to

$$g^{(p)}(0) = \frac{I_0\omega_0^2 R^4}{4c^2 d_1^2 d_2^2}\left(1 - \frac{W^2}{3\omega_0^2}\right), \tag{6.70}$$

relative to the peak amplitude in the quasimonochromatic limit. The $(1+u)^2$ factor multiplying the frequency-resolved Airy patterns in (6.66), where $|u| < W/\omega_0 \leq 1$, is responsible

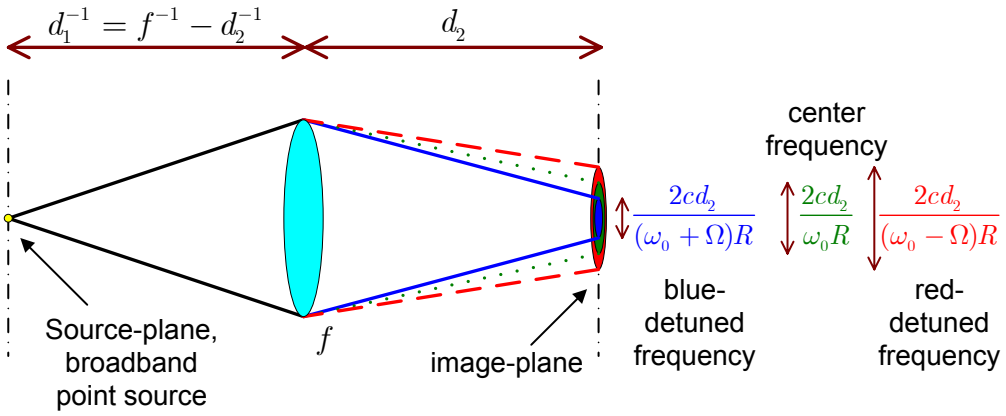

Figure 6-5: Image-plane spot diameters for different frequency components of a broadband point source.

for the increase in $g^{(n)}(0)$. This scaling favors the *positively*-detuned frequency contributions to the phase-insensitive point-spread function, and because of the quadratic scaling the average of the amplification for $u > 0$ and the attenuation for $u < 0$ is greater than one. Thus, the peak value increases with increasing bandwidth. On the other hand, the scaling for the frequency-resolved Airy patterns in the integrand of (6.67) is $(1-u)(1+u) = 1-u^2$, so *all* detuned frequencies are attenuated, which results in a smaller peak for the broadband phase-sensitive point-spread function.

The figures indicate narrowing of the main lobe in the broadband phase-sensitive case. The phase-insensitive point-spread function also has some narrowing, but it is hampered by a slowly-decaying tail. From a practical perspective this behavior is of little interest, because the curves plotted for $W = \omega_0/4$ show that the resolution benefit offered by the narrowing in the phase-sensitive point-spread function is merely a factor of 1.14, which we have taken to be the ratio of the first zero locations in the two functions. In addition, the tail of the phase-insensitive point-spread function traces the envelope of the oscillations in the phase-sensitive point-spread function, so no appreciable loss of resolution results from the slowly-decaying tail. Even in the $W = \omega_0$ asymptotic limit, the the resolution improvement of the broadband phase-sensitive point-spread function is only a factor of 1.38. In this limit, the tail of the broadband phase-insensitive point-spread function decays slower than the other cases, but the main lobe is tightly confined, yielding a e^{-2}-attenuation pulsewidth that is half of the first zero in the quasimonochromatic limit, so resolution degradation is not prominent.

Nonetheless, the difference between the behavior of the phase-insensitive and phase-sensitive point-spread functions as a function of the source bandwidth deserves closer examination to understand the underlying physics. First, recall that a source generating a complex-stationary baseband field around a center frequency ω_0 is a superposition of monochromatic field components which have phase-insensitive auto-correlations at each frequency and phase-sensitive cross-correlations between frequencies that sum to $2\omega_0$. Thus, the phase-insensitive correlation, measured at a given spatiotemporal coordinate $(\boldsymbol{\rho}, t)$, is a superposition of all the different auto-correlations at detuning frequencies Ω over the bandwidth of the source. On the other hand, the phase-sensitive correlation measured at $(\boldsymbol{\rho}, t)$ is a superposition of all the *cross-correlations* between frequency components detuned by $\pm\Omega$, over the (phase-sensitive) bandwidth of the source. Now, consider a point source at the source-plane, emitting signal and reference fields that have nonzero phase-insensitive auto-correlation and phase-sensitive cross-correlation. Due to (6.53), the frequency component—in either of the two fields—at $\omega = \omega_0 + \Omega$ will yield a spot on the image plane with radius $cd_2/(\omega_0+\Omega)R$. Thus, as shown in Figure 6-5, the lower frequency components yield broader spots on the image plane than the higher frequency components. If we are measuring the phase-insensitive auto-correlation (of either of the two fields) by scanning a point detector on the transverse plane, it decays slowly as $|\boldsymbol{\rho}|$ increases because of the large spots from the lower frequencies. However, this slowly-decaying tail does not cause a significant increase in the point-spread function width, because the weighting coefficient in (6.66) (the same coefficient that yields higher peak amplitude) amplifies positively-detuned frequencies and attenuates those that are negatively detuned. On the other hand, if we are measuring the phase-sensitive cross-correlation between the signal and reference fields,[9] we are in effect measuring the superposition of the cross-correlations between the $\omega_0 + \Omega$ signal-field component, and the $\omega_0 - \Omega$ reference-field component, where $\Omega \in [-\omega_0, \omega_0]$. For $\Omega > 0$, the former yields a narrow spot of radius $cd_2/(\omega_0 + \Omega)R$, and the latter yields a broad spot of radius $cd_2/(\omega_0 - \Omega)R$. Because the phase-sensitive cross-correlation is given by their product, however, the narrower radius from the higher frequency determines the radius within which there is appreciable phase-sensitive coherence. Furthermore, this coherence radius is symmetric in Ω, so, as the (phase-sensitive) bandwidth of the source increases, the width of the image-plane phase-sensitive point-spread function decreases. However, the leading

[9]The arguments apply to auto-correlations as well as cross-correlations, with no loss of generality.

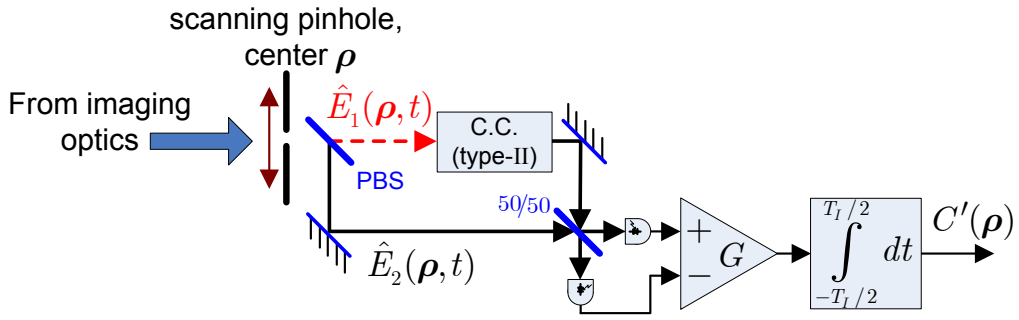

Figure 6-6: Detecting the image-plane phase-sensitive cross-correlation via optical phase-conjugation.

multiplication factor $1-u^2$ in (6.67) counteracts this advantage by attenuating the higher frequency contributions, such that the net reduction in the main lobe width is very small.

Notice that we have made no reference to the classical or quantum nature of the source in explaining the physics governing the point-spread functions' width. Thus, this effect is entirely a consequence of phase-sensitive versus phase-insensitive source correlations and scalar paraxial diffraction theory, which are valid in both classical and quantum theories of light. The quantum nature of the fields, therefore, does not play a role in determining the resolution capabilities of thin-lens correlation imaging, regardless of whether the source has phase-sensitive or phase-insensitive coherence. However, nonclassical field states may offer contrast advantages akin to that observed in the previous section, for particular measurement schemes, such as photocurrent correlation (coincidence counting). In particular, in this section we have determined that the phase-sensitive correlation differs from its phase-insensitive counterpart only in the broadband limit. Thus, if we opt to utilize a photocurrent correlation measurement, then the contrast will be significantly better when the broadband fields' state is maximally-entangled (nonclassical) and has low-brightness, which encompasses the biphoton state. Nonetheless, it is worth stating briefly that alternative schemes to measure phase-sensitive correlations can be devised. For example, with a sufficiently broadband phase-conjugator, the detection scheme in Figure 6-6 is also feasible for measuring the phase-sensitive cross-correlation between *classical* signal and reference field states (cf. the PC-OCT discussion in Chapter 4). In this figure, the signal field is first optically phase-conjugated, then the phase-insensitive cross-correlation between the conjugated-signal and reference is measured in a Michelson interferometer with equal delay in both arms. In such a scheme, the T-second averaged photocurrent will have an ensemble

average [21]

$$\langle C'(\boldsymbol{\rho})\rangle = 2q\eta AG\,\Re\big\{K_{1,2}^{(p)}(\boldsymbol{\rho},\boldsymbol{\rho},0)\big\}\,. \tag{6.71}$$

It is worth emphasizing that optical phase-conjugation is subject to quantum noise, which is approximately one-photon-per spatiotemporal mode (assuming unity conjugator gain) [21], i.e., the noise power is proportional to the bandwidth of the conjugator. Therefore, the signal-to-noise ratio is in general dominated by the shot-noise contribution of this spontaneous emission (quantum noise), which must be mitigated via time-averaging (cf. the signal-to-noise ratio (SNR) discussion for PC-OCT in Chapter 4 and the white-light interferometry SNR in Chapter 8).

6.4 Discussion

SPDC with vacuum-state inputs generates signal and reference fields in a zero-mean jointly-Gaussian state, with nonzero phase-insensitive auto-correlations and a phase-sensitive cross-correlation that fully determine their joint state. When the output state is driven to the low-brightness, low-flux limit, this Gaussian state becomes equivalent to a dominant vacuum state plus a weak biphoton contribution, where the biphoton wavefunction equals the phase-sensitive cross-correlation between the signal and reference fields. On the other hand, classical imagers have traditionally utilized optical sources in thermal states or coherent states, both of which are Gaussian states but have only nonzero phase-insensitive (auto- and cross-) correlations. Hence, quantum imaging experiments that rely on biphoton sources, as well as conventional classical imaging configurations, can be unified and generalized by studying the imaging characteristics of Gaussian-state sources. Furthermore, such states are fully characterized by their first and second moments, and are closed under linear transformations on the field operators. So, imaging configurations utilizing Gaussian-state sources, linear optical elements and free-space propagation, can be fully understood in both the classical and quantum regimes by tracking the evolution of the first and second moments of the fields, from the source plane to the detection planes.

A particularly relevant distinction that has been overlooked thus far is the phase-sensitive nature of the correlation between the two photons in a biphoton state, as opposed to the phase-insensitive correlation that is present between thermal-state fields. Phase-sensitive coherence has different propagation characteristics than phase-insensitive coher-

ence. Furthermore, complex-stationary phase-sensitive correlations have cross-frequency couplings that are not present in complex-stationary phase-insensitive correlations. Distinctions such as these often underlie the interesting observations and theoretical predictions in quantum imaging. However, phase-sensitive coherence is not exclusive to nonclassical states (such as the biphoton). Classical Gaussian states (random mixtures of coherent states) may very well have nonzero phase-sensitive (auto- and cross-) correlations, and those features in quantum imaging that stem from the phase-sensitive coherence between the two photons in a biphoton state can be replicated with classical phase-sensitive sources, as we have demonstrated for optical coherence tomography and ghost imaging in previous chapters [21, 23].

In this chapter we have continued our quest to ascertain and distinguish the truly quantum phenomena in quantum imaging theory and experiments, and the phase-sensitive coherence phenomena that can be exploited both in the classical and quantum regimes. To this end, we have performed Gaussian-state analysis of two significant experimental configurations in quantum imaging which use biphoton sources. In Section 6.2 we showed that the factor-of-two spatial compression in the far-field diffraction fringes of a transmission mask placed at the source plane is precisely due to the phase-sensitive cross-correlation between the signal and reference fields, in *both* the classical and quantum regimes. In particular, the only significant difference—insofar as this experiment is concerned—between phase-sensitive classical and quantum sources is the fringe contrast when photocurrent correlation measurements are employed. Narrowband classical Gaussian states can achieve acceptable contrast, but the contrast degrades severely when the source is broadband. On the other hand, with low-brightness quantum Gaussian states that are maximally-entangled, the contrast is high for both narrowband and broadband sources. Note that the strength of the background in the signature may be a relevant factor in determining whether a classical or quantum source is more desirable for a particular application. For example, in the previous chapter, we determined that biphoton-state ghost imaging contrast suffers dramatically in daytime operation, due to scattered background light collected by the bucket detector in the reference arm. On the other hand, in photolithographic imaging, in which extraneous noise may be eliminated by virtue of operation in a controlled environment, a biphoton-state source in combination with a two-photon absorber at the detection plane generates an optical image with no background, whereas a classical phase-sensitive source yields sig-

nificant background that requires postdetection processing prior to etching. Hence the contrast advantage offered by the biphoton state—which cannot be replicated by classical phase-sensitive light—is a desirable feature in this case.

In Section 6.3 we compared thin-lens imaging of a source plane transmission mask using incoherent phase-insensitive light to the same imaging arrangement using phase-sensitive light. When the sources are narrowband (quasimonochromatic), the point-spread functions of the two cases turn out to be identical, yielding no resolution difference between the various source possibilities. As the source bandwidth increases, the point-spread functions for the phase-insensitive and phase-sensitive correlation functions become narrower, but the phase-insensitive point-spread function develops a slowly-decaying tail. The differences between the two cases stem from complex-stationary source statistics, and frequency-dependent free-space diffraction. Once again, the biphoton state facilitates a high-contrast image and a convenient measurement apparatus (coincidence counting) for detecting phase-sensitive correlation, but it is not responsible for the physics governing the changes to the point-spread functions.

Although in Section 6.2 we have focused on a proof-of-principle experiment for quantum lithography with a biphoton source, the driving motivation for quantum optical lithography is a the N-fold ($N \in \mathbb{Z}^+$) improvement in etching resolution predicted for $N00N$-state signal and reference fields (a $N00N$ state is an equal-weight superposition of two pure states: N-photon signal field and vacuum-state reference, plus vacuum-state signal and N-photon reference field) [7]. These states are highly nonclassical (their P-representation in terms of coherent states is not a proper probability density function) and unfortunately generating $N00N$ states for $N > 2$ has proven challenging (the $N = 2$ case can be achieved with biphoton states, viz., the output of a 50/50 beam splitter when the two inputs are the signal and reference fields from SPDC operating in the low-brightness, low-flux regime). Thus far, the interference fringes for $N = 3$ and $N = 4$ have been demonstrated in proof-of-principle experiments [59, 60], showing a factor of 3 and 4 fringe compression respectively, and efforts continue to generate higher orders. $N00N$ states with $N > 2$ are no longer Gaussian states or any limiting form of Gaussian states, because their second-order moments do not determine the state. Therefore, the Gaussian-state analysis presented in this chapter does not generalize to $N > 2$ $N00N$ states. Nonetheless, to better appreciate the fundamental physics that leads to improved resolution with these sources, it is of great interest to extend

a unifying coherence theory to higher-order moments of continuous field operators, and perform an analysis for these moments to determine whether the advantages observed with these states are truly due to their nonclassical nature or due to a measurement of a $2N$th-order moment of the field operator.

The analysis presented in Sections 6.2 and 6.3 reveal that the physics governing the resolution improvement in these two experiments are *different*. In particular, the improvement in resolution that is observed in the Fourier-plane measurement is due to the difference in paraxial propagation of phase-sensitive and phase-insensitive correlations, and is valid in the quasimonochromatic regime as well as the broadband regime. Furthermore, to observe this effect with classical fields, it is preferable to utilize narrowband sources. On the other hand, the marginal improvement in resolution observed in Section 6.3 is a *strictly* broadband effect that manifests itself in complex-stationary phase-sensitive (and phase-insensitive) correlation functions. The two experiments capitalize on different properties of phase-sensitive coherence and therefore they are not experiments demonstrating equivalent physical principles [55].

In summary, we have presented a unified Gaussian-state analysis of two transverse imaging configurations, one that images the far-field diffraction fringe of a source-plane transmission mask, and one that measures the near-field image with a lens. We have shown that the far-field diffraction fringes obtained with classical phase-sensitive Gaussian-state light and nonclassical Gaussian-state light with low-brightness—such as the biphoton—differ only in contrast, viz., the fringe compression is a classical phenomenon owing to the far-field diffraction of phase-sensitive coherence. In the second experiment, we have demonstrated that the cross-frequency coupling in complex-stationary and broadband phase-sensitive light—whether classical or quantum—leads to a slightly narrower point-spread function than that obtained with quasimonochromatic phase-sensitive or phase-insensitive light. However, because of the enormous bandwidth that is necessary to observe any appreciable change in the point-spread functions, contrary to what is stated in [55], there is no practical advantage that is gained from this image acquisition configuration, beyond what is offered by quasimonochromatic phase-sensitive or phase-insensitive light.

Chapter 7

Gaussian-State Theory of Pulsed Parametric Downconversion

The previous chapters of this thesis focused on optical field states with complex-stationary second-order correlations. In other words, the phase-insensitive and phase-sensitive correlation functions are invariant to translations of the time origin. Chapter 3 showed that complex-stationary phase-sensitive coherence implies nonzero phase-sensitive correlations between all frequency pairs whose average equals the center frequency, an example of which is the phase-sensitive coherence between the signal and idler outputs from continuous-wave, spontaneous parametric downconversion [18, 52]. Furthermore, Chapter 4 analyzed an imaging configuration, namely optical coherence tomography, which utilizes the complex-stationary phase-sensitive cross-correlation between signal and reference source fields.

If we relax our assumption of complex-stationary correlations, a broader suite of phase-sensitive frequency correlations are permissible. In this chapter and the next, we shall analyze field states that have no correlation between distinct frequencies, but each frequency component has both phase-sensitive and phase-insensitive auto-correlations. Fourier transform duality then implies that such field states yield nonzero phase-sensitive correlation between all time index pairs whose average equals some center time reference. In this regard, this state is the frequency-dual to a phase-sensitive complex-stationary state.

As a prelude to considering imaging applications of a source with these statistics, it is appropriate to first analyze a physical process that is capable of generating optical fields with the desired correlation behavior. In this chapter we consider pulsed parametric down-

conversion in a collinear geometry, having mismatched group velocities such that the pump group velocity is between those of the signal and the idler,[1] and utilizing a pump pulsewidth (in space) that is much shorter than the length of the nonlinear medium (often a crystal). It is worth pointing out that this regime of parametric downconversion has been studied previously in considerable detail. An input/output relation has been obtained in [61], demonstrating that it can be utilized to spectrally-conjugate an optical pulse while spectrally compressing or stretching it. However, the derivations neglect the frequency response—therefore the finite bandwidth—of the interaction. In addition, the boundary effects due to the finite length of the crystal are not considered. Other prior work demonstrates both theoretically [62, 63] and experimentally [64] that this process generates coincident-frequency entangled photon-pairs over a broad bandwidth when the strong pump pulse interacts with the vacuum fluctuations in the crystal. However, these analyses are limited to the biphoton regime of the output fields, thus they do not generalize to arbitrary photon fluxes.

Our aim in this chapter is to derive an input/output description for this parametric downconversion process that not only encompasses prior work, but also remedies some of the limitations identified above. The chapter is organized as follows. In Section 7.1 we review classical optical pulse propagation in nonlinear media and derive the truncated coupled-mode equations for pulsed downconversion. Next, in Section 7.2, we solve these *classical* coupled-mode equations to obtain the signal and idler fields at the output facet of a finite-length crystal in terms of the fields at its input facet, assuming a nondepleting, short-duration, flat-top pump pulse. Although such pump pulses are experimentally unrealistic, this assumption simplifies the solution while preserving the most relevant parameters of the pump pulse, namely its intensity and duration. In Section 7.3, we transition from the classical solutions to a quantum operator-valued input/output description of the process, in which the strong pump field remains classical and only the signal and idler fields are quantized. In Section 7.4, we focus on long crystals, and simplify the input/output map to describe the fields that emerge from the crystal having interacted with the full longitudinal extent of the pump pulse. In the remainder of the chapter we utilize this simplified input/output map and revisit relevant applications of the downversion process. In particular, Section 7.5 discusses the frequency response and the bandwidth of spectral-conjugation, in

[1] In this chapter we shall revert to conventional terminology for the output fields from SPDC, i.e., we will call them signal and idler instead of signal and reference.

addition to the limitations on frequency-scaling of the baseband field envelopes. In Section 7.6, we take signal and idler input fields in their vacuum states, and fully characterize the jointly-Gaussian state of the resulting signal and idler output fields. In addition, we take the low-brightness, low-flux limit of this Gaussian state to derive the biphoton wavefunction and verify that it is in agreement with the prior biphoton-state analyses. We conclude in Section 7.7, where we summarize our accomplishments in this chapter and discuss some of the key conclusions.

7.1 Preliminaries

Let us begin with a review of optical pulse propagation in a nonlinear medium. Let $\vec{x}E(z,t)e^{ik_0 z - i\omega_0 t}$ denote a $+z$-propagating, finite-duration plane wave, with center frequency ω_0, center wave number k_0, and uniform linear polarization $\vec{x}$ chosen orthogonal to $\vec{z}$. Maxwell's equations require that the frequency components comprising the baseband envelope of this pulse satisfy the scalar wave equation [53, 65]

$$\left(\frac{\partial^2}{\partial z^2} + k^2(\omega_0+\Omega)\right)\left[E(z,\Omega)e^{ik_0 z}\right] = -\mu_0\,(\omega_0+\Omega)^2 P_{NL}(z,\omega_0+\Omega)\,, \tag{7.1}$$

for $\Omega \in [-\omega_0, \infty)$, where $E(z,\Omega) \equiv \int \mathrm{d}t\, e^{i\Omega t}E(z,t)$ represents the field component that is Ω-detuned from the center frequency,[2] and $k(\omega) \equiv \omega n(\omega)/c$ is the dispersion relation for the medium along the polarization vector of the field, which is expressed in terms of the refractive index $n(\omega)$ and the speed of light in vacuum, c.[3] On the right-hand side of the equation, μ_0 denotes the magnetic permeability of vacuum and $P_{NL}(z,\omega)$ denotes the frequency-ω and $\vec{x}$-polarized component of the induced material polarization with a nonlinear dependence on the field. This term is zero in linear media, but in nonlinear media it drives the scalar wave equation by coupling different frequencies in $E(z,\Omega)$.

Assuming that $E(z,\Omega)$ is a slowly-varying function of z, such that its second-order z-derivative is small, i.e., $|\partial^2 E(z,\Omega)/\partial z^2| \ll 2k_0|\partial E(z,\Omega)/\partial z|$, the second-order z-derivative

[2] To simplify notation we opt to distinguish the freqency-domain fields from their time-domain counterparts via the units of their second argument.

[3] Many nonlinear media are birefringent. To avoid introducing cumbersome vector notation, here we have assumed that either the extraordinary or the ordinary axis of the birefringent nonlinear medium is aligned with $\vec{x}$, and $n(\omega)$ denotes the refractive index for the corresponding axis.

in (7.1) can be simplified to yield

$$\left(i2k_0\frac{\partial}{\partial z}+k^2(\omega_0+\Omega)-k_0^2\right)E(z,\Omega)=-\mu_0\,(\omega_0+\Omega)^2e^{-ik_0z}P_{NL}(z,\omega_0+\Omega). \tag{7.2}$$

Furthermore, when $k(\omega_0+\Omega)$ has a convergent Taylor series over the entire bandwidth of the pulse, we obtain an infinite series equivalence,

$$k^2(\omega_0+\Omega)-k_0^2=\sum_{n=1}^{\infty}\alpha_n\Omega^n, \tag{7.3}$$

with

$$\alpha_n=\sum_{m=0}^{n}\frac{k_0^{(m)}k_0^{(n-m)}}{m!(n-m)!}\,, \tag{7.4}$$

and $k_0^{(n)}\equiv\partial^n k(\omega)/\partial\omega^n|_{\omega_0}$. Substituting (7.3) into (7.2) and inverse Fourier transforming the resulting expression yields the scalar wave equation governing pulse propagation in a broad class of nonlinear media,

$$\left(i2k_0\frac{\partial}{\partial z}+\sum_{n=1}^{\infty}i^n\alpha_n\left(\frac{\partial^n}{\partial t^n}\right)\right)E(z,t)=\mu_0e^{-ik_0z+i\omega_0t}\frac{\partial^2}{\partial t^2}P_{NL}(z,t)\,. \tag{7.5}$$

If the frequency dependence of $n(\omega)$, i.e., the dispersion, is negligible over the pulse bandwidth, we can truncate the infinite series in (7.5) after the first term, yielding the truncated wave equation

$$\left(\frac{\partial}{\partial z}+\frac{1}{v}\frac{\partial}{\partial t}\right)E(z,t)=\frac{-i}{2c\epsilon_0\omega_0n(\omega_0)}e^{-ik_0z+i\omega_0t}\,\frac{\partial^2}{\partial t^2}P_{NL}(z,t)\,, \tag{7.6}$$

where $v\equiv 1/k_0^{(1)}$ is the group velocity of the field in the medium and ϵ_0 is the dielectric permittivity of vacuum. We use this truncated form of the wave equation in subsequent analysis and find that a wealth of insight can be gained even from this simple first-order approximation.

Consider pulsed parametric downconversion in a second-order ($\chi^{(2)}$) nonlinear and birefringent crystal, whose input surface is placed on the $z=0$ plane and whose output plane is $z=L$. With no loss of generality, we denote the two fundamental axes of the crystal with $\vec{x}$ and $\vec{y}$. Collinear parametric downconversion relies on the interaction of three z-propagating optical pulses inside the crystal: an $\vec{x}$-polarized, high-intensity pump pulse

with center frequency ω_P, and weaker signal and idler pulses whose center frequencies, ω_S and ω_I respectively, satisfy $\omega_P = \omega_S + \omega_I$. The linear polarizations of the signal and idler fields, denoted by $\vec{x}_S$ and $\vec{x}_I$, are copolarized—and orthogonal to the pump—in Type-I systems ($\vec{x}_S = \vec{x}_I = \vec{y}$), and are orthogonal in Type-II systems, ($\vec{x}_S \perp \vec{x}_I$) [66]. Therefore, the total *positive-frequency* field inside the crystal is given by

$$\vec{\mathcal{E}}(z,t) = \vec{x}_S E_S(z,t) e^{ik_S z - i\omega_S t} + \vec{x}_I E_I(z,t) e^{ik_I z - i\omega_I t} + \vec{x} E_P(z,t) e^{ik_P z - i\omega_P t}\,, \tag{7.7}$$

where $E_m(z,t)$, for $m \in \{S, I, P\}$, denotes the baseband envelopes of the three optical pulses, and $k_m \equiv k_m(\omega_m)$ are the center wave numbers.

If the second-order nonlinear susceptibility is well approximated as spatially homogeneous and local (i.e., space-independent), as well as temporally constant and instantaneous (i.e., time-independent), then the nonlinear polarization vector takes on the simple form [53, 65, 67],

$$\left\{\vec{P}_{NL}(z,t)\right\}_\ell = \sum_{n,m} \chi^{(2)}_{\ell,m,n} \Re\left\{\vec{\mathcal{E}}(z,t)\right\}_m \Re\left\{\vec{\mathcal{E}}(z,t)\right\}_n\,, \tag{7.8}$$

where the subscripts ℓ, m, n refer to any one of the Cartesian coordinates $\vec{x}$, $\vec{y}$, $\vec{z}$, and $\chi^{(2)}_{\ell,m,n}$ is the corresponding tensor element of the second-order susceptibility. Substituting (7.8) into the truncated wave equation (7.6), and separating the terms which overlap in frequency and polarization, yields a system of three coupled differential equations [53, 67],

$$\frac{\partial}{\partial z} E_S(z,t) + \frac{1}{v_S}\frac{\partial}{\partial t} E_S(z,t) = i\frac{\omega_S \chi^{(2)}}{2c\, n_S(\omega_S)}\, e^{i\Delta k z} E_P(z,t) E_I^*(z,t)\,, \tag{7.9}$$

$$\frac{\partial}{\partial z} E_I(z,t) + \frac{1}{v_I}\frac{\partial}{\partial t} E_I(z,t) = i\frac{\omega_I \chi^{(2)}}{2c\, n_I(\omega_I)}\, e^{i\Delta k z} E_P(z,t) E_S^*(z,t)\,, \tag{7.10}$$

$$\frac{\partial}{\partial z} E_P(z,t) + \frac{1}{v_P}\frac{\partial}{\partial t} E_P(z,t) = i\frac{\omega_P \chi^{(2)}}{2c\, n_P(\omega_P)}\, e^{-i\Delta k z} E_S(z,t) E_I(z,t)\,, \tag{7.11}$$

for $0 \le z \le L$. Here v_m, for $m = S, I, P$, denotes the group velocities of the three pulses, $n_m(\omega_m)$ is the refractive index seen by each field at their respective center frequencies, and $\Delta k \equiv k_P - k_S - k_I$ is referred to as the center-frequency phase mismatch. To obtain these expressions we have assumed that the relevant elements of the nonlinear susceptibility tensor are equal, and the optical pulses are sufficiently narrowband, relative to their center frequencies, such that in each equation $\partial^2 P_{NL}(z,t)/\partial t^2 \approx -\omega_m^2 P_{NL}(z,t)$ is warranted.

The coupled-mode equations in (7.9)–(7.11) are a suitable starting point for numerical analysis of the interaction between these three pulses inside the crystal. However, in order to obtain an analytical solution, we assume that the pump pulse is much stronger relative to the signal and idler pulses, such that the coupling term on the right-hand side of (7.11) can be ignored. This yields a nondepleting pump pulse envelope $E_P(z=0, t-z/v_P)$, propagating at its group velocity inside the crystal without deformation. With this approximation, the coupled-mode equations simplify to

$$\frac{\partial}{\partial z}E_S(z,t) + \frac{1}{v_S}\frac{\partial}{\partial t}E_S(z,t) = i\frac{\omega_S \chi^{(2)}}{2c\, n_S(\omega_S)}\, e^{i\Delta k z} E_P(t-z/v_P) E_I^*(z,t)\,, \tag{7.12}$$

$$\frac{\partial}{\partial z}E_I(z,t) + \frac{1}{v_I}\frac{\partial}{\partial t}E_I(z,t) = i\frac{\omega_I \chi^{(2)}}{2c\, n_I(\omega_I)}\, e^{i\Delta k z} E_P(t-z/v_P) E_S^*(z,t)\,, \tag{7.13}$$

for $0 \le z \le L$, where we have simplified notation to $E_P(t-z/v_P) \equiv E_P(z=0, t-z/v_P)$.

It will be convenient for the remainder of this chapter to normalize the Volts/m electric fields to photon units, i.e., $\sqrt{\text{photons/s}}$. Because plane waves have infinite power, we confine our region of interest to a finite area R on the transverse plane, centered at the optical axis of the crystal. Then, with the help of the slowly-varying envelope approximation, the baseband envelopes of the signal, idler and pump magnetic fields are well-approximated by

$$\vec{H}_m(z,t) = (\vec{z} \times \vec{x}_m)\, n_m(\omega_m) \sqrt{\epsilon_0/\mu_0}\, E_m(z,t)\,, \tag{7.14}$$

for $m = S, I, P$. The short-time average photon flux of each pulse at a fixed z-plane is then obtained by integrating the z-directed Poynting vector over the transverse region of interest and normalizing by $\hbar\omega_m$, yielding $P_m(z,t) = \eta_m |E_m(z,t)|^2$, where

$$\eta_m = \frac{R\, n_m(\omega_m)}{2\hbar\omega_m \sqrt{\mu_0/\epsilon_0}}\,. \tag{7.15}$$

The photon-units fields are therefore $A_m(z,t) \equiv \sqrt{\eta_m} E_m(z,t)$, which yields (7.12) and (7.13) in normalized form as follows,

$$\frac{\partial}{\partial z}A_S(z,t) + \frac{1}{v_S}\frac{\partial}{\partial t}A_S(z,t) = i\kappa e^{i\Delta k z} A_P(t-z/v_P) A_I^*(z,t)\,, \tag{7.16}$$

$$\frac{\partial}{\partial z}A_I^*(z,t) + \frac{1}{v_I}\frac{\partial}{\partial t}A_I^*(z,t) = -i\kappa^* e^{-i\Delta k z} A_P^*(t-z/v_P) A_S(z,t)\,, \tag{7.17}$$

where we have conjugated the second equation for future convenience, and have defined a (possibly complex-valued[4]) coupling coefficient with units $\sqrt{\mathrm{m}^{-2}\mathrm{s}}$, to be

$$\kappa \equiv \chi^{(2)} \sqrt{\frac{\hbar \mu_0 \omega_I \omega_S \omega_P}{2Rc\, n_I(\omega_I)\, n_S(\omega_S)\, n_P(\omega_P)}}. \tag{7.18}$$

In order to obtain a solution to the coupled differential equations, it will be convenient to transform the variables into a pump-referenced time frame via

$$z' = z, \tag{7.19}$$

$$t' = t - z/v_P\,, \tag{7.20}$$

and eliminate the propagation phase by defining $A'_m(z',t') \equiv A_m(z',t')e^{-i\Delta k z'/2}$ for $m = S, I$, so that the coupled-mode equations become

$$\left[\frac{\partial}{\partial z'} + \frac{1}{\Delta v_{PS}}\frac{\partial}{\partial t'} + i\frac{\Delta k}{2}\right] A'_S(z',t') = i\kappa A_P(t') A'^{*}_I(z',t'), \tag{7.21}$$

$$\left[\frac{\partial}{\partial z'} + \frac{1}{\Delta v_{PI}}\frac{\partial}{\partial t'} - i\frac{\Delta k}{2}\right] A'^{*}_I(z',t') = -i\kappa^{*} A^{*}_P(t') A'_S(z',t'), \tag{7.22}$$

in which the group velocity mismatch terms are defined as

$$\Delta v_{xy} \equiv \left(v_y^{-1} - v_x^{-1}\right)^{-1}. \tag{7.23}$$

Note that the coupled-mode equations, written in the pump-referenced time frame, reveal two distinct solution regimes: $\Delta v_{PS}\Delta v_{PI} > 0$, in which both signal and the idler pulses are propagating in the same direction relative to the pump, and $\Delta v_{PS}\Delta v_{PI} < 0$, in which the two fields are counter-propagating relative to the pump. Not surprisingly, this counter-propagation is an essential ingredient to obtaining spectral conjugation, whose temporal equivalent—via properties of Fourier transforms—is given by phase-conjugation, in addition to time reversal of the pulse. Whereas (temporal) phase-conjugation is achieved by the downconversion process [53], the counter-propagating signal and idler fields in the pump frame-of-reference is responsible for the time-reversal component.

[4] κ is complex if and only if $\chi^{(2)}$ is complex.

7.2 Exact solution with flat-top pump pulse

Our goal in this section is to solve the coupled-mode equations, (7.21) and (7.22) for the signal and idler fields at $z' = L$ in terms of the fields that enter the nonlinear medium at $z' = 0$. We restrict our attention to $\Delta v_{PS}\Delta v_{PI} < 0$, and for concreteness we assume that the signal field propagates faster than the idler—yielding $\Delta v_{PS} < 0$ and $\Delta v_{PI} > 0$—but the ordering of the signal and idler group velocities may be swapped with no loss of generality.

Unfortunately, obtaining an analytic solution using an arbitrary pump pulse is tedious, at best. Therefore, we choose a simple flat-top pump pulse with duration T_P and with an envelope $A_P \in \mathbb{C}$, i.e.,

$$A_P(t) = \begin{cases} A_P & \text{for } 0 \le t < T_P, \\ 0 & \text{otherwise.} \end{cases} \tag{7.24}$$

Although it is very unlikely that any practical pump pulse will resemble this shape, this assumption simplifies the interaction boundaries inside the crystal and the form of the coupled differential equations, while retaining the duration and intensity of the pump as parameters. However, it is worth pointing out that this assumption does not account for phase modulation (in either time or frequency), which may be present in a practical pump pulse. The pump-referenced coordinate transformation, applied to a flat-top pump, transforms the parallelogram-shaped interaction regime in the (z, t)-plane, into a rectangle in the (z', t')-plane, as shown in Figure 7-1. The latter interaction region proves more convenient than the former for solving the coupled-mode equations with respect to boundary conditions.

We begin solving (7.21) and (7.22) noting that the pair of differential equations decouple when the pump field is zero, yielding the solutions,

$$A'_S(z', t') = A'_S\big(z' = 0, t' + z'/|\Delta v_{PS}|\big)e^{-i\Delta k z'/2}, \tag{7.25}$$

$$A'_I(z', t') = A'_I\big(z' = 0, t' - z'/\Delta v_{PI}\big)e^{-i\Delta k z'/2}. \tag{7.26}$$

Thus, when the pump is absent, the signal field propagates backwards in time along the characteristic lines $t' + z'/|\Delta v_{PS}| = C \in \mathbb{R}$, whereas the idler field propagates forward along $t' - z'/\Delta v_{PI} = C \in \mathbb{R}$. As a result, we can identify the three regimes for the input fields, based on their interaction with the pump, that are shown in Figure 7-2. First, the portion

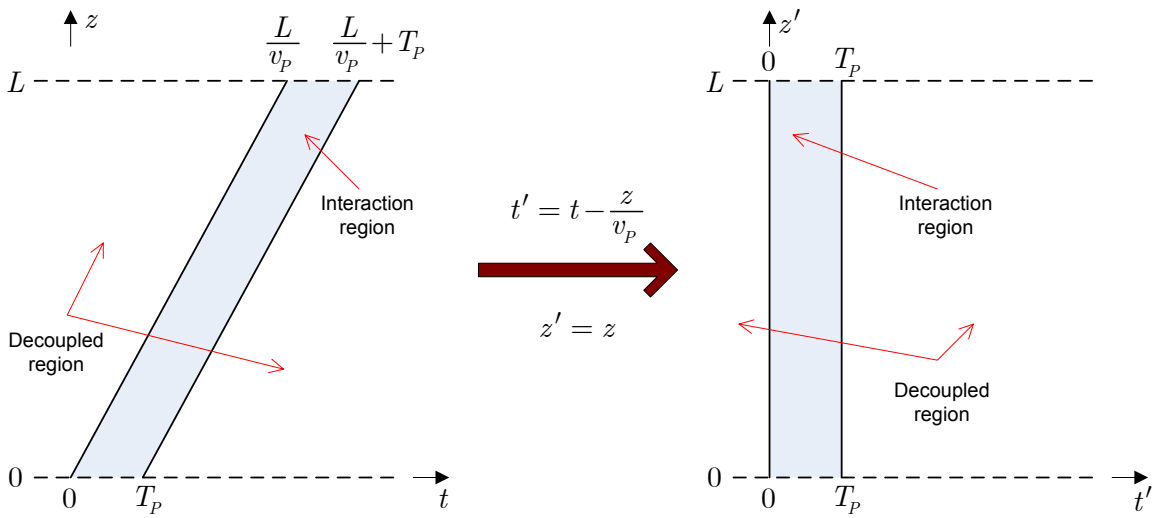

Figure 7-1: The interaction region inside the crystal, which is determined by the overlap of the pump pulse and the crystal, is shown in the laboratory frame of reference (z, t) and the pump frame of reference (z', t').

of signal field that enters the crystal when $t' < 0$ or $t' > T_P + L/|\Delta v_{PS}|$ (red, dashed lines at $z' = 0$) never overlaps with the pump inside the crystal, thus emerges unaltered at $z' = L$ after $L/|\Delta v_{PS}|$ propagation delay. Similarly, the idler input during $t' < -L/\Delta v_{PI}$ and $t' > 0$ (blue, dashed lines at $z' = 0$) exits at $z' = L$, unaltered, after $L/\Delta v_{PI}$ propagation delay. The second regime corresponds to the signal input for $t' \in [T_P, T_P + L/|\Delta v_{PS}|]$, and the idler input for $t' \in [-L/\Delta v_{PI}, 0]$, shown in Figure 7-2 with red and blue solid lines at $z' = 0$, respectively. The signal input in this time window catches up with the trailing edge of the pump inside the crystal ($t' = T_P, z' \in [0, L]$), initiating the nonlinear interaction. On the other hand, the idler field that enters the crystal in the corresponding time window is overtaken by the leading edge of the pump, while propagating inside the crystal ($t' = 0, z' \in [0, L]$). Thus, these signal and idler windows at $z' = 0$ are mapped one-to-one onto the right and left boundaries of the interaction rectangle, respectively, and constitute boundary conditions, for the coupled-mode equations, on these edges. The third and final input regime corresponds to $t' \in [0, T_P]$, for both the signal and the idler input fields (red and blue dash-dotted lines at $z' = 0$, respectively). In this time window the pump has only partially entered the crystal, thus the signal and idler inputs entering the medium in this time window immediately begin interacting. Both inputs in this time window are boundary conditions on the bottom edge of the interaction rectangle.

Let us now explain the three output regimes that result from the overall interaction.

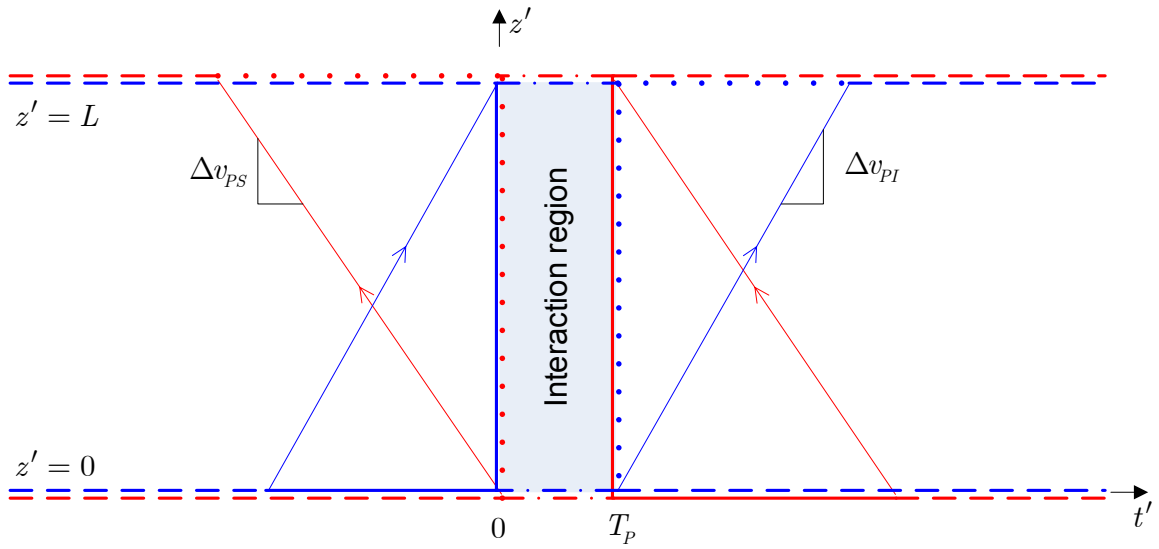

Figure 7-2: Time intervals of the signal (red) and idler (blue) inputs that undergo different interactions inside the crystal are shown at $z' = 0$. Similarly, time intervals of the output fields that result from different interaction regimes inside the crystal are marked at $z' = L$. Dashed line segments refer to input and output segments that do not overlap with the pump inside the crystal. The solid lines show the input field intervals that begin interacting with the pump inside the crystal and their one-to-one mapping onto the interaction region boundary. The dotted lines refer to the output fields that complete the interaction inside the crystal and separate from the pump, yielding a one-to-one mapping from the interaction rectangle. The dash-dotted segments indicate incomplete interactions due to the partial overlap between the pump and the crystal.

In the previous paragraph, we have already identified the first of these regimes as the unaltered signal and idler fields that exit during $t' \in (-\infty, -L/|\Delta v_{PS}|] \cup [T_P, \infty)$ and $t' \in (-\infty, 0] \cup [T_P + L/\Delta v_{PI}, \infty)$, respectively (red and blue dashed lines at $z' = L$). The second regime corresponds to outputs that result from a complete interaction across the full extent of the pump pulse. The signal that catches-up with the trailing edge of the pump pulse at $t' = T_P$, emerges from its leading edge—having completed the interaction over its full duration—at $t' = 0$, and completes the remainder of its propagation inside the crystal unaltered. Thus, the signal field resulting from the interaction ($t' = T_P, z' \in [0, L]$) emerges from the output facet of the crystal during $t' \in [-L/|\Delta v_{PS}|, 0]$ (red, dotted line at $z' = L$). An analogous argument can be made for the idler field, which indicates that the idler field resulting from the full interaction over the pump pulse ($t' = T_P, z' \in [0, L]$) emerges from the crystal during $t' \in [T_P, T_p + L/\Delta v_{PI}]$ (blue, dotted line at $z' = L$).[5] The final output window is $t' \in [0, T_P]$, during which the pump pulse is exiting the crystal. Thus,

[5]The ideal outputs from pulsed parametric downconversion corresponds to these two output intervals.

the signal and idler outputs during this window (red and blue dash-dotted lines at $z' = L$, respectively) correspond to interactions that begin as described in the previous regime, but prematurely terminate because the crystal ends before the fields can traverse the full extent of the pump pulse.

Based on the interaction regimes described above, the coupled differential equations should be solved inside the interaction rectangle $(z', t') \in [0, L] \times [0, T_P]$, subject to a signal boundary condition on $\{z' = 0, t' \in [0, T_P]\} \cup \{z' \in [0, L], t' = T_P\}$ (bottom and right edges), and an idler boundary condition on $\{z' = 0, t' \in [0, T_P]\} \cup \{z' \in [0, L], t' = 0\}$ (bottom and left edges). The signal field observed at the output facet of the crystal is obtained from the signal field solution on $\{z' \in [0, L], t' = 0\} \cup \{z' = L, t' \in [0, T_P]\}$ (left and top edges), and the idler output is obtained from its solution on $\{z' = L, t' \in [0, T_P]\} \cup \{z' \in [0, L], t' = T_P\}$ (top and right edges). This task is accomplished with Laplace transform techniques, the details of which are left to Appendix C. After the solutions are transformed back into (z, t) coordinates, the signal output for $t \in [L/v_S, L/v_P + T_P]$ is a linear transformation on the input fields,

$$A_S(z = L, t) = \int_0^{L/|\Delta v_{PS}|+T_P} \mathrm{d}\tau\, A_S(z{=}0, \tau) h_{SS}(t, \tau) + \int_{-L/\Delta v_{PI}}^{T_P} \mathrm{d}\tau\, A_I^*(z{=}0, \tau) h_{SI}(t, \tau), \quad (7.27)$$

and outside of this time window we simply have $A_S(z{=}L, t) = A_S(z{=}0, t{-}L/v_S)$. Similarly, the (conjugated) idler output for $t \in [L/v_P, L/v_I + T_P]$ is given by

$$A_I^*(z = L, t) = \int_0^{L/|\Delta v_{PS}|+T_P} \mathrm{d}\tau\, A_S(z{=}0, \tau) h_{IS}(t, \tau) + \int_{-L/\Delta v_{PI}}^{T_P} \mathrm{d}\tau\, A_I^*(z{=}0, \tau) h_{II}(t, \tau), \quad (7.28)$$

and by $A_I^*(z = L, t) = A_I^*(z = 0, t - L/v_I)$ otherwise.

It is a straightforward exercise to find the analytic expressions of $h_{mn}(t, \tau)$, for $m, n = S, I$, from (C.24) and (C.25), but we will not include them here because they do not have a direct bearing on subsequent derivations in this chapter. Instead, we note that three parameters are significant in these impulse responses: the characteristic frequency of the interaction $|\beta_P|$, where $\beta_P \equiv i\kappa A_P \sqrt{\Delta v_{PI} |\Delta v_{PS}|}$, a (dimensionless) interaction-strength

parameter $|\beta_P|T_P$, and the group-velocity mismatch ratio $r \equiv \Delta v_{PI}/|\Delta v_{PS}|$.

7.3 From classical fields to quantum field operators

Because light is fundamentally quantum mechanical, an accurate understanding of light phenomena requires a full quantum treatment. Our diligence in pursuing the exact classical solutions to the coupled-mode equations in the previous section will pay off in the simplicity of our transition to quantum field operators. To derive a quantum description of pulsed parametric downconversion, we follow the common quantization procedure: the signal and idler fields will be quantized, but the nondepleting pump field—having many more photons than the signal and idler fields—remains classical.

The classical signal and idler fields at the input facet of the crystal, $A_S(z=0,t)$ and $A_I(z=0,t)$, are quantized using the standard formalism in free-space [14], which yields photon-units quantum field operators, $\hat{A}_S(z=0,t)$ and $\hat{A}_I(z=0,t)$, satisfying the canonical commutator relations

$$[\hat{A}_m(z=0,t_1), \hat{A}_n^\dagger(z=0,t_2)] = \delta_{m,n}\,\delta(t_1-t_2), \tag{7.29}$$

$$[\hat{A}_m(z=0,t_1), \hat{A}_n(z=0,t_2)] = 0\,, \tag{7.30}$$

for $m,n = S,I$. The evolution of these field operators inside the crystal is determined by operator-valued analogs of the classical coupled-mode equations (7.16) and (7.17), i.e.,

$$\frac{\partial}{\partial z}\hat{A}_S(z,t) + \frac{1}{v_S}\frac{\partial}{\partial t}\hat{A}_S(z,t) = i\kappa e^{i\Delta k z} A_P(t-z/v_P)\,\hat{A}_I^\dagger(z,t)\,, \tag{7.31}$$

$$\frac{\partial}{\partial z}\hat{A}_I^\dagger(z,t) + \frac{1}{v_I}\frac{\partial}{\partial t}\hat{A}_I^\dagger(z,t) = -i\kappa^* e^{-i\Delta k z} A_P^*(t-z/v_P)\,\hat{A}_S(z,t). \tag{7.32}$$

In Appendix D, it is shown that these differential equations preserve commutators for all $z > 0$. Hence, the input/output operator map is given by the classical expressions (7.27) and (7.28) (equivalently, (C.24) and (C.25)), but with the classical fields $A_S(z=0,t)$, $A_I(z=0,t)$, $A_S(z=L,t)$ and $A_I(z=L,t)$ replaced by the free-space, photon-units quantum operators $\hat{A}_S(z=0,t)$, $\hat{A}_I(z=0,t)$, $\hat{A}_S(z=L,t)$ and $\hat{A}_I(z=L,t)$, respectively.

These operator-valued input/output relations for the signal and idler fields are exact solutions to the coupled-mode equations when the pump is a flat-top pulse. They in-

corporate the contributions from the desired full interaction inside the crystal, as well as those from nonideal interactions that occur close to the boundaries of the finite-length crystal. Furthermore, these expressions encompass a broad range of physical conditions: they are valid for arbitrary values of the center-frequency phase mismatch, the group-velocity mismatch—subject to the condition that the pump velocity remain between the signal and idler group velocities—the pump pulse duration[6] and the pump intensity. Unfortunately, their versatility in this regard precludes furthering our understanding of the output fields' coherence properties. Thus it is desirable to perform a series of approximations on the exact input/output relations that are based on the physical conditions which are relevant to this chapter.

7.4 Full-interaction dominated output regime

Having obtained a quantized input/output description for pulsed parametric downconversion, we are equipped to determine the conditions under which there exists a time window at the output that depends on the spectral conjugates of the input field operators. First, we assume that the center frequencies are phase-matched, so that $\Delta k = 0$. In addition, we restrict our window of interest to $t \in [L/v_S, L/v_P]$ for the signal field, and to $t \in [L/v_P + T_P, L/v_I + T_P]$ for the idler field. These time intervals have simple physical correspondences. L/v_S is the earliest time instant that a signal which interacts with the pump pulse may exit the output facet of the crystal, viz., it is the departure time (from $z = L$) of the field operator that enters the crystal at $t = 0$, together with the leading edge of the pump. L/v_P is the time instant the leading edge of the pump will emerge from $z = L$. Because the signal field propagates *fastest* inside the crystal, the signal output operator resulting from an interaction of input field operators over the full pump pulse duration will correspond to the intermediate window. Analogously, $L/v_I + T_P$ is the latest time instant that an idler input operator which interacts with the pump pulse may exit the crystal at $z = L$. In other words, the idler input operator exiting the crystal at $L/v_I + T_P$ has entered the crystal (from $z = 0$) at $t = T_P$, together with the trailing edge of the pump pulse. On

[6] Although our physical interpretations of the solution regions have assumed $T_P|\Delta v_{PS}| \ll L$, the mathematics of solving the coupled-mode equations *does not* require this assumption. Therefore (7.27) and (7.28) are valid for long pump pulses—particularly those that have a longitudinal extent longer than L so that the entire crystal is subsumed by the pump for a long time period—as well. In these cases, the output window of interest is $t' \in [0, T_P]$, which is *different* from the window of interest in the short-duration pump case. In this regime, $T_P \to \infty$ gives the continuous-wave results.

the other hand, $L/v_P + T_P$ is the time instant that the trailing edge of the pump exists the output facet of the crystal. Because the idler is the *slowest* propagating field in the medium the output idler operator window which results from input field operators interacting over the full duration of the pump pulse must be the intermediate time interval.

With these assumptions the operator-valued equivalent of (C.24) simplifies to[7]

$$\begin{aligned}\hat{A}_S(z{=}L,t) = &\int_0^{L/|\Delta v_{PS}|} \mathrm{d}\tau\, \hat{A}_S(z=0,\tau)\,\gamma\,\mu\big(\gamma(t-L/v_S-\tau),\min(\tau,T_P)\big)\\ &+\int_0^{L/|\Delta v_{PS}|} \mathrm{d}\tau\, r^{-1}\hat{A}_I^\dagger(z{=}0,-r^{-2}\tau)\,\gamma\,\nu\big(\gamma(t-L/v_S-\tau),0\big)\\ &+\int_0^{T_P} \mathrm{d}\tau\, \hat{A}_I^\dagger(z{=}0,\tau)\,r\gamma\,\nu\big(\gamma(t-L/v_S-\tau),\tau\big)\,, \end{aligned} \tag{7.33}$$

where $\gamma \equiv 2/(1+r^2)$. The impulse responses $\mu(t,\tau)$ and $\nu(t,\tau)$ are zero for $t<0$, and their second argument is defined for $\tau \in [0,T_P]$. Their Laplace transforms in the first variable are given by

$$V(s,\tau) \equiv \int \mathrm{d}t\, e^{-st}\,\nu(t,\tau) = e^{s\tau}\frac{(\beta_P/\zeta_0)\sin\big(\zeta_0(T_P-\tau)\big)}{\cos(\zeta_0 T_P)+(s/\zeta_0)\sin(\zeta_0 T_P)}\,, \tag{7.34}$$

$$M(s,\tau) \equiv \int \mathrm{d}t\, e^{-st}\,\mu(t,\tau) = e^{s\tau}\frac{\cos\big(\zeta_0(T_P-\tau)\big)+(s/\zeta_0)\sin\big(\zeta_0(T_P-\tau)\big)}{\cos(\zeta_0 T_P)+(s/\zeta_0)\sin(\zeta_0 T_P)}\,, \tag{7.35}$$

where $\zeta_0 \equiv \sqrt{|\beta_P|^2 - s^2}$, and $s \in \mathbb{C}$ is the transform-domain variable.

Similarly, the adjoint of the idler output operator for $t \in [L/v_P{+}T_P, L/v_I{+}T_P]$, obtained from (C.25), is given by

$$\begin{aligned}\hat{A}_I^\dagger(z{=}L,t) = &\int_{-L/\Delta v_{PI}}^{T_P} \mathrm{d}\tau\, \hat{A}_I^\dagger(z{=}0,\tau)\,r^2\gamma\,\mu\big(-r^2\gamma(t-L/v_I-\tau),\min(T_P,T_P-\tau)\big)\\ &+\int_{-L/\Delta v_{PI}}^{0} \mathrm{d}\tau\, r\hat{A}_S(z{=}0,-r^2\tau+T_P)\,r^2\gamma\,\nu\big(-r^2\gamma(t{-}L/v_I{-}T_P{-}\tau),0\big)e^{-i2\phi_P}\\ &+\int_0^{T_P} \mathrm{d}\tau\, \hat{A}_S(z{=}0,\tau)\,r\gamma\,\nu\big(-r^2\gamma(t-L/v_I-\tau),T_P-\tau\big)e^{-i2\phi_P}, \end{aligned} \tag{7.36}$$

where we have defined $\phi_P \equiv \angle\beta_P$.

In (7.33) and (7.36), the signal and idler inputs during $0<\tau<T_P$ contribute undesirable boundary effects because the pump is only partially inside the crystal during this time

[7]See last paragraph in Appendix C for discussion of this simplification.

interval. Let us consider the Laplace transform of the input contributions from this time window in (7.33), i.e.,

$$\int_0^{T_P} \mathrm{d}\tau \Big[\hat{A}_S(z=0,\tau)\, M\big(s/\gamma,\tau\big) + \hat{A}_I^\dagger(z=0,\tau)\, r\, V\big(s/\gamma,\tau\big) \Big] e^{-s(L/v_S+\tau)} \,. \tag{7.37}$$

The contribution from this portion of the inputs is a decaying function of time if and only if M and V are stable system functions for all $\tau \in [0, T_P)$. The poles of these system functions are given by the common roots of,[8]

$$\cos(\zeta_0 T_P) \pm s/|\beta_P| \Big|_{s/\gamma} = 0 \quad \text{and} \tag{7.38}$$

$$\tan(\zeta_0 T_P) + \zeta_0/s \Big|_{s/\gamma} = 0 \,, \tag{7.39}$$

with the exception of $s/\gamma = |\beta_P|$ (i.e., $\zeta_0 = 0$), because it is cancelled by a zero. All of these poles are in the left-half of the Laplace transform plane if and only if $|\beta_P| T_P < \pi/2$. This is the stable operation regime of pulsed parametric downconversion, within which the impulse response of the signal and idler inputs for all $\tau \in [0, T_P)$ will decay to zero as time progresses. If $|\beta_P| T_P < 1$, the real parts of all poles are strictly less than $-1/T_P$, so the time constant of the decay is no greater than T_P [68]. As $|\beta_P| T_P$ grows beyond 1 and approaches $\pi/2$, the time constant diverges towards infinity. On the other hand, when $|\beta_P| T_P > \pi/2$, there will be at least one pole in the right half of the Laplace transform plane, yielding an impulse response that increases exponentially with time. Hence, the contribution from the signal and idler inputs during $\tau \in [0, T_P]$ is no longer negligible.[9,10] Note that, in this gain regime, the amplified signal and idler will eventually become comparable to the pump field, thus invalidating the nondepleting pump approximation. The output fields therefore do not grow in time indefinitely, and pump dynamics must also be taken into account to obtain accurate results in this regime [61, 68, 69]. As a final note, we need not separately consider the transient input contributions to the idler output, because the spectrum of poles in the system functions of $\hat{A}_S(z = L, t)$ and $\hat{A}_I^\dagger(z = L, t)$ differ only by a positive scaling factor, which does not affect the stable regime.

[8] The analysis in this paragraph is based on a seminal paper by Fisher *et al.* [68].

[9] When $|\beta_P| T_P = \pi/2$ there is one pole at $s = 0$, so that the system is marginally stable. However, because the impulse response does not decay to zero, the transient regime still cannot be neglected.

[10] If $|\beta_P| T_P > \pi$ the zeros of these system functions (which are parameterized by τ) may cancel a subset of the real poles at a finite number of isolated τ values. However, because this does not happen for all $\tau \in [0, T_P]$, it does not affect the stability arguments presented herein.

For the remainder of this chapter we assume that $|\beta_P|T_P < \pi/2$. Because the time response from the inputs $\hat{A}_S(z=0,\tau)$ and $\hat{A}_I^\dagger(z=0,\tau)$ for $\tau \in [0,T_P)$, is a decaying function of time, their contribution to the output will be negligible when $t > L/v_S + T$ for some $T \gg T_P$, provided that the crystal is long enough to satisfy $T < L/|\Delta v_{PS}|$.[11] In this case, if we limit our window of interest for $\hat{A}_S(z=L,t)$ to

$$L/v_S + T < t < L/v_P, \tag{7.40}$$

and, for $\hat{A}_I(z=L,t)$ to

$$L/v_P + T_P < t < L/v_I + T_P - r^{-2}T, \tag{7.41}$$

then the undesirable contributions from the inputs during $\tau \in [0,T_P]$ are negligible. Next, we shift the signal and idler time windows by introducing

$$\hat{\mathcal{A}}_S(t) \equiv \hat{A}_S\big(z=L, t+(L/v_P + L/v_S + T)/2\big), \tag{7.42}$$

$$\hat{\mathcal{A}}_I(t) \equiv \hat{A}_I\big(z=L, t+T_P+(L/v_P + L/v_I - r^{-2}T)/2\big), \tag{7.43}$$

so that both of these observation windows are centered at $t=0$. With this shift, the simplified input/output relations become

$$\hat{\mathcal{A}}_S(t) = \hat{\mathcal{A}}_{S,W}(t)W(t) + \hat{\mathcal{A}}_{S,vac}(t)\big(1-W(t)\big), \tag{7.44}$$

$$\hat{\mathcal{A}}_I(t) = \hat{\mathcal{A}}_{I,W}(t)W(r^2t) + \hat{\mathcal{A}}_{I,vac}(t)\big(1-W(r^2t)\big), \tag{7.45}$$

where the window function is given by

$$W(t) \equiv \begin{cases} 1, & |t| \le T_0 = \frac{L}{2|\Delta v_{PS}|} - \frac{T}{2} \\ 0, & \text{otherwise,} \end{cases} \tag{7.46}$$

and $\hat{\mathcal{A}}_{m,vac}(t)$, for $m = S, I$, are auxiliary vacuum-state operators introduced to preserve commutator brackets. The key relation between the input field operators and the output

[11] If $|\beta_P|T_P < 1$, then $T = 3T_P$ guarantees that the contribution from the transient window has decayed by at least a factor of e^{-2}.

operators is a two-field frequency-domain Bogoliubov transformation,

$$\hat{\mathcal{A}}_{S,W}(\Omega) = e^{-i\Omega(T_0+T)}\Big[\hat{A}_S(\Omega)\, M\big(\Omega/\gamma\big) + r\hat{A}_I^\dagger(r^2\Omega)\, V\big(\Omega/\gamma\big)\Big], \tag{7.47}$$

$$r\hat{\mathcal{A}}_{I,W}(r^2\Omega) = e^{i\Omega(T_0+T)}\Big[r\hat{A}_I(r^2\Omega)\, M^*\big(\Omega/\gamma\big)\, e^{-i\Omega r^2 T_P} + \hat{A}_S^\dagger(\Omega)\, V^*\big(\Omega/\gamma\big)\, e^{i\Omega T_P + i2\phi_P}\Big], \tag{7.48}$$

where the frequency-domain operators are defined according to

$$\hat{f}(\Omega) \equiv \int_{-\infty}^{\infty} \mathrm{d}t\, e^{i\Omega t}\hat{f}(t)\,, \tag{7.49}$$

and, as before, we rely on the units of the argument to distinguish the frequency-domain operators from their time-domain counterparts. The field operators on the right-hand side of (7.47) and (7.48) all correspond to $z = 0$ operators; we have omitted this argument for brevity. The frequency responses are obtained by evaluating (7.34) at $s = -i\Omega$ and $\tau = 0$, and (7.35) at $s = -i\Omega$ and $\tau = T_P$, i.e.,

$$V(\Omega) = (\beta_P/\zeta_0)\sin(\zeta_0 T_P)\Big[\cos(\zeta_0 T_P) - i(\Omega/\zeta_0)\sin(\zeta_0 T_P)\Big]^{-1}, \tag{7.50}$$

$$M(\Omega) = e^{-i\Omega T_P}\Big[\cos(\zeta_0 T_P) - i(\Omega/\zeta_0)\sin(\zeta_0 T_P)\Big]^{-1}, \tag{7.51}$$

with $\zeta_0^2 = |\beta_P|^2 + \Omega^2$. These frequency responses are expressible in terms of the normalized (dimensionless) variables, $\Omega/|\beta_P|$ and $|\beta_P|T_P$. In Figure 7-3(a) we have plotted the frequency-domain envelope[12] of $V(\Omega)$, i.e., $(\beta_P/\zeta_0)\sin(\zeta_0 T_P)/|\cos(\zeta_0 T_P) - i(\Omega/\zeta_0)\sin(\zeta_0 T_P)|$, for several interaction strengths ranging from weak to strong, and in Figure 7-3(b) we have plotted its corresponding phase-modulation behavior, $\arctan\big((\Omega/\zeta_0)\tan(\zeta_0 T_P)\big)$, with $\phi_P = 0$. The zeros of $V(\Omega)$ occur at

$$\Omega'_m = |\beta_P|\sqrt{\big(m\pi/|\beta_P|T_P\big)^2 - 1}\,, \tag{7.52}$$

for $m \in \mathbb{Z} - \{0\}$. Therefore, its (baseband) bandwidth—defined here as the location of the first zero—is Ω'_1, and using the stability condition $|\beta_P|T_P < \pi/2$, we observe that $\Omega'_1 > \sqrt{3}|\beta_P|$ is always true. For very weak interactions, i.e., when $|\beta_P|T_P \ll \pi/2$, we obtain

[12] We plot the envelope and phase modulation to avoid tracking the π phase shifts when the envelope changes sign.

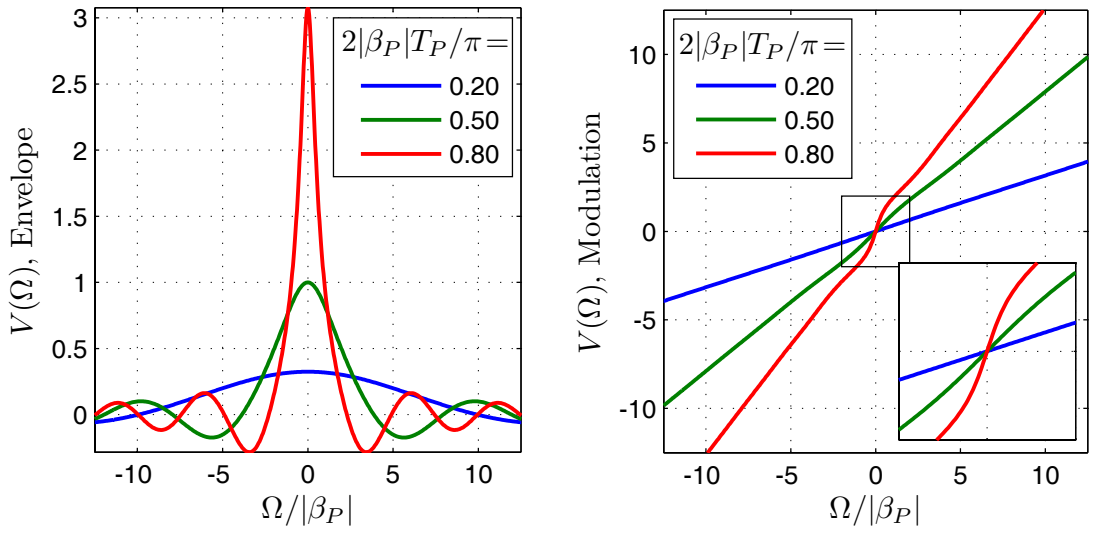

(a) Envelope **(b)** Phase modulation

Figure 7-3: The frequency-domain envelope and phase modulation of $V(\Omega)$ is plotted for three different values of the interaction-strength parameter, $|\beta_P|T_P < \pi/2$. In the latter plot, $\phi_P = 0$ is assumed.

$\Omega_1' \approx \pi/T_P$, which is independent of $|\beta_P|$, and equal to half the (baseband) bandwidth of the pump pulse.

When $|\Omega| \gg |\beta_P|$, the envelope of $V(\Omega)$ is well-approximated by a sinc-function,

$$|\beta_P|T_P \frac{\sin(\zeta_0 T_P)}{(\zeta_0 T_P)}, \tag{7.53}$$

so the tails of the frequency response decay as $|\beta_P|/|\Omega|$ regardless of the interaction strength. In the same regime, the phase modulation is approximately linear in Ω, with a slope proportional to T_P. However the overall phase modulation is linear only in the weak-interaction limit. As $|\beta_P|T_P$ approaches $\pi/2$ the phase becomes nonlinear for $|\Omega| < \sqrt{3}|\beta_P|$, as shown in the inset of Figure 7-3(b).

The peak of the frequency response occurs at $\Omega = 0$ and is equal to $\tan(|\beta_P|T_p)$, which rapidly diverges towards infinity as the interaction parameter approaches $\pi/2$. This is due to one of the system-function poles—as discussed previously from the Laplace transform domain perspective—approaching the imaginary axis from the left, and crossing to the right when $|\beta_P|T_p = \pi/2$. On the other hand, for $|\beta_P|T_p \ll 1$, the peak of the frequency response scales linearly with the interaction strength parameter, $|\beta_P|T_p$, hence the sinc-function approximation to the frequency response is appropriate for all frequencies.

In this section, we have started with a general (and exact) solution to the first-order truncated coupled-mode equations assuming a flat-top pump pulse, and worked our way through a series of approximations to derive the windowing equations in (7.44), (7.45) and the frequency-domain Bogoliubov transformations in (7.47), (7.48), which yield the input/output operator map when the boundary effects from the finite length crystal are negligible. In the following sections, we shall first study the implications of the parameter r in these equations, and then establish a Gaussian-state theory for the joint state of the signal and idler at the crystal's output facet.

7.5 Frequency-scaling and spectral phase conjugation

In the following discussion we assume that the crystal is long enough so that we can neglect the temporal windowing, and focus primarily on the role of $r \equiv \Delta v_{PI}/|\Delta v_{PS}|$ in the Bogoliubov relations, (7.47) and (7.48). r is a parameter that denotes the ratio of the group-velocity mismatch between the idler and pump pulse, to that between the pump and the signal pulse. The definition of group-velocity mismatch is given in (7.23), and it physically represents the walk-off (separation) velocity of pulses [66]. When $r \gg 1$ we have $v_P \approx v_I$, so that the interaction inside the crystal occurs between a short-duration window of the idler input field and a much longer duration window of the signal field. On the other hand, for $r \ll 1$ we have $v_S \approx v_P$, so that the signal pulse duration that interacts underneath the pump pulse (and inside the crystal) is very short relative to that of the idler input field. We shall see shortly that this difference in the duration of the interacting input pulses results in temporal compression or expansion.

Let us first consider the output signal field, $\hat{\mathcal{A}}_{S,W}(\Omega)$. When $r > 1$, we have $\gamma \equiv 2/(1+r^2) < 1$, so $M(\Omega/\gamma)$ and $V(\Omega/\gamma)$ correspond to compressing (7.50) and (7.51) along the frequency axis. In addition, the spectrally-conjugated idler input field is compressed in frequency by a factor of r^2 (note that the multiplier r in $r\mathcal{A}_I^\dagger(r^2\Omega)$ is necessary to preserve commutator brackets). Therefore, when the signal input is in a vacuum state, the signal output contains the spectrally-conjugated and spectrally r^2-compressed idler input field operator, subsequently filtered through the bandwidth-Ω_1'/γ filter, $V(\Omega/\gamma)$, and embedded in a filtered zero-point fluctuation contribution from the vacuum-state input signal. However, because $1/\gamma = (1+r^2)/2 < r^2$ for $r > 1$, the idler spectrum is compressed

by a greater factor than the frequency response V. Thus, the fraction of the idler spectrum that couples into the signal output (through the filter) increases with r, and in the limit $r \gg 1$ we have

$$\hat{\mathcal{A}}_{S,W}(\Omega) \approx e^{-i\Omega(T_0+T)}\Big[\hat{A}_S(\Omega)\, M\big(r^2\Omega/2\big) + r\hat{A}_I^\dagger(r^2\Omega)\, V\big(r^2\Omega/2\big)\Big], \tag{7.54}$$

so that the spectrally-conjugated idler field is compressed twice as much as V, yielding efficient coupling between the idler input and signal output over a (baseband) bandwidth of $2\Omega_1'$.

On the other hand, the $r < 1$ regime for $\hat{\mathcal{A}}_{S,W}(\Omega)$ yields frequency-broadening, which in time-domain is equivalent to pulse-compression, due to the time/frequency duality. Nevertheless, for $r < 1$ we have $1 > 1/\gamma = (1 + r^2)/2 > r^2$, so V broadens by a smaller factor than $r\hat{\mathcal{A}}_{I,W}(r^2\Omega)$. As r decreases, the fraction of the idler spectrum that couples into the signal output decreases as well, yielding

$$\hat{\mathcal{A}}_{S,W}(\Omega) \approx e^{-i\Omega(T_0+T)}\Big[\hat{A}_S(\Omega)\, M\big(\Omega/2\big) + r\hat{A}_I^\dagger(r^2\Omega)\, V\big(\Omega/2\big)\Big], \tag{7.55}$$

in the $r \ll 1$ limit. Therefore, the broadened spectrum of the (conjugated) idler input is limited by the cutoff frequency of V, i.e, $2\Omega_1'$. Hence, while it is possible to attain significant pulse-compression (spectral-broadening) of narrowband idler inputs (in conjunction with spectral conjugation), broadband pulse-compression is not feasible due to the finite interaction bandwidth.

It is unnecessary to separately consider the properties of the idler output because the expression in (7.48) is similar to that of (7.47), but with the important distinction that r^{-2} replaces r^2. Thus, when the idler input field is in a vacuum state, the idler output is comprised of the spectrally-conjugated and filtered signal input operator embedded in a filtered zero-point fluctuation contribution arising from the input idler, but because the frequency variable is scaled by r^{-2}, the spectral-compression ($r < 1$) and spectral-broadening ($r > 1$) regimes are the opposite of those observed in the signal output. Nevertheless, the conclusions for the compression and the broadening regimes of the signal output port apply in exactly the same manner to the corresponding regimes for the idler output.

The remaining possibility is equal group-velocity mismatch, i.e., $r = 1$, which is equivalent to $v_S^{-1} + v_I^{-1} = 2v_P^{-1}$, because we have assumed $v_S > v_P > v_I$. This condition is the

extended phase-matching condition [61, 62]. When it is satisfied, the Bogoliubov transformation given in (7.47) and (7.48) simplifies to

$$\hat{\mathcal{A}}_{S,W}(\Omega) = e^{-i\Omega(T_0+T)}\left[\hat{A}_S(\Omega)\, M(\Omega) + \hat{A}_I^\dagger(\Omega)\, V(\Omega)\right], \tag{7.56}$$

$$\hat{\mathcal{A}}_{I,W}(\Omega) = e^{i\Omega(T_0+T)}\left[\hat{A}_I(\Omega)\, M^*(\Omega)\, e^{-i\Omega T_P} + \hat{A}_S^\dagger(\Omega)\, V^*(\Omega)\, e^{i\Omega T_P + i2\phi_P}\right], \tag{7.57}$$

and the window durations in (7.44) and (7.45) become equal. Thus, when the idler input is in a vacuum state, the idler output contains the spectral conjugate of the signal input, after it has been filtered in frequency by $V(\Omega)$ and windowed in time by $W(t)$. The finite time-bandwidth product of the output pulse implies that at most $4\Omega_1' T_0$ modes of the input signal will have appreciable coupling to the idler output. Finally, note that the signal output field contains a similar spectrally-conjugated idler input when the signal input is in the vacuum state.

7.6 Coincident-frequency biphoton generation

In addition to spectral conjugation, the extended phase-matching condition facilitates generating entangled photon pairs with coincident frequencies, also referred to as DB-state biphotons [62], which have been proposed for quantum-enhanced timing measurements [70, 71]. Suppose $\hat{A}_S(t)$ and $\hat{A}_I(t)$ are in a multimode-vacuum product state. Then (7.56) and (7.57) constitute a two-field linear transformation on zero-mean, Gaussian-state inputs, so the outputs $\hat{\mathcal{A}}_{S,W}(t)$ and $\hat{\mathcal{A}}_{I,W}(t)$ are also in a zero-mean jointly-Gaussian state. This output state is completely determined by its second-order moments,

$$\langle \hat{\mathcal{A}}_{m,W}^\dagger(t_1)\hat{\mathcal{A}}_{n,W}(t_2)\rangle = \delta_{m,n}\, g^{(n)}(t_2 - t_1), \tag{7.58}$$

$$\langle \hat{\mathcal{A}}_{m,W}(t_1)\hat{\mathcal{A}}_{n,W}(t_2)\rangle = (1-\delta_{m,n})\, g^{(p)}(t_2 + t_1)\,, \tag{7.59}$$

for $m, n = S, I$. Here, $g^{(n)}(\tau) \equiv \mathcal{F}^{-1}\{S^{(n)}(\Omega)\}$, where the fluorescence spectrum is given by

$$S^{(n)}(\Omega) = |V(\Omega)|^2 = \frac{|\beta_P|^2 \sin^2(\zeta_0 T_P)}{\zeta_0^2 \cos^2(\zeta_0 T_P) + \Omega^2 \sin^2(\zeta_0 T_P)}\,, \tag{7.60}$$

and $g^{(p)}(\tau) \equiv \mathcal{F}^{-1}\{S^{(p)}(\Omega)\}$, with the phase-sensitive cross-correlation spectrum given by

$$S^{(p)}(\Omega) = M(\Omega)V^*(\Omega)e^{i\Omega T_P + i2\phi_P} = \frac{\beta_P \zeta_0 \sin(\zeta_0 T_P)}{\zeta_0^2 \cos^2(\zeta_0 T_P) + \Omega^2 \sin^2(\zeta_0 T_P)}\,. \tag{7.61}$$

Because of the $t_1 + t_2$ dependence in (7.59), $S^{(p)}(\Omega)$ determines the phase-sensitive cross-correlation strength between *equal-frequency* components of the signal and idler,[13] as opposed to the phase-sensitive spectrum of a complex-stationary Gaussian state, which—as studied in Chapter 3—determines the phase-sensitive cross-correlation between $\pm\Omega$-detuned frequency components.

In Figure 7-4(a) we have plotted $S^{(n)}(\Omega)$, which shows that the baseband bandwidth of the spectrum is given by Ω_1', as defined in (7.52). Furthermore, for $|\Omega| \gg |\beta_P|$ we have

$$S^{(n)}(\Omega) \approx \left(|\beta_P| T_P \frac{\sin(\zeta_0 T_P)}{\zeta_0 T_P}\right)^2, \tag{7.62}$$

so the tail of the spectrum decays as $|\beta_P|^2/\Omega^2$ as indicated by the dashed lines.

From (7.61), we note that $|S^{(p)}(\Omega)| = \sqrt{S^{(n)}(\Omega)(1 + S^{(n)}(\Omega))}$ for all $\Omega \in \mathbb{R}$. In Appendix E, we show that this is the maximum phase-sensitive cross-correlation spectrum, given $S^{(n)}(\Omega)$, and that it is *stronger* than what is achievable between two classical-state fields with $S^{(n)}(\Omega)$ as their fluorescence spectra. This phase-sensitive cross-correlation spectrum is plotted in Figure 7-4(b), where we have chosen $\phi_P = 0$.[14] Because the zeros of $S^{(n)}(\Omega)$ and $S^{(p)}(\Omega)$ coincide, both spectra have equal bandwidth by the definition we have adopted in this chapter. However, for $|\Omega| \gg |\beta_P|$ the spectrum simplifies to

$$S^{(p)}(\Omega) \approx |\beta_P| T_P \frac{\sin(\zeta_0 T_P)}{\zeta_0 T_P} = \sqrt{S^{(n)}(\Omega)}\,, \tag{7.63}$$

which implies that the tails of the phase-sensitive cross-correlation spectrum decay as $|\beta_P|/|\Omega|$, yielding a broader phase-sensitive spectrum than the fluorescence spectrum, as shown in the figure. In addition, the peak of the phase-sensitive spectrum is

$$S^{(p)}(0) = \frac{\tan(|\beta_P| T_P)}{\cos(|\beta_P| T_P)} = \tan(|\beta_P| T_P)\sqrt{1 + \tan^2(|\beta_P| T_P)}\,, \tag{7.64}$$

[13] The frequency-domain phase-sensitive cross-correlation is $\langle \hat{\mathcal{A}}_{S,W}(\Omega_1)\hat{\mathcal{A}}_{I,W}(\Omega_2)\rangle = 2\pi S^{(p)}(\Omega_1)\delta(\Omega_2 - \Omega_1)$.

[14] In the remainder of this chapter, with no appreciable loss of generality, we will assume that $\phi_P = 0$. To generalize this case to arbitrary ϕ_P, the $S^{(p)}(\Omega)$ results presented hereafter should be multiplied by $e^{i\phi_P}$.

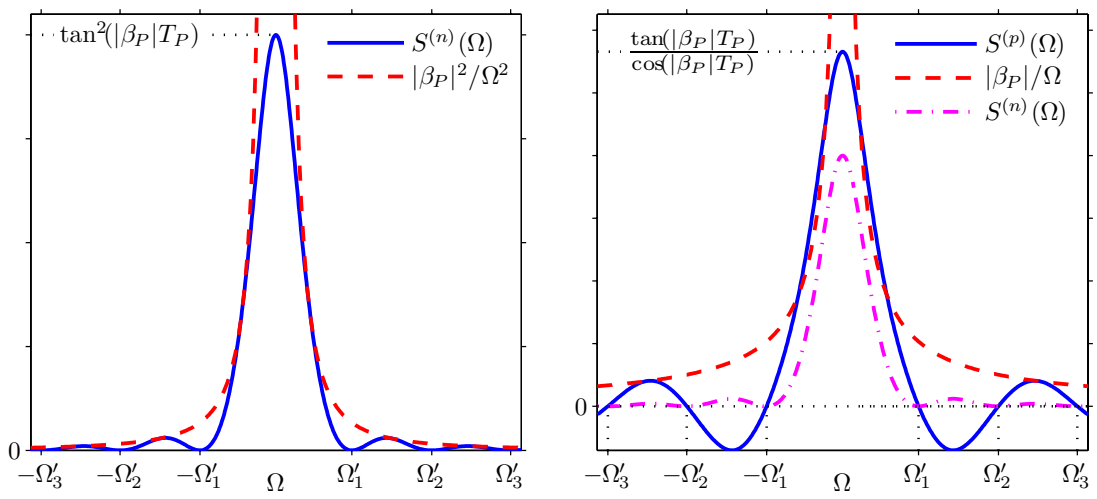

(a) Fluorescence spectrum **(b)** Phase-sensitive spectrum

Figure 7-4: The second-order correlation spectra of $\hat{\mathcal{A}}_{S,W}(t)$ and $\hat{\mathcal{A}}_{I,W}(t)$ are plotted against baseband frequency, Ω. (a) The common fluorescence spectrum of the two field operators. The dash-dotted envelope shows that the spectrum decays as $|\beta_P|^2/\Omega^2$. (b) The real-valued phase-sensitive cross-correlation spectrum ($\phi_P = 0$). For comparison, the fluorescence spectrum is included as dash-dotted line. $S^{(p)}(\Omega)$ decays as $|\beta_P|/|\Omega|$, which is appreciably slower than the decay rate of the fluorescence spectrum.

which is significantly greater than $S^{(n)}(0) = \tan^2(|\beta_P|T_P)$ when the interaction is weak ($|\beta_P|T_P \ll \pi/4$). These characteristics are pulsed-downconverter versions of behavior we have seen in earlier chapters where we considered the low-brightness regime of continuous-wave SPDC.

Because the field operators $\hat{\mathcal{A}}_{S,W}(t)$ and $\hat{\mathcal{A}}_{I,W}(t)$—prior to windowing—are obtained from continuous-time canonical transformations on vacuum-state $\hat{A}_S(t)$ and $\hat{A}_I(t)$, their joint output state is a minimum-uncertainty-product pure (Gaussian) state. Furthermore, as stated above, their phase-sensitive cross-correlation spectrum admits the maximum permissible magnitude, which is sufficient to prove that the output state is *nonclassical*. Thus, although the joint input state is the trivial classical state (vacuum), through continuous-time two-mode squeezing the outputs $\hat{\mathcal{A}}_{S,W}(t)$ and $\hat{\mathcal{A}}_{I,W}(t)$ emerge in a nonclassical, zero-mean, pure Gaussian state, with nonzero fluorescence spectra and maximum phase-sensitive cross-correlation.

The fields observed at the output facet of the crystal, however, are not $\hat{\mathcal{A}}_{S,W}(t)$ and $\hat{\mathcal{A}}_{I,W}(t)$, but a windowed portion of these fields, $\hat{\mathcal{A}}_S(t)$ and $\hat{\mathcal{A}}_I(t)$. Nonetheless, this is another linear operation, so $\hat{\mathcal{A}}_S(t)$ and $\hat{\mathcal{A}}_I(t)$ remain in a nonclassical, zero-mean, jointly-

Gaussian state, and now have Schell-model [13, 14] second-order moments

$$\langle \hat{\mathcal{A}}_m^\dagger(t_1)\hat{\mathcal{A}}_n(t_2)\rangle = \delta_{m,n}\, W(t_1)W(t_2)g^{(n)}(t_2 - t_1)\,, \tag{7.65}$$

$$\langle \hat{\mathcal{A}}_m(t_1)\hat{\mathcal{A}}_n(t_2)\rangle = (1 - \delta_{m,n})W(t_1)W(t_2)g^{(p)}(t_2 + t_1)\,, \tag{7.66}$$

with $m, n = S, I$. Note however, the joint state of $\hat{\mathcal{A}}_S$ and $\hat{\mathcal{A}}_I$ is in general a *mixed* state, because windowing the field operators involves vacuum-state injection via the beam-splitter relations (7.44) and (7.45). Nonetheless, in our regime of interest the window duration $2T_0$ is much broader than the widths of both $g^{(n)}(\tau)$ and $g^{(p)}(\tau)$ (which are $\sim 4\pi/\Omega_1'$), so apart from immediate vicinity of the window boundary, the fields inside the window are uncorrelated with—and therefore independent of—those outside of the window. Thus, the joint state of $\hat{\mathcal{A}}_S(t)$ and $\hat{\mathcal{A}}_I(t)$ can be approximated as being pure.

In the same regime (when the window duration significantly exceeds the width of the correlation functions), (7.65) and (7.66) can be approximated as

$$\langle \hat{\mathcal{A}}_m^\dagger(t_1)\hat{\mathcal{A}}_n(t_2)\rangle \approx \delta_{m,n} W^2\big((t_1 + t_2)/2\big)g^{(n)}(t_2 - t_1)\,, \tag{7.67}$$

$$\langle \hat{\mathcal{A}}_m(t_1)\hat{\mathcal{A}}_n(t_2)\rangle \approx (1 - \delta_{m,n})W^2\big((t_2 - t_1)/2\big)g^{(p)}(t_2 + t_1)\,, \tag{7.68}$$

for $m, n = S, I$, where the approximation for the latter relies on $W(t)$ being an even function. Then, the frequency-domain field operators—defined according to (7.49)—have the following nonzero correlation functions,

$$\langle \hat{\mathcal{A}}_m^\dagger(\Omega_1)\hat{\mathcal{A}}_m(\Omega_2)\rangle = \mathcal{W}(\Omega_-)S^{(n)}(\Omega_+)\,, \tag{7.69}$$

$$\langle \hat{\mathcal{A}}_S(\Omega_1)\hat{\mathcal{A}}_I(\Omega_2)\rangle = \mathcal{W}(\Omega_-)S^{(p)}(\Omega_+)\,, \tag{7.70}$$

where $m = S, I$, $\Omega_- \equiv \Omega_2 - \Omega_1$, $\Omega_+ \equiv (\Omega_2 + \Omega_1)/2$, and

$$\mathcal{W}(\Omega) = 2T_0 \frac{\sin(T_0\Omega)}{T_0\Omega}\,. \tag{7.71}$$

We can now identify the coincident-frequency nature of the phase-sensitive coherence between the signal and idler fields. Because $2T_0$ is much broader than the width of $g^{(p)}(\tau)$, the Fourier duality yields a phase-sensitive cross-correlation spectrum that is broad along

the Ω_+ axis, but narrow along the Ω_- axis. Hence $\hat{\mathcal{A}}_S$ and $\hat{\mathcal{A}}_I$ have appreciable phase-sensitive cross-correlation only when $\Omega_1 \approx \Omega_2$. When Ω_1 and Ω_2 differ more than π/T_0 the two fields decorrelate rapidly. On the other hand, when $\Omega_1 \approx \Omega_2$, the cross-correlation is appreciable for baseband frequencies up to Ω_1' in magnitude, beyond which the two fields have no appreciable cross-correlation. If we consider the fluorescence spectra of $\hat{\mathcal{A}}_S$ and $\hat{\mathcal{A}}_I$, we once again find that it is narrow along the Ω_- axis and broad along the Ω_+ axis, but this represents typical phase-insensitive fluorescence for a broadband thermal-state field, in which each frequency radiates (almost) independently.

In the low-brightness regime we have $S^{(n)}(\Omega) \ll 1$, so that the phase-sensitive cross-correlation spectrum obtained in (7.61) satisfies

$$|S^{(p)}(\Omega)| \approx \sqrt{S^{(n)}(\Omega)}\,. \tag{7.72}$$

If we then push into the low-flux regime, in which there is at most one signal/idler pair generated in the $2T_0$-second pulse window, we find that the first and second-order moments of $\hat{\mathcal{A}}_S(t)$ and $\hat{\mathcal{A}}_I(t)$, obtained from their jointly-Gaussian state characterized above, match those moments for the *unnormalizable* pure state

$$|\psi_{DB}\rangle = |\mathbf{0}\rangle_S|\mathbf{0}\rangle_I + \int_{-\infty}^{\infty}\int_{-\infty}^{\infty} \mathrm{d}\Omega_1 \mathrm{d}\Omega_2\, \psi(\Omega_1,\Omega_2)\, |\Omega_1\rangle_S|\Omega_2\rangle_I\,. \tag{7.73}$$

Here, $|\mathbf{0}\rangle_S|\mathbf{0}\rangle_I$ represents the multimode vacuum state of the signal and idler, and $|\Omega_1\rangle_S|\Omega_2\rangle_I$ is a pure product state representing a single signal photon at frequency-detuning Ω_1 (from the signal-field center frequency), and a single idler photon at frequency-detuning Ω_2. Thus, $|\psi_{DB}\rangle$ is a superposition of a predominant multimode vacuum-state contribution and a weak biphoton contribution having the wave function

$$\psi(\Omega_1,\Omega_2) \equiv \mathcal{W}(\Omega_-)\sqrt{S^{(n)}(\Omega_+)}\, e^{i\phi_P + i\pi u[-\sin(\zeta_0 T_P)]}\,, \tag{7.74}$$

where $\zeta_0 = \sqrt{|\beta_P|^2 + \Omega_+^2}$, and $u[\,\cdot\,]$ is the unit step function, which is equal to one when its argument is nonnegative and is equal to zero otherwise.

We have plotted $|\psi(\Omega_1,\Omega_2)|$ versus normalized signal and idler frequency variables, for a moderately long crystal ($L = 1$cm) in Figure 7-5(a) and for a very long crystal ($L = 3$cm) in Figure 7-5(b). Because the wavefunction *is* the phase-sensitive cross-correlation spectrum,

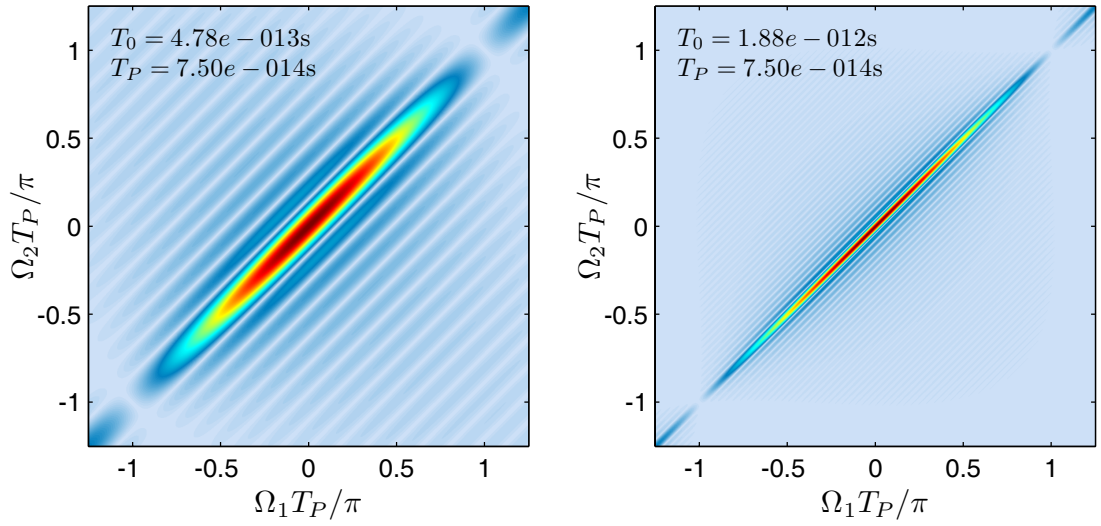

(a) $L = 1$cm **(b)** $L = 3$cm

Figure 7-5: Contour plots of the DB-state biphoton wavefunction magnitude from (7.74). The common parameters used in generating the figures are $|\beta_P| T_P = 7.182\pi \times 10^{-7}$, $|\Delta v_{PS}| = \Delta v_{PI} = 7.114 \times 10^3\, \mu$m/ps and $T_P = 75$ fs.

it too is narrow along the Ω_- axis and broad along Ω_+, as discussed earlier in this section. Therefore the individual photons in each pair are generated at nearly-coincident frequencies, within a positive-frequency band

$$|\Omega_1 - \Omega_2| < \pi/T_0 = \pi \left(\frac{L}{2|\Delta v|} - \frac{T}{2} \right)^{-1}, \tag{7.75}$$

where we have dropped the subscript for the group velocity mismatch because $r = 1$. Thus, the width of the wavefunction main lobe along its minor axis scales inversely with the crystal length, L. Note that T_0, which represents the time window in which we can neglect the boundary effects of the crystal, has some dependence on the interaction strength $|\beta_P| T_P$ through the variable T that was used in the time shift relations (7.42) and (7.43). Biphoton sources must have very low flux and brightness, so $|\beta_P| T_P \ll 1$, and T on the order of T_P will prevail. Thus, if $L/2|\Delta v|$ is comparable to T_P, the approximations pursued in this chapter must be revisited to incorporate the contributions from the photons that may be generated as the pump is entering the crystal. In the figures we have chosen $T = 3T_P$ such that these contributions are negligible over the $2T_0$-second window of interest. The frequency distribution of either the signal or idler photons, over an ensemble of biphotons generated by this process, is given by $S^{(n)}(\Omega)$, yielding a (passband) emission band $2\Omega_1' \approx 2\pi/T_P$, where

the approximation is due to $|\beta_P|T_P \ll 1$. This corresponds to the width of the wavefunction main lobe along its major axis.

Although we have derived (7.75) from a temporal-windowing argument that stems from the finite crystal length, the right-hand side of this expression is equal to the phase-matching (baseband) bandwidth, $2\pi|\Delta v|/L$, when T is negligible [62]. It is thus worth pointing out that the phase-matching bandwidth has been implicitly invoked in our derivations, when truncating the coupled-mode equations to first order (cf. (7.5) and (7.9)–(7.11)). Nonetheless, from that point forward, it does not have an explicit impact on the derivation.

In summary, pulsed parametric downconversion in the low-brightness, low-flux regime with extended phase matching yields, with very low probability, a pair of photons that have nearly-coincident frequencies, but may be generated within a broad frequency band that is proportional to the bandwidth of the pump pulse. The biphoton wavefunction in this regime is the stronger-than-classical phase-sensitive cross-correlation spectrum of the signal and idler.

7.7 Discussion

In this chapter we have provided a comprehensive analysis of parametric downconversion with a nondepleting, pulsed, flat-top pump, and with group-velocity ordering $v_S > v_P > v_I$ for the signal, pump and idler pulses respectively. We first derived the exact solution to the coupled-mode equations for the classical signal and idler fields, and then quantized the resulting input/output description by keeping the pump pulse classical and replacing the photon-units signal and idler fields with their corresponding operators. In performing this step we did not need to introduce any auxiliary operators to preserve the commutator brackets at the output, because the operator-valued coupled-mode equations (with a classical pump) preserve the commutator brackets throughout the nonlinear interaction.

The fundamental physical principle yielding spectral conjugation inside the crystal is the group-velocity ordering: as the pump overtakes the idler and the signal overtakes the pump, the trailing edge of the idler pulse and the leading edge of the signal pulse interact underneath the short-duration pump pulse, generating a time-inverted and conjugated idler component in the signal output and vice versa for the idler output. However, for a finite length crystal, there are additional contributions to the output arising from inter-

actions taking place as the pump pulse enters and exits the medium. The simplifications carried out in Section 7.4 determine the conditions under which these transient boundary effects diminish fast enough to become negligible. In particular, when $|\beta_P|T_P < 1$ and $L/\max\{|\Delta v_{PS}|, \Delta v_{PI}\} \gg 3T_P$, we are able to isolate a finite-duration time window, within which the output field operators is given by a frequency-domain Bogoliubov transformation on the two input field operators.

The remainder of the chapter contained an analysis of several relevant applications of pulsed parametric downconversion, using these time-windowed Bogoliubov transformations as the input/output operator map. The frequency responses in this map determine the interaction bandwidths imposed on coherent optical operations, such as frequency scaling and spectral conjugation. In the final section of this chapter, we assumed that the extended phase matching condition ($r = 1$) is satisfied, and determined the second-order correlation functions for the zero-mean Gaussian-state output fields when the input fields are in vacuum states. This yields a more general output state description for parametric downconverters generating DB-state biphotons. A formal connection to the biphoton regime was established by taking the low-brightness and low-flux limit of this Gaussian state. The biphoton wavefunction obtained in (7.74) is in agreement with prior derivations of this wavefunction, via perturbation analysis, whose validity is limited to the biphoton regime [62, 63]. However, it should be noted that perturbation-theory-based derivations permit arbitrary pump pulse shapes, whereas the analysis presented herein relies on a flat-top pump.

It is relevant to note at this juncture that the coincident-frequency structure of the phase-sensitive cross-correlation function in (7.70) is also observable in *classical* states. For example, assume that the two frequency-domain output field operators, $\hat{\mathcal{A}}_S(\Omega)$ and $\hat{\mathcal{A}}_I(\Omega)$, are in a zero-mean Gaussian state with nonzero second-order correlations,

$$\langle \hat{\mathcal{A}}_m^\dagger(\Omega_1)\hat{\mathcal{A}}_m(\Omega_2)\rangle = \mathcal{W}(\Omega_-)S^{(n)}(\Omega_+)\,, \tag{7.76}$$

$$\langle \hat{\mathcal{A}}_S(\Omega_1)\hat{\mathcal{A}}_I(\Omega_2)\rangle = \mathcal{W}(\Omega_-)S^{(n)}(\Omega_+)\,, \tag{7.77}$$

where $m = S, I$, and all functions are defined as before. This state mimics the correlations we have derived in (7.69) and (7.70), but the phase-sensitive cross-correlation spectrum is now $S^{(p)}(\Omega) = S^{(n)}(\Omega)$, so that this Gaussian state is a *classical* state, as detailed in Appendix E. The two classical fields having these correlations are individually in a low-

coherence thermal state, as is the case for the output of a continuous-wave parametric downconverter, but the Ω_1 frequency of the signal field has appreciable (classical) phase-sensitive correlation with the Ω_2 frequency component of the idler field when $\Omega_1 \approx \Omega_2$. However, this phase-sensitive cross-correlation is *weaker* than (7.70), which is achieved by a nonclassical Gaussian state with the same fluorescence spectra. Therefore, it is the strength of the phase-sensitive correlation spectrum compared to the fluorescence spectrum (of either field) that distinguishes a classical Gaussian state from a nonclassical one. Aside from this strength difference, coincident-frequency phase-sensitive coherence can be observed in both the classical and quantum regimes. In the next chapter, we shall exploit an optical source with such classical phase-sensitive coherence to propose a self-referencing interferometer for phase estimation.

As the final point in this chapter, let us briefly discuss the extension of Section 7.6 to $r \neq 1$. First, we define the scaled idler field operators, $\hat{\mathcal{B}}_I(t) \equiv r^{-1}\hat{\mathcal{A}}_I(t/r^2)$, and $\hat{\mathcal{B}}_{I,W}(t) \equiv r^{-1}\hat{\mathcal{A}}_{I,W}(t/r^2)$. Putting $\hat{A}_S(z=0,t)$ and $\hat{A}_I(z=0,t)$ in their vacuum states, we see from (7.47) and (7.48) that the joint state of $\hat{\mathcal{A}}_{S,W}(t)$ and $\hat{\mathcal{B}}_{I,W}(t)$ is a zero-mean Gaussian state with the nonzero correlation functions,

$$\langle \hat{\mathcal{A}}^\dagger_{S,W}(t_1)\hat{\mathcal{A}}_{S,W}(t_2)\rangle = \langle \hat{\mathcal{B}}^\dagger_{I,W}(t_1)\hat{\mathcal{B}}_{I,W}(t_2)\rangle = g^{(n)}(t_2 - t_1)\,, \tag{7.78}$$

$$\langle \hat{\mathcal{A}}_{S,W}(t_1)\hat{\mathcal{B}}_{I,W}(t_2)\rangle = g^{(p)}(t_2 + t_1)\,, \tag{7.79}$$

where we now have,

$$\mathcal{F}\big\{g^{(n)}(\tau)\big\} = S^{(n)}(\Omega/\gamma)\,, \tag{7.80}$$

$$\mathcal{F}\big\{g^{(p)}(\tau)\big\} = e^{i\Omega T_P(1-r^2)/2}\,S^{(p)}(\Omega/\gamma)\,, \tag{7.81}$$

where $S^{(n)}(\Omega)$ and $S^{(p)}(\Omega)$ were defined in (7.60) and (7.61) respectively, and $\gamma = 2/1 + r^2$ as before. Carrying out approximations analogous to (7.67) and (7.68), we arrive at

$$\langle \hat{\mathcal{A}}^\dagger_S(\Omega_1)\hat{\mathcal{A}}_S(\Omega_2)\rangle = \langle \hat{\mathcal{B}}^\dagger_I(\Omega_1)\hat{\mathcal{B}}_I(\Omega_2)\rangle = \mathcal{W}(\Omega_-)\,S^{(n)}(\Omega_+/\gamma)\,, \tag{7.82}$$

$$\langle \hat{\mathcal{A}}_S(\Omega_1)\hat{\mathcal{B}}_I(\Omega_2)\rangle = \mathcal{W}(\Omega_-)\,S^{(p)}(\Omega_+/\gamma)\,e^{i\Omega_+ T_P(1-r^2)/2}\,. \tag{7.83}$$

Therefore, we find that the two symmetry axes of the correlation functions for $\hat{\mathcal{A}}_S(\Omega)$ and

$\hat{\mathcal{A}}_I(\Omega)$ are now given by the *nonorthogonal* lines, $\Omega_2/r^2 \pm \Omega_1 = 0$. Furthermore, we find that all spectra are scaled by $1/\gamma$.

In this chapter, we have given a comprehensive analysis of pulsed parametric downconversion, set up to perform spectral conjugation of its inputs. The time-windowed, frequency-domain Bogoliubov transformations in (7.44), (7.45) and (7.47), (7.48) are the essential input/output operator mappings that facilitate our simple, yet rigorous and unifying, analysis of frequency-scaling, spectral conjugation and coincident-frequency entangled photon generation.

Chapter 8

Axial Imaging with Spectrally White Phase-Sensitive Light

In this chapter, we continue our exploration of nonstationary phase-sensitive correlations in optical pulses. The previous chapter studied collinear, type-II phase-matched and degenerate, pulsed parametric downconversion in the regime in which the pump pulse's group velocity inside the nonlinear medium ($\chi^{(2)}$ crystal) is between that of the signal and idler. The input/output relations for the signal and idler field operators, in appropriately chosen time windows at the output facet of the crystal, are single-frequency Bogoliubov transformations. This implies that vacuum input field-states generate signal and reference output fields in a zero-mean jointly-Gaussian state, with identical fluorescence spectra and a phase-sensitive cross-correlation between their equal-frequency components. This phase-sensitive correlation structure differs from that of phase-sensitive complex-stationary states, which is nonzero between $\pm\Omega$-detuned frequencies around the center frequency.

Having justified our ability to generate field states with such correlations, we turn our attention to imaging applications utilizing these correlations. In this chapter we propose an axial imaging configuration that uses two source fields that are in a spectrally-white and phase-sensitive state—such as the output of pulsed spontaneous parametric downconversion—to image the complex frequency response (magnitude and phase) of a linear time-invariant interaction without the need for a reference beam. The two features of the source state that facilitates this imaging configuration are the phase-sensitive nature of the cross-correlation at each frequency and the absence of correlation between distinct frequencies.

Because the source coherence is phase-sensitive, a receiver based on a conventional second-order interferometer will not be able to measure the desired interference signature from the received field states. The receiver that we will propose in this chapter is similar in concept to the PC-OCT interferometer from Chapter 4. In particular, first the phase-sensitive cross-correlation between two received fields will be mapped to phase-insensitive cross-correlation by conjugating one of the fields, and then they will be interfered in a Michelson interferometer to derive the desired interference signature. In addition, due to the nonstationary phase-sensitive coherence of the source, the conjugator utilized in this chapter will be a spectral conjugator (as opposed to the temporal phase-conjugator utilized in PC-OCT).

We have organized this chapter as follows. In Section 8.1, we introduce the imaging configuration and the relevant source statistics. We then derive the mean signature of this imager in Subsection 8.1.1. Subsection 8.1.2 analyzes the signal-to-noise ratio (SNR) of this imager in different operating regimes. Finally, Section 8.2 discusses the theoretical significance and the practical implementation challenges of this imaging scheme.

8.1 Self-referenced interferometry with phase-sensitive light

Consider the imaging configuration shown in Figure 8-1. Because we are interested in axial behavior we have suppressed all transverse spatial coordinates, and we follow block diagram conventions wherein all blocks are depicted in transmission, regardless of their implementation. We will also use quantum notation throughout this chapter, to facilitate the comparison between classical and quantum states of light.

In the transmitter portion of this imager, an optical source generates two fields, signal (S) and reference (R), in orthogonal polarizations and around a common center frequency ω_0. The photon-units (i.e., $\sqrt{\text{photons/s}}$) scalar baseband envelope operators, denoted by $\hat{E}_S(t)$ and $\hat{E}_R(t)$ respectively, satisfy the canonical commutator relations

$$[\hat{E}_m(t_1), \hat{E}_k^\dagger(t_2)] = \delta_{m,k}\, \delta(t_2 - t_1)\,, \tag{8.1}$$

$$[\hat{E}_m(t_1), \hat{E}_k(t_2)] = 0\,, \tag{8.2}$$

for $m, k = S, R$, and are assumed to be in a zero-mean, jointly-Gaussian state having iden-

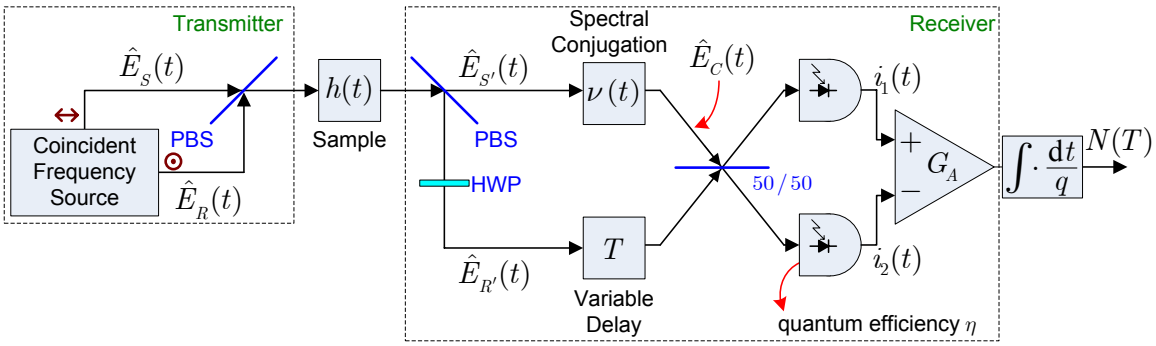

Figure 8-1: Block diagram of imager using phase-sensitive, spectrally-white signal and reference fields in orthogonal polarizations. The receiver consists of a signal-arm spectral conjugator and a reference-arm variable time delay, followed by a second-order (Michelson) interferometer. PBS: polarizing beam splitter, HWP: half-wave plate, q: electron charge.

tical phase-insensitive (normally-ordered) auto-correlations, and a nonzero phase-sensitive cross-correlation but no phase-insensitive cross-correlation and no phase-sensitive auto-correlations. For simplicity, we adopt Schell-model correlation functions [14],

$$\langle \hat{E}_m^\dagger(t_1)\hat{E}_m(t_2)\rangle = W(t_1)W(t_2)g^{(n)}(t_2-t_1) \approx W^2\big((t_1+t_2)/2\big)g^{(n)}(t_2-t_1)\,, \tag{8.3}$$

$$\langle \hat{E}_S(t_1)\hat{E}_R(t_2)\rangle = W(t_1)W(t_2)g^{(p)}(t_2+t_1) \approx W^2\big((t_2-t_1)/2\big)g^{(p)}(t_2+t_1)\,, \tag{8.4}$$

for $m = S, R$, where $|W(t)| \leq 1$ is a real and even function of duration T_0, which may be regarded as a gating function that truncates two infinite-duration, nonstationary random fields with coincident-frequency phase-insensitive auto-correlations $g^{(n)}(\tau)$ and a coincident-frequency phase-sensitive cross-correlation $g^{(p)}(\tau)$.[1] The approximations on the right-hand side follow from our assumption that $g^{(n)}(\tau)$ and $g^{(p)}(\tau)$ have durations much shorter than T_0.

The two source fields are combined via a polarizing beam splitter at the transmitter and then focused onto a particular transverse spot on the intended target. The interaction of the incident field with the target is modeled as linear, time-invariant, polarization independent and passive, such that the output fields from the interaction can be expressed as convolution relations,

$$\hat{E}_{m'}(t) = \int_{-\infty}^{\infty} \mathrm{d}\tau\, h(t-\tau)\hat{E}_m(\tau) + \hat{\mathcal{L}}_m(t)\,, \tag{8.5}$$

for $m = S, R$, where $h(t)$ denotes the impulse response in both polarizations, and $\hat{\mathcal{L}}_{m'}$ are

[1] $g^{(p)}(\tau)$ and $g^{(n)}(\tau)$ must satisfy inequality (E.10) (and inequality (E.16) if the state is classical).

vacuum-state operators introduced to preserve commutator relations.

The post-interaction field operators are then collected at the receiver and separated via another polarizing beam splitter. The reference field first propagates through a half-wave plate, and then a controlled variable time delay T, yielding the envelope $\hat{E}_{R'}(t-T)e^{i\omega_0 T}$ in the signal polarization. The signal field, on the other hand, is first spectrally-conjugated according to the idealized spectral-conjugation expressions in (7.44) and (7.56), written with our notation as[2]

$$\hat{E}_C(t) = W_C(t) \int_{-\infty}^{\infty} \mathrm{d}\tau \, \nu(t-\tau) \hat{E}^{\dagger}_{S'}(-\tau) + \hat{\mathcal{L}}_{C,v}(t) \,, \tag{8.6}$$

where $\nu(t)$ is the finite-bandwidth impulse response of the spectral conjugator, $\hat{\mathcal{L}}_{C,v}(t)$ is a vacuum-state auxiliary operator and $W_C(t)$ is a flat-top window function that is unity for $t \in [-T_C/2, T_C/2]$, and zero otherwise. Note that we have ignored a time delay in this input/output relation (cf. (7.42)) for analytic simplicity and with no loss of generality. Throughout this chapter, we will assume that the spectral conjugator is capable of conjugating the entire post-interaction signal pulse. Hence, we impose $T_0 \ll T_C$, and henceforth, ignore $W_C(t)$ in (8.6).

The final step in the Figure 8-1 configuration is to interfere $\hat{E}_C(t)$ and $\hat{E}_{R'}(t-T)e^{i\omega_0 T}$ in a second-order Michelson interferometer with dual-balanced detectors. We assume that the detectors both have quantum efficiency η, no dark current, but classical thermal noise on the photocurrents (due to post-detection electronics) with spectral density $S_{i_{\mathrm{th}}}$. The classical photocurrents from the two detectors, $i_m(t)$ for $m = 1, 2$, are differentially amplified and time-integrated to obtain the observed statistic,

$$N(T) = \frac{1}{q} \int_{-T_d/2}^{T_d/2} \mathrm{d}t \, G_A\big(i_1(t) - i_2(t)\big) \,, \tag{8.7}$$

where q is electron charge and the output is parameterized in terms of the time-delay T imposed on the reference field. Next, we will show that the mean of this statistic contains information pertinent to the target interaction impulse response $h(\cdot)$, as a function of the

[2] As discussed in Section 7.5, ideal spectral conjugation in a second-order ($\chi^{(2)}$) nonlinear crystal with pulsed pumping requires that the extended phase-matching condition is satisfied. With this the case, when the field is input through the signal port—with the idler port in a vacuum state—the spectrally-conjugated input signal field is observed at the idler output port, and vice versa for a field input through the idler port (cf. (7.45) with $r = 1$ and (7.57)). In this chapter, for concreteness, we have chosen to utilize the signal input port.

time delay T. This mean value—for each value of T—can be estimated by averaging $N(T)$ over multiple optical pulses.

8.1.1 Mean signature

For compactness, we refer to normally-ordered and phase-sensitive correlation functions according to

$$K^{(n)}_{m,k}(t_1,t_2) \equiv \langle \hat{E}^{\dagger}_m(t_1)\hat{E}_k(t_2)\rangle\,, \tag{8.8}$$

$$K^{(p)}_{m,k}(t_1,t_2) \equiv \langle \hat{E}_m(t_1)\hat{E}_k(t_2)\rangle\,, \tag{8.9}$$

respectively, where the subscripts m,k may denote any field label. The associated frequency spectra are defined, with *distinct* sign conventions, as

$$S^{(n)}_{m,k}(\Omega_1,\Omega_2) \equiv \int_{-\infty}^{\infty} \mathrm{d}t_1\mathrm{d}t_2\, e^{-i\Omega_1 t_1 + i\Omega_2 t_2} K^{(n)}_{m,k}(t_1,t_2)\,, \tag{8.10}$$

$$S^{(p)}_{m,k}(\Omega_1,\Omega_2) \equiv \int_{-\infty}^{\infty} \mathrm{d}t_1\,\mathrm{d}t_2\, e^{i\Omega_1 t_1 + i\Omega_2 t_2} K^{(p)}_{m,k}(t_1,t_2)\,, \tag{8.11}$$

from which we find that the spectra associated with the source correlations in (8.3) and (8.4) are given by

$$S^{(n)}_{m,m}(\Omega_1,\Omega_2) = \mathcal{W}(\Omega_-)\,\mathcal{G}^{(n)}(\Omega_+)\,, \tag{8.12}$$

$$S^{(p)}_{S,R}(\Omega_1,\Omega_2) = \mathcal{W}(\Omega_-)\,\mathcal{G}^{(p)}(\Omega_+)\,, \tag{8.13}$$

for $m = S,R$, where $\Omega_- \equiv \Omega_2 - \Omega_1$, $\Omega_+ \equiv (\Omega_1+\Omega_2)/2$,

$$\mathcal{G}^{(x)}(\Omega) \equiv \mathcal{F}\big\{g^{(x)}(t)\big\} \equiv \int_{-\infty}^{\infty} \mathrm{d}t\, e^{i\Omega t}\, g^{(x)}(t)\,, \tag{8.14}$$

for $x = n,p$, and $\mathcal{W}(\Omega) \equiv \mathcal{F}\{W^2(t)\}$. Consequently, the nonzero second-order moments of $\hat{E}_{S'}(t)$ and $\hat{E}_{R'}(t)$ are found to be

$$S^{(n)}_{m,m}(\Omega_1,\Omega_2) = H^*(\Omega_1)H(\Omega_2)\mathcal{W}(\Omega_-)\,\mathcal{G}^{(n)}(\Omega_+)\,, \tag{8.15}$$

$$S^{(p)}_{S',R'}(\Omega_1,\Omega_2) = H(\Omega_1)H(\Omega_2)\mathcal{W}(\Omega_-)\,\mathcal{G}^{(p)}(\Omega_+)\,, \tag{8.16}$$

for $m = S', R'$, where $H(\Omega) \equiv \mathcal{F}\{h(t)\}$ is the frequency response of the target interaction at Ω detuning from the center frequency ω_0.

The mean value of the derived statistic $N(T)$ is

$$\langle N(T) \rangle = 2G_A \eta \int_{-T_d/2}^{T_d/2} \mathrm{d}t \, \Re\{ K_{C,R'}^{(n)}(t, t-T) e^{i\omega_0 T} \}, \tag{8.17}$$

in terms of the phase-insensitive cross-correlation between the spectrally-conjugated signal and delayed reference fields. Chapter 7 shows that a pulsed parametric downconverter can generate signal and idler fields with femtosecond-scale coherence times and picosecond-scale pulsewidths, so with GHz-bandwidth avalanche photodiodes (T_d nanosecond-scale),

$$T_0 \ll T_C \ll T_d \tag{8.18}$$

is feasible. Then, with no appreciable loss of generality, we may extend the integration limits in (8.17) to infinity and derive the frequency-domain integral expression,

$$\langle N(T) \rangle = 2G_A \eta \mathcal{W}(0) \, \Re\left\{ \int_{-\infty}^{\infty} \frac{\mathrm{d}\Omega}{2\pi} \, H^2(\Omega) \mathcal{G}^{(p)}(\Omega) V^*(\Omega) e^{i(\Omega+\omega_0)T} \right\}, \tag{8.19}$$

where $V(\Omega) \equiv \mathcal{F}\{\nu(t)\}$ is the spectral conjugator's frequency response. Therefore, the mean signature from this imager is proportional to the real part of the inverse transform of $H^2(\Omega)$, filtered by the phase-sensitive coherence spectrum of the source and the frequency response of the spectral conjugator. Subject to the knowledge of the latter two functions, the magnitude and phase of $H(\Omega)$ can be inferred from this measurement without the need for a local reference beam. The frequency band over which the sample information can be retrieved, however, is the minimum of the conjugator bandwidth and that of the phase-sensitive spectrum, thus both are required to be broadband if a broadband $H(\Omega)$ is to be determined.

As an example, consider the mean signature when the source fields are in a *classical* zero-mean Gaussian state with the maximum real and positive-valued phase-sensitive cross-correlation spectrum,

$$\mathcal{G}^{(p)}(\Omega) = \mathcal{G}^{(n)}(\Omega) = (P_S \sqrt{2\pi}/\Omega_S) \, e^{-\Omega^2/2\Omega_S^2}, \tag{8.20}$$

where P_S is the signal and reference photon flux, and $2\Omega_S$ is the e^{-2}-attenuation (baseband) bandwidth of the Gaussian-shaped fluorescence spectrum. For analytic convenience we will take $W(t)$ to be a Gaussian pulse centered at zero, with e^{-2}-attenuation points at $\pm T_0/2$, so the Fourier transform of its square is given by

$$\mathcal{W}(\Omega) = (\sqrt{\pi}T_0/4)\, e^{-T_0^2\Omega^2/64}\,. \tag{8.21}$$

Let us assume that the target is a chirped, partially-reflecting mirror, i.e.,

$$H(\Omega) = re^{i\omega_0\tau_p + i\Omega\tau_g + i\Omega^2 b}\,, \tag{8.22}$$

where $0 < r \leq 1$ is its reflectivity, τ_p is its phase delay, τ_g is its group delay and b represents its second-order (group-delay) dispersion coefficient. In addition, suppose that the conjugator bandwidth significantly exceeds Ω_S, such that $\mathcal{G}^{(p)}(\Omega)V^*(\Omega) \approx |V|e^{-i\phi_V}\mathcal{G}^{(p)}(\Omega)$, where $|V|$ is the conjugator gain and ϕ_V is its phase. Then, evaluating (8.19) gives

$$\langle N(T)\rangle = \frac{G_A\eta|V|P_S T_0\sqrt{\pi}r^2}{2\big(1+16b^2\Omega_S^4\big)^{1/4}}\, \exp\Big\{-\Omega_S^2(T+2\tau_g)^2/\big[2(1+16b^2\Omega_S^4)\big]\Big\}$$
$$\times \cos\Big(\omega_0(T+2\tau_p) + 2b\Omega_S^4(T+2\tau_g)^2/(1+16b^2\Omega_S^4) - \phi_V - \phi_b\Big)\,, \tag{8.23}$$

where $\phi_b \equiv (1/2)\arctan[4b\Omega_S^2]$. Hence the signature is a Gaussian envelope that modulates a carrier of linearly increasing frequency. The dispersion coefficient may be estimated from the width of the interference fringe, the group delay is determined from the delay T that corresponds to the peak of the interference envelope, and the reflectivity can be ascertained from the peak value of the interference envelope. It is worth noting that the interference envelope has e^{-2}-attenuation width—as a function of T—equal to $4\sqrt{1+16b^2\Omega_S^4}/\Omega_S$, so the envelope broadens significantly only if the dispersion is strong enough to yield $16b^2\Omega_S^4 \gg 1$. When the dispersion coefficient is small, the linear frequency term in the carrier may be easier to determine.

8.1.2 Signal-to-noise ratio

We now turn to the signal-to-noise ratio (SNR) of this imaging configuration. Here we will focus on the single-pulse SNR, because averaging the measurements over M independent

pulses simply increases this SNR by a factor of M.

The variance of $N(T)$ can be expressed as $\langle \Delta N(T)^2 \rangle \equiv \sigma_{\text{th}}^2 + \sigma_{\text{shot}}^2 + \sigma_{\text{ex}}^2$, where the three terms represent thermal noise, shot noise and excess noise respectively. Thermal noise is additive white Gaussian noise on each photocurrent, yielding $\sigma_{\text{th}}^2 = 2G_A^2 S_{i_{\text{th}}} T_d / q^2$. The shot-noise variance is

$$\sigma_{\text{shot}}^2 = G_A^2 \eta \int_{-\infty}^{\infty} \frac{\mathrm{d}\Omega}{2\pi} \left[S_{C,C}^{(n)}(\Omega, \Omega) + S_{R',R'}^{(n)}(\Omega, \Omega) \right], \tag{8.24}$$

where the first term includes the signal-arm shot noise plus the shot noise of amplified spontaneous emission from spectral conjugation, and the second term is the shot noise from the reference arm. Finally, the excess noise is given by

$$\sigma_{\text{ex}}^2 = 2G_A^2 \eta^2 \, \Re \Bigg\{ \iint \frac{\mathrm{d}\Omega_1}{2\pi} \frac{\mathrm{d}\Omega_2}{2\pi} \Big[S_{C,R'}^{(n)}(\Omega_1, \Omega_2) S_{C,R'}^{(n)}(\Omega_2, \Omega_1) e^{i(\Omega_1 + \Omega_2 + 2\omega_0)T} + S_{C,C}^{(n)}(\Omega_1, \Omega_2) S_{R',R'}^{(n)}(\Omega_2, \Omega_1) e^{-i(\Omega_2 - \Omega_1)T} \Big] \Bigg\}. \tag{8.25}$$

To establish baseline performance, let us evaluate

$$\text{SNR} \equiv \frac{\langle N(T) \rangle^2}{\langle \Delta N(T)^2 \rangle} \tag{8.26}$$

for a partially-reflecting nondispersive mirror whose frequency response is given by (8.22) with $b = 0$ and $\tau_p = \tau_g$. In addition, to limit the spontaneous emission bandwidth, we take $V(\Omega) = V e^{-\Omega^2 / 4\Omega_V^2}$ as the frequency response of the spectral conjugator, with $V \in \mathbb{R}$ for convenience.

Consider first the classical, zero-mean, phase-sensitive, maximally-correlated Gaussian source state introduced in the previous section, with all nonzero second moments determined by (8.20) and (8.21). Evaluating the SNR at the reference arm delay that maximizes the interference signature ($T = -2\tau_g$) yields

$$\text{SNR}_{\text{c}} = \frac{\eta r^4 P_S^2 T_0^2 V^2 \pi / (1 + \gamma/2)}{\Omega_{\text{th}}^2 + r^2 P_S T_0 \sqrt{\pi} \left(1 + \frac{V^2}{\sqrt{1+\gamma}} \right) + 4 T_C V^2 \frac{\Omega_V}{\sqrt{2\pi}} + \frac{2\eta r^2 P_S T_0 V^2 \sqrt{\pi}}{\sqrt{1+\gamma}} \left(1 + r^2 \frac{P_S \sqrt{2\pi}}{\Omega_S} \sqrt{\frac{1+\gamma}{1+\gamma/2}} \right)}, \tag{8.27}$$

where $\Omega_{\text{th}}^2 = 8 S_{i_{\text{th}}} T_d / q^2 \eta$, $\gamma \equiv \Omega_S^2 / \Omega_V^2$, and the noise terms in the denominator from left to right correspond to, thermal noise, shot noise of the post-interaction signal and

reference fields, amplified spontaneous emission noise due to spectral conjugation, and the spontaneous-emission×reference plus signal×reference excess noise.

When thermal noise is not dominant, the SNR has two regimes depending on the brightness of the received fields. In the low-brightness regime, i.e., when $r^2 P_S\sqrt{2\pi}/\Omega_S \ll 1$, and with $V \geq 1$,[3] the dominant noise is amplified spontaneous emission, so we have

$$\mathrm{SNR_c} \approx \frac{\eta\pi}{4} r^4 P_S T_0 \left(\frac{P_S\sqrt{2\pi}}{\Omega_S}\right)\left(\frac{T_0\sqrt{\gamma}}{T_C(1+\gamma/2)}\right) \leq \frac{\eta\pi}{6} r^4 P_S T_0 \left(\frac{P_S\sqrt{2\pi}}{\Omega_S}\right), \tag{8.28}$$

where the upper bound is achieved when $\Omega_S = \Omega_V$ and $T_0 = T_C$, i.e., because spectral phase-conjugation generates one noise photon per temporal mode, the SNR is maximized when all temporal modes of the conjugator are utilized. Note that, broadband sources can achieve $P_S T_0 \gg 1$, so the SNR can be reasonable for bright classical sources interacting with $r \approx 1$ targets. However, the SNR decreases as the fourth-power of the mirror's reflectivity, so in high-loss scenarios the single-pulse SNR will suffer significantly. Furthermore, increasing the conjugator gain does not improve the SNR. Finally, recall that this SNR is improved by a factor of M after averaging $N(T)$ over M independent optical pulses to estimate its mean.

If, on the other hand, the received fields are bright, such that $r^2 P_S\sqrt{2\pi}/\Omega_S \gg 1$, then the signal×reference excess noise dominates the denominator of (8.27), saturating the SNR at

$$\mathrm{SNR_c} \approx \frac{\Omega_S T_0}{2\sqrt{2+\gamma}}, \tag{8.29}$$

in which the numerator is the time-bandwidth product (the number of temporal modes) of the source. In this regime, because the SNR is independent of the source power, averaging over multiple pulses is crucial to improving the SNR of the estimate.

Now suppose that the source is in a zero-mean Gaussian state with the same fluorescence spectra for the signal and reference as before, but the phase-sensitive cross-correlation is real, positive and the maximum permitted for *nonclassical* states, i.e.,

$$\mathcal{G}^{(p)}(\Omega) = \sqrt{\mathcal{G}^{(n)}(\Omega)\big(1+\mathcal{G}^{(n)}(\Omega)\big)}. \tag{8.30}$$

[3]Because there are V-independent terms in the denominator of $\mathrm{SNR_c}$, $V < 1$ does not improve performance, so we only consider $V \geq 1$.

The bright source regime, $\mathcal{G}^{(n)}(0) \gg 1$, then yields little improvement in favor of the nonclassical source, because in this regime $\mathcal{G}^{(p)}(\Omega) \approx \mathcal{G}^{(n)}(\Omega)$. However, for $\mathcal{G}^{(n)}(0) \ll 1$, $\mathcal{G}^{(p)}(\Omega) \approx \sqrt{\mathcal{G}^{(n)}(\Omega)}$, and the amplified spontaneous emission dominated SNR becomes,[4]

$$\mathrm{SNR_q} = \frac{\eta\pi}{2} r^4 P_S T_0 \left(\frac{T_0\sqrt{\gamma}}{T_C(1+\gamma)} \right) \leq \frac{\eta\pi}{4} r^4 P_S T_0 \,, \tag{8.31}$$

where satisfying the upper bound still requires $T_0 = T_C$ and $\Omega_S = \Omega_V$. Comparing this single-pulse SNR to (8.28)—resulting from a broadband classical source with identical fluorescence spectra—we obtain

$$\frac{\mathrm{SNR_q}}{\mathrm{SNR_c}} \approx \frac{\Omega_S}{P_S\sqrt{2\pi}} \gg 1 \,, \tag{8.32}$$

in which the last inequality follows from low source brightness. The SNR improvement in the quantum case is because the stronger phase-sensitive cross-correlation of the nonclassical state improves the numerator of the SNR expression, whereas the denominator, in both cases, is dominated by the same level of spontaneous emission. It is relevant to note, however, that best SNR is attained with a large number of photons in each pulse ($P_S T_0 \gg 1$), so classical sources that can generate higher photon flux than their quantum counterparts may yet achieve higher SNR. In addition, biphoton-state sources with $P_S T_0 \ll 1$ result in poor SNR performance because the signal photon is embedded in a large number of spontaneously-emitted noise photons.

8.2 Discussion

Nonstationary optical field-states that are spectrally white and phase-sensitive, can be utilized to estimate the full frequency response—magnitude and phase—of a linear time-invariant interaction. We have proposed, in this chapter, an imaging configuration that achieves this task for frequency responses which are independent of the polarization state of the incident light. In particular, two source fields in orthogonal polarizations interact with the target in either reflection or transmission. The post-interaction fields are then collected by a stand-alone receiver, which separates the two polarization components of the field, and interferes the spectrally-conjugated signal-arm with a time-delayed reference arm in a second-order (Michelson) interferometer. With a sufficiently broadband source and spectral

[4]Because $\mathcal{G}^{(n)}(0) = P_S\sqrt{2\pi}/\Omega_S \ll 1$ in this regime, excess noise will not be the dominant noise.

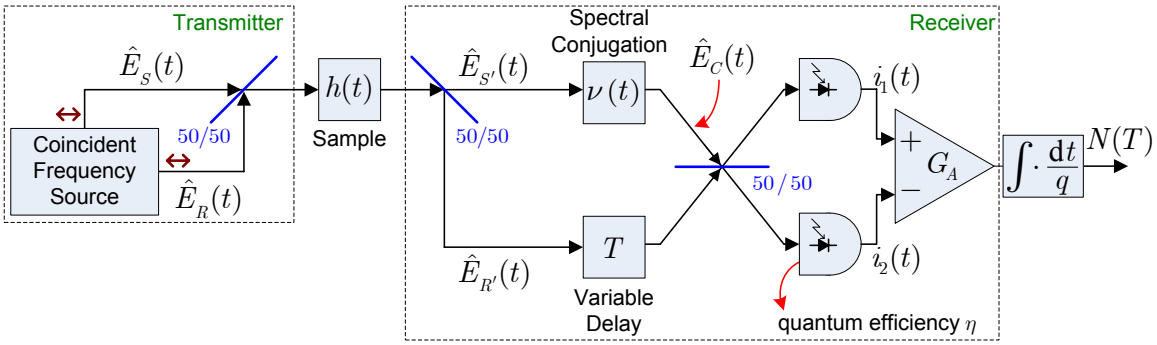

Figure 8-2: Block diagram of imager using phase-sensitive, spectrally-white, co-polarized signal and reference fields. The receiver consists of a signal-arm spectral conjugator and a reference-arm variable time delay, followed by a second-order (Michelson) interferometer. q is electron charge.

conjugator, the ensemble-average interference signature traces out the complex baseband impulse response of the interaction as a function of the reference-arm time delay. If the field collected by the receiver is dim (less than one photon per temporal mode), the single-pulse SNR is dominated by the amplified spontaneous emission of the spectral conjugator. On the other hand, for bright post-interaction fields, the signal and reference excess noise dominates the SNR denominator. In either scenario, multiple-pulse averaging is necessary to improve the mean-square estimation error. We have also shown that nonclassical source-states are beneficial—in terms of SNR—if the source is restricted to less than one photon per mode.

It is worthwhile to note that the optical spectral conjugator, in the Figure 8-1 configuration, utilizes one output port of a multiple-input, multiple-output interaction. Thus, the auxiliary outputs to which the input signal has appreciable coupling may be utilized for further information extraction. For example, if spectral conjugation is implemented via parametric downconversion as studied in Chapter 7, then the auxiliary port corresponds to the phase-insensitive amplification of the input, viz.,

$$\hat{E}_{C'}(t) = W_C(t) \int_{-\infty}^{\infty} \mathrm{d}\tau \, \mu(t-\tau) \hat{E}_{S'}(\tau) + \hat{\mathcal{L}}^{\dagger}_{C',v}(t) \,, \tag{8.33}$$

where $M(\Omega) \equiv \mathcal{F}\{\mu(t)\}$ satisfies $|M(\Omega)|^2 - |V(\Omega)|^2 = 1$, and $\hat{\mathcal{L}}^{\dagger}_{C',v}$ is an auxiliary, vacuum-state, non-Hermitian operator that does not commute with its adjoint. Therefore, $\hat{E}_{C'}(t)$ can be separately utilized for timing measurements, or for estimating $|H(\Omega)|^2$ to aid in the post-processing of the interference signature.

If the target interaction is polarization dependent (birefringent), then the imaging con-

figuration in Figure 8-1 will fail, because the signal and reference beams will be altered by different impulse responses. Nonetheless, the impulse response in either polarization can be measured by exploiting the phase-sensitive auto-correlation (rather than phase-sensitive cross-correlation) of classical or quantum source field states. The appropriately modified imaging configuration for this task is shown in Figure 8-2, in which the source generates co-polarized signal and reference fields, and the polarizing beam splitters are replaced with polarization-insensitive 50/50 beam splitters. It is trivial to verify that the mean signature of this imager is identical to (8.19) (up to a scaling of 1/4 due to loss in the two beam splitters), with $\mathcal{G}^{(p)}$ now representing the phase-sensitive *auto-correlation* spectrum of the source state *after* it is combined in the 50/50 beam splitter. The only difference occurs in the noise behavior, because now the signal and reference fields have nonzero phase-sensitive auto-correlations and a phase-insensitive cross-correlation. This does not affect the thermal noise or shot noise terms, but the excess noise expression in (8.25) becomes

$$\sigma_{\text{ex}}^2 = 2G_A^2\eta^2\,\Re\Bigg\{\iint \frac{\mathrm{d}\Omega_1}{2\pi}\frac{\mathrm{d}\Omega_2}{2\pi}\Big[S^{(n)}_{C,R'}(\Omega_1,\Omega_2)S^{(n)}_{C,R'}(\Omega_2,\Omega_1)\,e^{i(\Omega_1+\Omega_2+2\omega_0)T} + S^{(n)}_{C,C}(\Omega_1,\Omega_2)S^{(n)}_{R',R'}(\Omega_2,\Omega_1)\,e^{-i(\Omega_2-\Omega_1)T} + S^{(p)*}_{C,R'}(\Omega_1,\Omega_2)S^{(p)}_{C,R'}(\Omega_2,\Omega_1)\,e^{-i(\Omega_2-\Omega_1)T} + S^{(p)*}_{C,C}(\Omega_1,\Omega_2)S^{(p)}_{R',R'}(\Omega_2,\Omega_1)\,e^{i(\Omega_2+\Omega_1+2\omega_0)T}\Big]\Bigg\}, \quad (8.34)$$

where $*$ denotes complex-conjugation. Note that the first two terms here are identical to the previous case, but the latter two represent the extra noise contributions of the nonzero correlations. Nevertheless, for maximally-correlated, phase-sensitive classical and quantum sources, these additional terms at most double the excess noise contribution from the first two terms. Consequently, in shot-noise dominated operation the SNR of this imager is degraded—relative to the SNR of the previous case—by a factor of sixteen due to the beam splitter losses, and in excess-noise dominated operation the SNR is penalized by a factor of two.

Let us close this chapter by addressing implementation advantages and challenges of the proposed imaging configurations. The foremost advantage of this imager, over other phase-sensitive measurement schemes, such as optical coherence tomography, is the ability to derive both arms of the interferometer from the received beam. As a result, the source and the receiver can be constructed as separate self-contained units and placed appropriately to

interrogate a target in either reflection or transmission geometries. The two crucial elements of this imager are the source and the spectral conjugator. One can construct the source with the desired statistics by modulating the phase and amplitude of two coherent laser pulses. However, even with telecom grade electro-optical modulators, the bandwidth will be in the GHz range. It is more desirable to utilize nonlinear optical processes, such as spontaneous parametric downconversion (which was analyzed in Chapter 7), to generate high-flux and broadband (THz range) signal and reference optical pulses with the desired phase-sensitive cross-correlation.

The second crucial element to this imager is the spectral conjugator. In addition to parametric downconversion, spectral conjugation occurs in several nonlinear interactions, including pulsed four-wave mixing [72, 73], spectral four-wave mixing [74] and three-wave mixing with extended phase matching [61, 75]. Note that high resolution requires a broadband conjugator, and high SNR requires—at least—lossless spectral conjugation. Therefore, within the aforementioned processes, the one with the highest gain-bandwidth product should be utilized in this imager.

As with any interferometer, it is crucial that all components prior to detection have phase stability. In particular, the spectral-conjugator frequency response and the variable time delay—often implemented with a moving mirror—are the two components that must be phase stable. It was shown in Section 4.4 that random phase fluctuations in $V(\Omega)$, result in exponential decay of fringe visibility as a function of the fluctuation variance, and the same conclusion is true for nonuniform mirror motion.

In summary, we have proposed a new phase-sensitive imaging scheme that acquires the full frequency response of a linear time-invariant system, by interrogating this system with spectrally-white, phase-sensitive broadband light pulses. Phase-sensitive coherence, which retains absolute phase information, is a crucial feature of the source. The interaction of spectrally-white, phase-sensitive light with a linear time-invariant filter modifies the phase-sensitive spectrum of the input by the square of the complex-valued frequency response. Then, measuring the phase-sensitive correlation in an appropriate second-order interferometer, such as the one presented in this chapter, yields an estimate of the phase-sensitive spectrum, which contains a unique signature for the complex-valued frequency response of the filter. The SNR per pulse is shown to be dominated by conjugator spontaneous-emission noise or signal$\times$reference excess noise, so averaging over multiple pulses is necessary for high

SNR. Both classical and nonclassical field states with phase-sensitive coherence are suitable for such an imaging scheme, provided that their total photon flux and fluorescence spectra satisfy the requirements determined in this chapter.

Chapter 9

Conclusions

Quantum imaging can be broadly classified as imaging configurations utilizing sources that emit nonclassical optical states, but, so far, conventional photodetection-based measurement schemes at the receiver. The most commonly employed nonclassical state in quantum imaging to date has been a pair of multimode entangled photons, most often obtained from spontaneous parametric downconversion. The classical theory of light cannot account for such field states, so a strictly quantum description of light is required to quantify the performance of these imagers.

On the other hand, conventional optical imaging employs bright and high-flux thermal or coherent-state optical fields. All of the field states employed in conventional imaging applications are *classical*, in that they are coherent states or statistical mixtures thereof. Thus, a quantitatively accurate performance analysis for these conventional imagers is entirely within the realm of classical statistical optics and semiclassical photodetection theory: knowledge of the quantum mechanical nature of light is inconsequential to predicting the images obtained with such configurations.

The typical framework for the theoretical foundation of biphoton-state quantum imaging relies on wavefunctions, wherein the state of two photons is expressed as a superposition over the spatiotemporal modes of the optical field using wavefunction weighting. This approach, however, limits the analysis to such particle-like states of light, which excludes classical states. In contrast, conventional low-coherence optical imaging is concerned predominantly with the correlation functions of random classical fields, and pays no regard for the quantum mechanical properties of light. Thus, it does not encompass the biphoton regime of imaging.

These two incompatible mathematical frameworks have made it difficult to quantify the boundary between the classical and quantum regimes of optical imaging. Fortunately, these two regimes can be unified under Gaussian-state optical fields. As we have reiterated many times throughout this thesis, the output state of a parametric downconverter with vacuum inputs and a nondepleting pump, is a *nonclassical* zero-mean Gaussian state with phase-sensitive coherence between the two output fields. Moreover, its low-brightness, low-flux limiting form reduces to the biphoton state. Similarly, the thermal states and coherent states of classical imaging are both subsets of *classical* phase-insensitive Gaussian states. Therefore Gaussian states form a natural framework to seek the classical/quantum boundary in optical imaging.

The foremost effort in this thesis has been to rigorously establish this framework and unambiguously identify the boundary between the classical and quantum regimes of optical imaging, thereby providing a more complete understanding of the features observed in both regimes. The primary conclusion of the work presented herein is that almost all of the features observed in biphoton-state quantum imagers stem from the *phase-sensitive* nature of the coherence between the two photons, rather than their entanglement *per se*. Consequently, classical Gaussian states of light with phase-sensitive coherence emerges as a new subset of Gaussian-state optical sources that can achieve most benefits observed with the biphoton state, but at much higher photon flux, and without resorting to nonclassical sources and single-photon counters. In particular, our analysis of ghost imaging and two-photon imaging, in Chapters 5 and 6 respectively, has determined that classical phase-sensitive Gaussian states can replicate all features of the images obtained with a biphoton state. However, the image is embedded in a more prominent background when photocurrent correlation is used to measure the image signature. Nonetheless, an alternative method of measuring classical phase-sensitive correlations was studied in detail in Chapter 4 for phase-conjugate optical coherence tomography—and revisited in Chapter 8 for white-light interferometric imaging—in which the phase-sensitive coherence is converted to phase-insensitive coherence via an optical conjugator, and then a simple second-order interferometer is used to measure this correlation. Thus, the loss of contrast with classical phase-sensitive light, in general, does not preclude reasonable performance with other measurement schemes.

The prevailing conclusion from this thesis is that the only fundamental distinction be-

tween the image signatures of classical phase-sensitive light sources and those of nonclassical phase-sensitive sources—with photocurrent correlation employed as the measurement—is the image contrast, which is defined as the ratio of the dynamic range of the image to the featureless background level in which this image is embedded. In this thesis we have provided a detailed analysis of the contrast in both ghost imaging and two-photon imaging. The high contrast of the image signatures generated by two-field nonclassical Gaussian-state sources occurs because the phase-sensitive cross-correlation is responsible for image formation, whereas the phase-insensitive auto-correlation is responsible for the background, and the maximum of the former is *much stronger* than the latter in the low-brightness, low-flux limit. When the flux is driven low enough such that biphoton analysis with wavefunctions yields an approximate representation of the output state, there is at most one photon in either of the two fields, which completely eliminates the background term (however, care must be exercised with wavefunction analysis as this is an approximate representation of the state). Whether the contrast advantage observed in the low-flux regime is of practical relevance, however, strongly varies from one application to another. We have discussed two applications in this thesis that are excellent examples of this variation. Outdoor ghost imaging during daytime has little to gain from nonclassical low-flux phase-sensitive light, due to scattered background light from the atmosphere. Optical lithography, however, may benefit significantly from such a source state when all excess noise contributions are eliminated.

Although classical phase-insensitive coherence has been very well-understood for a long time, little attention has been devoted to the study of phase-sensitive coherence. This is partially due to natural illumination exhibiting only phase-insensitive coherence. However, with the increasing interest in biphoton imaging, phase-sensitive coherence has become central to understanding the properties of these imagers, as well as those of the classical phase-sensitive imagers proposed in this thesis. To satisfy this need, we have devoted Chapter 3, as well as parts of most of the subsequent chapters, to developing coherence theory for phase-sensitive light in free space. Much of the foundational work is laid out in Chapter 3, and the subsequent chapters develop paraxial propagation properties of phase-sensitive coherence tailored towards the specific application of interest.

Gaussian states with phase-sensitive coherence also encompass other states of recent interest, such as the DB state that consists of coincident-frequency entangled photon pairs. Chapter 7 was devoted to a rigorous derivation of the input/output description of the

pulsed parametric downconversion process that generates DB states. It determined that the output state is a zero-mean Gaussian state with spectrally-white phase-sensitive coherence. Analogous to the aforementioned biphoton state, the low-flux limiting form of this state is shown to reduce to the DB state. The white-noise property of the Gaussian-state output from this pulsed parametric downconverter is utilized in Chapter 8, in conjunction with a receiver that uses spectral conjugation, to theoretically demonstrate that one can obtain phase and magnitude information from a target interaction without a local reference beam. The imaging property of this configuration, as before, relies on the phase-sensitive coherence of the source, measured by means of optical (spectral) conjugation followed by a second-order Michelson interferometer. Therefore, phase-sensitive coherence has notable practical implications for new imaging configurations.

The work presented in this thesis can be expanded in several interesting directions. The phase-sensitive coherence theory in Chapter 3 is limited to scalar fields in isotropic media. It is of interest to extend this work to more complicated media. In particular, extending this theory to media that better represent biological samples [76] would assist in furthering the application-specific performance of PC-OCT. Chapter 4, which develops the theory for PC-OCT, would benefit significantly from a proof-of-principle experiment. The most significant remaining question in the ghost imaging analysis in Chapter 5 is the signal-to-noise ratio for classical-state ghost imagers, which will determine the optimum flux versus background-noise tradeoff. However, because computing the eighth-moment of Gaussian-state fields is cumbersome, a meaningful SNR expression has yet to be obtained. Although Chapter 6 provides a comprehensive understanding of the biphoton-state proof-of-principle experiment for quantum lithography, because the Gaussian-state framework falls short of encompassing N-photon entangled states (such as $N00N$ states), additional work in higher-order coherence theory is necessary to develop a complete understanding of N-photon quantum lithography [77]. Chapter 7 derives the output state of pulsed spontaneous parametric downconversion, whose low-flux limiting form is the DB state. Therefore, a general Gaussian-state analysis of the Hong-Ou-Mandel interference dip is a natural extension of this chapter that should be pursued. Finally, the Chapter 8 imaging configuration requires assessment of its signal-to-noise ratio in realistic scenarios, along with the evaluation of its implementation challenges. If a regime of interest can be identified, a proof-of-principle experiment would be of significant value.

In summary, in this thesis we have unified classical and biphoton-state quantum imaging within a Gaussian-state framework, and have unambiguously identified the boundary between classical and quantum Gaussian-state optical imaging. We have established that phase-sensitive coherence is the fundamental property of the biphoton state that yields an image signature in optical coherence tomography (OCT), ghost imaging, and two-photon imaging. We have expanded on this key conclusion by proposing phase-conjugate OCT, which uses classical phase-sensitive light and reaps the advantages in quantum OCT that were previously ascribed to the entanglement property of the biphotons. In addition, we have proposed phase-sensitive white-light interferometry with stand-alone transmitter and receiver units, which facilitates the acquisition of the complex-valued frequency response resulting from the interaction of the source fields with a target. As a foundation for the preceding analysis, we developed phase-sensitive coherence theory for free-space optical fields, studied the paraxial propagation of phase-sensitive coherence, and established mode-decompositions for arbitrary scalar Gaussian states. The union of the work presented in this thesis aims at improving our understanding of the fundamentals governing quantum and classical optical imaging. Phase-sensitive coherence has proven central to this task, as we have shown comprehensively that almost all characteristics of biphoton-state imagers are obtainable with classical phase-sensitive sources.

Appendix A

Proof for the Normal-Mode Decomposition

Here we provide a proof of Theorem 1. We shall find it convenient to work with the two real-valued quadratures $E_1(\mathbf{x}) \equiv [E(\mathbf{x}) + E^*(\mathbf{x})]/2$ and $E_2(\mathbf{x}) \equiv [E(\mathbf{x}) - E^*(\mathbf{x})]/2i$. The joint correlation-function matrix for these quadratures,

$$\mathrm{K}_Q(\mathbf{x}_1, \mathbf{x}_2) \equiv \left\langle \begin{bmatrix} E_1(\mathbf{x}_1) \\ E_2(\mathbf{x}_1) \end{bmatrix} \begin{bmatrix} E_1(\mathbf{x}_2) & E_2(\mathbf{x}_2) \end{bmatrix} \right\rangle , \tag{A.1}$$

is real, symmetric, and positive semidefinite. Our proof uses concepts from symplectic algebra, and parallels the proof of Williamson's Theorem for decomposing finite-dimensional, real, positive semidefinite matrices [34].

Let us first assume that $\mathrm{K}_Q(\mathbf{x}_1, \mathbf{x}_2)$ is positive definite, and later reconcile the case of positive semidefinite kernels. We begin by defining the nonsingular, anti-symmetric kernel

$$\mathrm{A}(\mathbf{x}_1, \mathbf{x}_2) = \int \mathrm{K}_Q^{1/2}(\mathbf{x}_1, \mathbf{x}') \, \mathrm{J} \, \mathrm{K}_Q^{1/2}(\mathbf{x}', \mathbf{x}_2) \, \mathrm{d}\mathbf{x}' , \tag{A.2}$$

which satisfies $\mathrm{A}(\mathbf{x}_1, \mathbf{x}_2) = -\mathrm{A}^T(\mathbf{x}_2, \mathbf{x}_1)$, where ^{T} indicates transpose, and

$$\mathrm{J} \equiv \begin{bmatrix} 0 & 1 \\ -1 & 0 \end{bmatrix} . \tag{A.3}$$

Because, $\mathrm{A}(\mathbf{x}_1, \mathbf{x}_2)$ is anti-symmetric, it admits a singular-value type decomposition of form

$$\mathrm{A}(\mathbf{x}_1, \mathbf{x}_2) = \sum_{m=1}^{\infty} \mu_m [\boldsymbol{\Phi}_m(\mathbf{x}_1)\boldsymbol{\phi}_m^T(\mathbf{x}_2) - \boldsymbol{\phi}_m(\mathbf{x}_1)\boldsymbol{\Phi}_m^T(\mathbf{x}_2)]\,, \tag{A.4}$$

where $\mu_m > 0$, for $m = 1, 2, \ldots$, and $\{\boldsymbol{\Phi}_m(\mathbf{x})\} \cup \{\boldsymbol{\phi}_m(\mathbf{x})\}$ is a complete, orthonormal set of eigenfunctions in the space of square-integrable functions. This eigenfunction decomposition can be found by diagonalizing the symmetric kernel $\int \mathrm{A}^T(\mathbf{x}', \mathbf{x}_1)\mathrm{A}(\mathbf{x}', \mathbf{x}_2)\,\mathrm{d}\mathbf{x}'$. Defining a new set of functions through the invertible transformations

$$\boldsymbol{\Xi}_m(\mathbf{x}) \equiv \frac{1}{\sqrt{\mu_m}} \int \mathrm{K}_Q^{1/2}(\mathbf{x}, \mathbf{x}')\boldsymbol{\Phi}_m^T(\mathbf{x}')\,\mathrm{d}\mathbf{x}' \tag{A.5}$$

and

$$\xi_m(\mathbf{x}) \equiv \frac{1}{\sqrt{\mu_m}} \int \mathrm{K}_Q^{1/2}(\mathbf{x}, \mathbf{x}')\boldsymbol{\phi}_m^T(\mathbf{x}')\,\mathrm{d}\mathbf{x}'\,, \tag{A.6}$$

yields another complete set of functions that obey

$$\int \boldsymbol{\Xi}_m^T(\mathbf{x})\,\mathrm{J}\,\boldsymbol{\Xi}_k(\mathbf{x})\,\mathrm{d}\mathbf{x} = \int \xi_m^T(\mathbf{x})\,\mathrm{J}\,\xi_k(\mathbf{x})\,\mathrm{d}\mathbf{x} = 0\,, \tag{A.7}$$

and

$$\int \boldsymbol{\Xi}_m^T(\mathbf{x})\,\mathrm{J}\,\xi_k(\mathbf{x})\,\mathrm{d}\mathbf{x} = \delta_{mk}\,. \tag{A.8}$$

Such a set of functions, with the completeness property expressed in matrix form as

$$\sum_{m=1}^{\infty} \begin{bmatrix} \boldsymbol{\Xi}_m(\mathbf{x}_1) & \xi_m(\mathbf{x}_1) \end{bmatrix} \mathrm{J} \begin{bmatrix} \boldsymbol{\Xi}_m^T(\mathbf{x}_2) \\ \xi_m^T(\mathbf{x}_2) \end{bmatrix} = \delta(\mathbf{x}_2 - \mathbf{x}_1)\,\mathrm{J}\,, \tag{A.9}$$

is called a *symplectic* basis. This particular symplectic basis, in addition, diagonalizes the original kernel of interest, according to

$$\begin{aligned} &\iint \boldsymbol{\Xi}_m^T(\mathbf{x}_1)\,\mathrm{J}^T\,\mathrm{K}_Q(\mathbf{x}_1, \mathbf{x}_2)\,\mathrm{J}\,\boldsymbol{\Xi}_k(\mathbf{x}_2)\,\mathrm{d}\mathbf{x}_1\,\mathrm{d}\mathbf{x}_2 \\ &\qquad = \iint \xi_m^T(\mathbf{x}_1)\,\mathrm{J}^T\,\mathrm{K}_Q(\mathbf{x}_1, \mathbf{x}_2)\,\mathrm{J}\,\xi_k(\mathbf{x}_2)\,\mathrm{d}\mathbf{x}_1\,\mathrm{d}\mathbf{x}_2 = \mu_m\delta_{mk} \end{aligned} \tag{A.10}$$

and

$$\iint \boldsymbol{\Xi}_m^T(\mathbf{x}_1)\,\mathrm{J}^T\,\mathrm{K}_Q(\mathbf{x}_1,\mathbf{x}_2)\,\mathrm{J}\,\xi_k(\mathbf{x}_2)\,\mathrm{d}\mathbf{x}_1\,\mathrm{d}\mathbf{x}_2 = 0\,, \tag{A.11}$$

which together imply that

$$\mathrm{K}_Q(\mathbf{x}_1,\mathbf{x}_2) = \sum_{m=1}^{\infty} \mu_m \begin{bmatrix}\boldsymbol{\Xi}_m(\mathbf{x}_1) & \xi_m(\mathbf{x}_1)\end{bmatrix} \begin{bmatrix}\boldsymbol{\Xi}_m^T(\mathbf{x}_2) \\ \xi_m^T(\mathbf{x}_2)\end{bmatrix}. \tag{A.12}$$

The final step is then to perform the (scaled) unitary transformation $\mathrm{K}(\mathbf{x}_1,\mathbf{x}_2) = \mathrm{U}_2\,\mathrm{K}_Q(\mathbf{x}_1,\mathbf{x}_2)\,\mathrm{U}_2^H$, where

$$\mathrm{U}_2 = \begin{bmatrix}1 & i \\ 1 & -i\end{bmatrix}, \tag{A.13}$$

which yields $\lambda_m = 2\mu_m$ and

$$\mathrm{V}_m(\mathbf{x}) = (1/2)\mathrm{U}_2 \begin{bmatrix}\boldsymbol{\Xi}_m(\mathbf{x}_1) & \xi_m(\mathbf{x}_1)\end{bmatrix} \mathrm{U}_2^H. \tag{A.14}$$

The completeness and orthogonality relations stated in Theorem 2 are then obtained by applying the same transformation to (A.9) and (A.7)–(A.8), respectively.

In order to assess the uniqueness of the $\{\mathrm{V}_m(\mathbf{x})\}$, recall that each distinct singular value, μ_m, of $\mathrm{A}(\mathbf{x}_1,\mathbf{x}_2)$ spans an input eigenspace of dimension 2. Therefore a new pair of input eigenfunctions spanning the same eigenspace can be obtained by the transformation

$$\begin{bmatrix}\boldsymbol{\Phi}'_m(\mathbf{x}) & \boldsymbol{\phi}'_m(\mathbf{x})\end{bmatrix} \equiv \begin{bmatrix}\boldsymbol{\Phi}_m(\mathbf{x}) & \boldsymbol{\phi}_m(\mathbf{x})\end{bmatrix} \mathrm{R}_m\,, \tag{A.15}$$

where

$$\mathrm{R}_m \equiv \begin{bmatrix}\cos(\theta_m) & -\sin(\theta_m) \\ \sin(\theta_m) & \cos(\theta_m)\end{bmatrix}, \tag{A.16}$$

for $\theta_m \in [0, 2\pi)$, is an arbitrary 2×2 rotation matrix. Thus, for each m, we have that $\begin{bmatrix}\boldsymbol{\Xi}_m(\mathbf{x}_1) & \xi_m(\mathbf{x}_2)\end{bmatrix} \mathrm{R}_m$ is also an admissible eigenfunction matrix. Transforming this general expression via U_2, gives the expression in the theorem statement.

The final issue we must address is dealing with positive semidefinite kernels. When K_Q has—possibly an infinite number of—zero eigenvalues, $\mathrm{A}(\mathbf{x}_1,\mathbf{x}_2)$ also becomes singular. Therefore, the proof given above should be followed only for the nonzero singular values

of A, and completeness statements should be ignored. The set $\{\mathbf{\Xi}_m(\mathbf{x}),\} \cup \{\xi_m(\mathbf{x})\}$, obtained from (A.6), is still symplectic, satisfying (A.7) and (A.8). However, it is no longer complete. To complete the basis, we must employ the symplectic variant of Gram-Schmidt orthogonalization [34] before proceeding with the remainder of the proof.

Appendix B

Classical Gaussian States with Arbitrary Cross-Correlations

Let us use $\hat{E}_S(\mathbf{x})$ and $\hat{E}_R(\mathbf{x})$ to denote the signal and reference field operators, where $\mathbf{x} = (\boldsymbol{\rho}, t)$ conveniently combines their space and time arguments. In this appendix we will construct a zero-mean, jointly Gaussian, *classical* state for these two quantum fields that has arbitrarily prescribed phase-insensitive and phase-sensitive cross-correlation functions,

$$K_{S,R}^{(n)}(\mathbf{x}_1, \mathbf{x}_2) \equiv \langle \hat{E}_S^\dagger(\mathbf{x}_1) \hat{E}_R(\mathbf{x}_2) \rangle \,, \tag{B.1}$$

$$K_{S,R}^{(p)}(\mathbf{x}_1, \mathbf{x}_2) \equiv \langle \hat{E}_S(\mathbf{x}_1) \hat{E}_R(\mathbf{x}_2) \rangle \,, \tag{B.2}$$

respectively. We only require that both functions be sufficiently well behaved that they can be regarded as kernels which map the Hilbert space of square-integrable functions onto itself. Under this regularity condition we can perform singular-value decompositions of these continuous kernels [78] to obtain

$$K_{S,R}^{(n)}(\mathbf{x}_1, \mathbf{x}_2) = \sum_{m=1}^{\infty} \eta_m \phi_m^*(\mathbf{x}_1) \Phi_m(\mathbf{x}_2) \,, \tag{B.3}$$

$$K_{S,R}^{(p)}(\mathbf{x}_1, \mathbf{x}_2) = \sum_{m=1}^{\infty} \mu_m \psi_m(\mathbf{x}_1) \Psi_m(\mathbf{x}_2) \,, \tag{B.4}$$

where $\{\phi_m(\mathbf{x})\}$, $\{\Phi_m(\mathbf{x})\}$, $\{\psi_m(\mathbf{x})\}$ and $\{\Psi_m(\mathbf{x})\}$, for $1 \leq m < \infty$, are four complete and orthonormal sets spanning square-integrable functions, and the coefficients η_m and μ_m are

real, finite, and nonnegative for all m.

Suppose we define two pairs of free-space, paraxial field operators, $\{\hat{E}_{S'}(\mathbf{x}), \hat{E}_{R'}(\mathbf{x})\}$ and $\{\hat{E}_{S''}(\mathbf{x}), \hat{E}_{R''}(\mathbf{x})\}$, having the modal expansions

$$\hat{E}_{S'}(\mathbf{x}) = \sum_{m=1}^{\infty} \hat{a}_{S',m}\phi_m(\mathbf{x})\,, \tag{B.5}$$

$$\hat{E}_{R'}(\mathbf{x}) = \sum_{m=1}^{\infty} \hat{a}_{R',m}\Phi_m(\mathbf{x})\,, \tag{B.6}$$

and

$$\hat{E}_{S''}(\mathbf{x}) = \sum_{m=1}^{\infty} \hat{a}_{S'',m}\psi_m(\mathbf{x})\,, \tag{B.7}$$

$$\hat{E}_{R''}(\mathbf{x}) = \sum_{m=1}^{\infty} \hat{a}_{R'',m}\Psi_m(\mathbf{x})\,. \tag{B.8}$$

In these expansions, $\{\hat{a}_{\ell,m}\}$, for $\ell = S', S'', R', R''$ and $1 \leq m < \infty$, is a set of photon annihilation operators, with the canonical commutation relations $[\hat{a}_{\ell,m}, \hat{a}^{\dagger}_{\ell',m'}] = \delta_{\ell,\ell'}\delta_{m,m'}$ and $[\hat{a}_{\ell,m}, \hat{a}_{\ell',m'}] = 0$.

Now, let us put the modes associated with the $\{\hat{a}_{\ell,m}\}$ into a zero-mean, jointly Gaussian state whose only nonzero phase-insensitive cross-correlations are,

$$\langle \hat{a}^{\dagger}_{S',m}\hat{a}_{R',m}\rangle = 2\eta_m\,, \tag{B.9}$$

and whose only nonzero phase-sensitive cross-correlations are

$$\langle \hat{a}_{S'',m}\hat{a}_{R'',m}\rangle = 2\mu_m\,, \tag{B.10}$$

whence

$$\langle \hat{E}^{\dagger}_{S'}(\mathbf{x}_1)\hat{E}_{R'}(\mathbf{x}_2)\rangle = 2K^{(n)}_{S,R}(\mathbf{x}_1, \mathbf{x}_2)\,, \tag{B.11}$$

$$\langle \hat{E}_{S''}(\mathbf{x}_1)\hat{E}_{R''}(\mathbf{x}_2)\rangle = 2K^{(p)}_{S,R}(\mathbf{x}_1, \mathbf{x}_2)\,. \tag{B.12}$$

Classical Gaussian states must have correlations that obey the Cauchy-Schwarz inequalities from (5.18) and (5.21), see [19]. Thus Eqs. (B.9) and (B.10) imply that the modal

auto-correlations must obey

$$\langle \hat{a}^{\dagger}_{S',m} \hat{a}_{S',m} \rangle \langle \hat{a}^{\dagger}_{R',m} \hat{a}_{R',m} \rangle \geq 4\eta_m^2 \,, \tag{B.13}$$

and

$$\langle \hat{a}^{\dagger}_{S'',m} \hat{a}_{S'',m} \rangle \langle \hat{a}^{\dagger}_{R'',m} \hat{a}_{R'',m} \rangle \geq 4\mu_m^2 \,, \tag{B.14}$$

for $1 \leq m < \infty$. We will take the modal auto-correlations to equal these lower bounds, by assuming that

$$\langle \hat{a}^{\dagger}_{S',m} \hat{a}_{S',m} \rangle = \langle \hat{a}^{\dagger}_{R',m} \hat{a}_{R',m} \rangle = 2\eta_m \tag{B.15}$$

$$\langle \hat{a}^{\dagger}_{S'',m} \hat{a}_{S'',m} \rangle = \langle \hat{a}^{\dagger}_{R'',m} \hat{a}_{R'',m} \rangle = 2\mu_m, \tag{B.16}$$

In addition, we assume that all modal correlations—aside from those which have already been specified—vanish. Equations (B.9), (B.10), (B.15) and (B.16) then determine the zero-mean, jointly Gaussian state of the four fields, $\{\hat{E}_{S'}(\mathbf{x}), \hat{E}_{R'}(\mathbf{x}), \hat{E}_{S''}(\mathbf{x}), \hat{E}_{R''}(\mathbf{x})\}$, which is the tensor product of the zero-mean, jointly Gaussian state of $\{\hat{E}_{S'}(\mathbf{x}), \hat{E}_{R'}(\mathbf{x})\}$ and that of $\{\hat{E}_{S''}(\mathbf{x}), \hat{E}_{R''}(\mathbf{x})\}$, because all their cross-correlations are zero. Defining the signal and reference fields via

$$\hat{E}_S(\mathbf{x}) = (\hat{E}_{S'}(\mathbf{x}) + \hat{E}_{S''}(\mathbf{x}))/\sqrt{2} \,, \tag{B.17}$$

$$\hat{E}_R(\mathbf{x}) = (\hat{E}_{R'}(\mathbf{x}) + \hat{E}_{R''}(\mathbf{x}))/\sqrt{2} \,, \tag{B.18}$$

thus yields a pair of field operators that are in a zero-mean, jointly Gaussian, *classical* state with the desired phase-sensitive and phase-insensitive cross-correlation functions.

Appendix C

Exact Solution to Coupled-Mode Equations

In this appendix, we solve the coupled-mode equations (7.21), (7.22) to obtain $A'_S(z'=L,t')$ and $A_I(z'=L,t')$ for $t' \in \mathbb{R}$, using the flat-top pump pulse given in (7.24), and the boundary conditions $A'_S(z'=0,t')$ and $A_I(z'=0,t')$ for all $t' \in \mathbb{R}$. As explained in Chapter 7, this requires solving

$$\left[\frac{\partial}{\partial t'} + \Delta v_{PS}\frac{\partial}{\partial z'} + i\frac{\Delta k \Delta v_{PS}}{2}\right] A'_S(z',t') = i\kappa A_P \Delta v_{PS} A'^*_I(z',t')\,, \tag{C.1}$$

$$\left[\frac{\partial}{\partial t'} + \Delta v_{PI}\frac{\partial}{\partial z'} - i\frac{\Delta k \Delta v_{PI}}{2}\right] A'^*_I(z',t') = -i\kappa^* A^*_P \Delta v_{PI} A'_S(z',t')\,, \tag{C.2}$$

for $(z',t') \in [0,L]\times[0,T_P]$, where the boundary conditions are $A'_S(z'=0,t')$ for $t' \in [0,T_P]$, $A'_S(z',t'=T_P)$ for $z' \in [0,L]$, $A'_I(z'=0,t')$ for $t' \in [0,T_P]$ and $A'_I(z',t'=0)$ for $z' \in [0,L]$, as depicted in Figure 7-2. In these differential equations we have allowed κ to be complex, and we reiterate that $\Delta v_{PS} < 0 < \Delta v_{PI}$.

Let us first find $A'_S(z',T_P)$ and $A'_I(z',t'=0)$ for $z' \in [0,L]$, in terms of $A'_S(z'=0,t')$ and $A_I(z'=0,t')$. Fortunately, in the absence of the pump, the solutions are given by (7.25) and (7.26), such that the boundary conditions correspond to line-segments on $z'=0$,

$$A'_S(z',T_P) = A'_S\big(0, T_P + z'/|\Delta v_{PS}|\big)\, e^{-i\Delta k z'/2}\,, \tag{C.3}$$

$$A'_I(z',0) = A'_I\big(0, -z'/\Delta v_{PI}\big)\, e^{-i\Delta k z'/2}\,. \tag{C.4}$$

Because we have a set of linear, constant coefficient, partial differential equations of two variables with boundary conditions on a rectangular region, it is convenient to utilize Laplace transform techniques [79]. However, we exercise care in choosing the appropriate Laplace transform for each of the two variables. We begin with the spatial coordinate, z'. All boundary conditions along the orthogonal axis, t', are defined on $z' = 0$, and we seek a solution for $z' > 0$, so using a *unilateral* Laplace transform is the most convenient. We define the fields that are Laplace-transformed in their first argument as

$$\widetilde{A}_S(q,t') \equiv \int_0^\infty \mathrm{d}z'\, e^{-qz'} A'_S(z',t')\,, \tag{C.5}$$

$$\widetilde{A}_I(q,t') \equiv \int_0^\infty \mathrm{d}z'\, e^{-qz'} A'^*_I(z',t')\,, \tag{C.6}$$

where we note that we have defined $\widetilde{A}_I(q,t')$ as the Laplace transform of the *conjugate* of the idler field, for convenience. Taking the unilateral Laplace transform of (C.1)–(C.2) makes use of the identity

$$\mathcal{L}_{z'}\Big\{\frac{\partial}{\partial z'} f(z',t')\Big\} = q\mathcal{L}_{z'}\big\{f(z',t')\big\} - f(z'=0,t')\,, \tag{C.7}$$

where $\mathcal{L}_{z'}$ denotes the Laplace transform. With this transformation, we obtain

$$\left(\frac{\partial}{\partial t'} + \Delta v_{PS} q_+\right)\widetilde{A}_S(q,t') - \Delta v_{PS} A'_S(0,t') = i\kappa A_P \Delta v_{PS} \widetilde{A}_I(q,t')\,, \tag{C.8}$$

$$\left(\frac{\partial}{\partial t'} + \Delta v_{PI} q_-\right)\widetilde{A}_I(q,t') - \Delta v_{PI} A'^*_I(0,t') = -i\kappa^* A^*_P \Delta v_{PI} \widetilde{A}_S(q,t')\,, \tag{C.9}$$

where $q_\pm \equiv q \pm i\Delta k/2$, and $0 \le t' \le T_P$. Differentiating (C.8) with respect to t' and then using (C.9) to eliminate the idler, we obtain a second-order, nonhomogenous, ordinary differential equation,

$$\left[\frac{\partial^2}{\partial t'^2} + (\Delta v_{PS} q_+ + \Delta v_{PI} q_-)\frac{\partial}{\partial t'} - (|\kappa A_P|^2 - q_+ q_-)\Delta v_{PS}\Delta v_{PI}\right]\widetilde{A}_S(q,t') = \widetilde{F}(q,t')\,, \tag{C.10}$$

where the driving term on the right-hand side of the equation is given by

$$\widetilde{F}(q,t') \equiv \Delta v_{PS}\left[\left(\frac{\partial}{\partial t'} + \Delta v_{PI} q_-\right) A'_S(0,t') + i\kappa A_P \Delta v_{PI} A'^*_I(0,t')\right]\,. \tag{C.11}$$

Notice that this term is due to nonzero boundary conditions on the lower edge of the (z', t') rectangle, which represent the signal and idler fields entering the crystal alongside the pump pulse.

The boundary conditions for this differential equation are given at $t' = 0$ and $t' = T_P$, and we seek a solution for $0 \leq t' \leq T_P$. Thus it is most convenient to derive the homogeneous and particular solutions of the differential equation using the *bilateral* Laplace transform. Defining these bilateral Laplace transforms as

$$\underline{\widetilde{A}}_m(q, s) \equiv \int_{-\infty}^{\infty} \mathrm{d}t' e^{-st'} \widetilde{A}_m(q, t'), \tag{C.12}$$

$$\underline{\widetilde{F}}(q, s) \equiv \int_{-\infty}^{\infty} \mathrm{d}t' e^{-st'} \widetilde{F}(q, t')\,, \tag{C.13}$$

for $m = S, I$, and taking the Laplace transform of (C.10), we obtain the algebraic equation

$$\left[s^2 + (\Delta v_{PS} q_+ + \Delta v_{PI} q_-)s - (|\kappa A_P|^2 - q_+ q_-)\Delta v_{PS} \Delta v_{PI}\right] \underline{\widetilde{A}}_S(q, s) = \underline{\widetilde{F}}(q, s)\,. \tag{C.14}$$

Setting the right-hand side to zero allows us to determine that the characteristic frequencies of the homogeneous equation are

$$s_{1,2} = -\alpha_+ \pm i\sqrt{|\beta_P|^2 - \alpha_-^2}\,, \tag{C.15}$$

with $\beta_P \equiv i\kappa A_P \sqrt{|\Delta v_{PS}| \Delta v_{PI}}$ and $\alpha_\pm \equiv (\Delta v_{PI} q_- \pm \Delta v_{PS} q_+)/2$. Thus, the full solution to (C.10) is

$$\widetilde{A}_S(q, t') = a_1 e^{s_1 t'} + a_2 e^{s_2 t'} + \frac{-i}{2\sqrt{|\beta_P|^2 - \alpha_-^2}} \int_{-\infty}^{t'} \mathrm{d}\tau \widetilde{F}(q, \tau) \Big(e^{s_1 (t' - \tau)} - e^{s_2 (t' - \tau)} \Big)\,, \tag{C.16}$$

where $a_1, a_2 \in \mathbb{C}$ are determined by the boundary conditions, $\widetilde{A}_S(q, T_P)$ and $\widetilde{A}_I(q, 0)$, and $\widetilde{A}_I(q, t')$ is found from (C.16), by substituting it into (C.8). It is worth pointing out that all of the variables in this equation may depend on the spatial frequency variable q, but to avoid notation clutter we have omitted explicit identification of this dependence.

We first use integration by parts in the last term of (C.16) to eliminate the derivative in (C.11), then solve for a_1 and a_2 using the boundary conditions. With this approach we

arrive at the following solution for $\widetilde{A}_S(q,t')$ for $t' \in [0,T_P]$:

$$\widetilde{A}_S(q,t') =$$
$$|\Delta v_{PS}|\Big\{ M_1(\alpha_-,0,t')\, e^{-|\Delta v_{PS}|q_+(T_P-t')}\underline{A}_S\big(|\Delta v_{PS}|q_+\big) + V(\alpha_-,0,t')\, e^{-\Delta v_{PI}q_-t'} r \underline{A}_I\big(\Delta v_{PI} q_-\big)$$
$$+\int_0^{t'} \mathrm{d}\tau\, A_S(0,\tau)\, e^{-\Delta v_{PI}q_-(t'-\tau)} M_2(\alpha_-,t',\tau) + \int_{t'}^{T_P} \mathrm{d}\tau\, A_S(0,\tau)\, e^{|\Delta v_{PS}|q_+(t'-\tau)} M_1(\alpha_-,t',\tau)$$
$$+\int_0^{t'} \mathrm{d}\tau\, r A_I^*(0,\tau)\, e^{-\Delta v_{PI}q_-(t'-\tau)} V(\alpha_-,\tau,t') + \int_{t'}^{T_P} \mathrm{d}\tau\, r A_I^*(0,\tau)\, e^{|\Delta v_{PS}|q_+(t'-\tau)} V(\alpha_-,t',\tau)\Big\}. \tag{C.17}$$

Similarly, we substitute (C.17) into (C.8), thereby obtaining the following expression for $\widetilde{A}_I(q,t')$ in the interval $0 \le t' \le T_P$:

$$\begin{aligned}\widetilde{A}_I(q,t') = \Delta v_{PI}\Big\{ & M_1(\alpha_-,0,t') e^{-\Delta v_{PI}q_-t'} \underline{A}_I\big(\Delta v_{PI} q_-\big) \\ & + V(\alpha_-,0,T_P-t') e^{-|\Delta v_{PS}|q_+(T_P-t')} r^{-1} \underline{A}_S\big(|\Delta v_{PS}|q_+\big) \\ & + \int_0^{t'} \mathrm{d}\tau\, A_I^*(0,\tau)\, e^{-\Delta v_{PI}q_-(t'-\tau)} M_1(\alpha_-,\tau,t') \\ & + \int_{t'}^{T_P} \mathrm{d}\tau\, A_I^*(0,\tau)\, e^{|\Delta v_{PS}|q_+(t'-\tau)} M_2(\alpha_-,\tau,t') \\ & + \int_0^{t'} \mathrm{d}\tau\, r^{-1} A_S(0,\tau)\, e^{-\Delta v_{PI}q_-(t'-\tau)} e^{-i2\phi_P} V(\alpha_-,T_P-t',T_P-\tau) \\ & + \int_{t'}^{T_P} \mathrm{d}\tau\, r^{-1} A_S(0,\tau)\, e^{|\Delta v_{PS}|q_+(t'-\tau)} e^{-i2\phi_P} V(\alpha_-,T_P-\tau,T_P-t')\Big\}, \end{aligned} \tag{C.18}$$

with $\phi_P \equiv \angle\beta_P$. The Laplace-domain signal and idler fields in the first two terms of (C.17) and (C.18) are given by

$$\underline{A}_S(s) \equiv \int_0^{L/|\Delta v_{PS}|} \mathrm{d}t\, e^{-st} A_S(z=0,t+T_P), \tag{C.19}$$

$$\underline{A}_I(s) \equiv \int_0^{L/\Delta v_{PI}} \mathrm{d}t\, e^{-st} A_I^*(z=0,-t)\,. \tag{C.20}$$

In other words, they represent Laplace transforms of the signal and idler portions—at the input facet of the crystal ($z=0$)—that map to the right and left boundaries of the inter-

action rectangle, respectively. In addition, the signal and idler fields inside the integrands are given in the absolute (z,t) frame of reference. We have expressed the solution in terms of three *causal* system functions,[1]

$$M_1(s,\tau',\tau) \equiv \frac{\big[\cos(\zeta_0\tau') + (s/\zeta_0)\sin(\zeta_0\tau')\big]\big[\cos\big(\zeta_0(T_P-\tau)\big) + (s/\zeta_0)\sin\big(\zeta_0(T_P-\tau)\big)\big]}{e^{-s(\tau-\tau')}\big[\cos(\zeta_0 T_P) + (s/\zeta_0)\sin(\zeta_0 T_P)\big]}\,, \tag{C.21}$$

$$M_2(s,\tau',\tau) \equiv \frac{(|\beta_P|/\zeta_0)^2\sin\big(\zeta_0(T_P-\tau')\big)\sin(\zeta_0\tau)}{e^{s(\tau-\tau')}\big[\cos(\zeta_0 T_P) + (s/\zeta_0)\sin(\zeta_0 T_P)\big]}\,, \tag{C.22}$$

$$V(s,\tau',\tau) \equiv \frac{\big[\cos(\zeta_0\tau') + (s/\zeta_0)\sin(\zeta_0\tau')\big](\beta_P/\zeta_0)\sin\big(\zeta_0(T_P-\tau)\big)}{e^{-s(\tau-\tau')}\big[\cos(\zeta_0 T_P) + (s/\zeta_0)\sin(\zeta_0 T_P)\big]}\,, \tag{C.23}$$

with $s\in\mathbb{C}$, $\zeta_0 \equiv \sqrt{|\beta_P|^2 - s^2} \in \mathbb{C}$ and $0 \le \tau,\tau' \le T_P$.

The first two terms in (C.17) and (C.18) are due to the boundary conditions at $t'=0$ and $t'=T_P$, whereas the last four terms are due to the boundary conditions at $z'=0$. Thus, the solutions account for the contributions from all boundaries, and inverse Laplace transforming both equations with respect to q will yield the general solution for the signal and idler fields inside $(z',t') \in [0,L]\times[0,T_P]$. However, our goal is to find the solutions on $z'=L$. Because the signal field in $t'\in[-L/|\Delta v_{PS}|,0]$, is found from $A'_S(z'=L,t') = A'_S(L+|\Delta v_{PS}|t',t'=0)$. we substitute $q = s/|\Delta v_{PS}| - i\Delta k/2$ in (C.17) and then take the inverse Laplace transform to obtain the solution in this time window. For $t'\in[0,T_P]$ we evaluate the inverse transform of (C.17) at $z'=L$. Finally, transforming the result back into (z,t) coordinates, we obtain the following full signal-field solution:

$$\begin{aligned}
&A_S(z{=}L,t) = \\
&\int_0^{\alpha_S} \mathrm{d}\tau\, A_S(z{=}0,\tau)\, e^{i\phi_S}\,\gamma\,\mu_2\Big(\gamma\big[L/|\Delta v_{PS}| - r^2(t'-\tau)\big],t',\tau\Big) \\
&+\int_{\alpha_S}^{L/|\Delta v_{PS}|+T_P} \mathrm{d}\tau\, A_S(z{=}0,\tau)\, e^{i\phi_S}\,\gamma\,\mu_1\big(\gamma(t-L/v_S-\tau),\alpha_S,\min(\tau,T_P)\big) \\
&+\int_{-L/\Delta v_{PI}}^{\alpha_S} \mathrm{d}\tau\, A_I^*(z{=}0,\tau)\, e^{i\phi_S}\, r\gamma\,\nu\Big(\gamma\big(L/|\Delta v_{PS}| + \min(t',-r^2t') - \tau\big),\max(0,\tau),\alpha_S\Big) \\
&+\int_{\alpha_S}^{T_P} \mathrm{d}\tau\, A_I^*(z{=}0,\tau)\, e^{i\phi_S}\, r\gamma\,\nu\big(\gamma(t-L/v_S-\tau),\alpha_S,\tau\big),
\end{aligned} \tag{C.24}$$

[1]Treating τ and τ' as parameters, the region of convergence for all three of the system functions includes $\Re\{s\}\to+\infty$.

for $t \in [L/v_S, L/v_P + T_P]$. Outside this time interval we have $A_S(z = L, t) = A_S(z = 0, t - L/v_S)$. In (C.24), μ_1, μ_2 and ν are zero if their first argument is negative, and they represent the inverse Laplace transforms of M_1, M_2 and V respectively. In addition, for the sake of brevity we have used $t' \equiv t - L/v_P$, $\alpha_S \equiv \max(0, t - L/v_P)$, $\gamma \equiv 2/(1 + r^2)$ and $\phi_S \equiv \Delta k \Delta v_{SI}(t - L/v_S - \tau)$.

Let us now consider the idler field at $z' = L$. The solution for $t' \in [0, T_P]$ is the inverse Laplace transform of (C.18) evaluated at $z' = L$. For $t' \in [T_P, T_P + L/\Delta v_{PI}]$, we use the equivalence $A'_I(z' = L, t') = A'_I(L - \Delta v_{PI}(t' - T_P)), t' = T_P)$, to map the right boundary of the interaction rectangle onto $z' = L$. Thus, substituting $q = -s/\Delta v_{PI} + i\Delta k/2$ in (C.18) and taking the inverse Laplace transform of the resulting expression yields the idler field in this window. Transforming the results into (z, t) coordinates, the full solution of the (conjugated) idler field at $z = L$ is

$$
\begin{aligned}
&A_I^*(z{=}L, t) = \\
&\int_{-L/\Delta v_{PI}}^{\alpha_I} \mathrm{d}\tau\, A_I^*(z{=}0, \tau)\, e^{i\phi_I}\, r^2\gamma\, \mu_1\big(-r^2\gamma(t - L/v_I - \tau), \max(0, \tau), \alpha_I\big) \\
&+ \int_{\alpha_I}^{T_P} \mathrm{d}\tau\, A_I^*(z{=}0, \tau)\, e^{i\phi_I}\, r^2\gamma\, \mu_2\Big(\gamma\big(L/|\Delta v_{PS}| - (t' - \tau)\big), \tau, t'\Big) \\
&+ \int_{0}^{\alpha_I} \mathrm{d}\tau\, A_S(z{=}0, \tau)\, e^{i\phi_I - i2\phi_P}\, r\gamma\, \nu\big(-r^2\gamma(t - L/v_I - \tau), \max(0, T_P - t'), T_P - \tau\big) \\
&+ \int_{\alpha_I}^{L/|\Delta v_{PS}| + T_P} \mathrm{d}\tau\, A_S(z{=}0, \tau)\, e^{i\phi_I - i2\phi_P} r\gamma\, \nu\Bigg(\gamma\Big[L/|\Delta v_{PS}| + T_P - \tau \\
&\qquad + \min\big(-r^2(t' - T_P), (t' - T_P)\big)\Big], \max(0, T_P - \tau), \max(0, T_P - t')\Bigg),
\end{aligned}
\tag{C.25}
$$

for $t \in [L/v_P, L/v_I + T_P]$. Outside of this time interval we have $A_I^*(z = L, t) = A_I^*(z = 0, t - L/v_I)$. For brevity, we have defined $\alpha_I \equiv \min(t - L/v_P, T_P)$, and $\phi_I \equiv \Delta k \Delta v_{SI}(t - L/v_I - \tau)$.

We have thus found the exact solutions to the coupled-mode equations in (7.21), (7.22) at the output facet of the crystal $z = L$, given the inputs at $z = 0$. It is a straightforward exercise to find the explicit expressions of the impulse responses introduced in (7.27) and (7.28) by combining the signal and idler integrals in (C.24) and (C.25), respectively.

The assumptions made in Section 7.4 facilitate further simplifications to these expressions. Let us first consider the signal output field in (C.24). If $t \in [L/v_S, L/v_P]$ and $\Delta k = 0$ are assumed, we have $\alpha_S = 0$ and $\phi_S = 0$. Thus, the first integral in (C.24) vanishes and

μ_2 no longer affects the output. In the second integral we can change the upper limit to $L/|\Delta v_{PS}|$ because the integrand is zero for $\tau > t - L/v_S$. Finally, in the third integral $\min(t', -r^2 t') = t'$ because $t' = t - L/v_P < 0$ in the window of interest, and $\max(0, \tau) = 0$. Therefore, this expression can be simplified to the form given in (7.33), where the impulse responses are redefined as

$$\mu(t, \tau) = \mu_1(t, 0, \tau)\,, \tag{C.26}$$

$$\nu(t, \tau) = \nu(t, 0, \tau)\,, \tag{C.27}$$

to simplify notation.

A similar set of simplifications can be carried out in (C.25), when $t \in [L/v_P + T_P, L/v_I + T_P]$ and $\Delta k = 0$. First, we have $\alpha_I = T_P$ and $\phi_I = 0$. Therefore, the second integral in (C.25) vanishes and μ_2 no longer contributes to the output. Also, in the last integral expression, $\min\big(-r^2(t' - T_P), (t' - T_P)\big) = -r^2(t' - T_P)$ and $\max(0, T_P - \tau) = \max(T_P - t') = 0$, so that (C.25) simplifies to the form given in (7.36).

Appendix D

Commutator Invariance of Truncated Coupled-Mode Equations

Assume that the photon-units signal and idler field operators at the input facet of the nonlinear crystal, $\hat{A}_S(z=0,t)$ and $\hat{A}_I(z=0,t)$, satisfy the canonical commutation relations stated in (7.29) and (7.30). In this appendix we show that the operator-valued, first-order truncated coupled-mode equations—given in (7.31) and (7.32)—imply

$$\frac{\partial}{\partial z}\big[\hat{A}_m(z,t_1),\hat{A}_n^\dagger(z,t_2)\big] = \frac{\partial}{\partial z}\big[\hat{A}_m(z,t_1),\hat{A}_n(z,t_2)\big] = 0\,, \tag{D.1}$$

for $m,n = S,I$ and $z > 0$.

Let us define the operator-valued Fourier transforms,

$$\hat{A}_m(z,\Omega) \equiv \int_{-\infty}^{\infty} \mathrm{d}t\, e^{i\Omega t}\hat{A}_m(z,t)\,, \tag{D.2}$$

for $m = S,I$. These frequency-domain signal and idler operators have similar canonical commutator brackets,

$$\big[\hat{A}_m(z=0,\Omega_1),\hat{A}_n^\dagger(z=0,\Omega_2)\big] = \delta_{m,n}\,2\pi\delta(\Omega_1-\Omega_2)\,, \tag{D.3}$$

$$\big[\hat{A}_m(z=0,\Omega_1),\hat{A}_n(z=0,\Omega_2)\big] = 0\,, \tag{D.4}$$

and the Fourier-transformed coupled-mode equations are

$$\frac{\partial}{\partial z}\hat{A}_S(z,\Omega)-i\frac{\Omega}{v_S}\hat{A}_S(z,\Omega)=i\kappa e^{i\Delta kz}\int_{-\infty}^{\infty}\frac{\mathrm{d}\Omega'}{2\pi}\,e^{iz(\Omega-\Omega')/v_P}A_P(\Omega-\Omega')\hat{A}_I^\dagger(z,-\Omega')\,, \quad \text{(D.5)}$$

$$\frac{\partial}{\partial z}\hat{A}_I(z,\Omega)-i\frac{\Omega}{v_I}\hat{A}_I(z,\Omega)=i\kappa e^{i\Delta kz}\int_{-\infty}^{\infty}\frac{\mathrm{d}\Omega'}{2\pi}\,e^{iz(\Omega-\Omega')/v_P}A_P(\Omega-\Omega')\hat{A}_S^\dagger(z,-\Omega')\,. \quad \text{(D.6)}$$

Using the definition of the commutator, $[\hat{A},\hat{B}]\equiv\hat{A}\hat{B}-\hat{B}\hat{A}$, and the chain rule for differentiation of operators,

$$\frac{\partial}{\partial z}\left(\hat{A}(z)\hat{B}(z)\right)=\left(\frac{\partial}{\partial z}\hat{A}(z)\right)\hat{B}(z)+\hat{A}(z)\left(\frac{\partial}{\partial z}\hat{B}(z)\right)\,, \quad \text{(D.7)}$$

we derive the following equivalences for the derivative of a commutator bracket:

$$\frac{\partial}{\partial z}\big[\hat{A}_m(z,\Omega_1),\hat{A}_n^\dagger(z,\Omega_2)\big]=\Big[\frac{\partial}{\partial z}\hat{A}_m(z,\Omega_1),\hat{A}_n^\dagger(z,\Omega_2)\Big]+\Big[\frac{\partial}{\partial z}\hat{A}_n(z,\Omega_2),\hat{A}_m^\dagger(z,\Omega_1)\Big]^\dagger, \quad \text{(D.8)}$$

$$\frac{\partial}{\partial z}\big[\hat{A}_m(z,\Omega_1),\hat{A}_n(z,\Omega_2)\big]=\Big[\frac{\partial}{\partial z}\hat{A}_m(z,\Omega_1),\hat{A}_n(z,\Omega_2)\Big]-\Big[\frac{\partial}{\partial z}\hat{A}_n(z,\Omega_2),\hat{A}_m(z,\Omega_1)\Big]\,. \quad \text{(D.9)}$$

Via (D.5) and (D.6), we have

$$\Big[\frac{\partial}{\partial z}\hat{A}_m(z,\Omega_1),\hat{A}_m^\dagger(z,\Omega_2)\Big]=i2\pi\frac{\Omega_1}{v_m}\,\delta(\Omega_1-\Omega_2)\,, \quad \text{(D.10)}$$

and

$$\Big[\frac{\partial}{\partial z}\hat{A}_m(z,\Omega_1),\hat{A}_m(z,\Omega_2)\Big]=0\,, \quad \text{(D.11)}$$

so that (D.8) and (D.9) are both zero for $m=n=S,I$. Thus, we need only consider $m=S$, $n=I$ to complete the proof of commutator bracket invariance. For this case, we have

$$\Big[\frac{\partial}{\partial z}\hat{A}_S(z,\Omega_1),\hat{A}_I^\dagger(z,\Omega_2)\Big]=\Big[\frac{\partial}{\partial z}\hat{A}_I(z,\Omega_2),\hat{A}_S^\dagger(z,\Omega_1)\Big]=0, \quad \text{(D.12)}$$

which yields (D.8) equal to 0. Using the coupled-mode equations we find

$$\Big[\frac{\partial}{\partial z}\hat{A}_S(z,\Omega_1),\hat{A}_I(z,\Omega_2)\Big]=-i\kappa e^{i\Delta kz}e^{iz(\Omega_1+\Omega_2)/v_P}A_P(\Omega_1+\Omega_2)\,, \quad \text{(D.13)}$$

and

$$\Big[\frac{\partial}{\partial z}\hat{A}_I(z,\Omega_2),\hat{A}_S(z,\Omega_1)\Big]=-i\kappa e^{i\Delta kz}e^{i(\Omega_1+\Omega_2)z/v_P}A_P(\Omega_1+\Omega_2)\,, \quad \text{(D.14)}$$

so that (D.9) also equals to zero.

Therefore, we conclude that the coupled-mode equations in (7.31) and (7.32), with an arbitrary pump pulse $A(t)$, preserve the commutator brackets in (7.29) and (7.30) for all $z > 0$. This guarantees that replacing the classical signal and idler fields in (C.24) and (C.25) with quantum operators yields commutator preserving input/output relations.

Appendix E

Classical versus Quantum Sum-Coordinate Correlations

Let $\hat{A}_1(t)$ and $\hat{A}_2(t)$ be two field operators, satisfying the commutation relations

$$[\hat{A}_m(t_1), \hat{A}_n^\dagger(t_2)] = \delta_{m,n}\,\delta(t_1 - t_2)\,, \tag{E.1}$$

$$[\hat{A}_m(t_1), \hat{A}_n(t_2)] = 0\,, \tag{E.2}$$

for $m, n = 1, 2$. In addition, assume they have identical second-order phase-insensitive (normally-ordered) auto-correlations,

$$\langle \hat{A}_m^\dagger(t_1)\hat{A}_m(t_2)\rangle = K^{(n)}(t_2 - t_1)\,, \tag{E.3}$$

for $m = 1, 2$, a phase-sensitive cross-correlation,

$$\langle \hat{A}_1(t_1)\hat{A}_2(t_2)\rangle = K_{1,2}^{(p)}(t_2 + t_1)\,, \tag{E.4}$$

and the remaining second-order moments (i.e., the phase-insensitive cross-correlation and the phase-sensitive auto-correlations) are arbitrary.

Suppose we define the operator

$$\hat{B}(t) \equiv h(t) \star \hat{A}_1(t) + \hat{A}_2^\dagger(-t), \tag{E.5}$$

where $\star$ denotes convolution, and evaluate its phase-insensitive auto-correlation function in terms of the moments of $\hat{A}_1$ and $\hat{A}_2$. We find that

$$\langle \hat{B}^\dagger(t_1)\hat{B}(t_2)\rangle = \int_{-\infty}^{\infty}\int_{-\infty}^{\infty} \mathrm{d}u_1 \mathrm{d}u_2\, h^*(u_1)h(u_2)\langle \hat{A}_1^\dagger(t_1-u_1)\hat{A}_1(t_2-u_2)\rangle + \langle \hat{A}_2(-t_1)\hat{A}_2^\dagger(-t_2)\rangle$$
$$+ \int_{-\infty}^{\infty} \mathrm{d}u\, h^*(u)\langle \hat{A}_1^\dagger(t_1-u)\hat{A}_2^\dagger(-t_2)\rangle + \int_{-\infty}^{\infty} \mathrm{d}u\, h(u)\langle \hat{A}_2(-t_1)\hat{A}_1(t_2-u)\rangle\,. \tag{E.6}$$

This expression simplifies to a function of $t_2 - t_1$, denoted hereafter as $K_B^{(n)}(t_2-t_1)$, that is given by

$$K_B^{(n)}(\tau) = \int_{-\infty}^{\infty}\int_{-\infty}^{\infty} \mathrm{d}u_1\, \mathrm{d}u_2\, h^*(u_1)h(u_2)K^{(n)}(\tau+u_1-u_2) + \big(K^{(n)}(\tau)+\delta(\tau)\big)$$
$$+ \int_{-\infty}^{\infty} \mathrm{d}u\, h^*(u)K_{1,2}^{(p)*}(-\tau-u) + \int_{-\infty}^{\infty} \mathrm{d}u\, h(u)K_{1,2}^{(p)}(\tau-u)\,, \tag{E.7}$$

where it is worthwhile to note that $\delta(\tau)$ in the second term is due to the nonzero commutator of $\hat{A}_2(t)$ with its adjoint.

Because $K_B^{(n)}(\tau)$ is a phase-insensitive (positive semidefinite) auto-correlation function, its Fourier transform is the nonnegative fluorescence spectrum, $S_B^{(n)}(\Omega) \geq 0$. Fourier transforming (E.7) and using this condition yields

$$\big(1+|H(\Omega)|^2\big)S^{(n)}(\Omega) + 2\Re\big\{S_{1,2}^{(p)}(\Omega)H(\Omega)\big\} + 1 \geq 0\,, \tag{E.8}$$

where $S^{(n)}(\Omega) \equiv \mathcal{F}\{K^{(n)}(\tau)\}$ is the fluorescence spectra of both $\hat{A}_1$ and $\hat{A}_2$, $S_{1,2}^{(p)}(\Omega) \equiv \mathcal{F}\{K_{1,2}^{(p)}(\tau)\}$ is their phase-sensitive cross-correlation spectrum, and $H(\Omega) \equiv \mathcal{F}\{h(\tau)\}$. Choosing $\angle H(\Omega) = -\angle S_{1,2}^{(p)}(\Omega) + \phi$, with $\phi = 0, \pi$, we are left with two quadratic inequalities of $|H(\Omega)|$,

$$S^{(n)}(\Omega)\,|H(\Omega)|^2 \pm 2|S_{1,2}^{(p)}(\Omega)||H(\Omega)| + S^{(n)}(\Omega) + 1 \geq 0\,. \tag{E.9}$$

These inequalities must be true for arbitrary $H(\Omega)$, and for all $\Omega \in \mathbb{R}$. This is possible if and only if the discriminant of the quadratic is nonpositive, i.e,

$$|S_{1,2}^{(p)}(\Omega)|^2 \leq S^{(n)}(\Omega)\big(1+S^{(n)}(\Omega)\big)\,. \tag{E.10}$$

This bound must be satisfied by an arbitrary joint state of the photon-units field operators, $\hat{A}_1(t)$ and $\hat{A}_2(t)$. However, if the state is *classical*, i.e., the joint state has a proper P-representation in terms of the coherent-state eigenkets of the field operators [14, 18], then the bound is tighter. To find this tighter bound, we utilize the stochastic process equivalence introduced in Chapter 2 for classical states: if the joint quantum state can be written as a statistical mixture of the coherent-state eigenkets of $\hat{A}_1(t)$ and $\hat{A}_2(t)$, then the same statistical mixture of the coherent-state *eigenfunctions* are a pair of stochastic processes, denoted by $A_1(t)$ and $A_2(t)$ respectively, with the phase-insensitive auto-correlations

$$\langle A_m^*(t_1)A_m(t_2)\rangle = K^{(n)}(t_2 - t_1)\,, \tag{E.11}$$

for $m = 1, 2$, and a phase-sensitive cross-correlation,

$$\langle A_1(t_1)A_2(t_2)\rangle = K_{1,2}^{(p)}(t_2 + t_1)\,. \tag{E.12}$$

Note that in these equations the angle brackets denote regular expectations over stochastic ensembles and not quantum averages.

Suppose we now define a new stochastic process,

$$B(t) \equiv h(t) \star A_1(t) + A_2^*(-t), \tag{E.13}$$

for some square-integrable function $h(t)$. Evaluating its phase-insensitive auto-correlation function, $K_B(\tau) \equiv \langle B^*(t)B(t+\tau)\rangle$, we obtain

$$\begin{aligned} K_B^{(n)}(\tau) = &\int_{-\infty}^{\infty}\int_{-\infty}^{\infty} \mathrm{d}u_1\mathrm{d}u_2\, h^*(u_1)h(u_2)K^{(n)}(\tau + u_1 - u_2) + K^{(n)}(\tau) \\ &+ \int_{-\infty}^{\infty} \mathrm{d}u\, h^*(u)K_{1,2}^{(p)*}(-\tau - u) + \int_{-\infty}^{\infty} \mathrm{d}u\, h(u)K_{1,2}^{(p)}(\tau - u), \end{aligned} \tag{E.14}$$

which is identical to (E.7) except for the absence of the $\delta(\tau)$ term. This absence is due to scalar stochastic processes being commutative, $\langle A_2(t_1)A_2^*(t_2)\rangle = \langle A_2^*(t_2)A_2(t_1)\rangle$.

Now, taking the Fourier transform of (E.14) to obtain the nonnegative fluorescence spectrum, and choosing the phase of $H(\Omega)$ properly, yields the inequalities,

$$|H(\Omega)|^2 S^{(n)}(\Omega) \pm 2|S_{1,2}^{(p)}(\Omega)||H(\Omega)| + S^{(n)}(\Omega) \geq 0\,, \tag{E.15}$$

where $S^{(n)}(\Omega)$, $S^{(p)}_{1,2}(\Omega)$ and $H(\Omega)$ are same as before. These inequalities require nonpositivity of the discriminant, which yields the following Cauchy-Schwarz bound for a pair of stochastic processes having a cross-correlation in the sum-coordinate,

$$|S^{(p)}_{1,2}(\Omega)| \leq S^{(n)}(\Omega). \tag{E.16}$$

The difference in the upper bounds of (E.10) and (E.16) implies that any joint state of $\hat{A}_1$ and $\hat{A}_2$ which violates (E.16) cannot have a proper P-representation, and therefore is a nonclassical state. However, the opposite direction of this statement is not true: a state that satisfies (E.16) is not, in general, guaranteed to be a classical state. The exception to this is the Gaussian state, because it is completely determined by its first- and second-order moments. In particular, a Gaussian state with its nonzero second-order moments having the form (E.3) and (E.4) is classical *if and only if* the correlation spectra satisfy (E.16). Hence, the upper bound in (E.16) is a well-defined classical/quantum boundary for two-field, jointly-Gaussian states which have stationary phase-insensitive auto-correlation functions but a phase-sensitive cross-correlation function depending on the sum of its time indices.

Finally, compare the classical upper bound in (E.16), to that found in (4.7) for a complex-stationary source. Because, complex-stationary phase-sensitive correlation implies cross-correlation between baseband frequencies that sum to 0, both $\pm\Omega$ frequencies contribute to the upper bound. On the other hand, in (E.16) distinct frequencies are uncorrelated, so the upper bound only depends on Ω.

Bibliography

[1] A. F. Abouraddy, M. B. Nasr, B. E. A. Saleh, A. V. Sergienko, and M. C. Teich, "Quantum-optical coherence tomography with dispersion cancellation," *Phys. Rev. A* **65**, 053817, 2002.

[2] M. B. Nasr, B. E. A. Saleh, A. V. Sergienko, and M. C. Teich, "Dispersion-cancelled and dispersion-sensitive quantum optical coherence tomography," *Opt. Exp.* **12**, 1353–1362, 2004.

[3] M. B. Nasr, B. E. A. Saleh, A. V. Sergienko, and M. C. Teich, "Demonstration of dispersion-canceled quantum-optical coherence tomography," *Phys. Rev. Lett.* **91**, 083601, 2003.

[4] D. V. Strekalov, A. V. Sergienko, D. N. Klyshko, and Y. H. Shih, "Observation of two-photon "ghost" interference and diffraction," *Phys. Rev. Lett.* **74**, 3600–3603, 1995.

[5] T. B. Pittman, Y. H. Shih, D. V. Strekalov, and A. V. Sergienko, "Optical imaging by means of two-photon quantum entanglement," *Phys. Rev. A* **52**, R3429, 1995.

[6] A. F. Abouraddy, B. E. A. Saleh, A. V. Sergienko, and M. C. Teich, "Quantum holography," *Opt. Express* **9**, 498–505, 2001.

[7] A. N. Boto, P. Kok, D. S. Abrams, S. L. Braunstein, C. P. Williams, and J. P. Dowling, "Quantum interferometric optical lithography: Exploiting entanglement to beat the diffraction limit," *Phys. Rev. Lett.* **85**, 2733–2736, 2000.

[8] M. D'Angelo, M. V. Chekhova, and Y. Shih, "Two-photon diffraction and quantum lithography," *Phys. Rev. Lett.* **87**, 013602, 2001.

[9] R. S. Bennink, S. J. Bentley, and R. W. Boyd, ""Two-photon" coincidence imaging with a classical source," *Phys. Rev. Lett.* **89**, 113601, 2002.

[10] A. Gatti, E. Brambilla, M. Bache, and L. A. Lugiato, "Ghost imaging with thermal light: Comparing entanglement and classical correlation," *Phys. Rev. Lett.* **93**, 093602, 2004.

[11] A. Gatti, E. Brambilla, M. Bache, and L. A. Lugiato, "Correlated imaging, quantum and classical," *Phys. Rev. A* **70**, 013802, 2004.

[12] F. Ferri, D. Magatti, A. Gatti, M. Bache, E. Brambilla, and L. A. Lugiato, "High-resolution ghost image and ghost diffraction experiments with thermal light," *Phys. Rev. Lett.* **94**, 183602, 2005.

[13] J. W. Goodman, *Statistical Optics*, Wiley, New York, Classics ed., 2000.

[14] L. Mandel and E. Wolf, *Optical Coherence and Quantum Optics*, Cambridge Univ., Cambridge, 1995.

[15] B. E. A. Saleh, A. F. Abouraddy, A. V. Sergienko, and M. C. Teich, "Duality between partial coherence and partial entanglement," *Phys. Rev. A* **62**, 043816, 2000.

[16] B. E. A. Saleh, M. C. Teich, and A. V. Sergienko, "Wolf equations for two-photon light," *Phys. Rev. Lett.* **94**, 223601, 2005.

[17] A. F. Abouraddy, B. E. A. Saleh, A. V. Sergienko, and M. C. Teich, "Entangled-photon Fourier optics," *J. Opt. Soc. Am. B* **19**, 1174–1184, 2002.

[18] J. H. Shapiro, "Quantum Gaussian noise," in *Proc. SPIE* **5111**, 382–395, 2003.

[19] J. H. Shapiro and K.-X. Sun, "Semiclassical versus quantum behavior in fourth-order interference," *J. Opt. Soc. Am. B* **11**, 1130–1141, 1994.

[20] B. I. Erkmen and J. H. Shapiro, "Optical coherence theory for phase-sensitive light," in *Proc. SPIE* **6305**, 63050G, 2006.

[21] B. I. Erkmen and J. H. Shapiro, "Phase-conjugate optical coherence tomography," *Phys. Rev. A* **74**, 041601(R), 2006.

[22] B. I. Erkmen and J. H. Shapiro, "Optical coherence tomography with phase-sensitive light," in *Proc. SPIE* **6305**, 630510, 2006.

[23] B. I. Erkmen and J. H. Shapiro, "Ghost imaging: what is quantum, what is not," `arXiv:quant-ph/0612070v1`, 2006.

[24] B. I. Erkmen and J. H. Shapiro, "Unified theory of ghost imaging with Gaussian-state light," *Submitted to Phys. Rev. A; e-print:* `arXiv:0712.3554v1 [quant-ph]`, 2007.

[25] R. M. Gagliardi and S. Karp, *Optical Communications*, Wiley, New York, 1976.

[26] R. G. Gallager, *Discrete Stochastic Processes*, Kluwer Academic, Massachusetts, 1996.

[27] H. P. Yuen and J. H. Shapiro, "Optical communication with two-photon coherent states—Part III: quantum measurements realizable with photoemissive detectors," *IEEE Trans. Inform. Theory* **26**, 78–92, 1980.

[28] J. H. Shapiro, "Quantum measurement eigenkets for continuous-time direct detection," *Quantum Semiclass. Opt.* **10**, 567–578, 1998.

[29] J. H. Shapiro, H. P. Yuen, and J. A. M. Mata, "Optical communication with two-photon coherent states—Part II: photoemissive detection and structured receiver performance," *IEEE Trans. Inform. Theory* **25**, 179–192, 1979.

[30] R. Loudon, *The Quantum Theory of Light*, Oxford Univ., New York, 3rd ed., 2000.

[31] H. P. Yuen, "Two-photon coherent states of the radiation field," *Phys. Rev. A* **13**, 2226–2243, 1976.

[32] Y. Shih, "Entangled photons," *IEEE J. Sel. Top. Quantum Electron.* **9**, 1455–1467, 2003.

[33] A. F. Abouraddy, B. E. A. Saleh, A. V. Sergienko, and M. C. Teich, "Role of entanglement in two-photon imaging," *Phys. Rev. Lett.* **87**, 123602, 2001.

[34] M. de Gosson, *Symplectic Geometry and Quantum Mechanics*, Birkhäuser, Basel, 2006.

[35] P. J. Schreier, L. L. Scharf, and C. T. Mullis, "Detection and estimation of improper complex random signals," *IEEE Trans. Inform. Theory* **51**, 306–312, 2005.

[36] P. J. Schreier and L. L. Scharf, "Second-order analysis of improper complex random vectors and processes," *IEEE Trans. Signal Process.* **51**, 714–725, 2003.

[37] H. P. Yuen and J. H. Shapiro, "Optical communication with two-photon coherent states—Part I: quantum state propagation and quantum noise reduction," *IEEE Trans. Inform. Theory* **24**, 657–668, 1978.

[38] J. M. Schmitt, "Optical coherence tomography (OCT): a review," *IEEE J. Sel. Top. Quantum Electron.* **5**, 1205–1215, 1999.

[39] P. H. Tomlins and R. K. Wang, "Theory, developments and applications of optical coherence tomography," *J. of Phys. D* **38**, 2519–2535, 2005.

[40] D. N. Klyshko, "A simple method of preparing pure states of the optical-field, a realization of the Einstein, Podolsky, Rosen experiment and a demonstration of the complementarity principle," *Usp. Fiz. Nauk.* **154**, 133–152, 1988.

[41] R. A. Fisher, "Optical phase conjugation for time-domain undoing of dispersive self-phase-modulation effects," *Opt. Lett.* **8**, 611–613, 1983.

[42] J. Feinberg, "Interferometer with a self-pumped phase-conjugating mirror," *Opt. Lett.* **8**, 569–571, 1983.

[43] J. B. Norman, "Phase-conjugate Michelson interferometers for all-optical image processing and computing," *Am. J. Phys.* **60**, 212–220, 1992.

[44] G. J. Tearney, B. E. Bouma, and J. G. Fujimoto, "High-speed phase- and group-delay scanning with a grating based phase control delay line," *Opt. Lett.* **22**, 1811–1813, 1997.

[45] A. Valencia, G. Scarcelli, M. D'Angelo, and Y. Shih, "Two-photon imaging with thermal light," *Phys. Rev. Lett.* **94**, 063601, 2005.

[46] R. S. Bennink, S. J. Bentley, R. W. Boyd, and J. C. Howell, "Quantum and classical coincidence imaging," *Phys. Rev. Lett.* **92**, 033601, 2004.

[47] M. D'Angelo, A. Valencia, M. H. Rubin, and Y. Shih, "Resolution of quantum and classical ghost imaging," *Phys. Rev. A* **72**, 013810, 2005.

[48] Y. Cai and S.-Y. Zhu, "Ghost imaging with incoherent and partially coherent light radiation," *Phys. Rev. E* **71**, 056607, 2005.

[49] G. Scarcelli, V. Berardi, and Y. Shih, "Can two-photon correlation of chaotic light be considered as correlation of intensity fluctuations?," *Phys. Rev. Lett.* **96**, 063602, 2006.

[50] A. Papoulis, *Probability, Random Variables, and Stochastic Processes*, McGraw-Hill, New York, 3rd ed., 1991.

[51] E. Brambilla, A. Gatti, M. Bache, and L. A. Lugiato, "Simultaneous near-field and far-field spatial quantum correlations in the high-gain regime of parametric down-conversion," *Phys. Rev. A* **69**, 023802, 2004.

[52] T. H. Kim, F. N. C. Wong, and J. H. Shapiro, "Efficient generation of polarization-entangled photons in a nonlinear crystal," *Laser Phys.* **16**, 1517–1524, 2006.

[53] R. W. Boyd, *Nonlinear Optics*, Academic Press, San Diego, 2nd ed., 2003.

[54] N. S. Kopeika and J. Bordogna, "Background noise in optical communication systems," in *Proc. IEEE* **58**, 1571–1577, 1970.

[55] Y. Shih, "Quantum imaging," *IEEE J. Sel. Top. Quantum Electron.* **13**, 1016–1030, 2007.

[56] J. F. Clauser, M. Horne, A. Shimony, and R. A. Holt, "Proposed experiment to test local hidden-variable theories," *Phys. Rev. Lett.* **23**, 880–884, 1969.

[57] D. Slepian, "Analytic solution of two apodization problems," *J. Opt. Soc. Am.* **55**, 1100–1115, 1965.

[58] K. A. O'Donnell and A. B. U'Ren, "Observation of ultrabroadband, beamlike parametric downconversion," *Opt. Lett.* **32**, 817–819, 2007.

[59] M. W. Mitchell, J. S. Lundeen, and A. M. Steinberg, "Super-resolving phase measurements with a multiphoton entangled state," *Nature* **429**, 161–164, 2004.

[60] J.-W. P. Philip Walther, M. Aspelmeyer, R. Ursin, S. Gasparoni, and A. Zeilinger, "De Broglie wavelength of a non-local four-photon state," *Nature* **429**, 158–161, 2004.

[61] M. Tsang, "Spectral phase conjugation via extended phase matching," *J. Opt. Soc. Am. B* **23**, 861–867, 2006.

[62] V. Giovannetti, L. Maccone, J. H. Shapiro, and F. N. C. Wong, "Extended phase-matching conditions for improved entanglement generation," *Phys. Rev. A* **66**, 043813, 2002.

[63] M. Tsang and D. Psaltis, "Spontaneous spectral phase conjugation for coincident frequency entanglement," *Phys. Rev. A* **71**, 043806, 2005.

[64] O. Kuzucu, M. Fiorentino, M. A. Albota, F. N. C. Wong, and F. X. Kaertner, "Two-photon coincident-frequency entanglement via extended phase matching," *Phys. Rev. Lett.* **94**, 083601, 2005.

[65] Y. R. Shen, *The Principles of Nonlinear Optics*, Wiley-Interscience, New Jersey, 2nd ed., 2003.

[66] G. Cerullo and D. Silvestri, "Ultrafast optical parametric amplifiers," *Rev. Sci. Instrum.* **74**, 1–18, 2003.

[67] S. A. Akhmanov, V. A. Vysloukh, and A. S. Chirkin, *Optics of Femtosecond Laser Pulses*, American Institute of Physics, New York, 1992.

[68] R. A. Fisher, B. R. Suydam, and B. J. Feldman, "Transient analysis of Kerr-like phase-conjugators using frequency-domain techniques," *Phys. Rev. A* **23**, 3071–3083, 1981.

[69] Y. Pu, J. Wu, M. Tsang, and D. Psaltis, "Optical parametric generation in periodically polled $KTiOPO_4$ via extended phase matching," *Appl. Phys. Lett.* **91**, 131120, 2007.

[70] V. Giovannetti, S. Lloyd, and L. Maccone, "Quantum-enhanced positioning and clock synchronization," *Nature* **412**, 417–419, 2001.

[71] V. Giovannetti, S. Lloyd, and L. Maccone, "Positioning and clock synchronization through entanglement," *Phys. Rev. A* **65**, 022309, 2002.

[72] D. A. B. Miller, "Time reversal of optical pulses by four-wave mixing," *Opt. Lett.* **5**, 300–302, 1980.

[73] M. Tsang and D. Psaltis, "Spectral phase conjugation with cross-phase modulation compensation," *Opt. Express* **12**, 2207–2219, 2004.

[74] D. Marom, D. Panasenko, R. Rokitski, P.-C. Sun, and Y. Fainman, "Time reversal of ultrafast waveforms by wave mixing of spectrally decomposed waves," *Opt. Lett.* **25**, 132–134, 2000.

[75] M. Tsang and D. Psaltis, "Spectral phase conjugation by quasi-phase-matched three-wave mixing," *Opt. Commun.* **242**, 659–664, 2004.

[76] W.-F. Cheong, S. A. Prahl, and A. J. Welch, "A review of the optical properties of biological tissues," *IEEE J. Quantum Electron.* **26**, 2166–2185, 1990.

[77] B. Picinbono and E. Boileau, "Higher-order coherence functions of optical fields and phase fluctutations," *J. Opt. Soc. Am.* **58**, 784–789, 1968.

[78] A. S. Deif, *Advanced Matrix Theory for Scientists and Engineers*, Abacus, New York, 2nd ed., 1991.

[79] F. B. Hildebrand, *Advanced Calculus for Applications*, Prentice Hall, New York, 2nd ed., 1976.